

## PDF hosted at the Radboud Repository of the Radboud University Nijmegen

The following full text is a publisher's version.

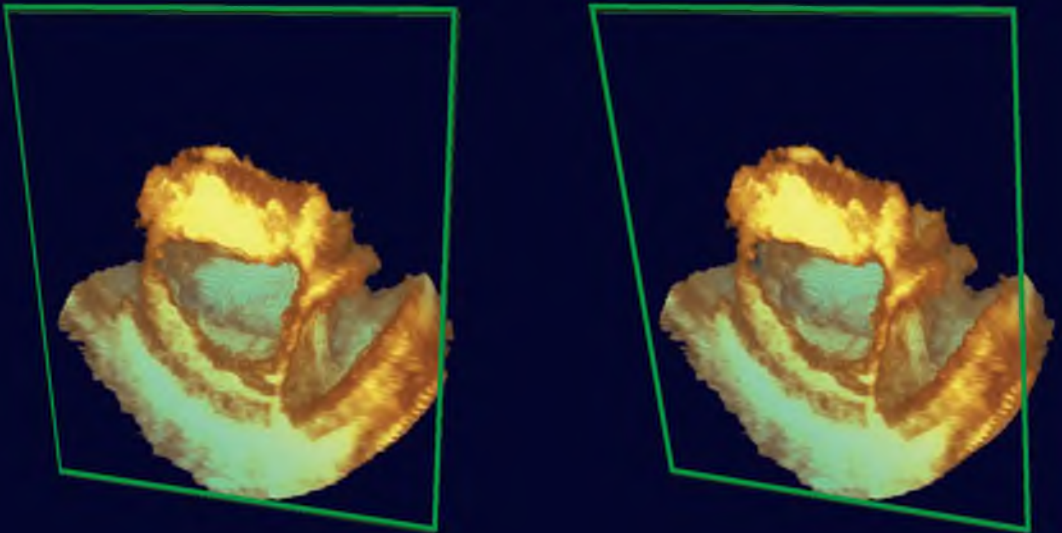
For additional information about this publication click this link.

<http://hdl.handle.net/2066/87192>

Please be advised that this information was generated on 2017-12-06 and may be subject to change.

# 2D and 3D Ultrasound Strain Imaging:

Methods and *in vivo* Applications



Richard Lopata

# **2D AND 3D ULTRASOUND STRAIN IMAGING**

**METHODS AND *IN VIVO* APPLICATIONS**

**RICHARD G.P. LOPATA**

2D and 3D ultrasound strain imaging: Methods and *in vivo* applications.  
Lopata, Richard G.P  
Thesis, Radboud University Nijmegen

ISBN 978-90-9025713-6

Typesetting and cover design in Adobe Indesign CS4  
Printed by Ipskamp Drukkers, Enschede, the Netherlands

© R.G.P. Lopata, Eindhoven, The Netherlands, 2010

All rights reserved. No part of this publication may be reproduced, stored in a retrieval system, or transmitted, in any form, or by any means, electronic, mechanical, photocopying, recording, or otherwise, without the prior written consent from the author.

The lyrics of 'Echoes', written by Pink Floyd, are property and copyright of their owners, Pink Floyd Ltd and EMI Records Ltd.

The lyrics 'Good Vibrations', written by Brian Wilson, Michael Love and Tony Asher, are property and copyright of their owners, Irving Music (BMI) and Nonesuch Records.

The lyrics of 'The Show Must Go On', written by Queen, are property and copyright of their owners, Queen and EMI Records Ltd.

# 2D AND 3D ULTRASOUND STRAIN IMAGING

METHODS AND *IN VIVO* APPLICATIONS

EEN WETENSCHAPPELIJKE PROEVE OP HET GEBIED VAN DE  
MEDISCHE WETENSCHAPPEN

PROEFSCHIFT

TER VERKRIJGING VAN DE GRAAD VAN DOCTOR  
AAN DE RADBOUD UNIVERSITEIT NIJMEGEN  
OP GEZAG VAN DE RECTOR MAGNIFICUS PROF. MR. S.C.J.J. KORTMANN  
VOLGENS HET BESLUIT VAN HET COLLEGE VAN DECANEN  
IN HET OPENBAAR TE VERDEDIGEN OP VRIJDAG 3 DECEMBER 2010  
OM 12.00 UUR PRECIES.

DOOR

RICHARD GODFRIED PAULUS LOPATA  
GEBOREN OP 27 FEBRUARI 1980  
TE OOSTERHOUT

### ***Promotores***

Prof. dr. ir. J.M. Thijssen

Prof. dr. R. de Groot

### ***Copromotores***

Dr. ir. C.L. de Korte

Dr. L. Kapusta

### ***Manuscriptcommissie***

Prof. dr. ir. C.C.A.M. Gielen (voorzitter)

Prof. dr. ir. D.F. Stegeman

Prof. dr. T. Delhaas, Maastricht University Medical Center

This research is supported by the Dutch Technology Foundation STW, which is the applied science division of NWO, and the Technology Programme of the Ministry of Economic Affairs (project number 06466).

Financial support by the Netherlands Heart Foundation for the publication of this thesis is gratefully acknowledged.

# CONTENTS

|                           |   |
|---------------------------|---|
| - CHAPTER 1: INTRODUCTION | 5 |
|---------------------------|---|

## PART-I: METHODS

|  |     |
|--|-----|
| - CHAPTER 2: 2D STRAIN IMAGING USING LINEAR ARRAY RF-DATA                                      | 25  |
| - CHAPTER 3: IMPROVED 2D STRAIN IMAGING USING FREE-SHAPE KERNELS OF RF-DATA                    | 51  |
| - CHAPTER 4: 2D STRAIN IMAGING USING SECTOR SCAN RF-DATA                                       | 69  |
| - CHAPTER 5: COMPARISON OF ONE-DIMENSIONAL AND TWO-DIMENSIONAL LEAST-SQUARES STRAIN ESTIMATORS | 85  |
| - CHAPTER 6: CORRELATION-WEIGHTED TRACKING OF TISSUE   | 103 |

## PART-II: 3D CARDIAC IMAGING

|   |     |
|---|-----|
| - CHAPTER 7: CARDIAC BIPLANE STRAIN IMAGING .....   | 113 |
| - CHAPTER 8: CARDIAC THREE-DIMENSIONAL STRAIN IMAGING .....                               | 131 |
| - CHAPTER 9: THREE-DIMENSIONAL SEGMENTATION OF THE HEART USING TEMPORAL INFORMATION ..... | 145 |

## PART-III: NON-CARDIAC APPLICATIONS

|   |     |
|---|-----|
| - CHAPTER 10: 2D STRAIN IMAGING IN VESSELS                  | 165 |
| - CHAPTER 11: 2D STRAIN IMAGING IN MUSCLES: THE CLEFT LIP   | 183 |
| - CHAPTER 12: BIPLANE STRAIN IMAGING IN MUSCLES: THE BICEPS | 195 |

|  |     |
|--|-----|
| <b>DISCUSSION &amp; SUMMARIES</b>                |     |
| - CHAPTER 13: DISCUSSION .....                   | 213 |
| - CHAPTER 14: SUMMARY                            | 221 |
| - CHAPTER 15: SAMENVATTING                       | 227 |
| <br>   |     |
| <b>REFERENCES</b>                                | 233 |
| <br>   |     |
| <b>PUBLICATIONS, AWARDS &amp; CONFERENCES</b>    |     |
| - PEER-REVIEWED PAPERS IN INTERNATIONAL JOURNALS | 249 |
| - AWARDS   | 251 |
| - CONFERENCE PROCEEDINGS                         | 252 |
| - CONFERENCE PRESENTATIONS                       | 255 |
| <br>   |     |
| <b>ACKNOWLEDGEMENTS / DANKWOORD</b>              | 259 |
| <br>   |     |
| <b>CURRICULUM VITAE</b>                          | 265 |



*"I'M NOT A GENIUS, I'M JUST A HARD -WORKING GUY"*  
- BRIAN D. WILSON (1996)

*"THE BIGGER THE BETTER ... IN EVERYTHING!"*  
- FREDDIE MERCURY (1980)

---

Overhead the albatross hangs motionless upon the air  
And deep beneath the rolling waves  
In labyrinths of coral caves  
The echo of a distant tide  
Comes willowing across the sand  
And everything is green and submarine.

...

(- *Echoes* by Pink Floyd)

---

---

# CHAPTER 1

## INTRODUCTION

ULTRASOUND  
STRAIN IMAGING  
OUTLINE

---



## ULTRASOUND

Ultrasound imaging, or echography, is used in clinical practice since the late 50s. Echography is known for its bed-side applicability, relatively low costs, non-invasive nature, absence of radiation hazard and high temporal resolution. These aspects make echography the imaging modality of choice for fetal imaging and cardiac applications (echocardiography). However, ultrasound is also used to image muscles, liver, kidneys, thyroid, breasts, brain and blood vessels. Furthermore, no adverse effects of ultrasound have become evident and international consensus is that present day equipment can be safely used in clinical practice.

### *Physics of ultrasound*

In general, ultrasound is defined as acoustic, or mechanical waves with a frequency that exceeds the range of the human hearing (> 20 kHz). Ultrasound imaging is based on the propagation and reflection of sound, with a frequency over 1 MHz, in biologi-

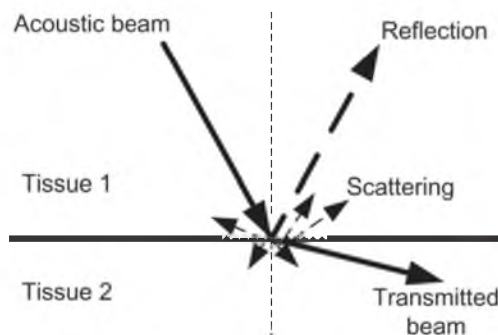


Figure 1.1 Schematic representation of the reflection and scattering of acoustic waves in tissue. It must be noted that scattering also occurs within tissue.

cal tissues and blood. With the introduction of new transducer materials and increased performance of electronic circuits, nowadays frequencies up to 50 MHz are used. The wavelength of the ultrasound wave propagation can be calculated using:

$$\lambda = \frac{c}{f} \quad (1.1)$$

with:

- $\lambda$  the wave length [m]
- $c$  the speed-of-sound in the tissue [m/s]
- $f$  the used ultrasound frequency [Hz].

The high frequency vibrations are generated by piezoelectric elements in the ultrasound probe, or ultrasound transducer. Piezoelectric material has the ability to transform electrical voltage into mechanical movement, *e.g.*, vibrations, and vice versa.

Ultrasound images are characterized by their often noisy appearance and hard reflections. Reflections are caused by transitions in acoustic impedance. The characteristic acoustic impedance (plane wave propagation) of tissue is defined as:

$$Z = \rho \cdot c \quad (1.2)$$

where;

- $Z$  the acoustic impedance [Ra]
- $\rho$  the tissue mass density [kg/m<sup>3</sup>].

If the impedance of two adjacent tissues differs, the ultrasound will be (partially) reflected (Fig. 1.1). These reflections result in bright edges in the ultrasound image. If the difference in impedance is high, for instance at the transition of liver ( $\rho = 1.0$  kg/dm<sup>3</sup>,  $c_{\text{speed}} = 1550$  m/s) and bone ( $\rho =$

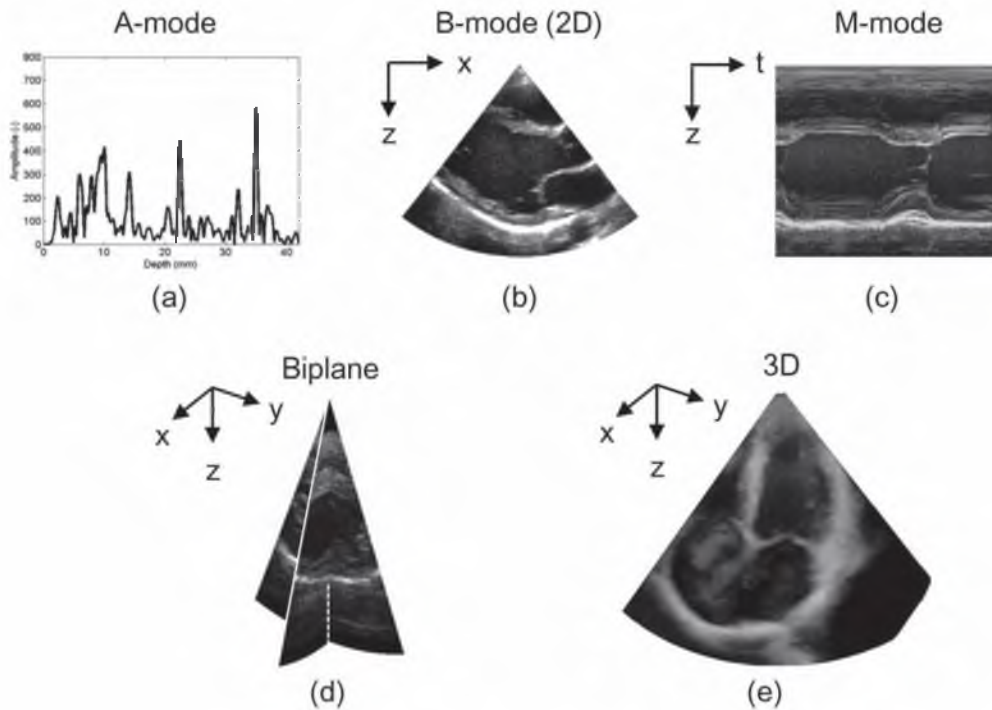


Figure 1.2 Different types of ultrasound data; a) A-mode; b) B-mode image of the heart; c) M-Mode image of the heart; d) Biplane image of the heart; e) 3D volume image of the heart.

$1.95 \text{ kg/dm}^3$ ,  $c_{\text{speed}} = 4000 \text{ m/s}$ ), almost total reflection occurs. Hence, a shadow is seen below the bone, caused by the large energy loss of the propagating ultrasound waves. For similar reasons, the lungs cannot be imaged using ultrasound.

The texture of the ultrasound images is caused by interference. Small structures in the tissue, such as blood cells, collagen fibers and micro-vessels, will act as scattering sources. These so-called point scatterers reflect the ultrasound omnidirectionally (Fig. 1.1). Interference of these backscattered waves at reception by the transducer will result in either amplification or damping of the resulting local wave amplitude. This interference pattern, also known as 'speckle', is seen in the 2D ultrasound images as small

white blobs and this speckle pattern may be somewhat different for different tissues. For instance, liver will have a smooth, granular appearance, whereas muscle images show a very coarse pattern, caused by the reflecting muscle fiber fascia.

In general, the transfer of the acoustic power  $P$  [W] can be described as:

$$P_{\text{transmission}} = P_{\text{reflection}} + P_{\text{scattering}} + P_{\text{absorption}} \quad (1.3)$$

The first term at the right of this equation occurs at interfaces between large anatomical structures. The second term at the right stands for reflections by small reflecting structures. Because the main part of the scattering is not directed towards the transducer, the scattered waves will be

finally absorbed. The last term represents the proportion of acoustic energy that is not available for echographic imaging because that part is absorbed by the tissue and directly transferred into heat. At the used diagnostic frequencies and transmission powers, the total resulting heat is not harmful for the patient. All in all, the acoustic power will be reduced at larger depths. The correspondingly lower wave pressure amplitude will decrease both the image brightness and the penetration depth. This phenomenon is known as attenuation. The attenuation is depending on depth according to a negative exponential containing the attenuation coefficient per unit of distance. This coefficient is approximately linearly dependent on the frequency of the ultrasound. Therefore, in logarithmic units, the attenuation coefficient in biological media is expressed in  $[\text{dB}/(\text{cm} \cdot \text{MHz})]$ . In most biological media the attenuation coefficient is on the order of  $0.5 [\text{dB}/(\text{cm} \cdot \text{MHz})]$ .

### *Imaging modes*

Figure 1.2 shows examples of the four, most commonly used ultrasound images. The A-mode (amplitude display) is a single echo-line, visualized on screen as a function of depth (Fig. 1.2a). A group of neighboring image-lines in so-called “brightness” mode (B-mode) display and scanned with a multi-element transducer, reveals a two-dimensional (2D) image of the tissue (Fig. 1.2b). This is the most commonly used imaging mode in ultrasound and it is known as the B-mode image. By sweeping or steering in the direction perpendicular to the B-mode

scan plane as well, biplane or three-dimensional (3D) volume images can be acquired (Fig. 1.2d-e). Furthermore, the times-series of a single A-line in brightness mode can be used to visualize motion of the tissue, which is known as M-mode (Fig. 1.2c).

Another application of ultrasound is Doppler imaging, which is used to assess blood flow in vessels, for instance in the coronary arteries of heart. There are several Doppler techniques, but an extensive discussion is beyond the scope of this thesis.

Next to the different imaging modes, contrast-enhanced ultrasound is available and seems especially beneficial for cardiovascular diagnosis, tissue perfusion studies and for local drug delivery.

The ultrasound transducer acquires the raw ultrasound data, also referred to as radio frequency (RF-)data (see Fig. 1.5 for an example). The B-mode image data are post-processed RF-data. In this thesis, first of all the RF-data is band-pass filtered. Next, the signal envelope is detected using the Hilbert transform for calculating the analytical signal and perform AM demodulation. Finally, log-compression is applied to enhance contrast. Several other cosmetic procedures are used in commercial equipment to improve images on screen, such as persistence (temporal averaging) and color look-up-tables.

### *Resolution & Transducers*

The temporal resolution of ultrasound data depends on the number of transmitted and received ultrasound signals per unit of time (*i.e.*, pulse repetition rate) and the image

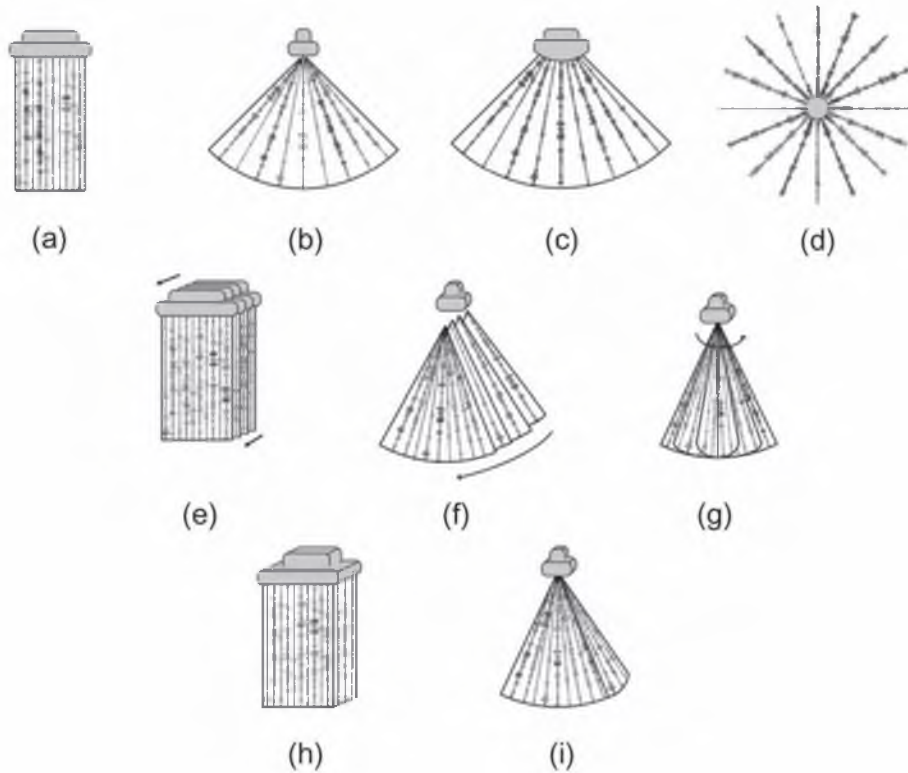


Figure 1.3. Two-dimensional and three-dimensional ultrasound probes; a) linear array transducer; b) phased array transducer; c) curved array transducer; d) intravascular transducer; e) mechanical 3D linear array (sweep); f) mechanical phased array; g) rotating phased array; i) linear matrix array; j) phased matrix array.

depth. For a single ultrasound beam, the depth  $d$  determines the echo acquisition time:

$$\Delta T = 2d/c \quad (1.4)$$

where the factor of 2 occurs because the ultrasound echo travels the distance from transducer to reflecting structure and back to the transducer. Consequently, acquiring  $N$  echo lines for a 2D image will increase the acquisition time  $N$  times and reduce the imaging rate (*i.e.*, frame rate) by a factor  $N$ .

The spatial resolution of ultrasound images depends on the used transducer

configuration and frequency. Along the ultrasound beam (the axial direction), the spatial resolution is defined by the length of the transmitted ultrasound pulse. A large bandwidth is beneficial to create a short ultrasound pulse, and hence to yield a higher spatial resolution.

The resolution perpendicular to the ultrasound beam (the lateral direction) depends primarily on the central frequency, and on the effective size of the transmitting aperture and the depth of the focus (*i.e.*, the f-number). So a high frequency yields a high lateral resolution. A drawback for the use of high frequency ultrasound is the



tissue penetration. The attenuation increases for higher frequencies (see previous section) and, hence, reduces penetration depth. So, high frequencies yield higher spatial resolution at the cost of image depth. For this reason, low frequency transducers (1-5 MHz) are more suitable for imaging large or deep-laying structures, such as the heart or the aorta.

Figure 1.3 shows the large variety of transducers, each with their own specific purpose. Linear arrays produce a rectangular grid with equally spaced ultrasound beams (Fig. 1.3a). Here, the spatial sampling rate is basically limited by the distance between the piezoelectric elements of the transducer, the pitch. Modern linear array transducers operate with a sub-array of, *e.g.*, 17 elements, to be able to achieve adequate beam focusing and preserve a reasonable number of scan lines as well.

A large number of transducers are designed to acquire sector scan images (Fig. 1.3b-c). These sector scans are displayed in a polar coordinate system. Therefore, the lateral sampling width is depth-dependent and not easily quantified. Sector scans are especially suited for imaging of non-superficial structures that require a large image view at greater depth. For instance, most echocardiographic images are acquired in sector scan format using a phased array transducers. The phased array transducer uses always all its elements to create beam steering and focusing. The smart use of delays results in an ultrasound beam that is steered over a range of different directions. When using this electronic steering, the angle may range from -45 to 45 degrees, or more. Hence, the resulting image repre-

sents a quarter of a circle. The advantage of a phased array transducer is its relatively small footprint, making it an excellent transducer for imaging the heart when positioned in between the ribs. A special type of sector scanning transducers is the convex (curved) array (1.3c). The surface of this array is curved but the electronic steering is identical to that of the flat linear array, thus extending the image view at greater depth while keeping a reasonable area width at shallow depths. This type of transducer is used *e.g.*, for abdominal diagnosis and for trans-fontanel scanning of the brain in neonates.

Besides electronic steering of elements of a transducer, motorized steering of the whole array is used. In doing so, all the elements are translated and/or rotated mechanically. This allows a array to perform a 'sweep' or a translation and image a 2D circular image for intravascular applications (Fig. 1.3d) or three-dimensional (3D) volume by acquiring a series of adjacent 2D images (Fig. 1.3e-g). The volume rate of mechanical 3D scanning is limited to around five volumes/s. Matrix-array transducers basically consist of a 2D array of small elements and have the capability of acquiring a whole volume ('pyramid') at a moderate volume rate of 20 - 70 Hz (Fig. 1.3h-i). However, at such high volume rates the acquired volumes are not large enough to image, for instance, the entire heart. For that reason, ECG-gated acquisition of sub-images is used to obtain a full 3D volume in four to seven consecutive heart beats.

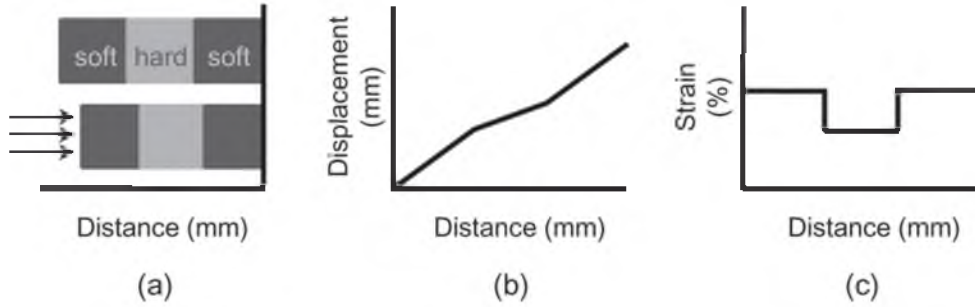


Figure 1.4 a) Model of one-dimensional tissue deformation for two soft materials and one hard material before and after compression; b) The relative displacement of the total tissue; c) the strain of the total tissue. The center tissue is less compressed due to higher stiffness.

## STRAIN IMAGING

Strain is defined as the relative deformation, *i.e.*, shortening or expansion, of structures due to an internal or external force. A one-dimensional example, illustrating tissue deformation and strain in one direction, is given in figure 1.4. If tissues with different stiffness are compressed by a force (Fig. 1.4a), the tissues will move and deform in the direction of that force (Fig. 1.4b). The strain [%] can be defined as:

$$\varepsilon = \frac{l_{new} - l_{old}}{l_{old}} \quad (1.5)$$

with  $l_{old}$  the original length of the tissue and  $l_{new}$  the compressed or extended length of the tissue. The strain reveals that the middle tissue compresses less than the surrounding tissue (Fig. 1.4c). This implies that the tissue is stiffer, or less elastic. Tissue elasticity is mostly defined as the Young's modulus [kPa]:

$$E = \frac{\sigma}{\varepsilon} \quad (1.6)$$

where  $\sigma$  is the stress in the tissue. A high Young's modulus indicates a high degree of tissue stiffness.

In the early nineties, Ophir et al. (1991) published their first findings on ultrasound strain imaging. Results showed the feasibility of measuring tissue strain by correlating 1D segments of raw ultrasound (radio frequency, RF-) data and thereby providing a strain image (see also Fig. 1.9a-b). Previous research was concerned mostly with measuring propagation of mechanically induced tissue vibrations (Parker et al. 1990; Nightingale 1995; Yamakoshi et al. 1998) and with Doppler-based techniques that were initially developed for blood flow measurements but were also applied on tissue (Trahey et al. 1988; Bohs & Trahey 1989; de Jong et al. 1990). Although cross-correlation techniques had been investigated earlier (Yagi et al. 1988), most studies involved A-mode ultrasound (Dickinson et al. 1982; Yagi et al. 1988) and M-mode (Adler et al. 1990).

At first, only one-dimensional (1D) segments of RF-data were correlated with those in the RF-lines in the next frame (Fig. 1.5). The cross-correlation peak of the

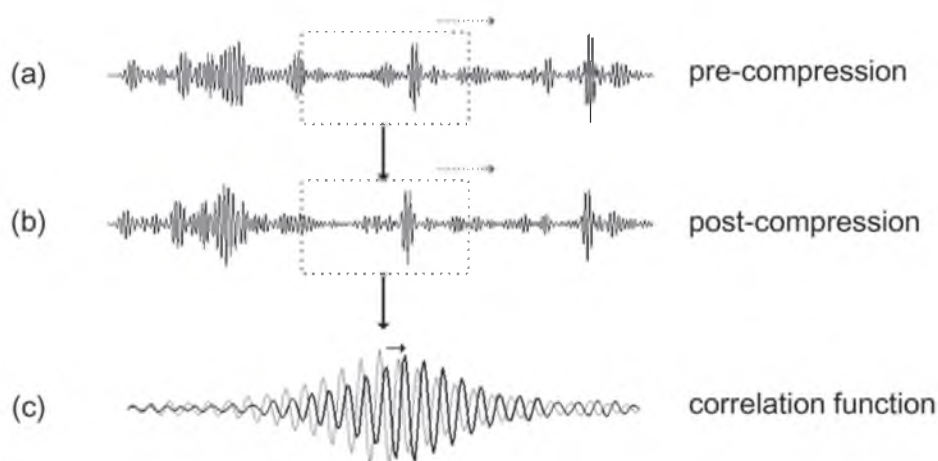


Figure 1.5 a) RF-line obtained in frame  $i$ ; b) RF-line obtained in frame  $i + 1$ ; c) The auto-correlation of RF-line a) (grey) and the cross-correlation of rf-line a) and b) (black). Please note the shift of the cross-correlation with respect to the auto-correlation function, indicating the displacement of the tissue.

RF- data windows was detected to obtain the displacement along the ultrasound beam, *i.e.* the axial displacement (Fig. 1.5). Next, the first-order spatial derivative of the displacement was calculated to obtain the strain data (Ophir et al. 1991; Kallel et al. 1998).

The Young's modulus was also reconstructed by Ophir et al (1991). Quantifying the Young's modulus has the advantage of obtaining an absolute measure of tissue elasticity, whereas strain images are still depending on the applied load. Controlled compression of the *in vitro* tissue with an external compression device enabled reconstruction of tissue elasticity since the applied stress was known, yielding so-called 'elastograms'. Figure 1.6 shows examples of B-mode images and elastograms for two types of tumors. The tumors seem indistinguishable in the B-mode images. However, a large contrast between tumor and surrounding tissue is observed in the elastograms (Fig.

1.6b and Fig. 1.6d), caused by the higher Young's modulus of the stiff tumor tissue. The elastograms provide more information on tissue structure than the B-mode images, which can also be judged from figure 1.7 where the elastograms of a kidney (Fig. 1.7a-c) and prostate (Fig. 1.7d-f) are shown.

After Ophir's 1991-paper, a vast amount of research was performed by several groups, mostly concerning strain imaging of tissues that were compressed with an external device, the so-called 'quasi-static' approach. *In vivo* application of the technique was shown in tumor (Ophir et al. 1999, Garra et al. 1997), breast (Céspedes et al. 1993a; Krouskop et al. 1998), kidney (Emelianov et al. 1995; Kallel et al. 1998), muscle tissue (Céspedes et al. 1993a; Kallel et al. 1998), prostate (Krouskop et al. 1998; Khaled et al. 2006) and deep venous thrombosis (Rubin et al. 2005).

Several other strain estimation approaches were investigated, such as

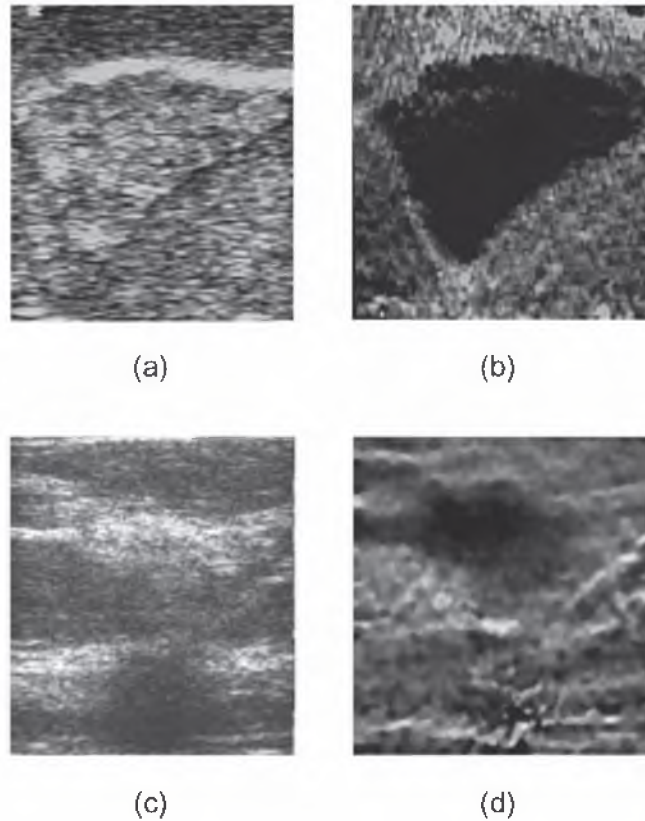


Figure 1.6 Examples of B-mode images and their corresponding elastograms; a) B-mode of a breast carcinoma *in vitro* and b) The corresponding elastogram; c) B-mode image of an *in vitro* invasive ductal carcinoma and d) The corresponding elastogram. Figures provided by and reproduced with kind permission of prof. dr. J. Ophir, University of Texas Medical School, Texas, USA.

adaptive strain estimation (Alam et al. 1998). Basically, the RF-data were stretched for a pre-defined range of strains and the best match was found using cross-correlation. The group of O'Donnell introduced zero-phase crossing estimation (Lubinski et al. 1999), a technique that yielded sub-sample displacement estimates by interpolating the (linear) phase signal of the cross-correlation function near the location of the cross-correlation peak. Spectral strain estimation, detection of changes in the spectrum of the RF-data was introduced by Konofagou et al. (1999).

In the late nineties and beyond, the technique was also applied in dynamic studies where the tissue strain is induced by a physiological deformation source or by contraction of the tissue itself. Applications of RF-based strain were found in arteries (de Korte et al. 1997; Maurice et al. 2008, chapter 10), the heart (Heimdal et al. 1998; d'Hooge et al. 2000a; Konofagou et al. 2000, chapter 7) and skeletal muscles (Deffieux et al. 2008 ; Chapter 12). The major problem with dynamic applications is the fact that tissue movement is uncontrolled, opposed to the quasi-static method,

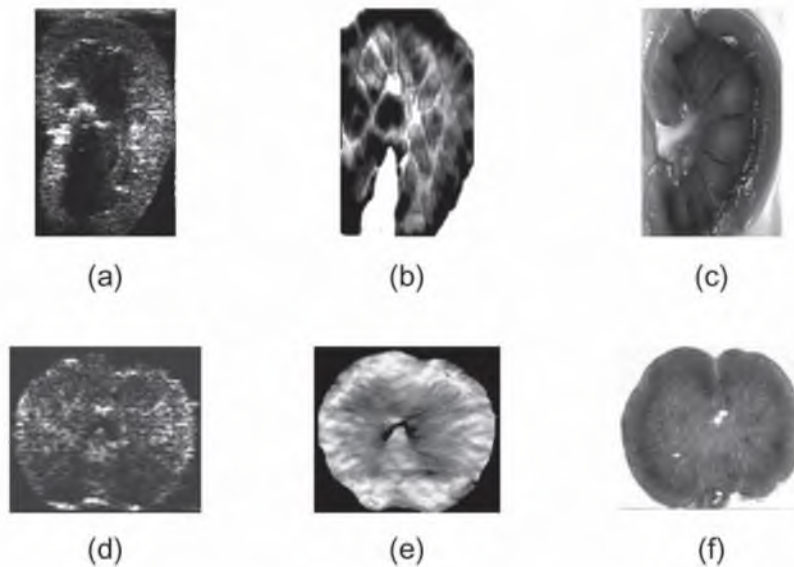


Figure 1.7 Examples of *in vitro* tissue elasticity imaging; a) B-mode image of a human kidney; b) Corresponding elastogram of the kidney; c) Picture of the dissected kidney; d) B-mode image of a canine prostate; e) Corresponding elastogram of the prostate; f) Histology image of the prostate. Figures provided by and reproduced with kind permission of prof. dr. J. Ophir, University of Texas Medical School, Texas, USA

and can be relatively large. However, large motion is not the major issue anymore. In general, RF-based strain measurements show the highest level of accuracy and precision for a deformation range of 0.1 – 5.0% (Varghese et al. 1997), depending on the signal-to-noise ratio and the used window size (see Chapter 2 and Céspedes et al 1999). If the frame rate of the ultrasound system is relatively low, the strain in the tissue can exceed this fundamental limit when comparing two consecutive images.

### *Two-dimensional strain imaging*

Two-dimensional strain imaging finds its main application in the heart. Initially, cardiac motion was assessed using colour mode 2D Tissue Doppler Imaging (TDI,

McDicken et al. 1992). However, the main disadvantage was the lack of ability to measure relative motion, *i.e.*, strain. This was overcome by Heimdal et al (1998), who introduced Tissue Doppler Imaging based strain rate imaging. This one-dimensional approach allowed for semi real-time strain rate and derived strain imaging, but required high 2D frame rate imaging. The main disadvantage, however, was the angle dependency. For two-dimensional strain estimation, the use of 2D data windows is required. This is not trivial, since the ultrasound data lack phase information in the lateral direction. Using conventional B-mode images, 2D speckle tracking techniques were already introduced to track tissue motion (Bohs and Trahey 1991; Chaturvedi et al. 1998; Ramamurthy and Trahey 1991). This speckle tracking yielded

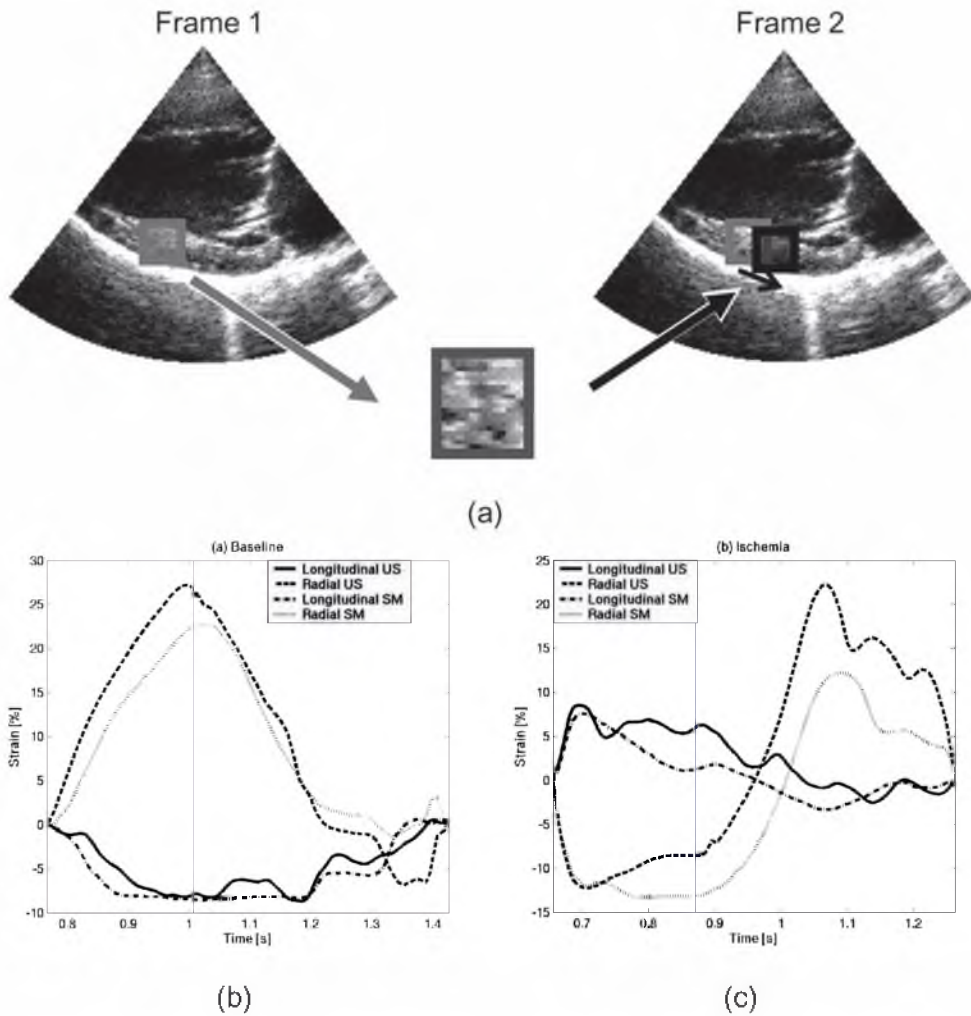


Figure 1.8 Cardiac 2D strain imaging: a) Schematic representation of 2D B-mode speckle tracking. A small segment of image frame 1 is matched with image data within the next frame 2; b) Typical longitudinal and radial strain curves of the myocardium over one cardiac cycle. The curves are measured with both ultrasound strain imaging (black) and sonomicroscopy (grey); c) Strain curves of one cardiac cycle within the ischemic heart. Figures provided by and reproduced with kind permission of dr. J. d’Hooge, Catholic University of Leuven, Leuven, Belgium.

2D deformation at relatively low frame rates and was angle independent (Leitman et al. 2004). However, speckle tracking required more processing and was, therefore, not real-time. This method was particularly popular for cardiac applications, since the large tissue motion and deformation makes matching of RF-data quite challenging.

However, the use of B-mode data resulted in a relatively lower sensitivity with respect to the TDI-based and RF-based strain techniques. An example of 2D speckle tracking is shown in figure 1.8.

Parallel to these developments, 1D and 2D RF-based strain imaging was performed in the heart (d’Hooge et al. 2000; d’Hooge

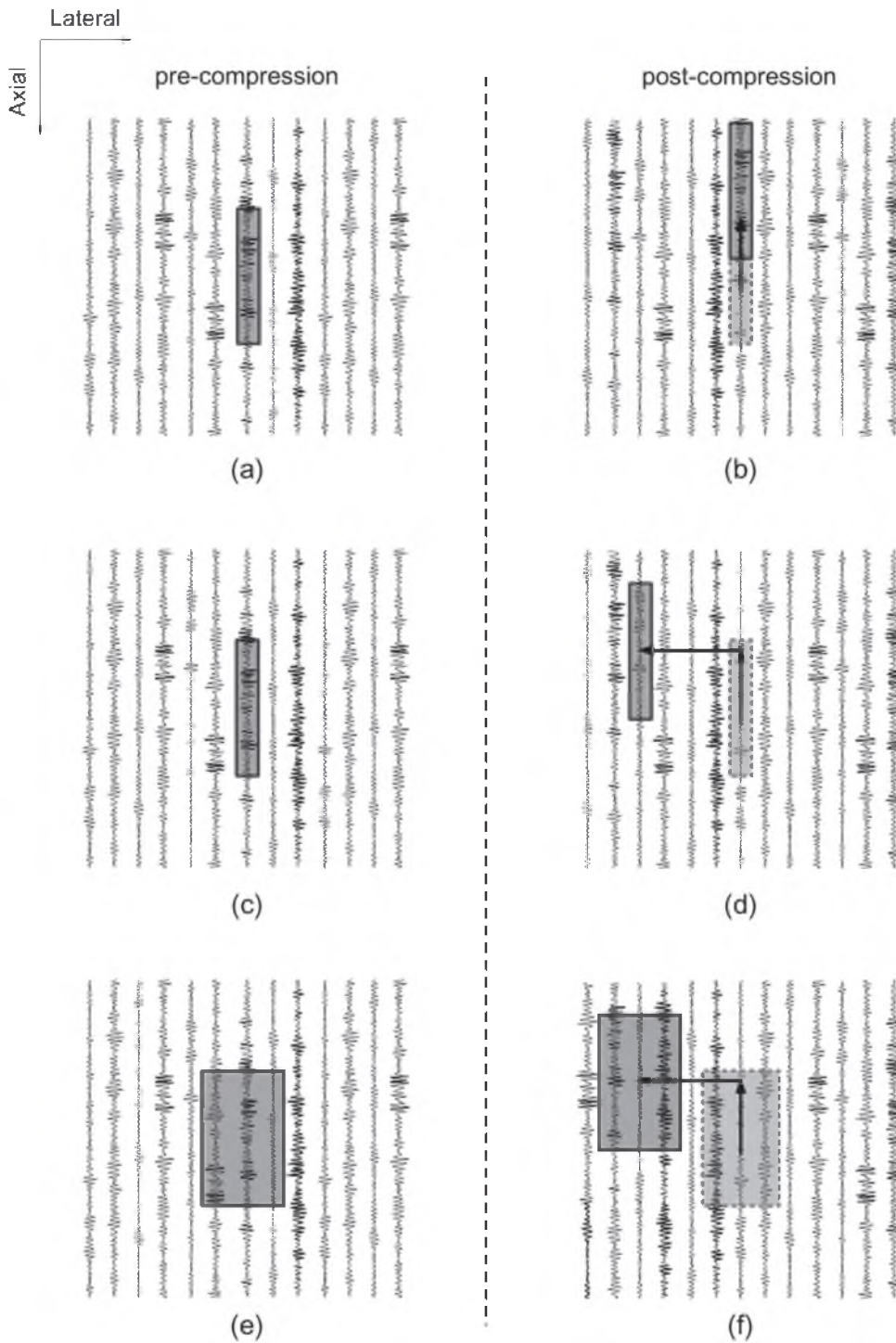


Figure 1.9 Schematic representation of displacement estimation using a) 1D pre-compression RF-data in b) a 1D post-compression search area; c) 1D pre-compression RF-data in d) a 2D post-compression search area; e) 2D kernels of pre-compression RF-data in f) a 2D post-compression search area.

et al. 2002a; Konofagou et al. 2002; Sutherland et al. 2004; Langeland et al. 2005a; Lee et al. 2007 ; Chapter 7). The use of RF-data enhances performance but requires a higher frame rate compared to speckle tracking. Furthermore, since RF-data is not commercially available, research on these technique remains limited to academia.

It was shown by Konofagou and Ophir (1998) that RF-data can be used to track both axial and lateral tissue motion by cross-correlating 1D pre-compression data with 2D post-compression data (Fig. 1.9c-d). The use of 2D pre- and post-compression data windows (Fig. 1.9e-f) was reported by several groups using cross-correlation (this thesis) and other pattern matching functions such as the sum-of-absolute-differences (Langeland et al. 2005). An extension of the zero-phase crossing method was provided by Chen et al. (2004) using synthetic, lateral phase.

The movement of tissue and presence of strain will lead to de-correlation of the RF-data, which can be depicted as a decrease in data similarity. Methods to re-correlate the data have been proposed for both 1D (Varghese et al. 1995) and 2D strain imaging methods (Konofagou and Ophir 1998, Chapter 2). Proper re-correlation of RF-data will result in a higher accuracy and precision of the strain data. Additionally, less high frame rates are required, enabling application of the technique to commercially available data, acquired at relatively low frame rate.

### *Three-dimensional strain imaging*

The introduction of three-dimensional ultrasound systems boosted research on 3D strain imaging. Biplane strain imaging was reported using RF-data acquired with mechanical probes (Yoshikawa et al. 2005) and matrix array transducers (Chapter 7 and 12). Biplane data yields the deformation in two orthogonal planes.

However, strain estimation using 3D full volume data is necessary to assess the full 3D strain tensor within 3D space. Meunier et al. (1998) and Konofagou & Ophir (2000b) investigated the effect of motion, deformation and rotation on the precision of 3D speckle tracking and strain imaging. Three-dimensional B-mode data was processed to estimate tissue motion and deformation using reconstructive 3D TDI (Støylen et al. 2003), 3D speckle tracking data (Chen et al. 2005; Jia et al. 2007; Song et al. 2007; Saito et al. 2008; Crosby et al. 2008) and image registration (Elen et al. 2008).

The use of RF-data for 3D tracking vs. conventional envelope data was investigated by Yu et al. (2006). Only few studies reported the first (preliminary) results on 3D RF-based strain imaging (Lindop et al. 2006; Said et al. 2006; Patil et al. 2007; Lopata et al. 2007). The sub-optimal temporal resolution of 3D (+ time) datasets remains a problem in particular in cardiological applications. However, new ultrafast 3D techniques ultrasound imaging techniques are on the rise (Deffieux et al. 2008) and may relax the present limitations.



## OUTLINE OF THESIS

In this thesis, the use of raw, radio frequency (RF) data for 2D and 3D strain imaging in actively deforming tissues is examined. The possible advantage of 2D RF-based displacement and strain imaging was examined.

In Chapter 2, different methods, interpolation schemes and the use of local alignment and stretching were examined for both RF-data processing and B-mode speckle tracking methods. The use of multi-scale displacement estimation was investigated as well as the dependency of strain accuracy on the used processing parameters. The methods were extended in Chapter 3 by allowing deformation of the used 2D data segments in order to improve correlation even further. The latter method was compared with conventional 1D and 2D displacement estimation and was applied on data of shearing and rotation structures. The applicability of the proposed methods was examined for phased array data (Chapter 4) and the accuracy of the displacement and strain estimates was reported. Furthermore, the use of 1D and 2D least-squares strain estimators was compared in Chapter 5. A tracking algorithm is illustrated in

Chapter 6 that transforms the frame-to-frame displacement estimates in the total, accumulated coordinates of the tissue over an entire contraction/relaxation cycle in deforming tissue. This is necessary to obtain the absolute strain for the entire contraction/relaxation cycle, rather than just measuring frame-to-frame strain, *i.e.*, strain rate.

In Chapter 7, the proposed methodology was applied to the heart. Ultrasound BiPlane strain imaging was performed in a study on the effect of a valvular aortic stenosis. The first *in vivo* results of this pilot study are presented, revealing both the feasibility and the possible clinical applications. Next, the 2D methodology was expanded to full 3D strain imaging and tested on 3D(+t) volume data of the heart in young children, yielding 3D strain within the heart (Chapter 8). The resulting cross-correlation data were also used as an additional feature for automated segmentation of the endocardium in the left ventricle (Chapter 9). However, the possible application of 2D and 3D strain imaging is not confined to the heart.

Furthermore, 2D ultrasound strain imaging was performed in vessels (Chapter 10) and in skeletal muscles (Chapter 11 and 12).



---

.

...

Cloudless everyday you fall upon my waking eyes  
Inviting and inciting me to rise  
And through the window in the wall  
Come streaming in on sunlight wings  
A million bright ambassadors of morning

...

...

.

(- *Echoes* by Pink Floyd)

---

---

# Part - I

---

---

# METHODS

---



---

# CHAPTER 2

## 2D STRAIN IMAGING USING LINEAR ARRAY RF-DATA

---

*Richard G.P. Lopata, Maartje M. Nillesen, Hendrik (Rik) H.G. Hansen,  
Inge H. Gerrits, Johan M. Thijssen & Chris L. de Korte*

---

Based on: **Performance Evaluation of Methods for Two-Dimensional Displacement and Strain Estimation using Ultrasound Radio Frequency Data.** R.G.P. Lopata, M.M. Nillesen, H.H.G. Hansen, I.H. Gerrits, J.M. Thijssen and C.L. de Korte, *Ultrasound in Medicine & Biology* 2009; 35(5): 796-812.

---

## ABSTRACT

In elastography, several methods for two-dimensional strain imaging have been introduced, based on both raw frequency data (RF) and speckle-tracking. Although the precision and lesion detectability of axial strain imaging in terms of SNRe and CNRe have been reported extensively, analysis of lateral precision is still lacking. In this paper, the performance of different 2D correlation RF- and envelope-based strain estimation methods was evaluated using simulation data and phantom experiments. Besides window size and interpolation methods for sub-sample displacement estimation, the influence of re-correlation techniques was examined. Precision and contrast of the measured displacements and strains were assessed using the difference between modeled and measured displacements, elastographic signal-to-noise ratio (SNRe) and contrast-to-noise ratio (CNRe). In general, a 2D coarse-to-fine displacement estimation method is favored, using envelope data for window sizes exceeding the theoretical upper bound for strain estimation. Using 2D windows of RF data resulted in better displacement estimates for both the axial and lateral direction than 1D RF-based or envelope-based techniques. Obtaining sub-sample lateral displacement estimates by fitting a pre-defined shape through the cross-correlation function (CCF) yielded results similar to those obtained with up-sampling of RF-data in the lateral direction. Using a CCF model was favored because of the decreased computation time. Local aligning and stretching of the windows (re-correlation) resulted in an increase of 2 – 17 and 6 – 7 dB in SNRe for axial and lateral strain estimates, respectively, over a range of strains (0.5 – 5.0%). For a simulated inhomogeneous phantom (2.0% applied strain), the measured axial and lateral SNRes were 29.2 and 20.2 dB, whereas, the CNRes were 50.2 dB and 31.5 dB, respectively. For the experimental data, lower SNRe (axial: 28.5 dB; lateral: 17.5 dB) and CNRe (axial: 39.3 dB; lateral: 31 dB) were found. In conclusion, a coarse-to-fine approach is favored using RF-data on fine scale. The use of 2D parabolic interpolation is favored to obtain sub-sample displacement estimates. Re-correlation techniques, such as local aligning and stretching, increase SNRe and CNRe in both directions.



## INTRODUCTION

In ultrasound strain imaging, or elastography, the displacement and deformation of tissue are estimated using pre- and post-compression image data. The strain data provide insight into the elastic properties of tissues (Ophir et al. 1991; Ophir et al. 1999). Deformation of tissue can be caused by either passive (or quasi-static) tissue compression (Céspedes et al. 1993a), or by an active process such as contraction of skeletal or cardiac muscle tissue (D'hooge et al. 2000; Kallel et al. 1998) or pulsatile blood flow in the arteries (de Korte et al. 2000a). One-dimensional (1D) strain imaging, the measurement of axial strain along the ultrasound beam, has been widely adopted and the possibilities and limitations in resolution, accuracy and detectability have been investigated (Céspedes et al. 1997; Kallel et al. 1996b; O'Donnell et al. 1994; Ophir et al. 1991; Varghese and Ophir 1997). However, tissue motion and deformation are not limited to a single dimension. Most tissues exhibit anisotropic mechanical and functional properties, compressibility and viscoelastic behavior. Hence, the necessity for measuring two-dimensional (2D) and even three-dimensional (3D) strain is evident.

Measuring strain in the lateral and elevational directions implies that the strain is assessed perpendicular to the ultrasound beam. Lateral resolution and the absence of direct phase information in the lateral direction results in lower accuracy for lateral strain estimates. Several approaches for 2D displacement and strain estimation were

reported in literature, based on both RF-data and signal envelope (speckle-tracking). The first 2D displacement, and velocity estimation methods were developed for blood flow velocity estimation (Trahey et al. 1988). For elastography, similar speckle-tracking methods were adapted using 2D data windows to estimate the displacements in both directions (Bohs and Trahey 1991; Chaturvedi et al. 1998; Ramamurthy and Trahey 1991). However, speckle-tracking resulted generally in noisy lateral displacement images (Lubinski et al. 1996). In addition to speckle-tracking, RF-based methods are commonly used, for instance in cardiac applications (Langeland et al. 2004). Furthermore, phase information was used for 2D displacement estimation (Chen et al. 2004). Konofagou introduced a highly accurate lateral displacement tracking method using 1D raw frequency data windows and weighted linear interpolation of existing RF-lines (Konofagou and Ophir 1998). This study implied that the use of 1D pre-compression windows of RF-data is preferred.

However, another study reported no significant difference between using 1D and 2D windows in cardiac applications (Langeland et al. 2005b). In addition to a difference in lateral window size, the axial window size is chosen independently and often with a lack of foundation. The axial window size is not always necessarily fixed, as for instance, in multi-resolution strain imaging (Varghese et al. 1998a). Furthermore, the so-called multi-step algorithms were recently introduced, using a variable, decreasing axial window size (Lopata et al. 2006; Shi and Varghese 2007).

Besides different approaches in terms of window size, the methods for sub-sample displacement estimation are diverse also. Up-sampling of RF or envelope data in the lateral direction is often used (Konofagou and Ophir 1998; Langeland et al. 2004) as well as fitting a pre-defined shape through the peak of the cross-correlation function (Konofagou and Ophir 1998; Langeland et al. 2003). In literature, no comparison can be found between these different interpolation schemes for lateral sub-sample displacement estimation.

Signal de-correlation caused by a relatively large compression of scattering particles is a major source of error in strain estimation. Temporal stretching has been successfully used to decrease the effects of de-correlation (Varghese et al. 1996). However, in an *in vivo* setting (arteries, heart, etc), the applicability of this technique seems troublesome. Adaptive strain estimation techniques have been introduced (Alam et al. 1998), as well as the use of initial strain estimates for local stretching of signal windows (Lopata et al. 2005). To our knowledge, a proper evaluation of the benefits of these techniques for the accuracy of the axial and lateral strain components is not available.

In this chapter, the performance of different strain estimation methods and strategies is evaluated when using 2D windows of RF-data and windows of signal envelope data. A single resolution approach is compared with a coarse-to-fine approach. The influence of the window size in both directions is investigated as well as the performance of the most commonly used interpolation methods for sub-sample displacement estimation. Enhancing signal correlation is

also known as re-correlation (Konofagou and Ophir 2000b). The benefit of re-correlation techniques, such as local aligning and stretching, in terms of axial and lateral strain accuracy, is examined in homogeneous and inhomogeneous tissue models. The accuracies of the various methods are compared using finite element modeling, simulated ultrasound data and experimental data obtained in gelatin/agar phantoms. The displacement errors are assessed by comparing the measured displacements with the finite element models. Furthermore, elastographic signal-to-noise and contrast-to-noise ratio are used to quantify the accuracy and detectability of the axial and lateral strain measurements for the different approaches.

## **MATERIALS**

### *Simulation study*

A simulation study was performed for proper validation of displacement and strain estimation methods. The major advantages of simulated data are *a priori* knowledge of the governing translation and deformation within the structure that is imaged, as well as the well controlled signal-to-noise ratio (SNR). Two different phantoms were simulated with Finite Element Modeling (FEM), using SEPRAN software (Septra BV, The Hague, NL) on a Unix platform. First, a three-dimensional model of a homogeneous, isotropic cubic phantom (5 cm x 5 cm x 5 cm) was simulated. This block was assumed

to be linearly elastic and incompressible (Poisson ratio of 0.495). Secondly, an identical block was constructed with a hard cylindrical inclusion (diameter = 1.0 cm) in the center of the phantom. The latter model is commonly used for algorithm validation and contrast-to-noise analysis of strain images. The model was originally developed as a soft tissue mimicking phantom with a hard lesion or tumor (Céspedes et al. 1993a; Kallel et al. 1996b; Ponnekanti et al. 1995). Again, incompressibility of the material was assumed (Poisson ratio = 0.495) and the linear elasticity modulus of the cylinder ( $E_{\text{inclusion}} = 60 \text{ kPa}$ ) was four times higher than that of the surrounding tissue ( $E_{\text{background}} = 15 \text{ kPa}$ ). Three-dimensional linear-elastic elements were used to solve the FEM for an applied deformation in the vertical direction (axial deformation). For the homogeneous phantom, the applied axial strains were 0.5%, 1.0%, 2.0% and 5.0%. The inhomogeneous phantom was simulated for an applied axial deformation of 2.0%. The FEM solutions for the inhomogeneous phantom are shown in figure 2.1a-d. The ranges of axial and lateral displacements are listed in Table 2.1.

Linear 2D images (Fig. 2.1e-f) of the deforming phantoms were simulated using the Field II© simulation software (Jensen 1996; Jensen and Svendsen 1992). The characteristics of the simulated US system were chosen to correspond closely with the transducer (L3-11) of the SONOS 7500 real-time 3D system (Philips Medical Systems, Bothell, USA) used for the phantom experiments. A linear array was simulated, with a 7.5 MHz center frequency. The total number of elements

was set to 288, using 64 elements in transmit mode and 128 elements in receive with a pitch of 135  $\mu\text{m}$  and an element height of 6 mm. The distance between lines was equal to the pitch. The aperture in transmission and receive had a fixed lateral and elevation focus at 70 mm (*i.e.* the focus is set below the phantom). Dynamic focusing was used in transmit and receive mode, with focal zones every 2.0 mm. The simulation was performed for 225 RF-lines, representing a rectangular sector with a depth of 70 mm and a width of 30.4 mm. The sampling frequency used to digitize the RF-data was 60 MHz.

First, a 3D matrix of randomly distributed scatterers was generated using MATLAB© (The Mathworks Inc., Natick, MA, USA). The maximum beam width at -20dB in the lateral and elevational direction was determined to be 2.5 mm and 8.0 mm, respectively. This implies that only scatterers within a 4.0 mm radius will actually contribute to the resulting RF-line. Therefore, a slice of only 5 cm x 5 cm x 1 cm in the middle part of the entire scatter-matrix was sufficient for 2D image simulation. The total amount of scatterers within this slice was  $3.5 \cdot 10^6$ , fulfilling the requirement that the smallest sampling volume should at least contain 10 scattering particles. When this criterion is met, fully developed speckle is guaranteed in the simulated US image (Oosterveld et al. 1985). The scatterers were moved according to the FEM solutions describing the movement within the phantom after applying the deformation. Since only 2D US data were simulated, the modeled elevational movement was not taken into account in this study to avoid de-correlation

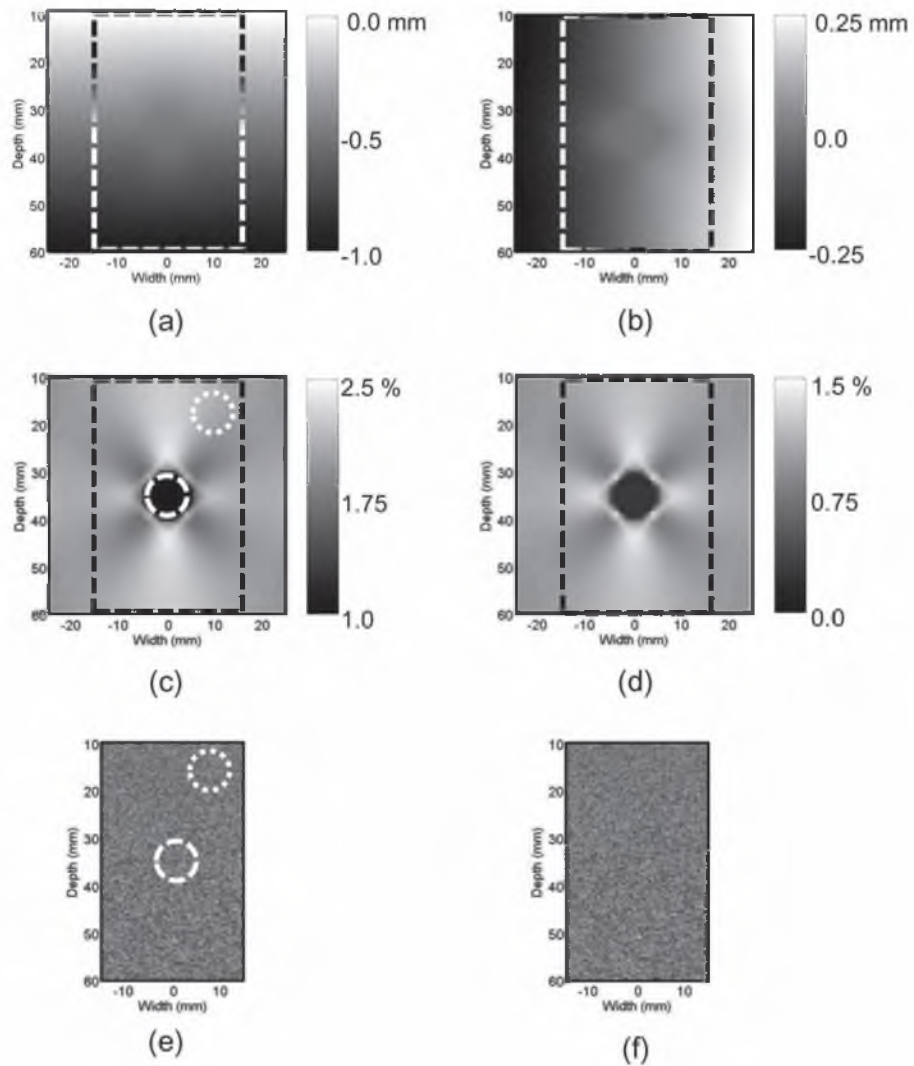


Figure 2.1 The solutions of the finite element model; the displacement in axial direction (a) and lateral direction (b) and the strain in axial (c) and lateral (d) direction. The dashed, rectangular region corresponds to the field of view of the simulated US images. Simulated US images of an inhomogeneous phantom before (e) and after 2.0% compression (f). The white, dashed circle indicates the ROI within the inclusion and the white, dotted circle is the background region-of-interest, both used for SNR<sub>e</sub> and CNR<sub>e</sub> analysis.

caused by out-of-plane motion. Using these simulation settings and models, RF-data was simulated for both phantoms for each level of compression. Examples of B-mode images are shown in figure 2.1e-f.

### *Phantom Study*

The homogeneous and the inhomogeneous tissue-mimicking phantoms that were used in the simulation study were

**Table 2.1 Displacements and strains in the simulated homogeneous phantom.**

| Applied axial strain (%) | Lateral strain (%) | Axial displacements (mm) | Lateral displacements (mm) |
|--------------------------|--------------------|--------------------------|----------------------------|
| -0.5                     | 0.25               | -0.25 – 0                | -0.06 – 0.06               |
| -1.0                     | 0.50               | -0.50 – 0                | -0.12 – 0.12               |
| -2.0                     | 0.99               | -1.00 – 0                | -0.25 – 0.25               |
| -5.0                     | 2.48               | -2.00 – 0                | -0.62 – 0.62               |

also constructed for experimental validation. First, a homogeneous phantom was made of 8.0% by weight gelatin (Dr. Oetker, Ede, The Netherlands) solution in water. An additional 1.0% by weight agar-agar (Boom, Meppel, The Netherlands) was added to the solution for stiffening of the gelatin. Tissue scattering was mimicked by scattering particles (40 - 63  $\mu\text{m}$  SiC, E. Merck, Darmstadt, Germany) of which 2.0% by weight was added to the gelatin / agar solution. The same solution was used for the surrounding tissue of the inhomogeneous phantom. The stiff cylinder was made with 8.0% by weight gelatin and 3.0% by weight agar-agar and 1.0% by weight scattering particles. Based on earlier findings reported by our group, the experimental Young's Moduli should be approximately  $123 \pm 2$  kPa in the inclusion and  $36 \text{ kPa} \pm 0.5$  kPa in the surrounding tissue (de Korte et al. 1997b). Hence, the higher agar concentration will result in an approximately four times stiffer inclusion (de Korte et al. 1997b; Madsen et al. 2005). A rod with a diameter of 1.0 cm was placed in a cubic-shaped mold (10 x 10 x 10 cm), before the gelatin solution with 1.0% agar

was added. During solidification of this block, scattering particles tended to sink towards the bottom of the block. Therefore, a lower concentration of scattering particles was added to the inclusion mixture, resulting in equal brightness of both the cylinder and the background tissue. After solidification of the mixture, the cylinder was removed and the remaining space was filled with the 3.0% agar-gelatin solution.

### *RF acquisition*

The raw 2D ultrasound data were recorded with a SONOS 7500 real-time 3D system (Philips Medical Systems, Bothell, USA), equipped with a 2D linear array transducer (L11-3) with a central frequency of 7.5 MHz. The radio-frequency data were digitized at a sampling rate of 39 MHz and transmitted to a PC-based workstation using a USB 2.0 interface. The gelatin/ agar-agar phantoms were deformed using an automated plate compressor set-up. The rigid top plate was translated vertically by a micromanipulator at a resolution of 20  $\mu\text{m}$ . The transducer of the ultrasound system

was anchored in the center of the top plate. The phantoms were lubricated at the top and bottom side to fulfill free-slip boundary condition. The phantoms were lubricated at the top and bottom side to fulfill free-slip boundary condition. Since the gelatin-agar phantoms are visco-elastic, a minimum of ten conditioning cycles was performed before each data acquisition. The phantom was compressed by lowering the top plate over a distance of 2.0 mm, *i.e.* a maximum of 2.0% applied strain. Ultrasound data were acquired after applying the deformation while no motion occurred.

## METHODS

A 2D algorithm was developed to estimate displacements and strains in the axial (depth) and lateral (width) direction. The displacements were estimated using both the RF- data and the demodulated data (*i.e.* signal envelope). In general, a pre-compression window was correlated with a window in the post-compression data that was larger in both dimensions, thus automatically defining (and limiting) the possible axial and lateral displacements. The axial and lateral displacements were estimated simultaneously by calculating the shifts of the peak of the cross-correlation function (CCF) in both directions. Whether to apply the CCF to the RF- data or to the envelope data is discussed in the next section. All algorithms were implemented in MATLAB (The Mathworks Inc., Natick, MA, USA).

The remaining section of the Methods

section follows the same structure as the Results for clarity and comparison. For all simulation settings, please consult Table 2.2.

### *2D coarse-to-fine displacement estimation*

Opposed to a 2D approach with a fixed window size, an iterative coarse-to-fine approach was chosen (Chen et al. 2007; Lopata et al. 2006; Shi and Varghese 2007) for initially finding the global displacements of the signal windows at a coarse scale. The resolution in the axial direction was refined at each iteration step by decreasing the window size in the axial direction by a factor 2 down to the desired resolution. The overlap of the windows in the axial direction was set to 75% of the used window size. The maximum shift in the axial direction was fixed at 50% of the used window size. In other words, a decrease in window size resulted in a decrease of the maximum possible displacement of the peak in the axial direction, assuming that previous displacements were valid and accurately estimated. The sub-sample resolution of the displacement estimates was achieved by fitting a parabolic function through the peak of the CCF in both directions. The axial displacement estimates were smoothed using a median filter with a fixed size of 2.4 mm x 1.5 mm. Considering the lower resolution in the lateral direction, lateral displacements were filtered with a 2.4 mm x 2.7 mm median filter. The filtered displacements were used as input for subsequent iterations. The coarse displacement estimates were linearly interpolated to a finer scale and used

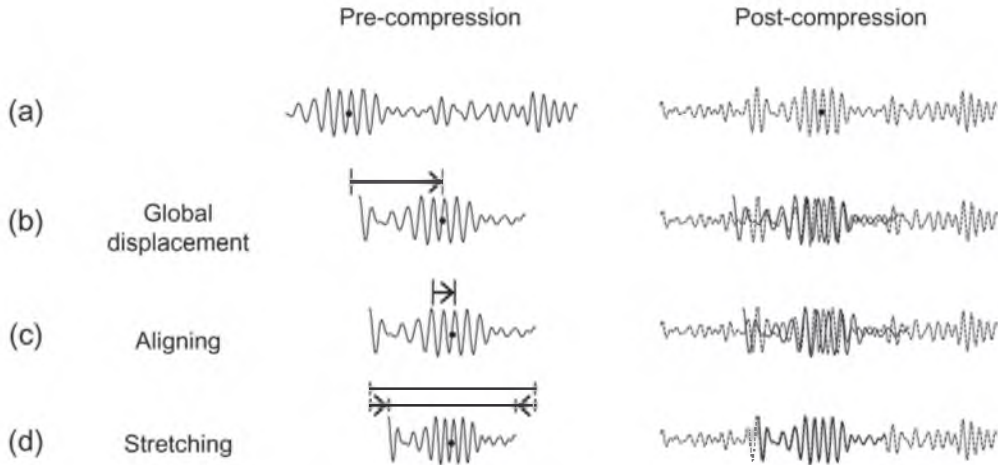


Figure 2.2. Schematic representation of the different steps of the displacement estimation method (left column) and the effect of compression on signal correlation (right column). Segments of simulated RF-data (a) at equal depth before (left) and after (right) compression are used. The black dot indicates the center point of the used signal window. During the coarse-to-fine iterative procedure (b), global displacements are estimated and used in consecutive iterations to align the pre- and post-compression signal windows (right). In the next step (c) the signals are aligned at sub-sample level (left) using interpolation to enhance correlation (right). In the final step of local stretching (d), a previous strain estimate is used to deform the signal (left) for final re-correlation (right).

to move the centre of the post-compression window in a next window. The errors in the axial and lateral displacement estimation were investigated using the simulation data. An error is present since deformation of the structure will cause de-correlation of the data. Furthermore, the data in the lateral direction are under-sampled and no phase information can be used in this direction to calculate displacements.

First, two comparative studies were executed between conventional displacement estimation and the iterative coarse-to-fine method for a range of: a) axial kernel sizes; b) lateral kernel sizes. Conventional displacement estimation denotes a single step cross-correlation of pre- and post-compression data and not at multiple scale. Furthermore, the influence of kernel sizes was examined for both RF-based and

envelope-based displacement estimation. The axial and lateral displacements were estimated, using both RF-data and signal envelope, for a decreasing axial pre-compression size from coarse (4.0 mm) to fine scale (0.13 mm) and a fixed lateral window size (Table 2.2). For the conventional method, a fixed post-compression window size of 8.0 mm x 1.5 mm was used. For the coarse-to-fine method, the axial post-compression window was set to be two times larger than the pre-compression window, resulting in a decreasing post-compression axial kernel size at finer scale.

In earlier studies, 1D or 2D pre-compression windows were correlated with large 2D windows for assessment of lateral displacement (Konofagou and Ophir 1998; Langeland et al. 2004). Using larger post-compression window sizes enables tracking

**Table 2.2 Overview of the performed simulations and the different settings and conditions in the simulation study.**

|                                       | 2D displacement estimation:<br>Axial window size |  | 2D displacement estimation:<br>Lateral window size |   |
|---------------------------------------|--|--|--|---|
|                                       | Method tested                                    |  | Method tested                                      |   |
| Coarse-to-fine                        |  |  |  |   |
| Axial window size (pre)               | <i>Coarse-to-fine:</i><br><b>4.0–0.13 mm*</b>    | <i>Conventional:</i><br><b>4.0–0.1 mm*</b> | 4.0, 2.0, 1.0 mm <sup>†</sup>                      |   |
| window size (post)                    | <b>8.0–0.26 mm</b>                               | <b>8.0 mm</b>                              | 8.0, 4.0, 1.0 mm                                   |   |
| Lateral window size (pre)             | 0.68 mm  |  | <i>Coarse-to-fine:</i><br><b>3.40–0.14 mm</b>      | <i>Conventional:</i><br><b>3.40–0.14 mm</b> |
| window size (post)                    | 1.5 mm   |  | <b>3.8–0.55 mm</b>                                 | <b>3.80 mm</b>                              |
| Interpolation method                  | CCF – Parabolic                                  |  | CCF – Parabolic                                    |   |
| Aligning & Stretching                 | No   |  | No   |   |
| Simulated Phantom<br>(applied strain) | Homogeneous ( <b>2.0, 5.0%</b> )                 |  | Homogeneous (2.0%)                                 |   |
| Experimental data<br>(applied strain) | None   |  | None   |   |
| Analysis                              | RMSE displacements (Fig. 3)                      |  | RMSE displacements (Fig. 4)                        |   |

**Bold** indicates that simulation conditions are varied and differ from the other simulations.

\* The displacements were estimated using RF-data and signal envelope for all used window sizes;

§ The displacements were estimated using signal envelope for the largest axial window. RF-data were used for all consecutive steps.

of large lateral displacements, but can result in erroneous lateral displacement estimates when more than one peak in the CCF is present. In general, the lateral window sizes were fixed in this study. However, to examine the influence of window size in the lateral direction, the displacements in both directions were estimated for a pre-compression window size of 1, 3, 5, 11 and 25 lines (0.14 - 3.4 mm) combined with a post-

compression window that was 6 lines larger (see also Table 2.2 for further information). The same range of pre-compression lateral window sizes was also compared with a fixed post-compression window size. In this case, the largest lateral post-compression kernel size of 31 lines (4.19 mm), as used in the previous test, was chosen.

The elastographic signal-to-noise ratio (SNRe) and contrast-to-noise ratio (CNRe)



| Interpolation  | Re-correlation using<br>Aligning & Stretching                             |
|--|---|
| Yes  | Yes   |
| 4.0, 2.0, 1.0 mm <sup>§</sup><br>8.0, 4.0, 2.0 mm                    | 4.0, 2.0, 1.0 mm <sup>§</sup><br>8.0, 4.0, 2.0 mm                         |
| 0.68 mm<br>1.5 mm  | 0.68 mm<br>1.5 mm   |
| <b>CCF – Parabolic, cosine, spline</b><br><b>RF – Spline, linear</b> | CCF – Parabolic   |
| No   | <b>Method tested</b>  |
| Homogeneous (2.0%)   | Homogeneous ( <b>0.5, 1.0, 2.0, 5.0%</b> )<br><b>Inhomogeneous</b> (2.0%) |
| None   | <b>Inhomogeneous (2.0%)</b>   |
| RMSE displacements (Fig. 5)<br>Computation time (Table 2.3)          | Strain images (Fig. 6, 8, 9)<br>SNRe, CNRe (Fig. 7, 10)                   |

are commonly used in the field of elastography to assess the accuracy of strain estimation methods (Bilgen and Insana 1997; Varghese and Ophir 1997):

$$SNR_e = \frac{\mu}{\sigma} \quad (2.1)$$

$$CNR_e = \frac{2(\mu_{background} - \mu_{inclusion})^2}{\sigma_{background}^2 + \sigma_{inclusion}^2} \quad (2.2)$$

where  $\mu$  is the mean measured strain, and  $\sigma$  is the standard deviation of the measured strain in a region-of-interest. However, the magnitude of the measured SNRe or CNRe can be strongly influenced by the choice of regularization method, the amount of smoothing and the choice of strain estimator. In the simulation study, the exact displacements and strains can be retrieved from the finite element models. Hence,

the error between modeled and measured, unfiltered, displacements was available and used as a measure of displacement estimate accuracy, avoiding any effects of smoothing and strain estimators. In this study, the root-mean-squared error (RMSE) of the estimated displacement values was used:

$$RMSE = \sqrt{\frac{\sum_{i=1}^M \sum_{j=1}^N (\delta_{i,j}^{meas} - \delta_{i,j}^{model})^2}{MN}} \quad (2.3)$$

where  $\delta_{i,j}^{meas}$  is the measured displacement on pixel coordinates  $(i,j)$  and  $\delta_{i,j}^{model}$  the corresponding displacement value of the finite element model. If the errors are obeying a normal distribution, the RMSE will equal the standard deviation.

### Interpolation

For accurate strain estimation, a sub-sample resolution in the axial direction and a sub-line lateral resolution of the displacements need to be obtained. In a previous study (Lopata et al. 2005), the RF-data (or the signal envelope) were interpolated using a spline interpolation algorithm. In a study by Konofagou et al, (weighted) linear interpolation of the RF-data was performed (Konofagou and Ophir 1998). A sub-line resolution of 1/100th line would require the interpolation of 100 RF-lines in between the measured lines. This is a time consuming process. A different approach could be interpolation of the CCF peak. Both up-sampling, as well as assuming a particular shape of the CCF peak, are possible interpolation schemes. Up-sampling of

the CCF function is still time consuming. However, assuming an analytical shape of the peak leads to straightforward solutions of the peak shift and is, therefore, more computationally efficient. Two examples are a parabolic shape of the CCF peak in the axial direction (Ophir et al. 1991) and fitting a cosine function through the CCF peak (Céspedes et al. 1995; de Jong et al. 1991). These two analytical functions were also used in the lateral direction (Langeland et al. 2003; Lopata et al. 2006). In the present study, the different interpolation schemes are compared. The CCF-peak was interpolated in both directions by fitting a parabolic function (A), fitting a cosine function (B), and by up-sampling the CCF function using spline interpolation (C). Also RF and envelope data were up-sampled using spline interpolation (D), and linear interpolation (E) by a factor of 100. To make a fair comparison between methods A-C and D-E, axial sub-sample displacement estimates are required. However, for methods D-E, new lines were generated by interpolating the RF-data using linear and spline interpolation. The use of such an interpolation technique in the axial direction would result in a very large amount of data (100 times more samples for a displacement resolution of 1/100th sample point). Furthermore, the computational load would become enormous. Hence, a 1D parabolic interpolation of the CCF peak in the axial direction was performed to obtain sub-sample axial displacement estimates for methods D and E. The global displacements were found using the coarse-to-fine algorithm (Table 2.2). In the last iteration, the displacements were estimated using the

five interpolation methods A-E. Again, the accuracy of the unfiltered displacements was estimated by means of RMSE analysis. In this case, the computation time was also monitored.

### *Re-correlation using aligning and stretching*

After obtaining displacements (and strains) at the desired or optimal resolution, further improvement of displacement- and strain accuracy can be obtained by means of so-called aligning and stretching (Alam and Ophir 1997; Lopata et al. 2006; Varghese et al. 1996). During the coarse-to-fine phase of the algorithm, the center of the post-compression window is translated using integer values of the previously measured displacements (Fig. 2.2a-b). However, correlation increases significantly when matching the pre- and post-compression window on sub-sample level in both directions using spline interpolation (Fig. 2.2c). Note that re-aligning should not be confused with up-sampling of the signal for sub-sample displacement estimation.

Global temporal stretching has been reported previously by other groups (Konofagou and Ophir 1998; Varghese et al. 1996). The deformation of the signal due to compression of the scattering particles is partially cancelled, which improves correlation. However, the applicability of global stretching in *in vivo* data is not trivial. After aligning, the axial strain can be estimated. These axial strain estimates are used to perform local stretching of the data (Fig. 2.2d).

The effect of aligning and stretching on the accuracy of displacement and strain estimates was examined using the simulated data of both the homogeneous phantom model (at applied strains of 0.5, 1.0, 2.0 and 5.0%) as for the inhomogeneous phantom (2.0% applied strain). First, the coarse-to-fine algorithm was used, followed by aligning and stretching (Table 2.2). The stretching procedure requires axial strain estimates. Furthermore, the SNRe and CNRe were assessed in addition to the RMSE analysis, thus strain in both directions was needed. A 1D least-squares strain estimator (LSQSE) was used to calculate the axial and lateral strain with a fixed size of 2.9 and 5.4 mm, respectively (Kallel and Ophir 1997). For SNRe and CNRe analysis of the inhomogeneous phantom data, two ROIs were defined, one in the center of the inclusion and one in the background (Fig. 2.1e). SNRe of the inhomogeneous strain images was obtained in the outer region. To examine the effect of measurement noise, random noise was added to the simulation data of the inhomogeneous phantom. The analysis was repeated for decreasing sonographic signal-to-noise ratios (SNRs = 60, 40, 30, 20 and 10 dB).

### *Phantom Study*

In the homogeneous and hard inclusion phantom, the displacements and strains were estimated using the optimal settings as found in the simulation study as described in the previous section.

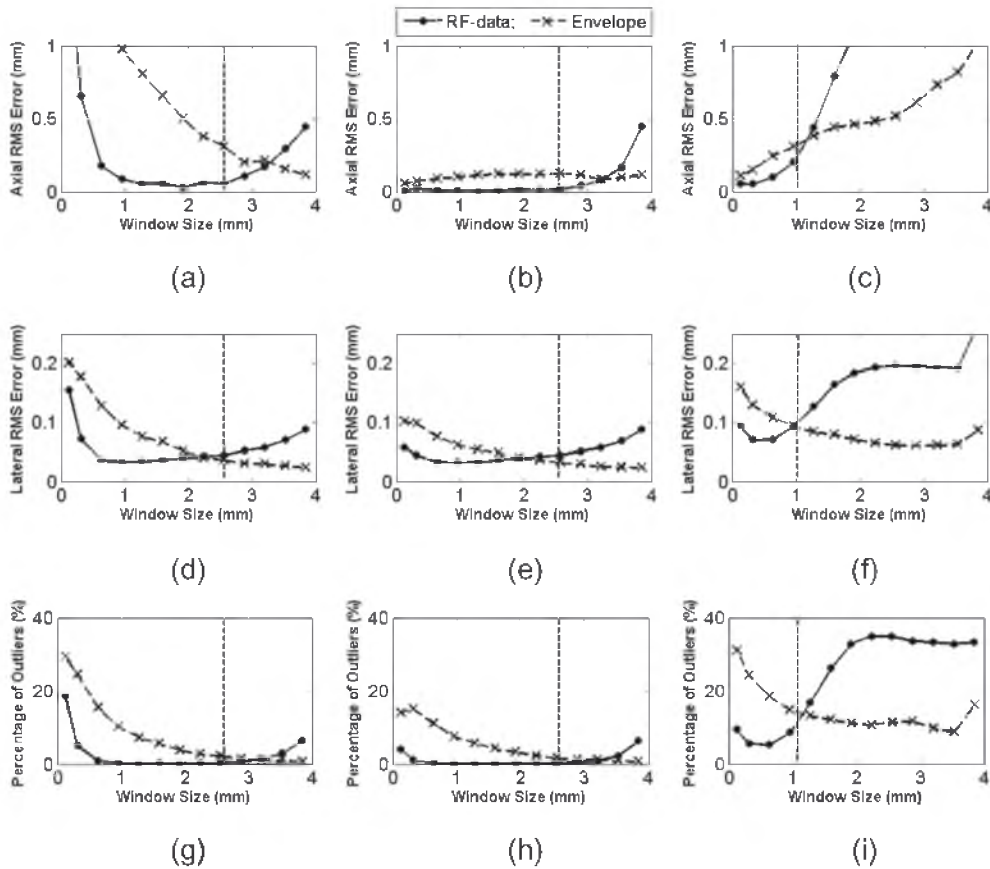


Figure 2.3. The root-mean-squared error of the axial displacements (a-c) and the lateral displacements (d-f) of a homogeneous phantom and the percentage of outliers (g-i) are plotted as function of the pre-compression axial window size (see Table 2.2). In the left column, the RMS error of the axial and lateral displacements and the outliers are shown when using the conventional method and a simulated homogeneous phantom (2.0% applied strain). For the same simulation data, the RMSE values and the percentage of outliers are reported when using coarse-to-fine displacement estimation (middle column). The RMSE of the displacements and outliers are also shown for a homogeneous phantom at an applied strain of 5.0% (right column) using again the coarse-to-fine method. The dashed lines indicate the theoretical upper limit of the axial window size up to which the applied strain can be measured.

## RESULTS

### *2D coarse-to-fine displacement estimation*

The RMSEs of the axial and lateral displacements of the simulated homogeneous

phantom using both RF and envelope data are shown in figure 2.3. For the homogeneous phantom at an applied strain of 2.0%, the axial and lateral displacements become less accurate for decreasing window size when no coarse-to-fine approach is used (Fig. 2.3a, Fig. 2.3d). When the coarse-to-fine algorithm is used, more accurate

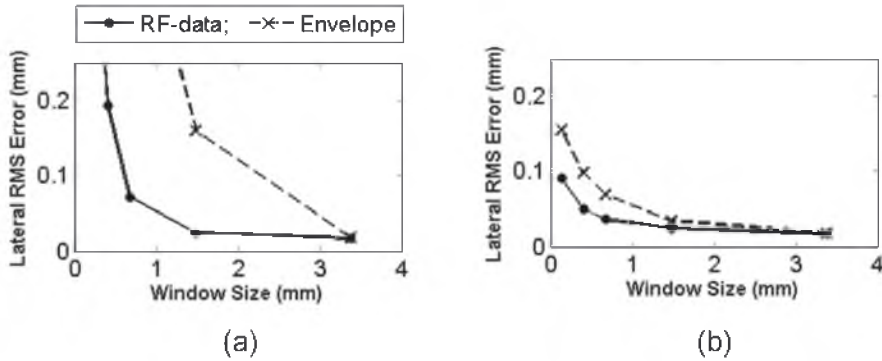


Figure 2.4. Lateral root-mean-squared error for increasing lateral window size; a) when using a fixed post-compression search, and b) when the post-compression window size was relative to the used pre-compression window (see Table 2.2).

displacements are estimated for both RF and envelope data (Fig. 2.3b, Fig. 2.3e). In general, the displacements in both the axial and lateral directions are estimated more precisely when using RF-data and at smaller axial window sizes. In the case of 5.0% applied strain (Fig. 2.3, right column), the RMSE values are higher compared to the RMSE values at 2.0% strain (Fig. 2.3, middle column). As before, RF-based estimates at smaller axial window sizes outperform envelope data. When the cross-correlation had several peaks or a peak at the border of the CCF, erroneous or no displacement estimates were found, so-called ‘outliers’. The percentage of these bad fits is shown in the lower row of figure 2.3. Again, the coarse-to-fine algorithm applied to RF-data, at smaller window sizes, outperforms the conventional displacement estimation method and the use of envelope data. However, at large window sizes, envelope-based displacements are more accurate than RF and are necessary for global displacement tracking.

Figure 2.4 shows the RMSE of the lateral

displacements versus the lateral window size for a large fixed post-compression window size (Fig. 2.4a) and for a window size that is 0.81 mm larger than the pre-compression window (Fig. 2.4b). In general, the RMSE is smaller for a larger lateral window size. Furthermore, the estimates are more accurate at smaller pre-compression lateral window sizes when the post-compression window is adjusted with respect to the pre-compression window size (Fig. 2.4b). The RMSE for the 1D pre-compression window (*i.e.* lateral window size = 0.14 mm) is higher compared to all 2D windows.

### Interpolation

The distributions of the axial and lateral RMSE are shown in figure 2.5 for all five interpolation methods. The errors, computation time and percentage of outliers are listed in Table 2.3. Considering the shape of these histograms, it can be stated that the errors are symmetrically distributed and that the RMSE is practically equivalent

**Table 2.3 Comparison of different interpolation methods.**

| Interpolation Method | Axial Error (mm)  | Lateral Error (mm) | Computation Time (hr-min-s) | Percentage of outliers (%) |
|----------------------|-------------------|--------------------|-----------------------------|----------------------------|
| A) Parabolic 2D(CCF) | $0.07 \pm 15.77$  | $0.21 \pm 38.36$   | 0-4-19                      | 0.16                       |
| B) Cosine 2D (CCF)   | $0.07 \pm 15.77$  | $0.21 \pm 38.34$   | 0-3-57                      | 0.16                       |
| C) Spline 2D (CCF)   | $0.17 \pm 12.72$  | $0.14 \pm 36.60$   | 0-18-37                     | 0.50                       |
| D) Spline (RF)       | $-0.18 \pm 23.97$ | $0.30 \pm 43.99$   | 54-21-16                    | 0.02                       |
| E) Linear (RF)       | $0.01 \pm 22.17$  | $0.50 \pm 44.51$   | 52-43-40                    | 0.02                       |

to the standard deviation. A first glance at the listed standard deviations of the RMSE values (Table 2.3) shows that the lateral accuracy is approximately two times lower for all interpolation methods. The differences between the interpolation methods are small, although the axial and lateral errors for method D and E are slightly higher and lower for method C. However, the high computational load of RF interpolation is illustrated by the relatively long process-

ing time. Since also the number of outliers with no outcome is of the same order for all methods (0 – 0.5%), parabolic or cosine interpolation is a valid method to determine sub-sample displacements.

### *Aligning and stretching*

Figure 2.6 shows the displacements, strains and cross-correlation values of the homoge-

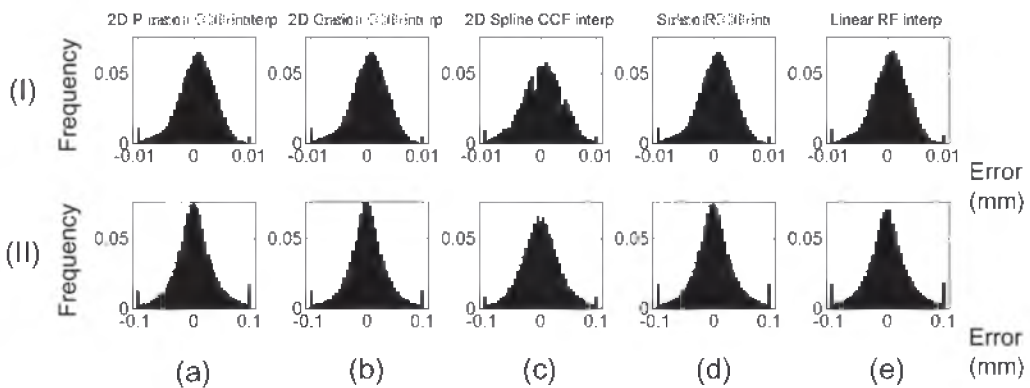


Figure 2.5. Histograms of the error distributions of the unfiltered axial (I) and lateral (II) displacements when the cross-correlation function is interpolated using: a) 2D parabolic interpolation; b) 2D cosine interpolation; c) 2D spline interpolation, and, when the RF-data is interpolated in the lateral direction, using: d) spline interpolation and e) linear interpolation of the RF-data. For the latter two, a 1D parabolic fit of the CCF was performed in the axial direction. The corresponding bias, RMSE, computation time and percentage of outliers are listed in Table 2.3.

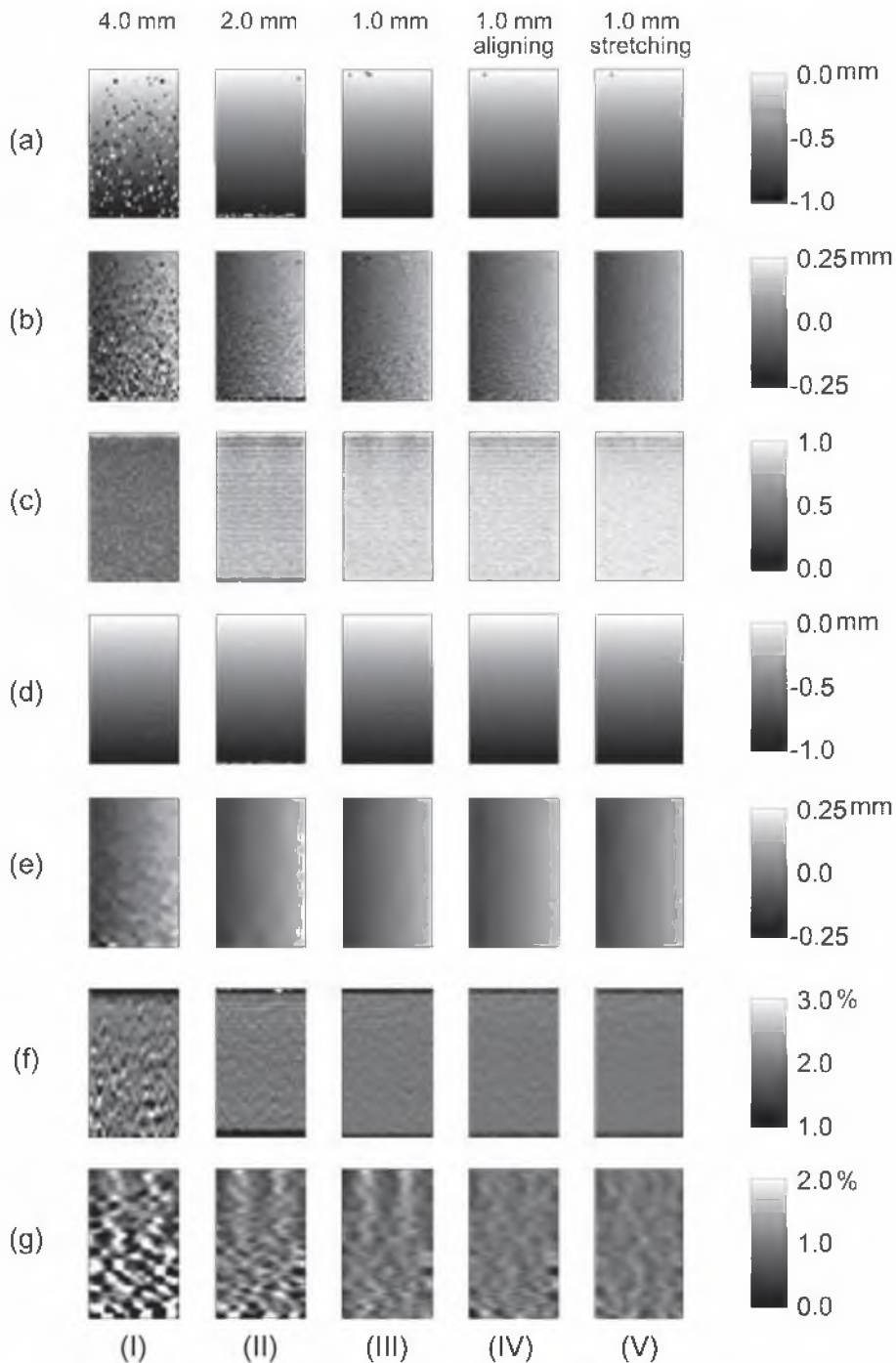


Figure 2.6. Results of the simulation study of the homogeneous phantom at 2.0% applied strain for consecutive steps of the algorithm (see also Table 2.2): a) the unfiltered axial displacement estimates; b) the unfiltered lateral displacement estimates; c) the measured maximum cross-correlation values; d) the filtered axial displacement estimates; e) the filtered lateral displacement estimates; f) the axial strain and g) the lateral strain. First the coarse-to-fine strain estimation was performed (I-III), followed by aligning (IV) and stretching (V).

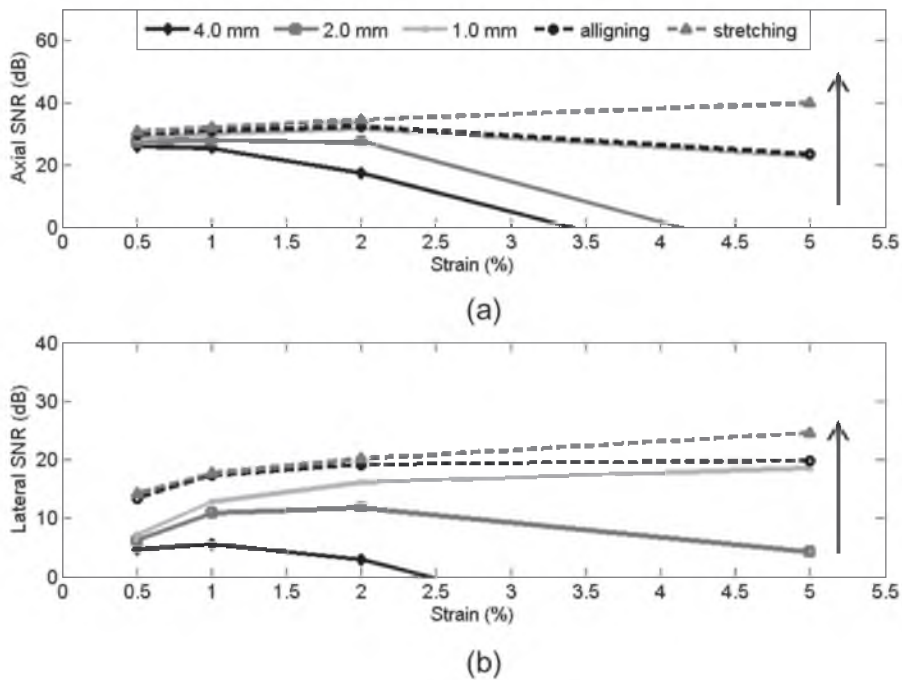


Figure 2.7. The calculated elastographic signal-to-noise ratio (SNRe) for the simulated homogeneous phantom as a function of applied strain for all steps of the algorithm. The SNRe was calculated for the axial strain (a) and lateral strain (b).

neous phantom (2.0% applied strain) for all steps of the algorithm. This figure illustrates the increase in precision for each step. The unfiltered and filtered displacements show a smoother distribution with each step (Fig. 2.6a-b and Fig. 2.6d-e) and the cross-correlation values show a visible increase towards a value of 1.0 (Fig. 2.6c). Especially the axial and lateral strain are visibly enhanced for each step of the procedure (Fig. 2.6f-g).

To quantitatively assess the improvement of the elastograms of the homogeneous phantom, the axial and lateral SNRe were calculated for each step of the algorithm for the entire range of applied strains. The results are shown in figure 2.7. The axial SNRe improves for each step of the algorithm over the entire range. The

increase in axial SNRe, when aligning and stretching is performed, is especially higher for larger strains. For instance, the increase in SNRe after aligning and stretching is 2.2 dB for an applied strain of 0.5% and 17.2 dB for 5.0% strain. The final SNRe ranges from 31 dB at 0.5% strain up to 40 dB for 5.0% applied strain. In general, the SNRe in the lateral direction is lower (14 – 25 dB) than in the axial direction. The lateral SNRe is also significantly improved due to aligning and stretching. After aligning and stretching, the SNRe increased 7.0 dB for the lowest applied load of 0.5%. This is slightly higher compared to the 6 dB increase when 5.0% strain is applied.

The effect of the coarse-to-fine algorithm with aligning and stretching is also given



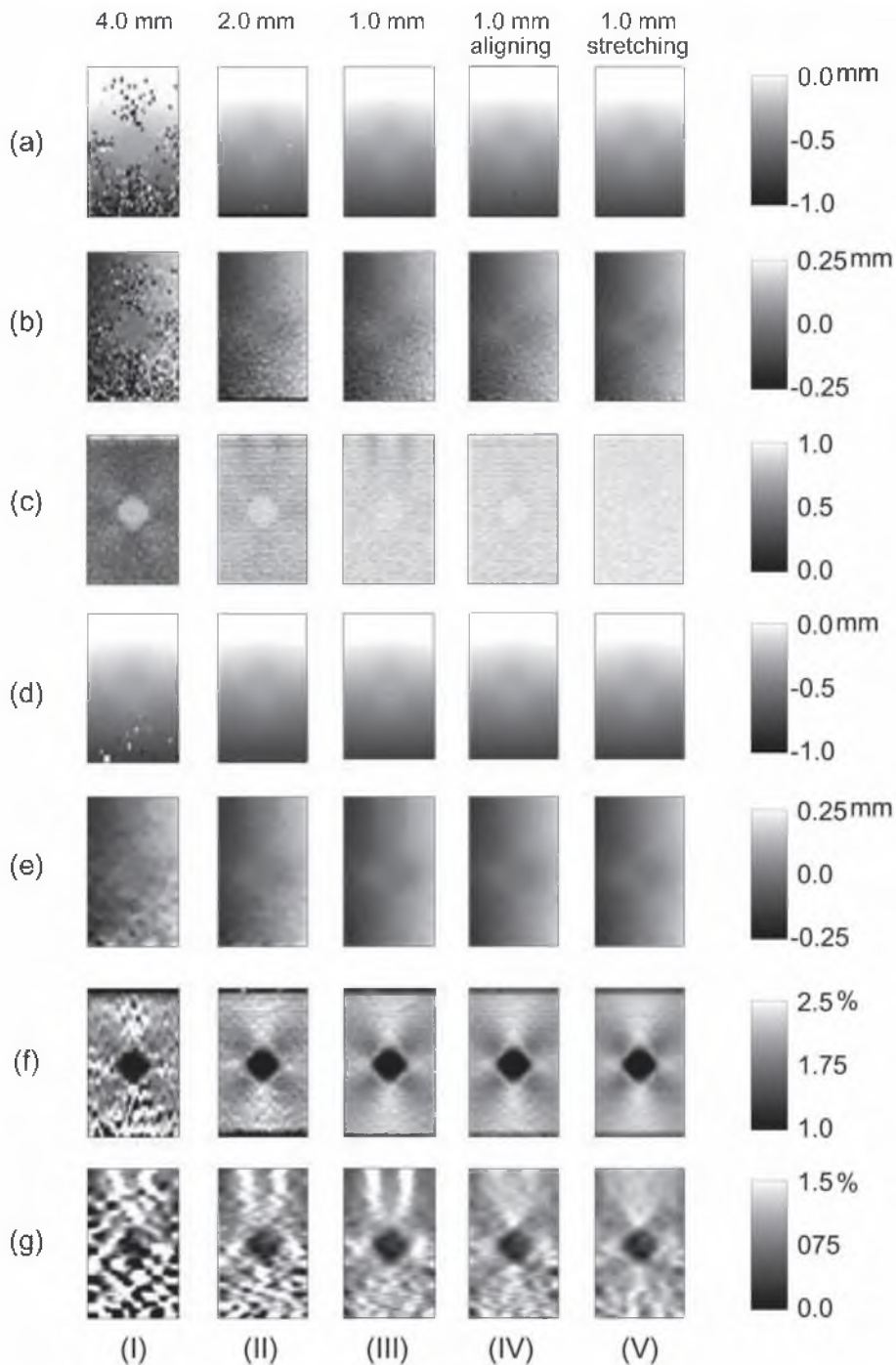


Figure 2.8. Results of the simulation study of the inhomogeneous phantom at 2.0% applied strain for all consecutive steps of the algorithm (see also Table 2.2): a) the unfiltered axial displacement estimates; b) the unfiltered lateral displacement estimates; c) the measured maximum cross-correlation values; d) the filtered axial displacement estimates; e) the filtered lateral displacement estimates; f) the axial strain and g) the lateral strain. First the coarse-to-fine strain estimation was performed (I-III), followed by aligning (IV) and stretching (V).

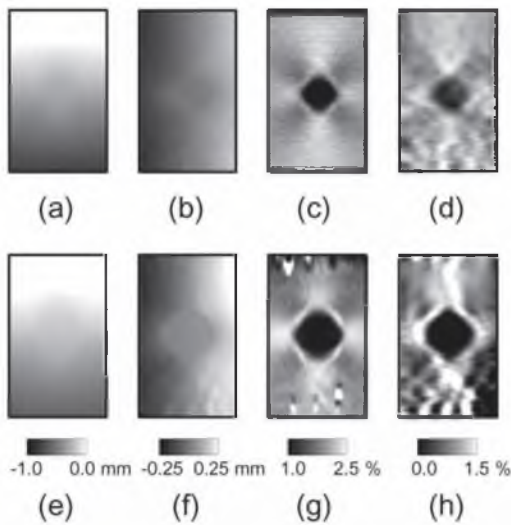


Figure 2.9. Comparison of estimated displacements and strains for the simulated inhomogeneous phantom (top row) and the inhomogeneous gelatin phantom (lower row). The axial (a) and lateral displacement images (b) and the axial (c) and lateral elastograms (d) are shown.

for the inhomogeneous phantom simulation (Fig. 2.8, 2.0% applied strain). Again, visual inspection reveals the improvement in displacement estimates (Fig. 2.8a-b, Fig. 2.8d-e), cross-correlation values (Fig. 2.8c) and strain estimates (Fig. 2.8f-g). Note the relatively high maximum cross-correlation values in the inclusion for the initial, large windows and the improvement of the surrounding tissue after reducing the window size and applying aligning and stretching (Fig 2.8c I-V). Especially the lateral elastogram shows improvement after aligning and stretching (Fig. 2.8g), although the noise in the lower half of the image is higher. The simulation data were compared with the experimental phantom data in figure 2.9 and figure 2.10. The inclusion seems to be larger in the gelatin phantom

(Fig. 2.9c-d). Besides some image artifacts, the displacement and strain images show a close resemblance. A similar deterioration of the estimated strain may be observed in the lower half of the lateral elastogram (Fig. 2.9d).

Opposed to the homogeneous simulations, a variation of strain occurs within the chosen ROIs in the inhomogeneous phantom. The SNRe is limited by the variation of strain within the chosen ROI. Therefore, theoretical maximum SNRe and CNRe could be calculated from the FEM solutions and compared with the measured values (Fig. 2.10). The axial, theoretical SNRe was 31.4, compared to a value of 29.2 and of 28.5 dB in the simulation and phantom data, respectively. The expected axial CNRe was 57.3 dB and the Field simulation data revealed a CNRe of 50.2. However, the obtained CNRe in the phantom was considerably lower (39.3dB). In the lateral direction, the theoretical lateral SNRe and CNRe were 26.9 and 53.4 dB, respectively. Lower values were observed in the simulation data (SNRe = 20.2 dB and CNRe = 31.5 dB) as well as in the phantom (SNRe = 17.5 dB and 31.0 dB).

For decreasing sonographic signal-to-noise ratio, the axial SNRe and CNRe showed a slight decrease. For an SNRs of 60 dB, no significant changes were observed. However, for SNRs = 10 dB, the axial SNRe and CNRe decreased with -0.2 dB and -1.0 dB, respectively. The effect on lateral accuracy and contrast was larger. The lateral SNRe decreased -4.5 dB, whereas the CNRe was -6.8 dB lower.

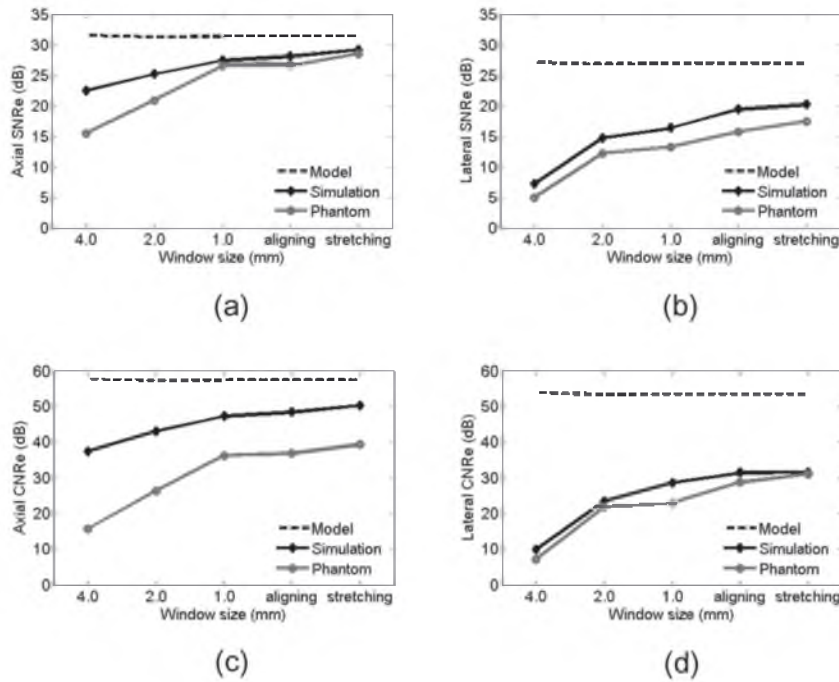


Figure 2.10. The elastographic signal-to-noise ratio of the axial (a) and lateral strains (b) and the corresponding elastographic CNRe in both directions (c-d) for all steps of the strain estimation algorithm. The maximum SNRe and CNRe are calculated using the finite element model (black dashed line). The measured SNRe and CNRe are shown for the simulated data (black solid line) and the phantom study (grey solid line).

## DISCUSSION

In this chapter, an extensive evaluation of the performance of 2D strain estimation methods is given. The choice of window size and interpolation method is often made without substantial argumentation, or foundation. One of the aims of this study was to offer a framework for optimal and accurate estimation of displacements and strains. Besides the proposed coarse-to-fine approach, re-correlation techniques such as local aligning and stretching, were introduced and investigated. The simulation and phantom studies revealed the potentials but also the limitations of strain estimation

using linear array data.

The coarse-to-fine approach outperformed a direct (or single-step) displacement estimation for larger strains ( $> 1.0\%$ ). The RMSE analysis, summarized in figure 2.4, revealed that RF-data yield better displacement estimates on a fine scale, as compared to envelope data, in both the axial and the lateral direction. The lower RMSE of the lateral displacements may be misleading, since the magnitude of the lateral displacements is only a quarter of the maximum axial displacement (due to the Poisson's ratio of 0.5 and motion to the left and right side with zero motion on the central axis) and the maximum RMSE of 0.2 mm corresponds with an error of  $\pm 1.5$  scan lines.

On a coarse scale, it is preferred to use envelope data. The point of intersection of the error curves can be explained as follows: The high RMSE of RF-based displacement estimates at larger window sizes is caused by de-correlation of the RF-signals. Theoretically, strain imposes a limit on the length of the axial window size,  $|\epsilon|f_c T = 1/2$ , with  $\epsilon$  de axial strain,  $f_c$  the center frequency (MHz) and  $T$  the window length in seconds (Céspedes et al. 1999). In our method this limit is 2.6 mm for 2.0% strain and 1.0 mm for 5.0% strain. The limits are indicated by the dashed lines in figure 2.3. The RF-based displacement estimates become more accurate near (and below) this bound as expected (see Fig. 2.3). Lateral results are consistent with the axial results. The RF-based lateral displacements are again more accurate below the axial theoretical window size limit. This is not a trivial finding, since no phase information is present in the lateral direction. Hence, an intersection point was not expected. A probable explanation could be the enhanced correlation in the axial direction beyond this limit. For very small axial window lengths ( $< 1.0$  mm) the RMSE increased again. A probable cause is that a smaller amount of data points is used for CCF calculation, resulting in an ill-defined peak of the CCF, which is also supported by the vast increase in outliers (Fig. 2.3, lower row).

Lateral window size analysis revealed that the 1D window had a poor performance compared to 2D windows and that accuracy improved with window size. It is favorable to use a post-compression area that is related to the pre-compression window size. However, a homogeneous phantom was examined,

so the influence of rotation and shearing of structures will remain minimal. Furthermore, a large number of lines was available and lateral movement was relatively small. It may be questioned whether very large windows would be beneficial and possible when performing, for instance, cardiac strain imaging. It should be noted that the concept of decreasing window size (coarse-to-fine) was not applied in the lateral direction.

Close examination of the accuracy of the five different interpolation methods revealed that straightforward parabolic or cosine interpolation can compete with spline interpolation of the CCF, or up-sampling of RF-data in the lateral direction, in terms of displacement noise. No significant difference in accuracy was found.

Spline interpolation of RF-data was also considered in this study, although not widely applied in literature. However, in a previous study, spline interpolation proved to be the most accurate 2D interpolation method for reconstruction of down-sampled RF-data (Lopata et al. 2005). Both spline and linear interpolation of RF-lines yielded a low number of outliers but the error was slightly higher compared to the CCF-based methods (method A-C). Considering the computation time and performance in terms of accuracy of the five methods, fitting a pre-defined shape of the CCF to calculate the displacement is favored.

The SNRe of the axial and lateral strain improves significantly for each step of the used algorithm in both the homogeneous and the inhomogeneous phantom. The SNRe of the estimates obey the shape of the Strain Filter (Varghese and Ophir 1997)

before aligning and stretching are applied (see Fig. 2.7). However, after re-correlation, the axial and lateral SNRe are higher for increasing applied strain. Stretching reduces de-correlation effects and the remaining variance is of the same order of magnitude for all strains. Stretching yields the largest improvement of axial SNRe at larger strains, which is a result of re-correlation in the axial direction. However, the lateral SNRe increased more after aligning than after stretching. Hence, aligning is crucial for improvement of lateral SNRe, whereas stretching will improve in particular the axial SNRe in areas with high strain.

For the inhomogeneous simulation data, a similar increase in SNRe was observed for each step of the algorithm. However, the SNRe values are lower compared to those obtained for the homogeneous simulation data at 2.0% applied strain. Even the theoretical SNRe is lower. This observation might be explained by a larger variance of the theoretical and also the measured strain in the chosen ROI caused by the inclusion (see Fig. 2.1e-f and Fig. 2.10). Besides an improvement in accuracy, an increase in CNRe can be observed and the shape of the CNRe curves resembles that of the SNRe. The CNRe is considerably lower in both the simulation and the phantom study, particularly in the lateral direction. Of course the lack of phase information in lateral direction will decrease the SNRe and CNRe, but also smoothing by the median filter, or the used least-squares strain estimator, might be a reason.

In general, the lack of phase information and low sampling rate in lateral direction results in lower accuracy and contrast

of lateral strain estimates. Compared to the theoretical upper limits, the lateral SNRe and CNRe are approximately 4.5 dB and 15 dB, respectively, lower than in the axial direction. The lateral CNRe curves for the simulation and phantom experiments are almost identical. However, no reasonable explanation could be found for this phenomenon.

Both simulation and experimental data show an increase of the noise in the lateral strains in the lower part of the image (Fig. 2.8-2.9). This effect has been attributed to the increasing beam width, since a higher beam overlap will drastically decrease the accuracy of lateral displacement estimates (Konofagou and Ophir 1998). In our study, the transmit focus was at a depth of 7 cm, so beam widening will not be a major cause. However, this effect in the lower image part might as well be caused by the large displacement by compression of scatterers in the lower part of the phantom (the scatterers move upwards in the scan lines). It must also be noted that the selected ROI in the background (upper right corner) is a region with no visible artifacts (and optimal strain). This optimal choice of ROI is a possible bias of this study. Furthermore, the inclusion appears to be larger in the phantom. A possible explanation could be that some surrounding tissue was removed when pulling out the metal rod. Furthermore, the gelatin of the inclusion may have been too warm when added and mixed with the gelatin of the surrounding tissue.

The authors are aware of the limitations of this study. The simulated and experimental data were obtained with a linear array transducer yielding scan lines with equal

spacing. Especially for cardiac applications, a phased array transducer will be used. Whether similar conclusions can be drawn using phased array data is not yet clear and requires further investigation, although preliminary results showed good results in phased array data (Lopata et al. 2006). Furthermore, the accuracy of displacement and strain estimates depends on the used center frequency and bandwidth. In this study, only one center frequency and one bandwidth, matching with the available linear array transducer, were used. Scaling these results up to higher or lower frequencies might provide a good indication of the performance at other frequencies. Several methods for matching pre- and post-compression data are available in literature, for instance the sum-of-absolute differences (Langeland 2003) or the Lagrangian strain estimator (Maurice and Bertrand 1999). This study was limited to the cross-correlation function method that is a widely accepted technique.

Comparison with other methods is difficult, since different data (phased array, etc), different transducer settings and different models are used. A study of multi-resolution elastography reported axial SNRe values of 30 dB at 0.5% strain and 8 dB at 5.0% strain (Varghese et al. 1998a). The multi-step study (Shi and Varghese 2007) showed improvement at larger strains, but our proposed method at optimal settings provides higher axial SNRe at larger strain values. In a theoretical study by Konofagou, similar results were found in lateral SNRe although different simulation data was used (Konofagou et al. 2000). A higher SNRe was reported when using RF instead of

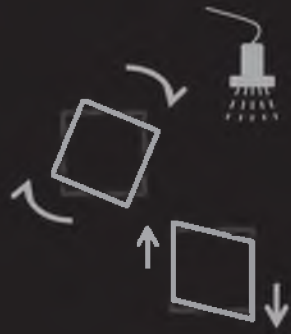
envelope data, which is in accordance with our findings. For 1.0% lateral strain and a centre frequency of 7.5 MHz, the SNRe was approximately 30 dB. Comparison remains troublesome, since the theoretical SNRe in our simulations and the used pitch were lower. Interpolating their findings to a pitch of 135 micrometer would imply a lateral SNRe of 10-14 dB. The comparison between simulations and experimental data was performed at a different centre frequency and cannot be compared with our study. In a study by Chaturvedi et al (1998), lateral CNRe values < 17.5 dB were reported, which are lower compared to our phantom study. This difference is probably caused by the higher modulus contrast used in our study.

## CONCLUSION

In conclusion, close examination and evaluation of 2D CCF and RF-based strain estimation techniques shows that a coarse-to-fine method, using 2D windows outperforms 1D or one-step methods. Furthermore, different interpolation methods yield sub-sample displacement estimates with the same accuracy. However, the computational efficiency of a straightforward 2D parabolic or cosine fit is decisive. Additional re-correlation, aligning and stretching, enhances the accuracy of the displacement and strain estimates significantly. However, a limitation of the proposed approach is the necessity of *a priori* knowledge of displacements and strains.



Handwritten text in a box, possibly a list of instructions or a small poem.





---

# CHAPTER 3

## IMPROVED 2D STRAIN IMAGING USING FREE-SHAPE KERNELS OF RF-DATA

---

*Richard G.P. Lopata, Hendrik (Rik) H.G. Hansen, Maartje M. Nillesen,  
Johan M. Thijssen, Livia Kapusta & Chris L. de Korte*

---

Based on: **Methodical Study on the Estimation of Strain in Shearing and Rotating Structures using Radio-Frequency Ultrasound based 1D and 2D Strain Estimation Techniques.** R.G.P. Lopata, H.H.G. Hansen, M.M. Nillesen, J.M. Thijssen, L. Kapusta and C.L. de Korte, *IEEE Transactions on Ultrasonics, Ferroelectrics & Frequency Control* 2010; 57(4), pp. 855-865.

---

## ABSTRACT

This simulation study is concerned with: 1) the feasibility of measuring rotation using RF-data and 2) the assessment of the performance of strain estimation in shearing and rotating structures. The performance of three different radio frequency (RF) based methods is investigated. Linear array ultrasound data of a deforming block were simulated (axial shear strain = 2.0, 4.0 and 6.0%, vertical strain = 0.0, 1.0 and 2.0%). Furthermore, data of a rotating block were simulated over an angular range of 0.5° to 10°. Local displacements were estimated using a coarse-to-fine algorithm using 1D and 2D pre-compression kernels. A new estimation method was developed in which axial displacements were used to correct the search area for local axial motion. The study revealed that this so-called 'free-shape' 2D method outperformed the other two methods and produced more accurate displacement images. For higher axial shear strains, the variance of the axial strain and the axial shear strain reduced by a factor of four to five. Rotations could be accurately measured up to 4.0 - 5.0°. Again, the free-shape 2D method yielded the most accurate results. After reconstruction of the rotation angle, the mean angles were slightly underestimated. The precision of the strain estimates decreased with increasing rotation angles. In conclusion, the proposed 'free-shape' 2D method enhances the measurement of (axial shear) strains and rotation. Experimental validation of the new method still has to be performed.

## INTRODUCTION

Ultrasound strain imaging, or elastography, is a technique that measures local strain in biological tissue and organs (Céspedes et al. 1993a; O'Donnell et al. 1994; Ophir et al. 1991; Ophir et al. 1999). The strain data might be used to reconstruct the elastic properties of the tissue (Kallel and Bertrand 1996a; Skovoroda et al. 1995). Originally, the displacements and strains were estimated using one-dimensional (1D) time delay estimation (Ophir et al. 1991; O'Donnell et al. 1994; Kallel et al. 1996b; s et al. 1996). In the last decade, two-dimensional (2D) estimation techniques have been developed, using both B-mode data (Trahey et al. 1988; Chaturvedi et al. 1998) and raw, radio frequency (RF-) data (Konofagou and Ophir 1998; Chen et al. 2004). These 1D and 2D strain imaging techniques are being used primarily for cardiovascular applications (d'Hooge et al. 2000; de Korte et al. 1998), breast and prostate tumor research (Garra et al. 1997; Khaled et al. 2006).

Several groups have been investigating the opportunity of shear strain imaging and its possible applications (Konofagou et al. 2000a; Techavipoo et al. 2004; Thitaikumar et al. 2005). For instance, shear strain imaging has been of interest for characterization of breast tumors (Thitaikumar et al. 2007; Thitaikumar et al. 2008) and cardiovascular applications (Han et al. 2008; Nottin et al. 2008; Shaw et al. 2008; Ahlgren et al. 2009; Luo et al. 2009). Rotation, and especially torsion, are of great interest in cardiovascular research (Han et al. 2008; Shaw et al. 2008; Luo et al. 2009).

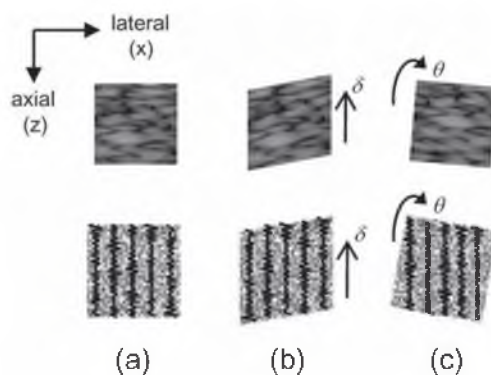


Figure. 3.1. Example of a small segment of normal B-mode image data (a), after shearing (b) and after rotation (c). The position of the measured RF-lines relative to the scatter movement is also illustrated (lower row).

Besides clinical relevance, a practical issue is the negative effect of shearing or rotation on strain image quality during free-hand palpation (Hall et al. 2003; Brusseau et al. 2007).

Axial shear strain has been measured using RF-data (Konofagou et al. 2000; Thitaikumar et al. 2005). However, rotation and torsion measurements have been performed solely with 2D B-mode speckle tracking techniques (Hui et al. 2007; Takeuchi et al. 2007; Tournoux et al. 2008) and optical flow techniques (Maurice and Bertrand 1999; Suhling et al. 2005; Angelini et al. 2006). RF-data have the advantage of providing phase information, resulting in higher resolution and sensitivity for time delay estimation (Chapter 2). A principal question is whether one can measure axial or lateral strain and rotation using RF-data? Furthermore, it is of great interest to know the limits on rotation measurements and the effect of rotation on strain accuracy using RF-data.

Ironically, the higher sensitivity of RF-data is problematic for shearing or rotat-

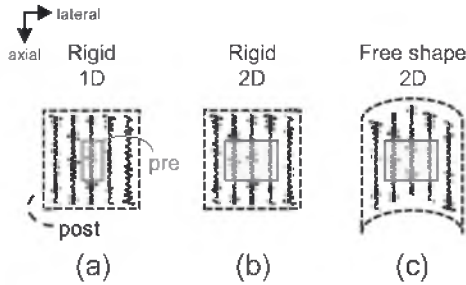


Figure 3.2 Schematic representation of 2D cross-correlation of pre-compression RF-data (grey) with a larger 2D window of post-compression RF-data (black) in case of conventional ('rigid') 1D kernel matching (a), rigid 2D kernel matching (b) and free-shape kernel matching (c).

ing structures. The displacement patterns during shearing and rotation reveal large gradients orthogonal to the displacement direction, which disable the match of 2D RF-data windows and corrupt its outcome. An approach based on image registration could help to overcome this issue. Non-rigid registration is most frequently performed on B-mode data (Ledesma-Carbayo et al. 2006; Elen et al. 2008). It seems impossible to apply 2D non-rigid registration on RF-data without maintaining the axial phase information. In this chapter, a 'free-shape' 2D kernel matching is introduced, which actually is a straightforward deformation of the 2D post-compression data segments to match them to the pre-compression data. This is achieved by correcting each RF-line for the corresponding, local, axial displacement. Hence, the post-compression windows do not necessarily have a square shape anymore, depending on the axial displacement field (see Methods section for extensive explanation).

In this simulation study, the ability to measure axial and lateral strain in combi-

nation with axial shearing and the combination of axial and lateral shearing, *i.e.* rotation, was examined. A comparative study was performed using RF-based 1D and 2D strain estimation methods. The results of these conventional algorithms were compared to those obtained with the so-called 'free-shape' 2D strain method. The limits on rotation angle measurements were investigated as well as the influence of axial shearing and rotation on strain accuracy and vice versa.

## MATERIALS

A block containing  $3.5 \cdot 10^6$  randomly positioned point scatterers (5 cm x 5 cm x 1 cm) was generated using MATLAB® (The Mathworks Inc., Natick, MA, USA). This block was used to simulate pre-compression RF-data using Field II® (Fig. 3.1a). Next, the block of point scatterers was deformed to generate the 'post-compression' scatter configurations for axial deformation, shearing or rotation. First, the scatterers were translated to simulate an axial shear strain of  $\epsilon_{xz} = 2.0, 4.0$  and  $6.0\%$ , without any vertical or horizontal strain present (see also Fig. 3.1b), by simply translating the scatter points in the axial direction, using the center as the reference point:

$$z' = z - \epsilon_{xz} \left( \frac{x - x_{min}}{x_{max} - x_{min}} \right) \quad (3.1)$$

To examine the influence of strain on axial shear strain measurements, also a vertical load corresponding to  $\epsilon_{zz} = 1.0\%$  and  $2.0\%$

deformation was applied to the block for all cases of axial shearing. The blocks were assumed to be linearly elastic and nearly incompressible. Consequently, the Poisson's ratio was set to 0.495. For a vertical deformation of 1.0% and 2.0%, the resulting horizontal strains were  $\varepsilon_{xx} = 0.5$  and 0.99%, respectively.

$$x' = x \cdot \cos \alpha + z \cdot \sin \alpha \quad (3.2)$$

$$z' = -x \cdot \sin \alpha + z \cdot \cos \alpha \quad (3.3)$$

Secondly, simulations were performed of blocks of scatterers that were rotated over 0.5°, 1.0° to 5.0° and 10.0° (see Fig. 3.1c). The center of the scatterer matrix was used as axis of rotation.

$$x' = (1 + \nu \cdot \varepsilon_{zz}) \cdot x \quad (3.4)$$

$$z' = (1 - \varepsilon_{zz}) \cdot z \quad (3.5)$$

The rotation simulations were repeated while applying a vertical deformation ( $\varepsilon_{zz} = 1.0$  and 2.0%). These modified, 'post-compression', scatterer configurations were again convolved (Field II ©) with an ultrasound RF-pulse to simulate the post-compression ultrasound data.

Field II© was used to simulate linear 2D ultrasound images (Jensen et al. 1996). A linear array transducer was simulated with a center frequency  $f_c = 8.73$  MHz. The linear array consisted of a total number of 288 elements, of which 128 were used in transmit and receive mode. The pitch was set to 135  $\mu\text{m}$  and the element height was 6 mm. The fixed lateral and elevational focus of the transducer was positioned in

the middle of the block, *i.e.*, at 35 mm (the top of the volume lies at 10 mm depth). Dynamic focusing was used with focal zones every 2.0 mm to obtain a uniform beam profile (Chapter 2). Pre- and post-compression RF-data were simulated using the simulated volumes of scatterers and were sampled at 39 MHz. The simulation was performed for 225 RF-lines, resulting in a rectangular image with a depth of 70 mm and a width of 30.4 mm. The number of scatterers per smallest sampling volume was 10, which is sufficient to ensure that the speckle of the ultrasound images is fully developed (Oosterveld 1985).

## METHODS

Two-dimensional displacement and strain estimation can be performed by cross-correlating 1D or 2D windows of pre-compression RF-data with a larger 2D post-compression window (Fig. 3.2a-b). Using a larger 2D post-compression window allows for the estimation of lateral displacements, regardless whether a 1D or 2D pre-compression window is used (Konofagou and Ophir 1998; Chapter 2). Consequently, the windows of RF-data have a rectangular shape. However, in case of axial shearing (and rotation), a lateral gradient is found in the axial displacement of the scatterers. Neighboring RF-lines are shifted relatively to each other in the axial direction and the post-compression window ('search area') is in fact skewed compared to the original data (see Fig. 3.1b). This

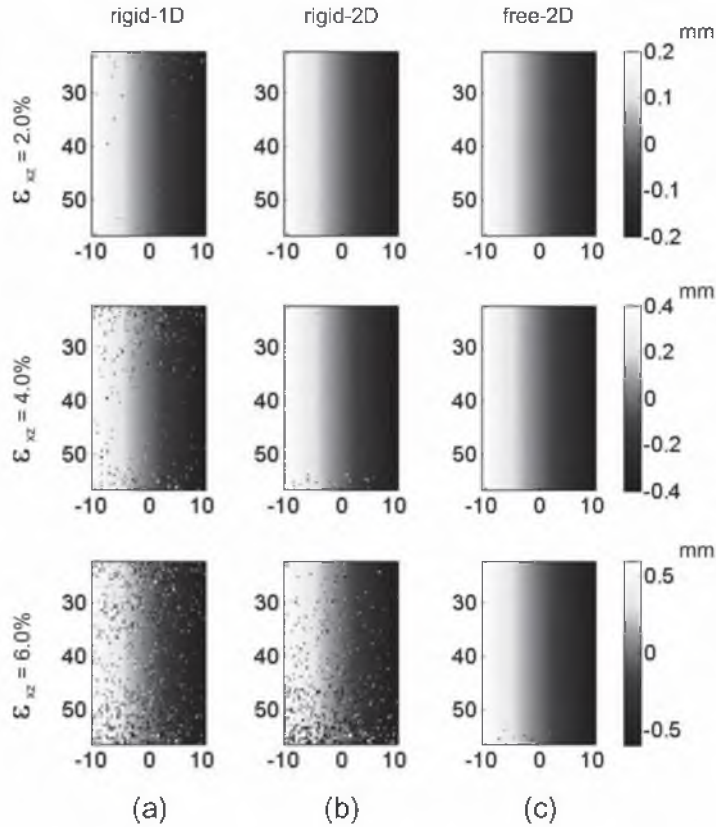


Figure 3.3 The measured, unfiltered, axial displacements using rigid 1D (a) and 2D (b) kernel matching and free-shape 2D kernel matching (c) for an applied axial shear strain of 2.0% (top row), 4.0% (middle row) and 6.0% (lower row).

implies that correction of the post-compression RF-data for the axial displacements would result in a better match and enhance the cross-correlation. This straightforward approach, correcting each RF-line for the measured axial displacement, results in so-called ‘free’ shape post-compression windows (Fig. 3.2c). This proposed method may be especially beneficial for axial shearing and rotation data, considering the large lateral gradient in the axial displacements (see Fig. 3.1). It must be noted that lateral correction would not be possible considering the often small sub-sample values and

the noisy nature of the lateral displacement estimates. The ‘free shape’ method can only be used in an iterative algorithm, since global (or ‘previous’) displacement estimates are required for the correction procedure.

The simulated data were processed using a coarse-to-fine 2D displacement estimation algorithm using 2D parabolic interpolation and additional re-correlation techniques (Chapter 2). For the three coarse-to-fine iterations, the axial window size was set to 4.0, 2.0 and 1.0 mm with an overlap of 75%. The lateral pre-compression window was set to 1 line for 1D and 5 lines (0.68 mm)

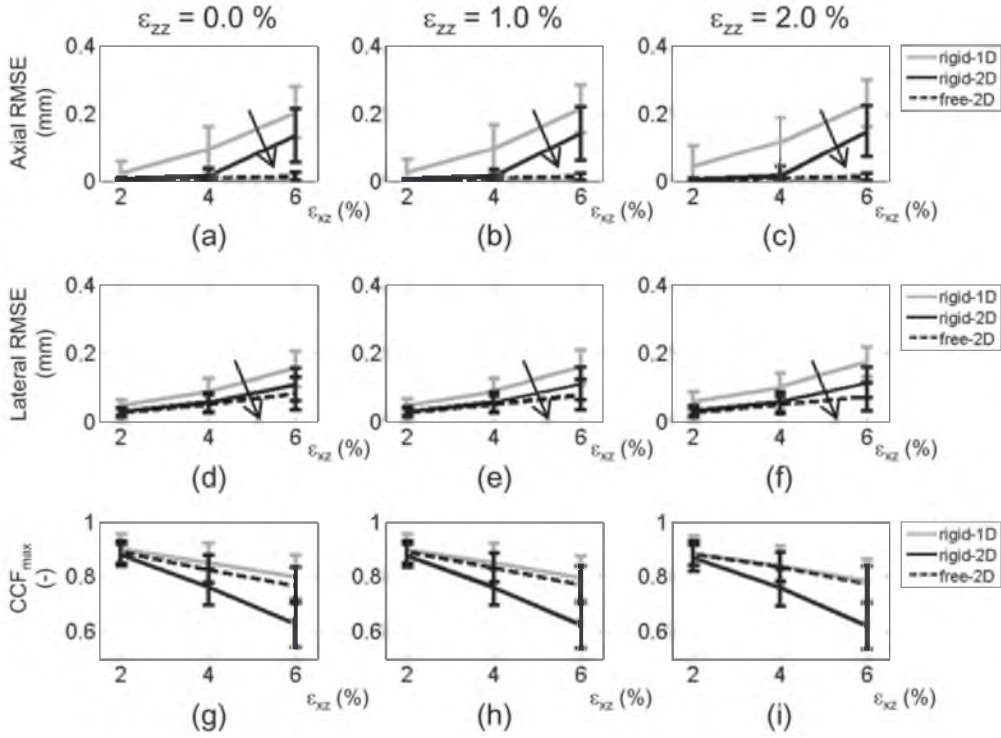


Figure 3.4 The root-mean-squared-error (RMSE) between the measured and ‘true’ axial displacements (top row), lateral displacements (middle row) and the measured maximum cross-correlation values as a function of shear load ( $\epsilon_{xz}$ ) for all three methods. The results are shown for an applied axial load ( $\epsilon_{zz}$ ) of 0.0% (left column), 1.0% (middle column) and 2.0% (right column).

for 2D window matching for all iterations (Konofagou and Ophir 1998; Chapter 2). For the first iteration (coarse scale search), the lateral post-compression window was set to 43 lines (5.80 mm), defining a large search area. The signal envelope was used during the first iteration, since 2D B-mode speckle tracking can estimate the global displacements despite the large axial shearing or rotation that is present. The lateral post-compression window was cropped to 11 lines (1.5 mm) for all subsequent iterations. All window sizes used for aligning and stretching were equal to the settings of the last coarse-to-fine iteration. The axial and lateral displacement data were smoothed

using a median filter of 2.8 mm x 1.5 mm (axial x lateral). The axial and lateral strains were calculated using a 1D LSQSE with a kernel length of 2.8 mm (Kallel et al. 1997). It is noted that the vertical strain ( $\epsilon_{zz}$ ) corresponds to the axial strain and the horizontal strain ( $\epsilon_{xx}$ ) is equivalent to the lateral strain, since, linear array data were used in this study.

The three algorithms were applied to the simulated RF-data. The conventional 1D and 2D strain estimation using rectangular, rigid 2D kernels of post-compression RF-data are in this chapter referred to as ‘rigid-1D’ and ‘rigid-2D’, respectively, whereas ‘free-2D’ is used for the proposed

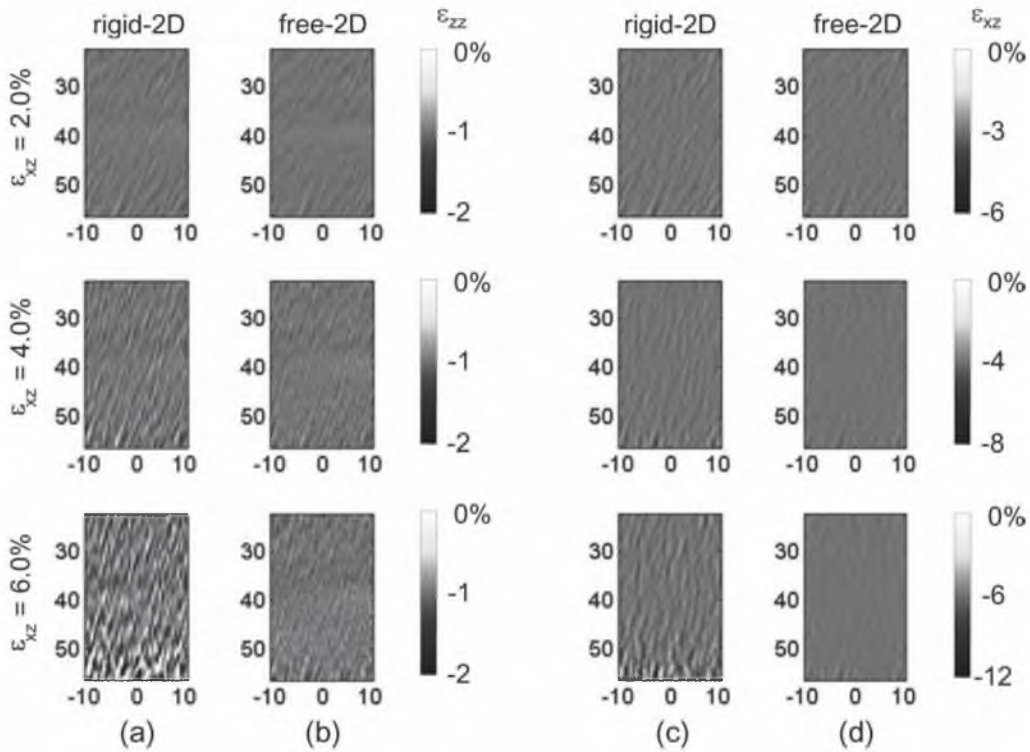


Figure 3.5 The resulting axial strain ( $\epsilon_{zz}$ ) images for the rigid-2D (a) and free shape-2D method (b) for an applied vertical strain of 1.0% and an applied shear strain of 2.0% (top row), 4.0% (middle row) and 6.0% (bottom row). The resulting shear strain images ( $\epsilon_{xz}$ ) for the rigid-2D (c) and free shape-2D method (d) for an applied vertical strain of 1.0% and an applied shear strain of 2.0% (top row), 4.0% (middle row) and 6.0% (bottom row).

free shape method. The free-2D method differed from the conventional approaches after the first, coarse iteration. The displacement estimates were now used to deform the post-compression 2D window of RF-data for all subsequent iterations. The displacements and strains were estimated, as well as the axial shear strains and rotation angle in the corresponding simulations. The root-mean-squared error (RMSE) and maximum cross-correlation ( $CCF_{max}$ ) for a square region in the middle of the image (34 mm x 21 mm) were also calculated to facilitate comparison of the different methods. The differences in RMSE were tested using a

two-sample t-test (95% confidence interval). The strain results were normally distributed. Therefore, the mean and standard deviation were computed and the significance of the differences in variance was tested using the F-test for variances (99% confidence interval). For the rotation data, a circular region around the axis of rotation was omitted from analysis, since large artifacts occurred due to noise in the small displacement estimates near the axis of rotation (see Discussion).



**Table 3.1 Measured mean strain  $\pm$  standard deviation for all shearing simulations (N = 21039)**

|                    |                         | Applied load : $\epsilon_{zz} = 1.0\%$ |                  |                  | Applied load : $\epsilon_{zz} = 2.0\%$ |                  |                  |
|--------------------|-------------------------|--|------------------|------------------|--|------------------|------------------|
|                    |                         | <i>rigid-1D</i>                        | <i>rigid-2D</i>  | <i>free-2D</i>   | <i>rigid-1D</i>                        | <i>rigid-2D</i>  | <i>free-2D</i>   |
| Axial strain (%)   | $\epsilon_{zz} = 2.0\%$ | -1.00 $\pm$ 0.04                       | -1.00 $\pm$ 0.04 | -1.00 $\pm$ 0.05 | -2.00 $\pm$ 0.06                       | -2.00 $\pm$ 0.05 | -2.00 $\pm$ 0.05 |
|                    | $\epsilon_{zz} = 4.0\%$ | -0.99 $\pm$ 0.12                       | -0.99 $\pm$ 0.11 | -0.99 $\pm$ 0.08 | -1.99 $\pm$ 0.13                       | -1.99 $\pm$ 0.10 | -1.99 $\pm$ 0.09 |
|                    | $\epsilon_{zz} = 6.0\%$ | -0.99 $\pm$ 0.30                       | -0.97 $\pm$ 0.34 | -0.98 $\pm$ 0.11 | -1.98 $\pm$ 0.33                       | -1.97 $\pm$ 0.35 | -1.98 $\pm$ 0.09 |
| Lateral strain (%) | $\epsilon_{zz} = 2.0\%$ | 0.52 $\pm$ 0.27                        | 0.51 $\pm$ 0.24  | 0.52 $\pm$ 0.22  | 1.01 $\pm$ 0.32                        | 1.01 $\pm$ 0.27  | 1.01 $\pm$ 0.25  |
|                    | $\epsilon_{zz} = 4.0\%$ | 0.52 $\pm$ 0.44                        | 0.52 $\pm$ 0.44  | 0.53 $\pm$ 0.39  | 1.01 $\pm$ 0.56                        | 1.02 $\pm$ 0.48  | 1.03 $\pm$ 0.40  |
|                    | $\epsilon_{zz} = 6.0\%$ | 0.53 $\pm$ 0.76                        | 0.54 $\pm$ 0.80  | 0.59 $\pm$ 0.62  | 1.05 $\pm$ 0.81                        | 1.04 $\pm$ 0.85  | 1.11 $\pm$ 0.61  |
| Shear strain (%)   | $\epsilon_{zz} = 2.0\%$ | -2.00 $\pm$ 0.07                       | -2.00 $\pm$ 0.08 | -2.00 $\pm$ 0.09 | -2.00 $\pm$ 0.12                       | -2.00 $\pm$ 0.10 | -2.00 $\pm$ 0.09 |
|                    | $\epsilon_{zz} = 4.0\%$ | -3.99 $\pm$ 0.21                       | -3.99 $\pm$ 0.18 | -3.99 $\pm$ 0.18 | -3.99 $\pm$ 0.24                       | -3.99 $\pm$ 0.19 | -3.99 $\pm$ 0.17 |
|                    | $\epsilon_{zz} = 6.0\%$ | -5.99 $\pm$ 0.61                       | -5.99 $\pm$ 0.65 | -5.99 $\pm$ 0.16 | -5.99 $\pm$ 0.65                       | -5.99 $\pm$ 0.65 | -5.99 $\pm$ 0.14 |

## RESULTS

### *Axial Shearing*

Figure 3.3 shows the measured, unfiltered, axial displacement images for the three different applied axial shear loads and the three estimation methods. The displacement images revealed more noise for larger axial shear strain. At first glance, the ‘free-shape’ 2D method yielded less noisy displacement images. The accuracy of the three methods can be assessed using figure 3.4. For all methods, the RMSE increases with increasing axial shear strain. The rigid-1D method showed the highest RMSE in both axial and lateral direction for all applied axial shear strains ( $p < 0.001$ ). The axial RMSE curves revealed a significantly smaller error using the free-2D method compared to the

rigid-2D technique for 6% axial shear strain ( $p < 0.001$ ), whereas the lateral RMSE curves decreased significantly for 4 and 6% axial shear strain ( $p < 0.03$ ). The lateral displacements were lower and the lateral RMSE seems lower than the axial RMSE. However, both the axial and lateral RMSE of free-2D decreased with 50% compared to rigid-1D and 33% compared to rigid-2D (Fig. 3.4a-f). Furthermore, the influence of applying a vertical load on the block seemed to have little influence on the RMSE. An increase in maximum cross-correlation was observed for free-2D as compared to rigid-2D (Fig. 3.4g-i) and approached the 1D curves. Still, the cross-correlation values for rigid-1D seemed slightly higher (see Discussion).

Axial shear strain images and axial strain images are shown in figure 3.5 for rigid-2D and free-2D. The figures corroborate the

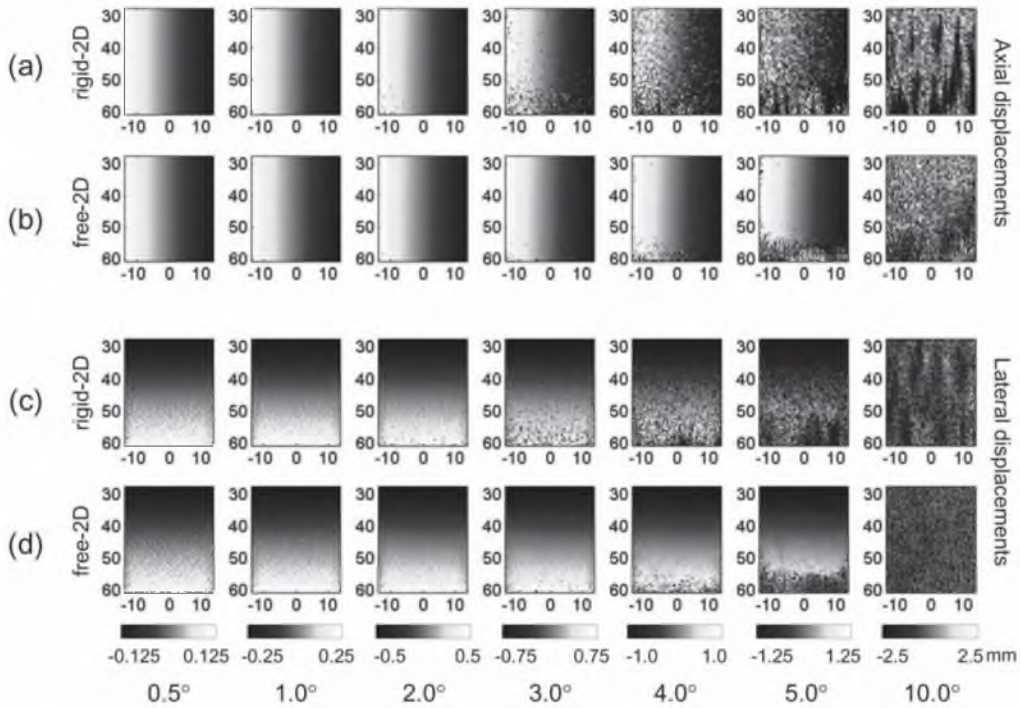


Figure 3.6 The measured, unfiltered, axial displacements using the rigid-2D (a) and free shape-2D method (b) for increasing applied rotation ( $0.5^\circ - 10^\circ$ ) and the measured, unfiltered, lateral, displacements using the rigid 2D (c) and free shape-2D methods (d).

RMSE results that the free-2D technique is especially beneficial for higher axial shear strains and both the axial ( $\epsilon_{zz}$ ) and axial shear strain ( $\epsilon_{xz}$ ) images were less noisy. The mean values and standard deviations of the axial, lateral and axial shear strains are listed in Table 3.1. Again, the differences between the three methods are small for  $\epsilon_{xz} = 2.0\%$  and  $4.0\%$ . In general, the differences in mean values are small but the variances reduce when using the free-2D method, especially for larger axial shear strain ( $4\% - 6\%$ ). For an axial shear strain of  $6.0\%$ , the measured mean axial shear strain values were equal for all methods, but the variance was four to five times higher for rigid-1D and rigid-2D ( $p < 0.001$ ) as compared to

free-shape 2D. The variance on the axial strain reduced approximately by a factor of three to four ( $p < 0.001$ ). The decrease in lateral strain variance was only a factor 0.2 ( $p < 0.001$ ).

### Rotation Measurements

The measured, unfiltered, axial and lateral displacement images obtained with rigid-2D and free-2D are shown in figure 3.6. The displacement images revealed that rotation can be measured up to  $4.0^\circ$  without any deterioration. As before, the free-2D method appeared to be able to handle the rotational movement better, consider-

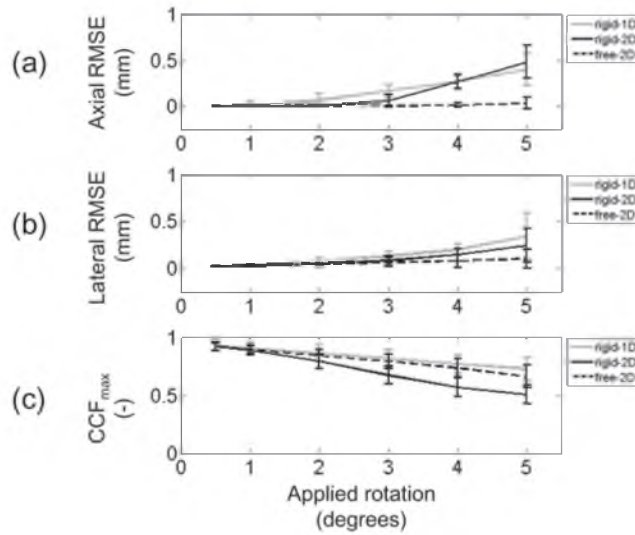


Figure 3.7 The root-mean-squared-error (RMSE) of difference between the measured and ‘true’ axial displacements (a), the RMSE of the lateral displacements (b) and the measured maximum cross-correlation values (c) all as a function of applied rotation angle for the three estimation methods.

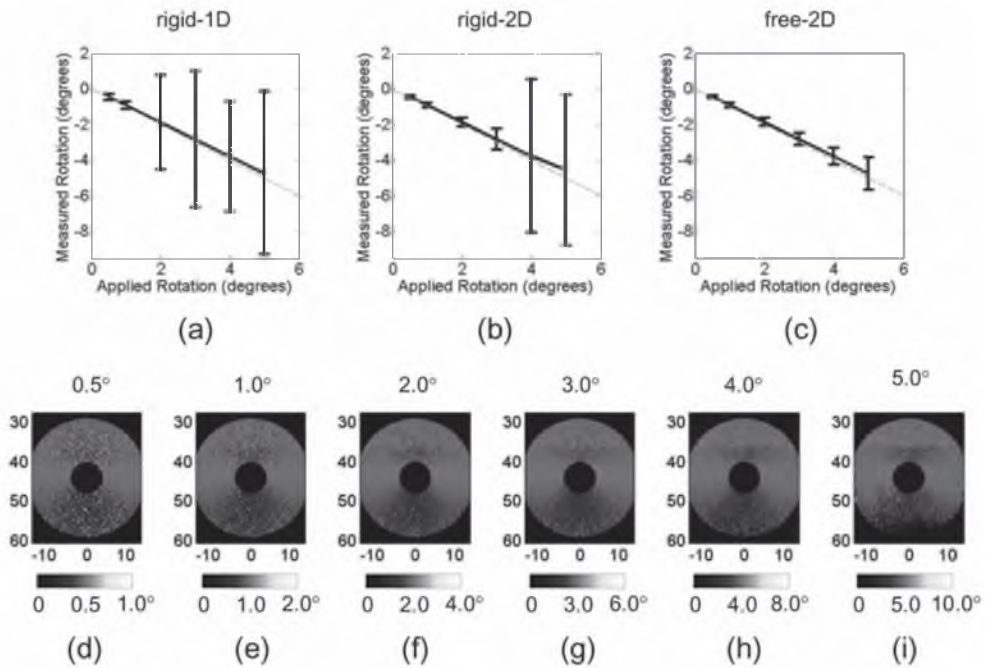


Figure 3.8 The measured mean rotation angle and variance for the rigid-1D (a), rigid-2D (b) and free shape-2D method (c). The true rotations are indicated for comparison (gray dashed line). 2D images of the resulting rotation angle as measured with the free-2D method are shown for 0.5° - 5° (d-i).

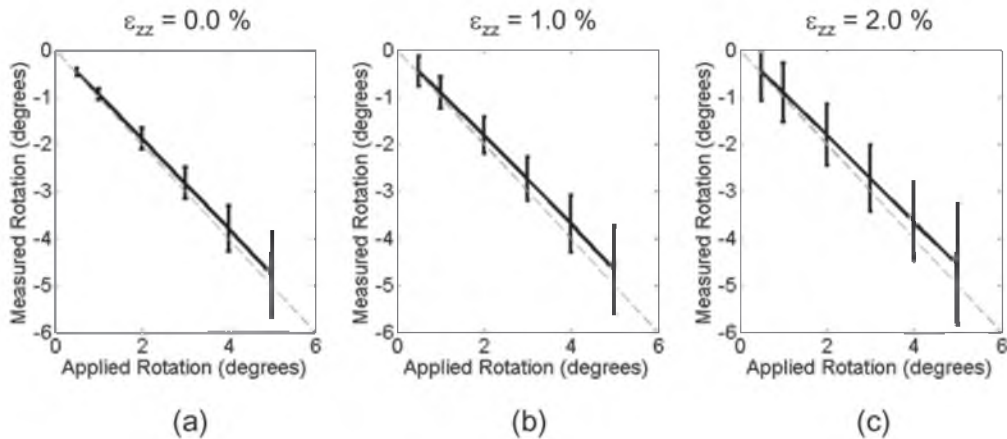


Figure 3.9 The measured mean rotation angle (using the free shape-2D method) for an applied load of 0.0% (a), 1.0% (b) and 2.0% (c) axial strain ( $\epsilon_{zz}$ ). The variance is shown (error bars) as well as the true rotations (grey dashed lines).

ing the smoother (unfiltered) displacement images. However, both algorithms failed at 5.0° in the regions with large lateral displacements and no accurate displacements were measured at 10.0°. The axial and lateral RMSE showed an increase for larger rotation angles for all three methods (Fig. 3.7). The differences in terms of RMSE and maximum cross-correlation are similar to those obtained in the study on axial shearing (Fig. 3.4). The axial RMSE seemed to decrease by 90% and 80% for 4.0° and 5.0°, respectively, when using free-2D instead of rigid-2D ( $p < 0.001$ ), whereas the lateral RMSE decreased by 40 to 90% ( $p < 0.001$ ). The cross-correlation of free-2D increased by 0 – 0.17 compared to rigid-2D, but was again slightly outperformed by the rigid-1D algorithm (see Discussion).

Figure 3.8 shows the measured rotation angle and accuracy for the three methods. The variance on the measured angle decreased with respect to the rigid 1D method using 2D techniques and improved for the free-2D method at larger angles. For

the last method, the rotation angle images are shown for the cylindrical region-of-interest (Fig. 3.8d-i). The images revealed that the angle is underestimated in the lower part of the images below the focus. This can also be noticed from the mean rotation angle curves in figure 3.8a-c. For larger angles, artifacts were found in the lowest part of the image, which can also be seen in the displacement images (Fig. 3.6).

The rotation was also measured in rotating structures after deformation. In general, the variance of the measured rotation angles increased when 1.0% and 2.0% strain was applied (Fig. 3.9). The curves showed a slightly larger underestimation and larger error bars with increasing applied strain. The strain values were reconstructed (Fung-Kee-Fung et al. 2005) and the mean axial and lateral strain values and the corresponding standard deviations are listed in Table 3.2. The free-2D method resulted in less bias and variance of both the axial and lateral strain estimates, especially at larger rotation angles ( $> 3^\circ$ ,  $p < 0.001$ ). For

Table 3.2 Measured mean strain  $\pm$  standard deviation for all rotation simulation (N = 15228)

|                  |                    | Applied load : $e_{zz} = 1.0\%$ |                  |                  | Applied load : $e_{zz} = 2.0\%$ |                  |                  |
|------------------|--------------------|---------------------------------|------------------|------------------|---------------------------------|------------------|------------------|
| Angle            |                    | <i>rigid-1D</i>                 | <i>rigid-2D</i>  | <i>free-2D</i>   | <i>rigid-1D</i>                 | <i>rigid-2D</i>  | <i>free-2D</i>   |
| Axial strain (%) | 0.5°               | -1.00 $\pm$ 0.02                | -1.00 $\pm$ 0.02 | -1.00 $\pm$ 0.02 | -1.99 $\pm$ 0.04                | -2.00 $\pm$ 0.02 | -2.00 $\pm$ 0.02 |
|                  | 1.0°               | -1.01 $\pm$ 0.03                | -1.01 $\pm$ 0.03 | -1.00 $\pm$ 0.04 | -2.00 $\pm$ 0.04                | -2.00 $\pm$ 0.03 | -1.99 $\pm$ 0.04 |
|                  | 2.0°               | -1.03 $\pm$ 0.07                | -1.03 $\pm$ 0.08 | -1.00 $\pm$ 0.07 | -2.02 $\pm$ 0.09                | -2.02 $\pm$ 0.07 | -1.99 $\pm$ 0.08 |
|                  | 3.0°               | -1.07 $\pm$ 0.20                | -1.06 $\pm$ 0.20 | -1.00 $\pm$ 0.09 | -2.05 $\pm$ 0.21                | -2.05 $\pm$ 0.20 | -1.99 $\pm$ 0.09 |
|                  | 4.0°               | -1.14 $\pm$ 0.41                | -1.10 $\pm$ 0.70 | -1.00 $\pm$ 0.12 | -2.07 $\pm$ 0.52                | -2.09 $\pm$ 0.62 | -1.98 $\pm$ 0.10 |
|                  | 5.0°               | -1.19 $\pm$ 3.88                | -0.14 $\pm$ 7.39 | -0.98 $\pm$ 0.19 | -1.41 $\pm$ 7.60                | -0.72 $\pm$ 9.6  | -1.84 $\pm$ 1.18 |
|                  | Lateral strain (%) | 0.5°                            | 0.50 $\pm$ 0.19  | 0.49 $\pm$ 0.13  | 0.50 $\pm$ 0.12                 | 0.99 $\pm$ 0.23  | 0.99 $\pm$ 0.16  |
| 1.0°             |                    | 0.48 $\pm$ 0.23                 | 0.48 $\pm$ 0.21  | 0.49 $\pm$ 0.20  | 0.98 $\pm$ 0.28                 | 0.98 $\pm$ 0.22  | 0.98 $\pm$ 0.19  |
| 2.0°             |                    | 0.45 $\pm$ 0.37                 | 0.46 $\pm$ 0.39  | 0.49 $\pm$ 0.34  | 0.95 $\pm$ 0.50                 | 0.95 $\pm$ 0.40  | 0.98 $\pm$ 0.32  |
| 3.0°             |                    | 0.42 $\pm$ 0.59                 | 0.43 $\pm$ 0.65  | 0.51 $\pm$ 0.52  | 0.93 $\pm$ 0.72                 | 0.94 $\pm$ 0.76  | 1.01 $\pm$ 0.50  |
| 4.0°             |                    | 0.36 $\pm$ 1.01                 | 0.40 $\pm$ 1.48  | 0.56 $\pm$ 0.84  | 0.85 $\pm$ 1.17                 | 0.87 $\pm$ 1.47  | 1.03 $\pm$ 0.88  |
| 5.0°             |                    | 0.36 $\pm$ 7.55                 | -0.09 $\pm$ 4.62 | 0.48 $\pm$ 1.08  | -0.54 $\pm$ 12.0                | 0.41 $\pm$ 6.13  | 0.93 $\pm$ 1.22  |

4° rotation, the axial variance was six times lower, and the lateral variance decreased by 40%. The method was able to measure axial strain properly and accurately up to 4° rotation angle. For 5°, the axial variance increased tenfold. However, the axial and lateral variances were five to nine times lower, compared to the rigid techniques. Obviously, the variance of the lateral strain estimates was higher as compared as the axial strain, but the improvement in bias is still evident. Similar to the (axial) shearing simulations, the lateral variance was lower when using the free-2D method, and the improvement, if present, was still significant ( $p < 0.001$ ).

## DISCUSSION

In this study, an assessment of strain imaging in axial shearing or rotating structures was performed using three different methods and simulated data using only one (state-of-the-art) linear array transducer configuration. The principal findings of this chapter are:

- The ‘free-shape’ 2D displacement estimation method outperformed conventional 1D and 2D algorithms, especially when large axial shearing or rotation is present
- Axial shear strain can be measured accurately using the aforementioned technique and has little influence on the axial and lateral strain estimates.

- Rotation can be measured in non deformed tissue up to  $4^\circ$  to  $5^\circ$ .

In deforming tissue, the presence of rotational movement decreases the accuracy of strain estimates dramatically.

It is not surprising that the free-2D method outperforms the other algorithms in case of severe axial shearing. The applied axial shear strain results in a large lateral gradient of the axial displacements and the proposed method corrects exactly for this phenomenon. Free-2D method is a straightforward way to overcome problems caused by large axial shearing and rotational movement. In the coarse-to-fine algorithm, the axial correction was performed using rounded axial displacement values, *i.e.* integers only, to maintain computational efficiency. Interpolated re-shaping of the post-compression RF-data during the re-correlation phase of the algorithm enhanced the cross-correlation even more, but at the cost of a large computational load. The 1D and 2D strain estimators, when using an axial window size of 1.0 mm take up 8 to 12 minutes for five iterations (coarse-to-fine (3x), aligning, stretching). An additional six minutes were required when using the free-shape 2D method, roughly increasing the computation time with 50%. This was consistent for other window sizes. Hence, the proposed method may not be a real-time application in its current form, but efficient coding and implementation in C-code would obviously decrease the computational load.

It must be noted that the performance of the free-2D method was also investigated (results not shown) for a range of axial window sizes (0.2 – 2.0 mm) and revealed a constant performance independent of

the axial window size in terms of axial and lateral RMSE.

The variance of the axial strain and shear strain decreased significantly when using 2D strain estimators. However, the bias increased (see Table 3.1). The improvement of axial displacement and strain estimates in terms of strain variance is larger compared to the lateral results. For instance, the variance of the axial strain and the axial shear strain decreased by a factor 3 to 5, but the variance of the lateral strain decreased less (-20%). In fact, it is trivial that lateral strain estimates seem less affected by the use of free-2D. Only the axial translation is corrected for, not the lateral. Furthermore, the variance of the lateral strain remains higher due to a lower lateral resolution and the absence of phase information. However, the bias of the lateral strain estimates increased significantly for higher rotation angles (see Table 3.2) and increased more compared to the axial strain results.

The use of RMSE and strain results analysis for comparison of the different methods is favored over the well-known elastographic signal-to-noise and contrast-to-noise ratios (SNRe and CNRe, respectively). The RMSE is calculated using the displacements, avoiding the effects of median filtering or LSQ smoothing on strain accuracy. However, RMSE assessment is only possible when the exact displacement is known and that forms a major limitation for phantom experiments. The maximum cross-correlation values were also considered. Apparently, the rigid-1D method yielded the highest CCFmax values. The cross-correlation of the rigid-1D strain estimator outperformed the 2D methods. However, using

2D kernels is more robust and results in less noisy displacement data and less outliers (Chapter 2). This can also be deduced from the RMSE results and Table 3.1. The strain results reveal that especially the variability is reduced by using the free-2D technique. However, the bias increased when using the 2D methods (see Table 3.1). Hence, the CCFmax seemed to be a bad measure for comparison of the three methods. This can be explained by the fact that the 1D technique is less influenced by the axial motion caused by the axial shear strain. The rigid-2D method will fail and the free-2D method will introduce errors caused by the interpolation and re-correlation. Hence, 2D windows will outperform 1D windows in terms of robustness and precision (*i.e.* variance), but might introduce bias and therefore reduce accuracy. This algorithm is a sliding window technique and the motion compensation is performed for each window. However, motion compensated post-compression RF-data is not generated. In such data, the cross-correlation would be a good measure and should show similar results as the RMSE-curves.

It must be noted, that especially in case of bias, the SNRe would have been a bad measure for precision. Over-estimation of strain would have led to higher SNRe, or would possibly disguise the fact that the variance had increased, whereas under-estimation could imply that the noise increased.

The rotation results seem promising, especially when considering the fact that rotation might be considered as a combination of axial and lateral shearing and translational motion (Meunier and Bertrand

1995), and the RF-data cannot be corrected line-by-line for lateral motion. It appears that for angles  $> 4.0^\circ$ , the axial gradient in the lateral displacements prevents accurate displacement measurements. Furthermore, the displacement and strain results show large artifacts at the lower part of the images. Again, lateral correction is not possible using RF-data, which limits the applicability of this method. B-mode data could be used in combination with non-rigid registration techniques, although further research is required. It must be noted that displacement and rotation precision will be spatially depended, since the 3 and 9 o'clock region of the phantom consist of axial motion and the top and bottom motion is largely lateral (Meunier 1998). The influence of rotation on strain estimates is large and increasing rotation has a negative effect on strain accuracy and vice versa. For both 1D and 2D strain imaging methods using fixed kernels, the axial and lateral strain were under-estimated. Especially the lateral strain accuracy increased when using the free-2D method. The variances increased for all methods when applying a vertical load. No explanation for the underestimation of the rotation angle beyond the acoustic focus can be given. Other artifacts were found near the axis of rotation. The displacements in this area are relatively small but can still be subject to noise. Hence, the two-argument atan2-function that is used for rotation angle calculation may corrupt rotation estimates around the center of rotation.

This study has several limitations. First of all, this is a methodical study using simulation data generated with only one transducer configuration. However, the authors

are aware that experimental work and *in vivo* validation should be the next, obvious step. Especially *in vivo*, a comparison with B-mode speckle tracking techniques should be made. Furthermore, the methodology of this study could be adapted to enable an investigation of the ability to measure torsion, which is of great interest for cardiovascular applications. The ultrasound data were simulated using a single type of linear array transducer, for only one center frequency with a fixed bandwidth, a large number of elements, relatively small pitch and infinite signal-to-noise ratio. The simulated transducer was based on a commercially available system (Chapter 2). The influence of transducer characteristics like beam diffraction/focusing on the performance of RF-based strain, axial shearing and rotation measurements is beyond the scope of this study. Furthermore, these simulations are predefined theoretical deformations and are not based on Finite Element Models. This gives the advantage that there are no boundary effects present in the displacement and strain fields. Lesion detectability and spatial resolution were not assessed in this study. It must also be noted that only the case of axial shearing was examined. Lateral shearing cannot be corrected for using the free-2D method and was therefore omitted.

Coarse-to-fine displacement algorithms are sensitive to the accuracy of the initial displacement estimates. If the rough displacement cannot be estimated, the algorithm will fail in all consecutive steps. This is also a drawback of the free-2D method, where each separate RF-line within the 2D search area is shifted according to the measured displacements. This is also illustrated by the displacement results of 5.0° and 10.0° rotation angles. Hence, the first global assessment is crucial for the final result.

## CONCLUSION

In conclusion, a ‘free-shape’, RF-based 2D displacement algorithm improves 2D strain estimation in case of significantly axial shearing and rotating structures. Rotation can be measured using RF-data up to 4° to 5°. Normally, strain accuracy deteriorates significantly for larger rotation angles, but this can be overcome using the proposed method.





Handwritten text in a box, possibly a list or notes.



---

# CHAPTER 4

## 2D STRAIN IMAGING USING SECTOR SCAN RF-DATA

---

*Richard G.P. Lopata, Hendrik (Rik) H.G. Hansen, Maartje M. Nillesen,  
Johan M. Thijssen, Livia Kapusta & Chris L. de Korte*

---

Based on: **Methodical Study on the Estimation of Strain in Shearing and Rotating Structures using Radio-Frequency Ultrasound based 1D and 2D Strain Estimation Techniques.** R.G.P. Lopata, H.H.G. Hansen, M.M. Nillesen, J.M. Thijssen, L. Kapusta and C.L. de Korte, *IEEE Transactions on Ultrasonics, Ferroelectrics & Frequency Control* 2010; 57(4), pp. 855-865.

---

## ABSTRACT

The goal of this study was to investigate the applicability of conventional 2D displacement and strain imaging techniques to phased array radio frequency data (RF). Furthermore, the possible advantages of aligning and stretching techniques for the reduction of decorrelation artefacts was examined. Data from both realistic simulations and phantoms were used in this study. Recently, the used processing concepts were successfully applied to linear array data. However, their applicability to sector scan data is not trivial due to the polar grid. Homogeneous and inhomogeneous tissue phantoms were simulated at a range of strains (0 to 5%) using Field II©. The inhomogeneous phantom, a commonly used tumor/lesion model, was also constructed using gelatin/agar solutions. A coarse-to-fine displacement algorithm was applied, using aligning and stretching to enhance re-correlation. Vertical and horizontal strains were reconstructed from the axial and lateral displacements. Results revealed that the error on displacement estimates was lower when using 2D data windows rather than 1D windows. For regions at large depths and large insonification angles, the allowed lateral window size was limited. Still, 1D windows resulted in larger errors. The re-correlation techniques resulted in a significant increase in the Elastographic Signal-to-Noise Ratio (SNRe) and Contrast-to-Noise Ratio (CNRe) of the vertical and horizontal strain components. An increase of the SNRe of 5 to 20 dB was observed over a range of strains (0.5 to 5.0%). In the inhomogeneous phantom, a vertical SNRe of 27.7 dB and a horizontal SNRe of 16.7 dB were measured in the background. The vertical and horizontal CNRe were 35 dB and 23.1 dB, respectively. For the experimental data, lower SNRe (vertical: 19.1 dB; horizontal: 11.4 dB) and CNRe (vertical: 33.3 dB; horizontal: 12.5 dB) were found. In conclusion, 2D window matching of sector scan data is feasible and outperforms 1D window matching. Furthermore, the use of re-correlation techniques enhances both precision and contrast of strain images.

## INTRODUCTION

Strain imaging, or elastography, is a technique to measure the deformation of tissue (Ophir et al. 1991; Ophir et al. 1999). The resulting strain images may be used to estimate the elastic and mechanical properties of tissue. The technique has been adapted for a large variety of applications, such as the detection of lesions and tumors (Céspedes et al. 1993a), breast tumors (Garra et al. 1997), atherosclerotic plaques (de Korte et al. 2000a), and blood clots (Emelianov et al. 2002). Quasi-static and external compression of phantoms or tissues are often used (Céspedes et al. 1993a; Varghese et al. 1996; Konofagou and Ophir 1998). The technique can also be applied to assess functional properties of actively deforming tissue such as skeletal muscle (Kallel et al. 1998; Tanter et al. 2002) and the heart (d’Hooge et al. 2000a; Konofagou et al. 2002; d’Hooge et al. 2002; Luo et al. 2007). In most applications, linear array transducers are used. An advantage of linear array transducers is the equidistant, parallel spacing of the ultrasound beams.

In a clinical setting, phased array transducers are often used for cardiac applications. The pyramid shape of the image sector and the small footprint of the transducer are required to perform intracostal imaging of the entire adult heart. New real-time 3D techniques are becoming more and more available. The pyramid-shaped sector scan data of 2D and 3D matrix array systems are comprised in a polar coordinate system with non-equidistant line spacing. Matrix array transducers are not only used

for cardiac strain imaging, but can be used for several applications where high frame-rates are required, for instance measuring 2D and 3D skeletal muscle deformation (Lopata et al. 2006).

Diverging ultrasound beams are also a property of data acquired with a curved array transducer. This type of transducers is especially designed to image large organs both at shallow and at larger imaging depths and it can also be used for strain imaging. Examples are strain imaging of the vessel wall in larger vessels such as the aorta (Hansen et al. 2008) and the detection of tumors in the liver or prostate (Khaled et al. 2006). However, these data suffer from the same divergence of ultrasound beams which results in axial and lateral strains that are not aligned with the directions of the strains of interest. The difference in coordinate system is certainly an issue for skeletal muscle, (prostate) tumors and long-axis acquisitions of the left ventricle. Moreover, it must be noted that the misalignment is always the case in vessels (besides the exception of intravascular strain imaging) and for the short axis view of the heart’s left ventricle, since these geometries require different corrections and/or projections (Ribbers et al. 2007, Lee et al. 2007).

It was previously shown that de-correlation reduces tracking precision (Alam and Ophir 1997). The effects of de-correlation can partly be overcome by global stretching of the RF-data (Varghese et al. 1996). This method works fine for homogeneous tissue deformed by an external compression device, but not always *in vivo*, where the deformation might be non-uniformly distributed. Besides, the applied or present strain cannot

be controlled in actively deforming tissue. Especially at limited frame rate, the deformation rate can become too high, which leads to high de-correlation of post-deformation signals which may cause inaccuracies and biased strain estimates (Alam and Ophir 1997). Besides, large translations of signal segments will cause problems for smaller search windows. Therefore, a relatively high frame rate is required, for instance in cardiac applications, to suppress these effects (Langeland et al. 2005a, Luo et al. 2007).

In Chapter 2, regarding RF-based 2D strain imaging, the effects of local techniques such as window aligning and local stretching were evaluated using linear array data. A significant increase in the SNRe of strain estimates in both the axial and lateral directions was observed and the contrast of the lesion showed similar improvement. Besides lesion detection, the local aligning and stretching techniques might especially be beneficial for data obtained in uncontrolled, strongly deforming structures such as skeletal muscle and the heart.

The study also revealed that the processing of 2D windows of RF-data is favorable and increases the precision of the measured displacements compared to the 1D condition. As mentioned above, the data of phased array and curved array transducers are collected in a non-Cartesian coordinate systems with non-equidistant line spacing. Hence, the use of 2D windows for displacement and strain estimation is not trivial and despite expected robustness, the potential applicability was questioned (Langeland et al. 2005b; Langeland 2007).

In this chapter, the applicability of 2D windows for estimation of strain in two dimensions using phased array RF-data is investigated. An iterative, correlation-based coarse-to-fine displacement estimation algorithm was implemented (Shi and Varghese 2007) using 2D data kernels and a fast 2D parabolic interpolation of the cross-correlation peak (Lopata et al. 2006; Chapter 2) and its performance was analyzed. This method was previously evaluated using linear array ultrasound data and is now applied to phased array data. Secondly, the applicability and benefits of re-correlation techniques, *i.e.*, aligning and local stretching, on phased array RF-data is examined.

A commonly used lesion/tumor model was chosen, since it enables the assessment of accuracy, precision (elastographic signal-to-noise ratio, SNRe) and detectability (elastographic contrast-to-noise ratio, CNRe) of a technique. Additionally, the chosen setup allows a comparison with linear array based strain estimation techniques and with other studies. Another approach would be using simulated cardiac data sets. This approach has been extensively investigated by several groups in other studies (Lee et al. 2007, Lee and Konofagou 2008, Luo et al. 2008). However, the aim of this study is assessment of the performance of the method and not the ability to measure cardiac strain. SNR can be measured using a homogeneous phantom and CNR can only be adequately measured using an inclusion phantom. The technique was experimentally validated using simulations and data of gelatin/agar phantoms.

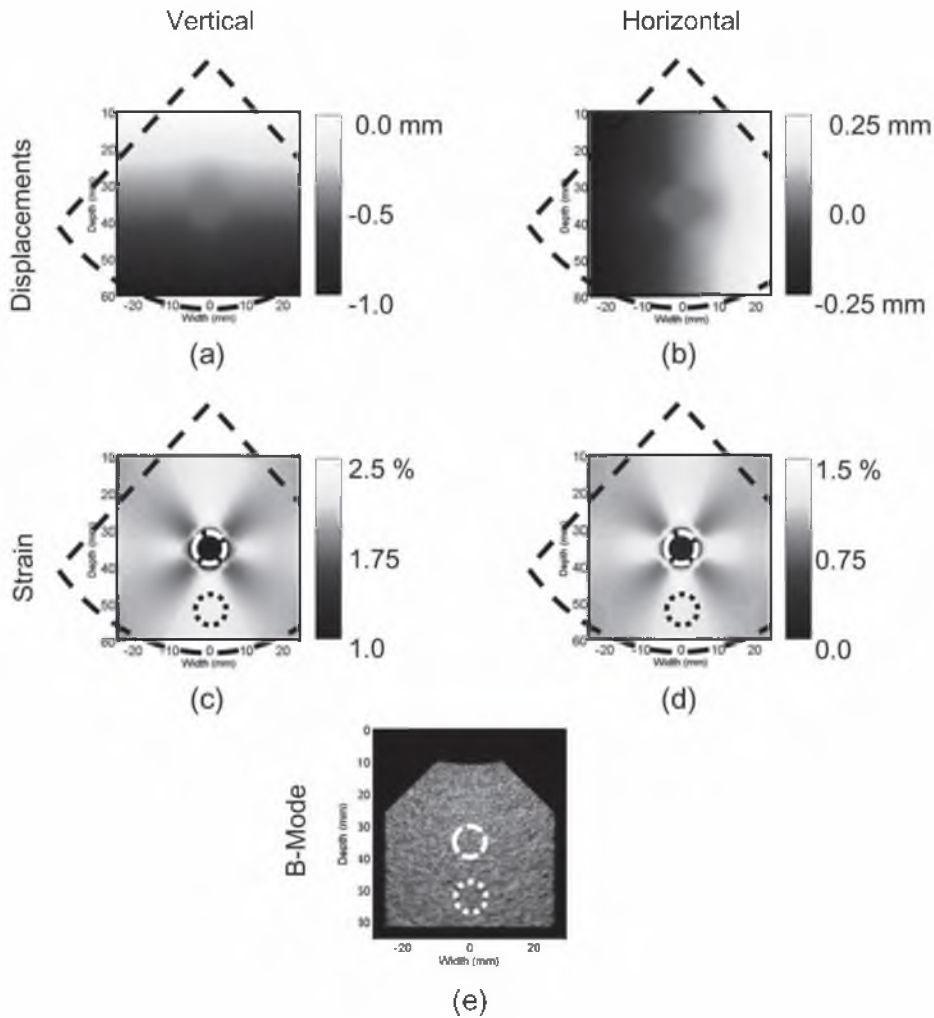


Figure 4.1 The solutions of the finite element model; the displacement in vertical direction (a) and horizontal direction (b) and the strain in vertical (c) and horizontal (d) direction. The dashed, rectangular region corresponds to the field of view of the simulated US images. An example of a simulated ultrasound image of the inhomogeneous phantom is shown (e). The white, dashed circle indicates the ROI within the inclusion and the white, dotted circle is the background region-of-interest, both used for SNRe and CNRe analysis.

## MATERIALS

### *Simulation study*

Raw (RF) ultrasound phased array data of a homogeneous and an inhomogeneous

tissue mimicking phantom were simulated to evaluate the performance of the 2D strain algorithm. The inhomogeneous phantom was originally developed as a phantom mimicking soft tissue with a hard lesion or tumor (Céspedes et al. 1993a; Ponnekanti et al. 1995; Kallel et al. 1996b).

**Table 4.1 Displacements and strains in the simulated homogeneous phantom.**

| <b>Applied axial strain (%)</b> | <b>Lateral strain (%)</b> | <b>Axial displacements (mm)</b> | <b>Lateral displacements (mm)</b> |
|---------------------------------|---------------------------|---------------------------------|-----------------------------------|
| -0.5                            | 0.25                      | -0.25 – 0                       | -0.06 – 0.06                      |
| -1.0                            | 0.50                      | -0.50 – 0                       | -0.12 – 0.12                      |
| -2.0                            | 0.99                      | -1.00 – 0                       | -0.25 – 0.25                      |
| -5.0                            | 2.48                      | -2.00 – 0                       | -0.62 – 0.62                      |

A homogeneous and an inhomogeneous phantom were simulated as described previously by our group (Chapter 2). The applied average vertical deformations of the homogeneous phantom were 0.5%, 1.0%, 2.0%, 3.0%, 4.0% and 5.0%, respectively. The range of the resulting vertical and horizontal displacements is listed in Table 4.1. The finite element method (FEM) model of the inhomogeneous phantom was solved for the case of 2.0% applied average vertical deformation. The displacements and strains of the phantom are shown in figure 4.1a-d.

Two-dimensional sector scan images were simulated using the Field II© ultrasound simulation software (Jensen 1996). A phased array transducer was modeled for a center frequency of 3.5 MHz, corresponding with the center frequency of the X4 matrix array transducer of the SONOS 7500 real-time 3D system (Philips Medical Systems, Bothell, USA) used for the experimental phantom study. The simulated transducer consisted of a phased array of 128 elements, using all elements in both transmit and receive mode, no apodization was implemented. The pitch was set to 50%

of the wavelength with an element width of 198  $\mu\text{m}$  (45 % of the wavelength) and an element height of 6 mm. The aperture had a fixed transmit focus, set in the center of the phantom (at 35 mm). To obtain a more homogeneous beam width, dynamic focusing was used by adding so-called receive focal zones every 4.0 mm. For each image, a total of 121 RF-lines was simulated with an incremental angle of 0.75 degrees, resulting in a total image sector of 90 degrees. The digital sampling frequency was set to 30 MHz.

The input of the Field II© software was a 3D matrix of randomly placed point-like scattering particles. Since the -20 dB elevational beam width was determined to be smaller than 1.0 cm for all echo depths, a “tissue” slice of 5 cm x 5 cm x 1 cm was used for 2D image simulation rather than using the entire block. The total amount of scatterers within the slice volume was  $3.5 \cdot 10^6$ , which is equal to 10 scatterers / resolution cell. This number is sufficient to guarantee fully developed speckle in the US image (Oosterveld et al. 1985). For the post-compression images, the scattering particles were translated using the solutions of the



FEM of the tissue mimicking phantoms. RF-data of both phantoms was simulated for the different levels of compression. An example of a 2D sector scan B-mode image is shown in figure 4.1e.

### *Phantom Study*

The inhomogeneous phantom was constructed using gelatin/agar solutions for assessment of the SNRe and CNRe of the method using a real phantom and experimental ultrasound signals. A block of soft tissue was made using a mixture that consisted of a 8% by weight gelatin (Dr. Oetker, Ede, The Netherlands) solution in water with an addition of 1% by weight agar-agar (Boom, Meppel, The Netherlands). Furthermore, 2.0% by weight scattering particles (40 - 63  $\mu\text{m}$  SiC, E. Merck, Darmstadt, Germany) were added for mimicking tissue scattering. The cylindrical inclusion consisted of 8.0% by weight gelatin and 3.0% by weight agar-agar solution. The resulting inclusion was approximately four times stiffer than the inclusion (Chapter 2), consistent with the used FEM.

## **METHODS**

### *2D coarse-to-fine displacement estimation*

For an extensive overview of the used approach, we refer to Chapter 2. In the present chapter, a coarse-to-fine displace-

ment estimation algorithm was used to estimate the axial and lateral displacements. Two-dimensional windows of data were cross-correlated and the resulting peak was detected using a 2D parabolic interpolation for fast and accurate 2D sub-sample displacement estimation. The algorithm used the signal envelope at coarse scale (first step) and RF-data for all subsequent steps. The axial window size was set to 8.0, 4.0 and 2.0 mm, respectively, for the pre-compression window, and was two times bigger in the post-compression window (16.0, 8.0 and 4.0 mm, respectively).

To examine the influence of lateral window size, the displacements were estimated using 1, 3, 5, 7, 9, 11, 15, 21 lines, respectively, in the pre-compression kernel. The post-compression kernel was extended with 3 lines on both sides. It must be noted that the effective kernel size becomes larger for increasing depth. For this reason, the lateral kernel size is expressed in lines instead of mm. The root-mean-squared error (RMSE) was calculated using the unfiltered displacements and the theoretical displacements of the FEM solutions. This error criterion was chosen, since the direct influence on displacement precision can be measured without the influence of filtering or of the used strain estimator. The SNRe was also measured for a circular ROI centered in the phantom (Fig. 4.1e).

### *Re-correlation using aligning and stretching*

Next, the effect of aligning and stretching was examined. The coarse-to-fine proce-

cedure was repeated for pre-compression axial window sizes of 8.0, 4.0 and 2.0 mm and 5 lines in the lateral direction. As before, the post-compression windows were two times larger. After the final coarse-to-fine step, the pre- and post-compression data were aligned at sub-sample level using the measured displacements after median filtering and spline interpolation. The axial displacements were filtered with a median filter of 11 x 5 pixels. A filter of 11 x 11 pixels was used for the lateral displacements. In case of phased array data, the vertical and axial strains are not aligned. The axial strain is used to stretch the 2D kernel of RF-data in the axial direction to enhance correlation (Chapter 2).

The axial and lateral strains (and shear components) were calculated using a least-squares strain estimator of 4.9 mm in the axial direction and 11 samples (*i.e.* 11 lines kernel width) in the lateral direction (Kallel and Ophir 1997). The vertical and horizontal displacements and strains were reconstructed from the axial and lateral displacements/strains using a transformation of the coordinate system (see Appendix Ch-4 and Fig. 4.7). The RMSE, SNRe and CNRe (in the inhomogeneous phantom only) were calculated for all steps of the algorithm, *i.e.* coarse-to-fine, aligning and stretching, for all simulated data sets.

### *Phantom Study*

The phantom was deformed using an automated compressor setup. The transducer of the ultrasound system (US) was anchored in the center of the top plate. The plate was moved to compress the phantom

in steps of 0.5 mm up to a total of 5.0 mm (0.5% to 5.0% strain). After each applied deformation step, 2D phased array images were acquired. The raw BiPlane data were recorded with a Philips SONOS 7500 real-time 3D system, equipped with a 4MHz 3D matrix array transducer (X4), and were sampled at 19.5 MHz. The displacements and strains were estimated using the optimal settings as found in the simulation study. Next, the simulated and experimental data were compared in terms of SNRe and CNRe.

## RESULTS

Figure 4.2 shows the RMS errors for the measured axial and lateral displacements as a function of lateral pre-compression window size. The analysis was performed for six different regions of the B-mode sector image. Each ROI contained an equal amount of pixels for fair comparison. As expected, the axial RMSE was found to be lower than the lateral RMSE, except for region 'd'. For the other regions, the RMSEs were found to be higher for larger image depths and larger angles. In general, the use of 2D windows yielded lower RMSEs compared to a lateral window size of a single line. It seems that a minimum in RMSE is present for lateral window sizes between 3 and 11 lines. There is an abrupt decrease in RMSE when comparing the 1D kernels to the most narrow 2D kernel of 3 lines.

The SNRe of the vertical and horizontal strains is shown in figure 4.3. SNRe was

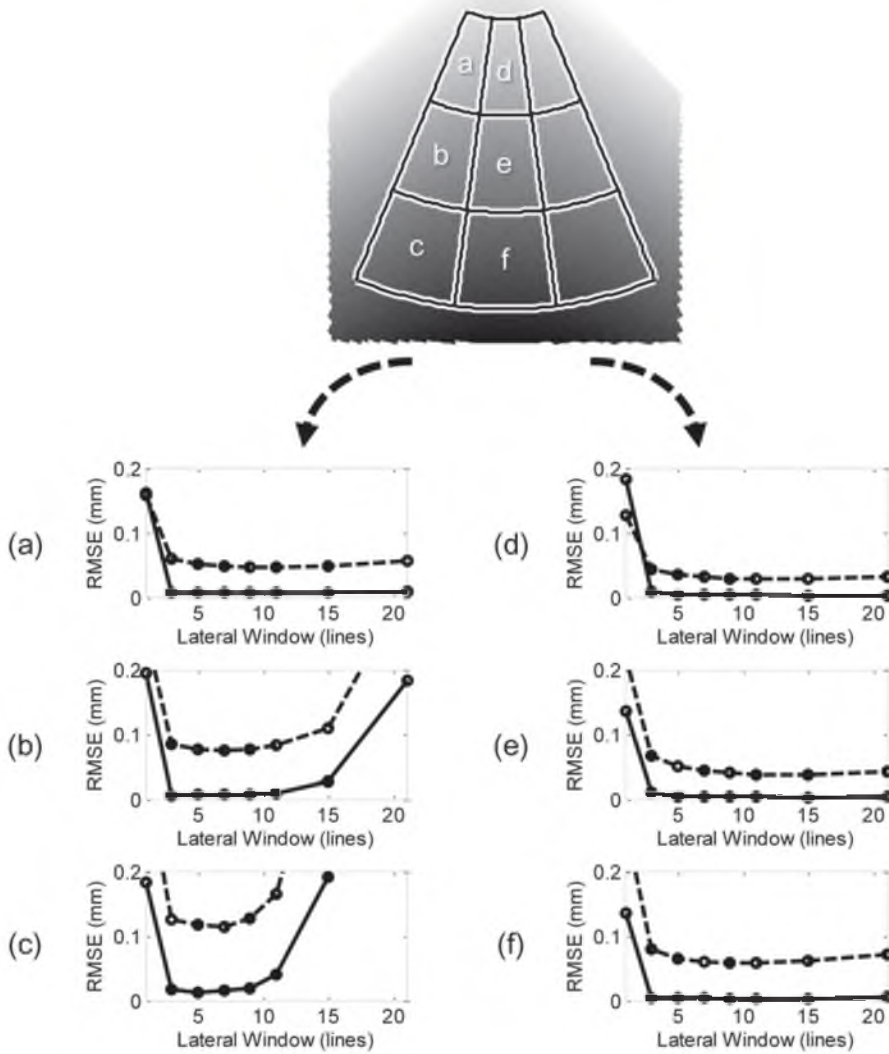


Figure 4.2. Axial (solid) and lateral (dashed) root-mean-squared error for increasing lateral kernel size for six different regions (a-f) within the homogeneous phantom at 2.0% applied load

derived from the indicated regions (a, and b) in the homogeneous phantom for strains ranging from 0.5 to 5.0%. The shape of the SNRe curves is similar to the strain filter (Varghese and Ophir 1997) for the first three steps of the strain estimation procedure (coarse-to-fine). After aligning and stretching, an increase in SNRe is observed in vertical and horizontal directions. Although, for

smaller applied (vertical) strains ( $\leq 1.0\%$ ), there is some benefit from using aligning and stretching (+ 6 to 8 dB), a much greater improvement was observed for 5.0% strain (+ 21 dB). The final range of vertical SNRe is 33-37 dB for the inner region (b) and only 23-33 dB for the outer region (a), due to the larger angle between ultrasound beam and axial deformation. For the horizontal

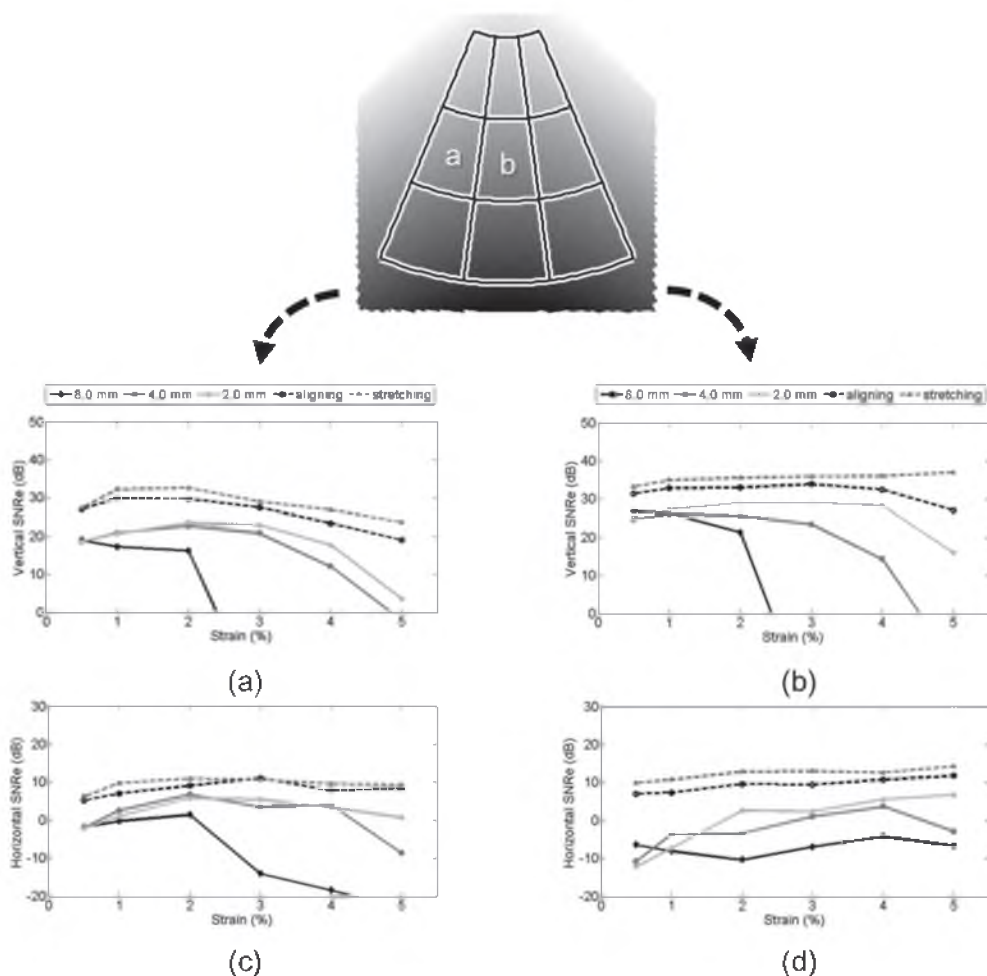


Figure 4.3. The calculated elastographic signal-to-noise ratio (SNRe) for the simulated homogeneous phantom as a function of applied strain (0.5 – 5.0%) for all steps of the algorithm. The vertical and horizontal SNRe are given for two regions in the homogeneous phantoms at the outer (a) and the middle section (b).

strains, the final range for region (b) is 10 – 14 B. The increase in SNRe after aligning (5 – 19 dB) is significantly higher compared to stretching (2 – 3.5 dB). The vertical and horizontal SNRe are shown for the entire image in figure 4.4 for the cases of 2.0% and 5.0% applied load. The SNRe of the strains in both directions decreased significantly for increasing insonification angle, especially for 5% load.

The modeled (FEM) and the measured

displacement and strain images are shown in figure 4.5a-h. In the inhomogeneous phantom, variation of the strain occurs within the chosen ROIs (Fig. 4.1c-e). The theoretical maximum SNRe and CNRe were calculated from the FEM solutions and compared with estimated values from the simulated images (see Fig. 4.5 and Table 4.2). The theoretical and measured vertical SNRe were 28.2 and 27.7 dB, respectively (Fig. 4.5i). The corresponding obtained

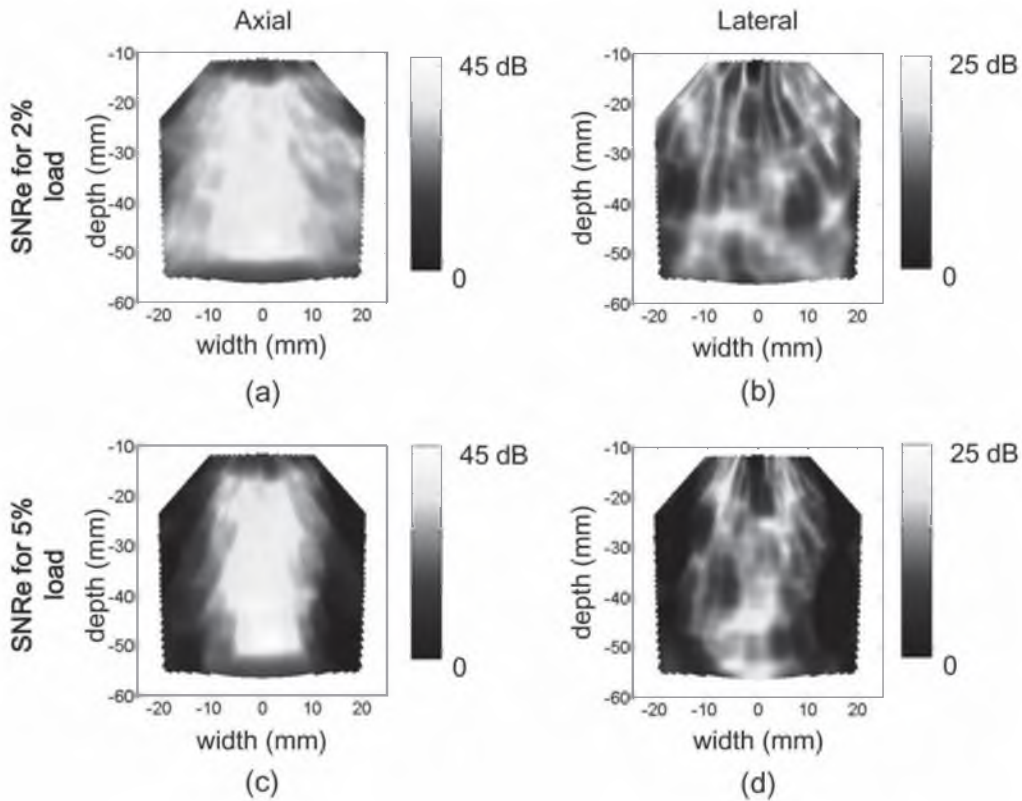


Figure 4.4. The calculated vertical and horizontal elastographic signal-to-noise ratio (SNRe) for the simulated homogeneous phantom images at 2.0% and 5.0% applied load. Each SNRe value was calculated for a region of 11 x 11 strain pixels.

vertical CNRe was 35.0 dB compared to a theoretical value of 40 dB. In the horizontal direction, the theoretical SNRe and CNRe were 23.2 and 36.1 dB, respectively. The obtained maximum values in the simulations were 16.7 and 23.1 dB (Fig. 4. 5j-l).

The quality of the strain images of the phantom is illustrated in figure 4.6 and the SNRe and CNRe values are listed in Table 4.2. The mean and standard deviation of the SNRe and CNRe, based on ten datasets, are given for the vertical and horizontal strain (Fig. 4. 6). The used regions correspond with the used regions in the simulation study (Fig. 4.1e). The vertical SNRe of 19

dB was approximately 9 dB lower compared to the simulation study, but the CNRe was almost identical. The horizontal SNRe and CNRe were 11.4 dB and 12.5 dB, respectively, almost 5 and 10 dB lower than in the simulated data.

## DISCUSSION

The main finding of the first part of the study is that the use of 2D pre- and post-compression windows is to be preferred over 1D pre-compression windows, but that the

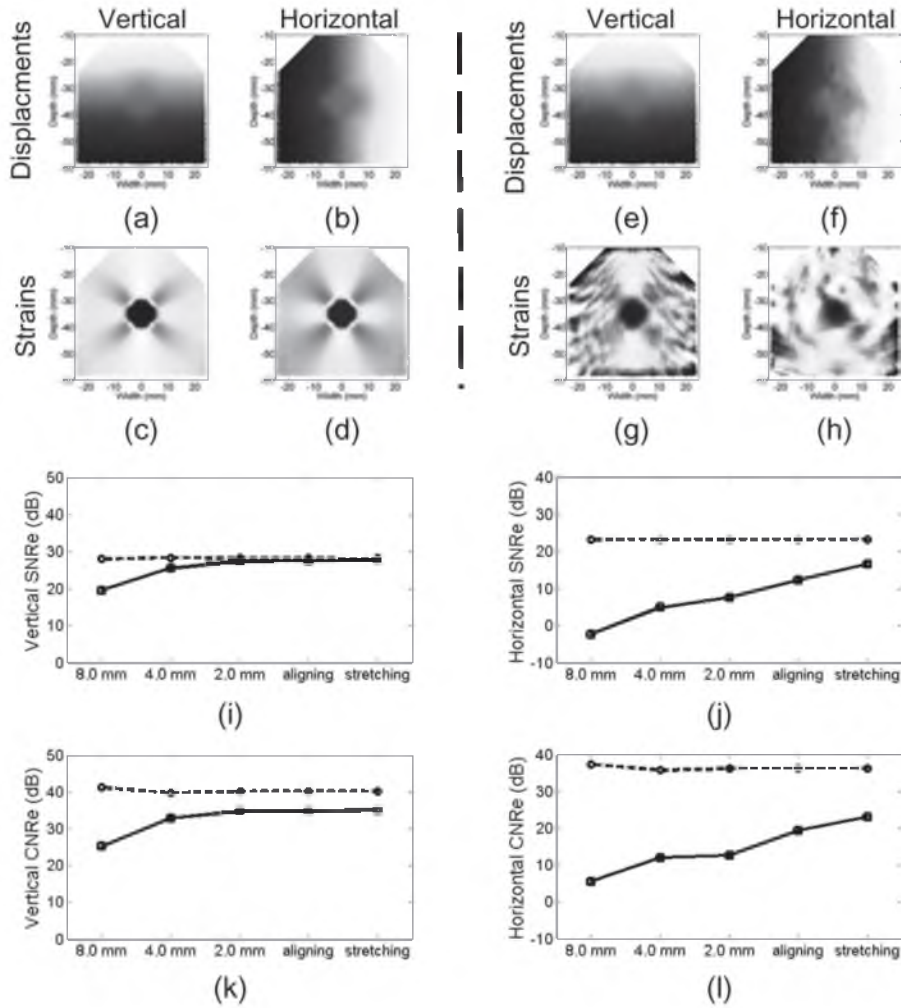


Figure 4.5. The FEM displacements and strain images (a-d) and the measured displacement and strain images (e-h). The elastographic signal-to-noise ratio and contrast-to-noise ratio of the simulated data of an inhomogeneous phantom for all steps of the strain estimation algorithm (solid lines): i) the SNRe of the vertical strain; j) the SNRe of the horizontal strain; k) CNRe of the vertical strain; k) CNRe of the horizontal strains. The maximum theoretical SNRe and CNRe are calculated using the finite element model (dashed lines).

lateral window size should be limited. The upper sector image region ('d' in Fig. 4.2) has the smallest distance between RF-lines and the lowest insonification angle. Therefore, the RF-lines may be considered similar to linear array data. The results also showed close resemblance to those obtained from linear data, in which the largest lateral

window size yielded the lowest axial and lateral RMSEs (Chapter 2). At greater depths, the RMSE values became higher for increasing lateral window sizes. The upper limit on the used lateral window size was also clearly visible for all outer regions. This phenomenon is probably caused by the larger insonification angle and by scatterer

Table 4.2 Comparison of the SNRe and CNRe values (final step of the algorithm)

|            | Vertical SNRe<br>(dB) | Vertical CNRe<br>(dB) | Horizontal SNRe<br>(dB) | Horizontal CNRe<br>(dB) |
|------------|-----------------------|-----------------------|-------------------------|-------------------------|
| FE Model   | 28.2                  | 40.0                  | 23.2                    | 36.1                    |
| Simulation | 27.7                  | 35.0                  | 16.7                    | 23.1                    |
| Experiment | 19.1                  | 33.3                  | 11.4                    | 12.5                    |

movement (will be discussed in detail further on). But for all depths andinsonification angles, the use of 2D windows improved the performance of the algorithm. The transition from 1D to 2D in terms of RMSE seems quite abrupt. However, no explanation of this phenomenon could be given and intermediate kernel sizes are not available. The optimization of the lateral window length revealed a minimum for the error of the axial and lateral displacement estimates. The authors would like to point out that this ‘optimal window length’ probably depends on experimental condi-

tions, *i.e.*, the frequency characteristics of the used transducer, incremental angles, applied strain, horizontal movement, etc.

Analysis of the SNRe and CNRe of the strain components revealed an improvement for each step of the coarse-to-fine algorithm. Re-aligning significantly improves horizontal strains by up to + 19.0 dB. This is in accordance with previous work (Konofagou and Ophir 1998; Chapter 2) despite the non-equidistant line spacing. Stretching yields a large improvement of the accuracy of vertical strain, especially at higher applied strains (+10 dB at 5.0% applied strain).

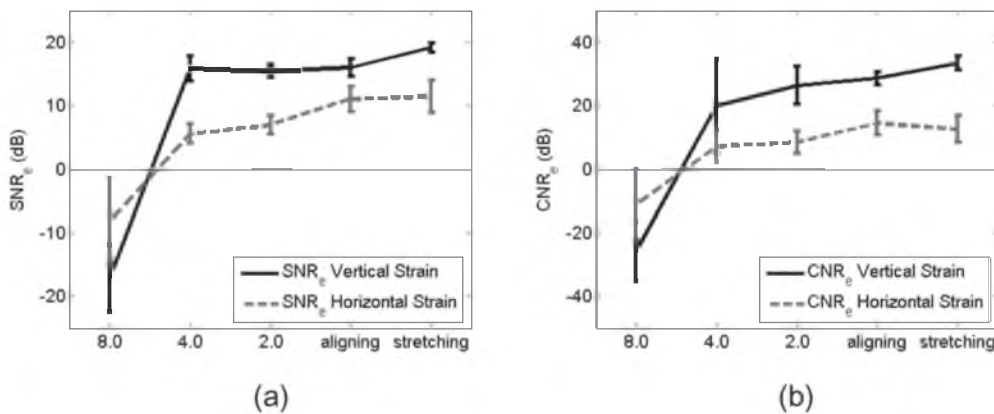


Figure 4.6. The mean and standard deviation of the measured SNRe and CNRe for experimental data of an inhomogeneous phantom (n = 10) for all steps of the strain estimation algorithm: a) SNRe of the vertical (black, solid) and horizontal strain (grey, dashed); b) CNRe of the vertical (black, solid) and horizontal strains (grey, dashed).

Hence, aligning is necessary for an improvement of horizontal SNRe and stretching for vertical strains, which is again in accordance with our findings in a study of linear array data and proves that aligning and stretching is also beneficial for sector scan data. A strain of 5.0% is not uncommon in cardiac data, depending on the frame rate. Therefore, stretching will enhance the strain precision.

For the inhomogeneous simulation and phantom data, a similar increase in SNRe was observed for each step of the algorithm. The theoretical and measured SNRe values are lower compared to those obtained for the homogeneous simulation data at 2.0% applied strain. This can be explained by a different mean strain and corresponding variance in the chosen ROI caused by the inclusion (Fig. 4.1c-e). In general, the CNRe is lower in the simulation and phantom study compared to the theoretical upper-limit (Fig. 4.5 and Fig. 4.6), probably caused by the use of median filtering and LSQ strain estimation. The horizontal SNRe and CNRe are considerably lower in simulations as well as the phantoms study, which is probably caused by the lower lateral sampling, the increasing spacing between RF-lines, the lack of phase information and the lower absolute horizontal strain which is approximately 50% of the vertical strain.

In this study, we used a simulation and phantom model often used in performance assessment of elastographic techniques. In this way, a good comparison with previous work could be performed. It is clear that the geometry in cardiac application is different, but also in this application, radial and circumferential strain will be estimated from axial and lateral estimates (Lee et al. 2007).

The RMSE and SNRe analysis reveal less precision of displacement and strain estimates for larger insonification angles. This is illustrated by the strain images, that reveal an increase of noise in all strains. This is observed in both the simulation study (Fig. 4.5) and the experimental data (not shown). The angle between the vertical and horizontal scatter movement increases with an increasing insonification angle. Hence, scatterers move through the RF-lines at an angle. This phenomenon is not present when using linear array data. Consequently, the re-correlation techniques are less beneficial, since the measured displacements and strains are less aligned with the present displacements and strains. Besides, vertical precision is lower due to the larger lateral contribution to the vertical strain.

It is often questioned whether 2D kernels are applicable, valid and beneficial for 2D strain estimation, when diverging line data are used (Langeland et al. 2005b; Langeland 2007). The simulation and phantom studies do not indicate any problem for the strain estimation using 2D windows. Moreover, the use of 2D windows outperforms the 1D case in terms of precision, despite the lower precision at larger insonification angles. However, this issue is less problematic in cardiovascular data, where the strains of interest are more often the radial and circumferential strain, obeying a coordinate system that is better aligned with the phased array data. Besides, 2D windows enable the use of 2D parabolic interpolation. It should be noted that parabolic interpolation was chosen since this analytic interpolation scheme is fast and accurate (Chapter 2).



## CONCLUSION

In conclusion, the use of 2D kernels of RF-data for 2D displacement and strain estimation is beneficial when the data are present in a polar grid as in sector scanning by phased array transducers. Furthermore, the precision and contrast of both strain components can be enhanced using re-correlation techniques, such as aligning and stretching. In general, the SNRe and CNRe is lower compared to linear array data and the performance decreases with increasing depth and insonification angle. This approach can also be used for demodulated B-mode sector data.

## APPENDIX

Sector scan data of a phased array transducer obey a polar grid (see Fig. 4.7). Initially, the displacements along and perpendicular to the ultrasound beam are measured, *i.e.*, the axial ( $\epsilon_{ax}$ ) and lateral displacements ( $\epsilon_{lat}$ ), respectively (Fig. 4.7). To reconstruct the displacements, in the actual vertical (z) and horizontal (x) direction, the rotation matrix is used to transform the measured displacement values in polar coordinates into Cartesian values of the displacements (x and z):

$$(z(r, \theta), x(r, \theta)) = (\delta_{ax}(r, \theta), \delta_{lat}(r, \theta)) \cdot \mathbf{R} \quad (4.1)$$

with  $r$  the radius and  $\theta$  the angle of the received ultrasound beam with respect to the z-axis.  $z(r, \theta)$  is the vertical displacement

vector and  $x(r, \theta)$  is the horizontal displacement, both in polar coordinates.  $\mathbf{R}$  is the rotation matrix:

$$\mathbf{R} = \begin{bmatrix} \cos \theta & \sin \theta \\ -\sin \theta & \cos \theta \end{bmatrix} \quad (4.2)$$

After determining the spatial gradients of both displacement vectors  $z$  and  $x$  in the lateral ( $\partial/\partial\theta$ ) and axial direction ( $\partial/\partial r$ ), the vertical and horizontal strains are reconstructed using:

$$\begin{bmatrix} \epsilon_{zz} & \epsilon_{zx} \\ \epsilon_{xz} & \epsilon_{xx} \end{bmatrix} = \begin{bmatrix} \frac{\partial z}{\partial r} & \frac{\partial z}{\partial \theta} \\ \frac{\partial x}{\partial r} & \frac{\partial x}{\partial \theta} \end{bmatrix} \cdot \mathbf{R} \quad (4.3)$$

with  $\epsilon_{zz}$  the vertical strain,  $\epsilon_{xx}$  the horizontal strain and  $\epsilon_{zx}$  and  $\epsilon_{xz}$  the shear strains. This result in:

$$\begin{aligned} \epsilon_{zz} &= \frac{\partial z}{\partial r} \cos \theta - \frac{\partial z}{\partial \theta} \sin \theta \\ \epsilon_{xx} &= \frac{\partial x}{\partial r} \sin \theta + \frac{\partial x}{\partial \theta} \cos \theta \\ \epsilon_{xz} &= \frac{\partial x}{\partial r} \cos \theta - \frac{\partial x}{\partial \theta} \sin \theta \\ \epsilon_{zx} &= \frac{\partial x}{\partial r} \sin \theta + \frac{\partial x}{\partial \theta} \cos \theta \end{aligned} \quad (4.4)$$

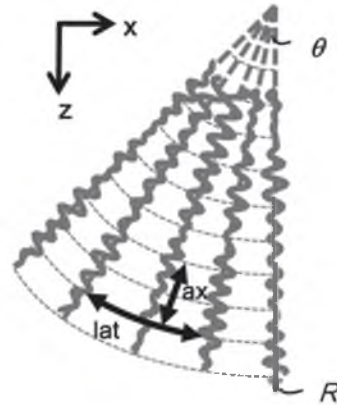


Figure. 4.7. Schematic representation of phased array sector scan data and the two coordinate systems (polar and Cartesian).



---

# CHAPTER 5

## COMPARISON OF ONE-DIMENSIONAL AND TWO-DIMENSIONAL LEAST-SQUARES STRAIN ESTIMATORS

---

*Richard G.P. Lopata, Hendrik (Rik) H.G. Hansen, Maartje M. Nillesen,  
Johan M. Thijssen & Chris L. de Korte*

---

Based on: **Comparison of One-Dimensional and Two-Dimensional Least-Squares Strain Estimators for Phased Array Displacement Data.** R.G.P. Lopata, H.H.G. Hansen, M.M. Nillesen, J.M. Thijssen and C.L. de Korte, *Ultrasonic Imaging* 2009; 31(1): 1-16.2010; 57(4), pp. 855-865.

---

## ABSTRACT

In this chapter, the performance of one-dimensional and two-dimensional least-squares strain estimators (LSQSE) is compared. Furthermore, the effects of kernel size are examined using simulated raw frequency data of a widely adapted hard lesion / soft tissue model. The performance of both methods is assessed in terms of root-mean-squared errors (RMSE), elastographic signal-to-noise ratio (SNRe) and contrast-to-noise ratio (CNRe). RMSE analysis revealed that the 2D LSQSE yields better results for phased array data, especially for larger insonification angles. Using a 2D LSQSE enabled the processing of unfiltered displacement data, in particular for the lateral / horizontal strain components. The SNRe and CNRe analysis showed an improvement in precision and almost no loss in contrast using 2D LSQSE. However, the RMSE images for different kernel sizes revealed that the optimal 2D kernel size depends on the region-of-interest and showed that the LSQ kernel size should be limited to avoid loss in resolution.

## INTRODUCTION

Ultrasound strain imaging (ultrasound elastography), is a technique to measure the deformation, or mechanical properties, of biological tissue (Ophir et al. 1991; Ophir et al. 1999). The technique has been used in a wide variety of applications for quantification of tissue deformation and motion, and for palpation purposes. For instance, deformation can be induced quasi-statically to detect hard lesions in soft tissues (Céspedes et al. 1993a; Garra et al. 1997; Kallel et al. 1999). On the other hand, strain imaging can also be performed in arteries to characterize atherosclerotic plaques (de Korte et al. 2000b; Schmitt et al. 2007) or in actively deforming tissue such as the heart in order to measure cardiac function (d’Hooge et al. 2002b; Konofagou et al. 2002).

Various techniques have been proposed to measure tissue movement and deformation. However, only a small number of these techniques, such as adaptive strain imaging and image registration, yield the strain instantaneously (Alam et al. 1998; Elen et al. 2008; Srinivasan and Ophir 2003; Zahiri-Azar and Salcudean 2008). Most techniques are based on correlation of pre- and post-compression raw frequency (RF) data and yield only the two-dimensional (2D) displacement of the tissue (Konofagou and Ophir 1998; Langeland et al. 2003; Chapter 2). The (relative) deformation, or strain, is obtained by applying a derivative operation on the calculated displacement data (Ophir et al. 1991).

Taking the first order derivative of noisy displacement data will result in noise ampli-

fication in the strain images (elastograms) (Céspedes and Ophir 1993b; Kallel and Ophir 1997). Median filtering or averaging of the strain images is one possibility to reduce this effect (Ophir et al. 1991; Varghese et al. 1996). Another approach is strain calculation using multiple displacement values, an approach for which a number of differentiators has been proposed: The one-dimensional (1D) least-squares strain estimator (LSQSE) was introduced by Kallel & Ophir (Kallel and Ophir 1997) and has been used in numerous studies (Konofagou and Ophir 1998; Lee and Konofagou 2008; Chapter 2). In several studies, alternative differentiators were examined and compared (Luo et al. 2004; Srinivasan et al. 2002). Low-pass filter characteristic is a common property for all of these methods. Besides these low-pass adapted differentiators, assumptions on the motion field can also be made and used to smooth strain images (Lubinski et al. 1996; Sumi and Sato 2008).

The discrete differentiator methods are all operating in one dimension. However, RF-based 2D and 3D strain imaging techniques are on the rise. A limitation of the LSQSE is that it is mostly applied on linear array data. In cardiac ultrasound applications, phased array transducers are generally used. The data of phased array transducers are obtained in a polar coordinate system. A number of studies with phased array data can be found (Langeland et al. 2005a; Lee et al. 2007). In previous work, 2D and 3D planes were fitted through displacement data to obtain the first order spatial derivatives (Lopata et al. 2006; Lopata et al. 2007). This is in fact a 2D version of the LSQSE method. The amount of regularization has

increased, since neighboring data in two or more directions are used. Signal-to-noise is often gained at the cost of detectability or contrast. Furthermore, there is a trade-off between resolution and signal-to-noise and contrast-to-noise (Alam et al. 2000; Righetti et al. 2002). Nevertheless, quantitative analysis of the effect of applying these plane fitting methods and the effect of kernel size in multiple directions was not the focus in previous work.

In this chapter, the aforementioned technique of 2D plane fitting is examined and the performance of this 2D LSQSE compared to the common 1D technique. The effect of 1D and 2D kernel sizes, pre-filtering of displacement data and the choice of precision metric was examined using simulated sector scan data of inhomogeneous tissue phantoms. The methods were also tested using experimental phantom data.

## MATERIALS

### *Simulation study*

To evaluate the performance of the strain estimators, a commonly used inhomogeneous phantom was simulated using SEPRAN© (Septra BV, The Hague, NL) and Field II© (Jensen 1996). This lesion or tumor model consists of a hard cylindrical inclusion in a soft block of surrounding tissue. The presence of the hard inclusion enables CNRe measurements in addition to SNRe analysis (Céspedes et al. 1993a; Kallel

et al. 1996). The ability of both SNRe and CNRe measurements and the wide employment of this model allows for a comparison with previous studies.

A Finite Element Model (FEM) of this tissue mimicking phantom was implemented and its mechanical response to an applied load was simulated using SEPRAN. A hard cylindrical inclusion with a diameter of 1 cm and a Young's modulus (E) of 60 kPa was centered in a block (5 cm x 5 cm x 5 cm) of softer surrounding tissue (E=15 kPa). Both materials were isotropic, linear elastic, and almost incompressible (Poisson ratio = 0.495). The FEM models were solved for an applied average vertical deformation of 2.0% using 3D linear-elastic elements.

Field II© was used to simulate two-dimensional sector scan images (Jensen 1996). A phased array transducer was modeled, consisting of 128 elements. All elements were used in both transmit and receive mode. The center frequency was set to 3.5 MHz and the speed of sound was assumed to be 1540 m/s. The pitch was 50% of the wavelength. The element width was set to 198  $\mu\text{m}$  width (45 % of the wavelength) with an element height of 6 mm. The transmit focus of the aperture was fixed and was centered in the phantom (35 mm depth). Dynamic focusing was used in receive mode to obtain a more homogeneous beam width by adding so-called receive focal zones every 4.0 mm (Jensen 1996). The phased array data obey a polar grid. A total of 121 RF-lines were simulated with an incremental angle of 0.75 degrees, resulting in a total image sector of 90 degrees. The data were digitized with a sampling frequency of 30 MHz.

The input of Field II© was an *in silico* tissue with homogeneous echogenicity. A 3D matrix of point-shaped scattering particles was generated, with the particles placed at random in a volume of 50 mm x 50 mm x 10 mm. A slab of 10 mm width was used, since the -20 dB elevational beam width was found to be 8 mm. The total amount of scatterers within the slice volume was  $3.5 \cdot 10^6$ , a sufficient amount to guarantee fully developed speckle in the ultrasound image (Oosterveld et al. 1985). For the post-compression images, the scattering particles were translated using the solutions of the FEM of the tissue mimicking phantom for the applied load.

### *Phantom study*

The aforementioned inhomogeneous tissue-mimicking phantom was also constructed for experimental validation<sup>16</sup>. A cylinder was made with 8.0% by weight gelatin (Dr. Oetker, Ede, The Netherlands) solution in water with an additional 3.0% by weight agar-agar (Boom, Meppel, The Netherlands) and 1.0% by weight scattering particles (40 - 63  $\mu\text{m}$  SiC, E. Merck, Darmstadt, Germany). The surrounding tissue consisted of 8.0% by weight gelatin, 1.0% agar-agar and 2.0% scattering particles. The higher agar concentration resulted in an approximately four times stiffer inclusion (de Korte et al. 1997b; Madsen et al. 2005). Raw, radio frequency data of the phantom were recorded during deformation using a SONOS 7500 medical ultrasound system (Philips Medical Systems, Bothell, USA), with an X4 transducer ( $f_c = 3.5$

MHz). The angle between the RF-lines was 0.75 degrees. The inclusion phantom was deformed using an automated compressor set-up. The RF-data were acquired after an applied load of 2.0% (after ten conditioning cycles). The phantoms were lubricated at the top and bottom side to fulfill free-slip boundary condition.

## METHODS

### *2D coarse-to-fine displacement estimation*

A 2D coarse-to-fine displacement estimation algorithm was used to estimate the axial and lateral displacements simultaneously. Two-dimensional windows of pre- and post-compression data were cross-correlated. The peak of the cross-correlation function was detected and 2D parabolic interpolation was used for fast and accurate 2D sub-sample displacement estimation (Chapter 2). The algorithm used the signal envelope at coarse scale (first step) and RF-data for all subsequent steps. For the pre-compression window, the axial window size was set to 8.0 mm for the initial step and smaller for the subsequent steps (4.0 and 2.0 mm, respectively). The post-compression window was two times bigger (16.0, 8.0 and 4.0 mm, respectively). The lateral window size was 5 lines (pre-compression) and 11 lines (post-compression) for each iteration of the coarse-to-fine algorithm. Local aligning and stretching of the post-compression data was used in the final iteration step to

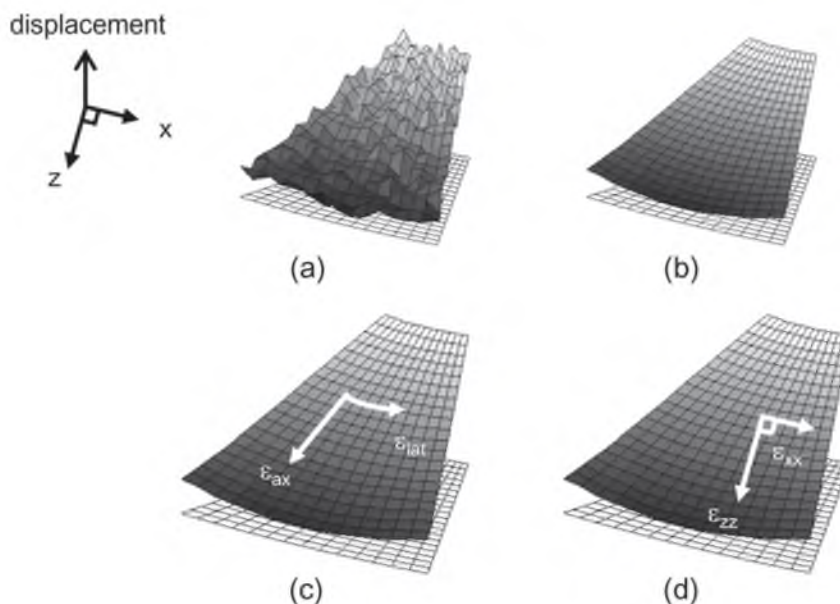


Figure 5.1 Schematic representation of 2D linear regression: (a) The unfiltered displacement field; (b) the resulting displacement field after fitting a 2D plane through the measured displacements; (c) the first order derivatives in the axial and lateral direction yield the axial ( $\epsilon_{ax}$ ) and lateral strain ( $\epsilon_{lat}$ ); (d) the Cartesian strains, the derivatives in the z and x-direction ( $\epsilon_{zz}$ ,  $\epsilon_{xx}$ ).

enhance the correlation between pre- and post-compression data (Chapter 2 & 3). Data windows were re-correlated using previous estimates of the axial and lateral displacements (aligning) and the axial strain (stretching). These last two additional steps produced significant improvement in the precision and contrast of displacement and strain estimates in phased array data (Lee et al. 2007; Chapter 2 & 3).

### *Least-squares strain estimation*

The one-dimensional Least-Squares Strain Estimator (1D LSQSE) was introduced and thoroughly described by Kallel & Ophir (Kallel and Ophir 1997) and has been widely adapted ever since (Konofa-

gou et al 1998; Srinisivan et al 2003). The main concept of LSQSE is a linear curve fit through a kernel of displacement estimates. The directional coefficient of this linear curve is a low-pass filtered estimate of the local strain. Especially in noisy displacement data, the use of an LSQSE outperforms a simple first-order differentiation strategy significantly, although at the cost of reduced spatial resolution (Alam et al. 2000; Righetti et al. 2002).

In this study, the performance of the 1D LSQSE applied on phased array displacement data is examined and compared to the performance of a 2D LSQSE. The possible advantage of a 2D plane fit is the use of displacements of neighboring windows. The concept of a 2D LSQSE is illustrated in figure 5.1. A 2D plane is fitted through the



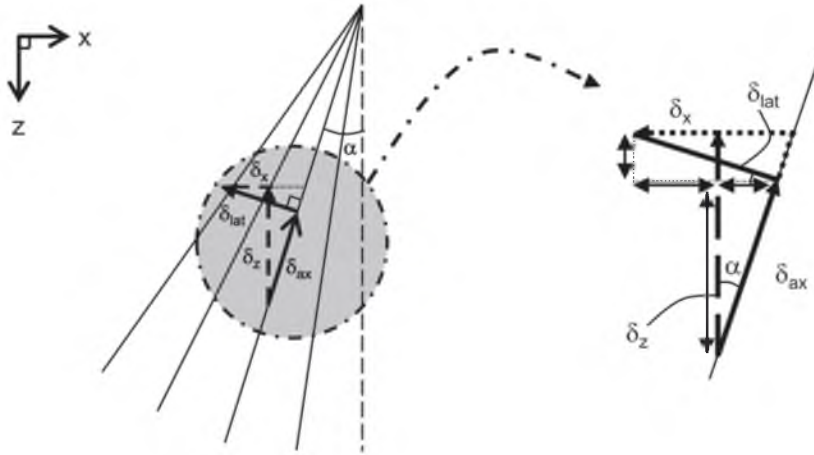


Figure 5.2 Schematic representation of the transformation of the measured displacements into the displacements in the x and z-direction. The measured displacements  $\delta_{ax}$  and  $\delta_{lat}$ , respectively parallel and perpendicular to the ultrasound beam, are rotated with respect to the steering angle,  $\alpha$ , yielding the displacements  $\delta_z$  and  $\delta_x$  in the Cartesian coordinate system.

noisy displacement estimates (Fig. 5.1a-c) The plane equation is given by:

$$\delta = \alpha x + \beta y + \gamma \quad (5.1)$$

where:  $\delta$  is the displacement,  $x$  and  $y$  are the pixel coordinates,  $\alpha$  and  $\beta$  are both directional coefficients and  $\gamma$  is an offset value. The derivation of the least-squares solution for  $\alpha$ ,  $\beta$  and  $\gamma$  may be found in Appendix Ch-5.

The measured displacements are parallel to the ultrasound beam (axial direction) and perpendicular to the ultrasound beam (lateral direction) and obey a polar grid (see Fig. 5.2). The 2D LSQSE yields the derivatives of the displacement of interest in both the axial and lateral direction simultaneously (Fig. 5.1d). In case of the axial displacements, this will result in the axial strain and the axial shear strain. However, to reconstruct the true strains in the vertical (z) and horizontal direction (x), a trans-

formation of coordinate system is necessary (Fig. 5.1e). The transformation of the polar displacements and strains to a Cartesian transformation system is described in the Appendix.

### Comparison 1D and 2D LSQSE

The performance of the 1D and 2D LSQSE methods was examined and a comparison was made. The strains in the axial, lateral, vertical (z) and horizontal (x) direction were calculated from the unfiltered displacement data using both the 1D and 2D method. The LSQSE strain images were computed for a large range of LSQ kernels. The kernel size was varied in both directions separately and ranged from the smallest size (3 pixels) to a relatively large number of displacement values of 51 pixels. Hence, the smallest 2D plane was fitted through 3 x 3 values and the largest fit was 51 x 51 pixels. It may be

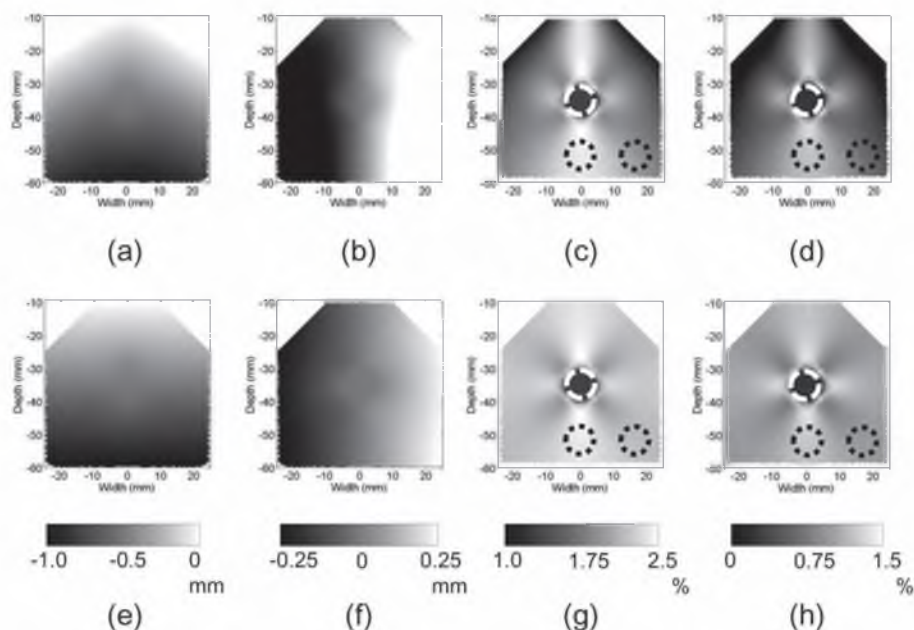


Figure 5.3. The solutions of the finite element model for the used image sector; the displacement in axial direction (a) and lateral direction (b) and the axial (c) and lateral strain, (d) the displacement in vertical direction (e) and horizontal direction (f) and the corresponding vertical and horizontal strains (g-h). The white, dashed circle indicates the ROI within the inclusion and the black, dotted circles are the background regions-of-interest (in both the center and outer region), both used for elastographic signal-to-noise ratio and contrast-to-noise ratio (SNRe and CNRe) analysis.

noted that the kernel size is expressed in strain pixels in both directions, since the polar coordinate system of the RF-data prohibits the use of mm. The resulting strains were compared with the theoretical or 'true' strains. Figure 5.3 shows the four displacement (a, b, e & f) and strain (b, c, g & h) components within the simulated image sector. Since the 'true' strain images of the FEMs are available, it was possible to calculate the root-mean-squared error (RMSE) between the measured and modeled strains. This measure was chosen, to quantify the precision of the methods and to assess the influence of smoothing on strain image resolution. Besides RMSE

analysis, the elastographic signal-to-noise (SNRe) and elastographic contrast-to-noise (CNRe) were calculated (Bilgen and Insana 1997; Varghese and Ophir 1997). For a more detailed analysis, the RMSE, SNRe and CNRe were calculated for the three regions-of-interest (ROIs) indicated in the theoretical strain images in figure 5.3.

Finally, the influence of displacement filtering prior to the strain estimation was investigated. A regularization of the displacement estimates is normally performed by median filtering. In this study, the axial displacements were filtered with a median filter of 11 x 5 pixels. A slightly larger filter (median filter, 11 x 11 pixels) was used for

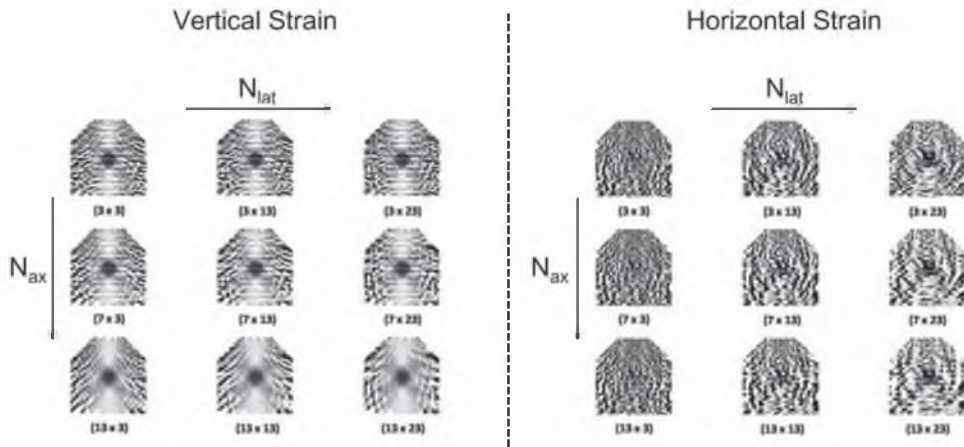


Figure 5.4. Vertical (left) and horizontal strain images (right) for different axial ( $N_{ax}$ ) and lateral kernel sizes ( $N_{lat}$ ) resulting from the one-dimensional least-squares-strain-estimator (1D LSQSE) on unfiltered displacement data.

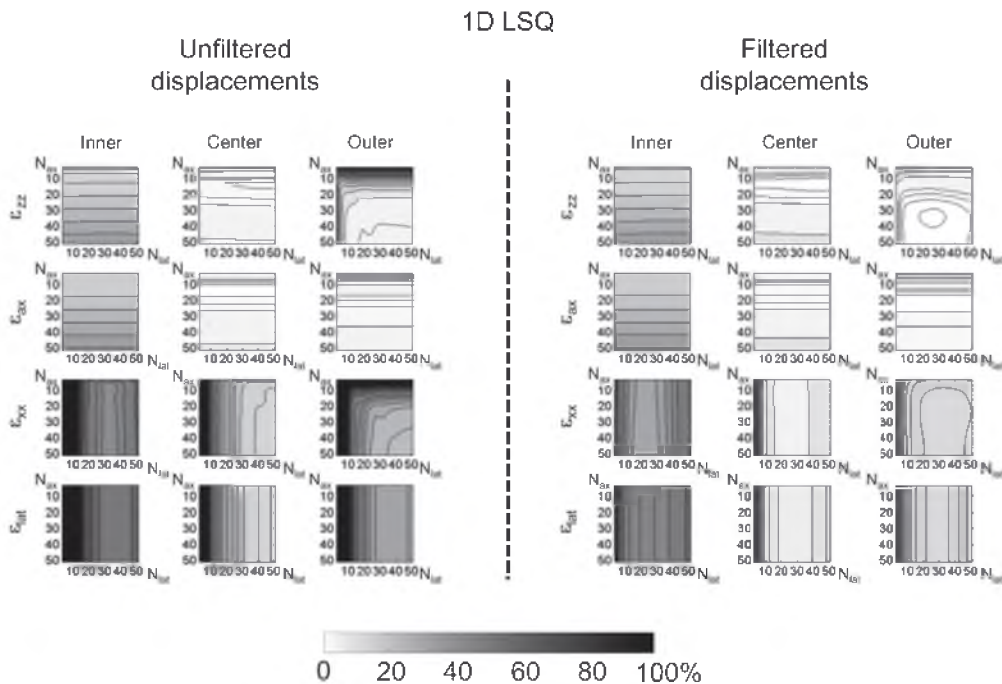


Figure 5.5. Contour plots of the measured root-mean-squared error (RMSE, %) for the 1D LSQSE on unfiltered (left) and filtered displacement data (right) for all strain components ( $\epsilon_{zz}$ ,  $\epsilon_{ax}$ ,  $\epsilon_{yx}$ ,  $\epsilon_{lat}$ ) within the three ROIs (inclusion, center-background, right-background). The axis represent the increasing axial ( $N_{ax}$ ) and lateral kernel size ( $N_{lat}$ ), the contours indicate the RMSE.

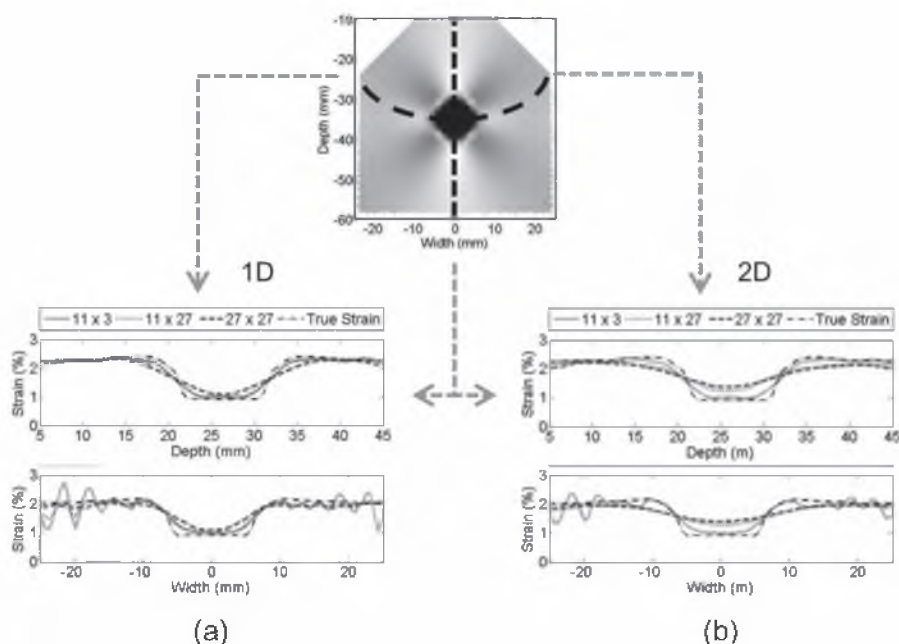


Figure 5.6. The simulated axial strain image (top middle) and the vertical strain curves for different kernel sizes of the 1D LSQSE (a). The curves are shown for an axial cross-section (upper) and lateral cross-section (lower) of the strain image. The vertical strain curves for a 2D LSQSE with different kernel sizes are shown (b) for again an axial cross section (upper) and lateral cross-section (lower).

the lateral displacements considering the decreased quality of the lateral displacement estimates with respect to the axial displacement estimates (Chapter 2 & 3). The strains were calculated, now from the filtered displacements, using the 1D and 2D LSQSE.

The phantom data were also processed using the aforementioned algorithms and settings. The strain images were generated for the same range of LSQ kernel sizes using the displacement data after median filtering. The SNRe and CNRe were calculated for five independent measurements and the results were averaged.

## RESULTS

The results for the 1D LSQ are shown in figures 5.4 to 5.6a. The vertical and horizontal strain images for several kernel sizes are shown in figure 5.4, using the unfiltered displacement data. Small LSQSE kernels revealed a striped pattern in the vertical strain images and very noisy horizontal strain images. The vertical strain images improved for increasing axial kernel sizes, which seems trivial. However, the vertical strain images seemed smooth and accurate in the middle part of the image but were particularly noisy at the left and right outer regions. The contribution of the axial shear strain is larger in these areas (see Appendix

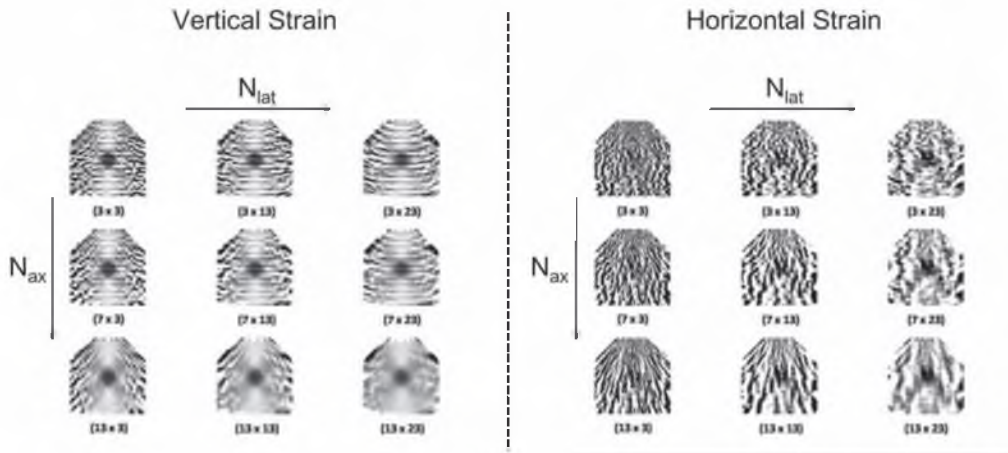


Figure 5.7. Vertical (left) and horizontal strain images (right) for different axial ( $N_{ax}$ ) and lateral kernel sizes ( $N_{lat}$ ) resulting from the 2D LSQSE on unfiltered displacement data.

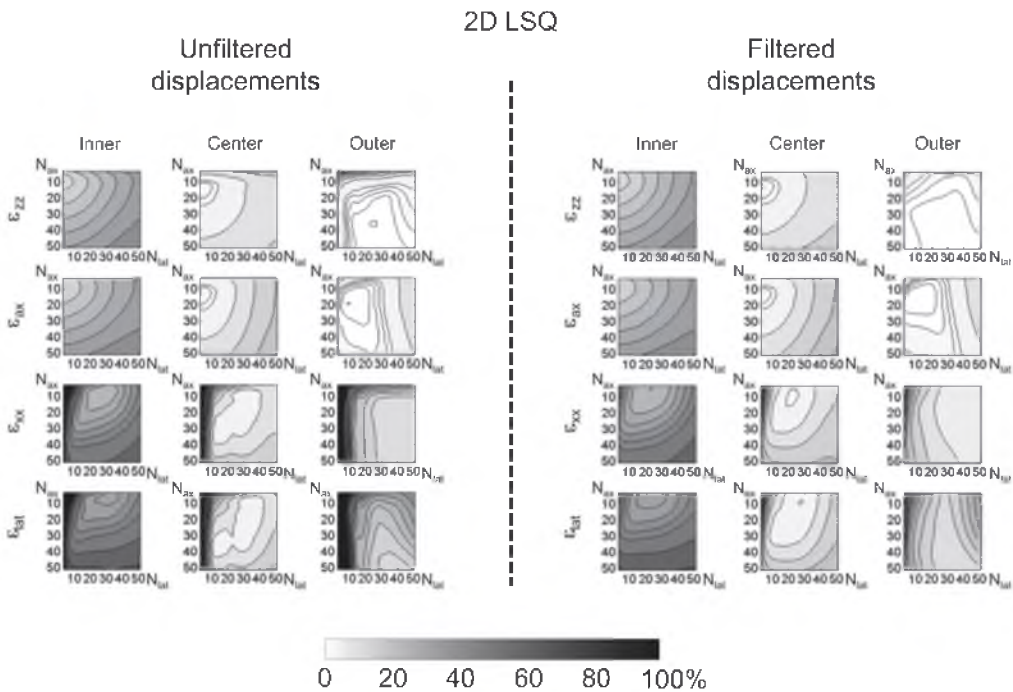


Figure 5.8. Contour plots of the measured root-mean-squared error (%) for the 2D LSQSE on unfiltered (left) and filtered displacement data (right) for all strain components ( $\epsilon_{zz}$ ,  $\epsilon_{xx}$ ,  $\epsilon_{yy}$ ,  $\epsilon_{lat}$ ) within the three ROIs (inclusion, center-background, right-background). The axis represent the increasing axial ( $N_{ax}$ ) and lateral kernel size ( $N_{lat}$ ), the contours indicate the RMSE.

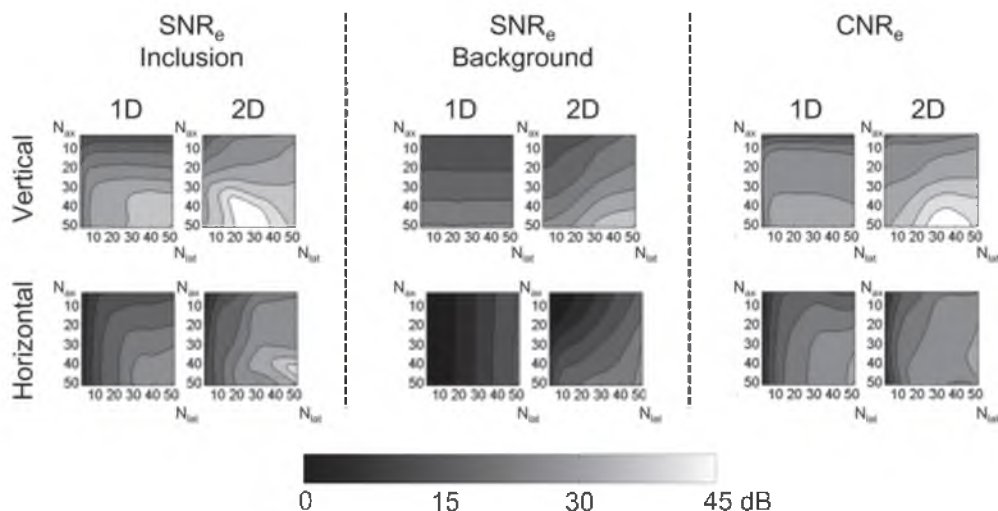


Figure 5.9. The  $SNR_e$  for the inclusion (left) and for a region in the background (middle) and the  $CNR_e$  for both the vertical and horizontal strain (upper and lower row, respectively), comparing the 1D and 2D LSQSE.

Ch-5), but these regions did not improve even for larger lateral kernel sizes. In other words, additional smoothing of the lateral derivative of the axial displacements did not enhance strain smoothness for the outer regions. For larger lateral kernel sizes, the horizontal strain images gradually improved and eventually revealed the inclusion in the center.

An extensive overview and comparison of the influence of LSQSE kernel size on the strain accuracy can be found in figure 5.5. This figure shows the contour plots of the measured RMSE as a function of axial and lateral LSQSE kernel size. The shown RMSE was calculated for both the measured strains (axial, lateral) as the reconstructed strains ( $z$ ,  $x$ ) in the three ROIs indicated in figure 5.3. Furthermore, the analysis was repeated using the median filtered displacements (Fig. 5.5, right). Figure 5.5 revealed that the influence of the used LSQSE kernel size depended on the region-of-interest (inclusion, center-

background, right-background). The axial and lateral strain RMSEs only depended on the axial and lateral kernel size, respectively. However, the RMSE of both the vertical and horizontal strain was influenced by the kernel size in both directions. This seems trivial, since  $\epsilon_{zz}$  and  $\epsilon_{xx}$  are reconstructed using a combination of both the axial and lateral normal and shear strain components (see Appendix Ch-5). The inclusion reveals higher RMSEs for all strain components (vertical RMSE > 17%, horizontal RMSE > 40%). After median filtering (Fig. 5.5, right), the RMSEs are lower and smaller LSQSE kernels can be used for all strain components.

Vertical strain curves were plotted for an axial and a lateral cross-section of the vertical strain image (Fig. 5.6). The difference in strain traces is shown for three different kernel sizes for the 1D LSQSE (Fig. 5.6a). The influence of the lateral kernel size for the axial cross-section is negligible. However,

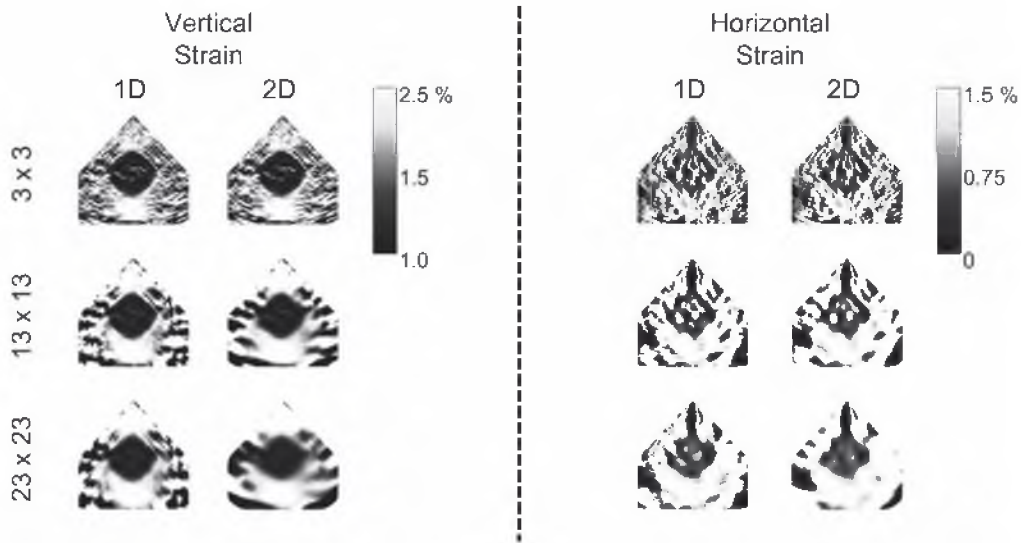


Figure 5.10. Vertical and horizontal strain images resulting from the one-dimensional least-squares-strain-estimator (LSQSE) and two-dimensional LSQSE on filtered displacement data of the gelatin/agar phantom with a hard cylindrical inclusion. The images were generated using a  $3 \times 3$ ,  $13 \times 13$  and  $23 \times 23$  1D and 2D LSQSE.

this was not the case for larger insonification angles. First, the strain improved when the lateral kernel size ( $N_{\text{lat}}$ ) was increased from 3 to 27 pixels (Fig. 5.6a, lower). Finally, an improvement was seen after an increase in axial kernel size ( $N_{\text{ax}}$ , from 11 to 27 pixels). The decrease in noise level of the strain is especially apparent in the outer regions.

The analysis was repeated for the 2D LSQSE and the results are shown in figure 5.6b to 5.8. Figure 5.6b shows curves of  $\epsilon_{zz}$  for the indicated cross-sections as a function of 2D LSQSE size. The curves show a higher level of smoothness. However, the contrast is reduced even more compared to the 1D LSQSE (see Fig. 5.6a). Figure 5.7 shows the elastogram for different 2D LSQSE kernels. Visual inspection revealed that the largest improvement in smoothness is found in the horizontal strain images and in the outer regions of the vertical strain images for

larger 2D LSQSEs, which is in correspondence with the findings in figure 5.8.

A similar analysis as presented in figure 5.5 was performed using the proposed 2D LSQSE (see Fig. 5.8). The contour plots of the measured RMSE as a function of axial and lateral LSQSE kernel size are again given for the unfiltered and filtered displacements for the three ROIs and for all strain components. A dependence on both kernel sizes is found for all strain components now since a square grid of displacement is used (2D plane), also for the axial and lateral strain. In general, the RMSE values were lower compared to the 1D LSQSE. For instance, the minimum RMSE of the horizontal strain in the center background ROI is 15%, but reduces to less than 5% for the 2D method. Besides, the 1D LSQSE required a large lateral kernel size ( $N_{\text{lat}} > 41$  pixels) compared to the 2D method.

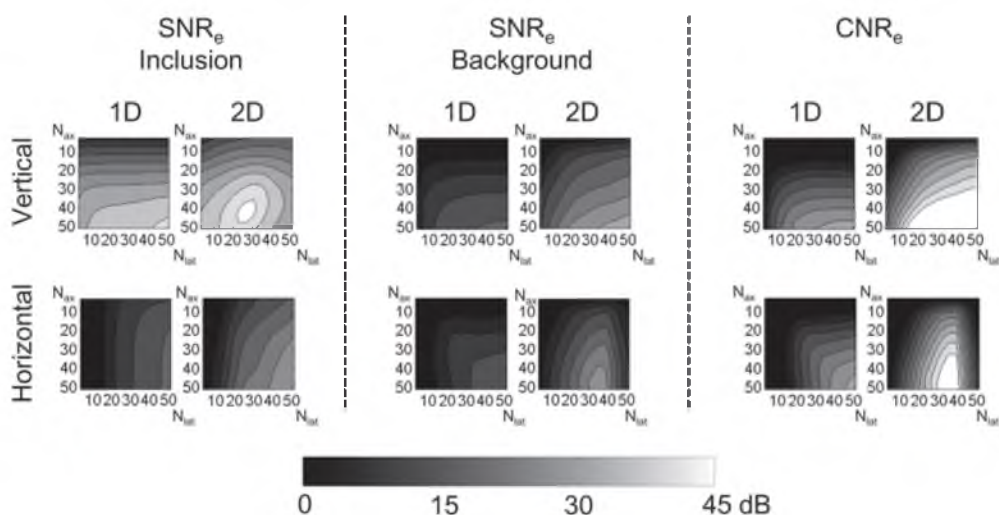


Figure 5.11. The average  $\text{SNR}_e$  for the inclusion (left) and for a region in the background (right) and the  $\text{CNR}_e$  for both the vertical and horizontal strain (upper and lower row, respectively), comparing the 1D and 2D LSQSE ( $N = 5$ ).

Furthermore, the kernel size could be decreased in one direction when more data were used in the other direction, especially for the lateral and horizontal strains, respectively. The use of median filtering slightly decreased the RMSE values, but the effect was less compared to the results of the 1D LSQSE.

The elastographic signal-to-noise ( $\text{SNR}_e$ ) and contrast-to-noise ( $\text{CNR}_e$ ) are shown in Figure 5.9 for both reconstructed strains ( $\epsilon_{zz}$  and  $\epsilon_{xx}$ ) for the inclusion and the right background ROI. The results are shown for all combinations of kernel sizes for the 1D and 2D LSQSE. The  $\text{SNR}_e$  and  $\text{CNR}_e$  are better for the 2D LSQSE. The  $\text{SNR}_e$  in the inclusion and in the background are 10-15 dB higher when using a 2D LSQSE. The  $\text{SNR}_e$  in the inclusion revealed that the vertical strain require the largest kernel size in the axial direction but not in the lateral kernel size for the 2D case. The opposite was found for the horizontal strain images.

However, the  $\text{SNR}_e$  in the background ROI and the  $\text{CNR}_e$  are better for the largest kernel sizes in both directions.

Figure 5.10 shows vertical and horizontal strain images of the gelatin/agar phantoms, generated with a 1D or 2D LSQSE for three sets of kernel sizes. The range of strains is in good correspondence with the finite element model. The difference between these experimental elastograms for larger 1D or 2D kernels is similar to the simulation data. A low-strain artifact is present in the horizontal strain (above the inclusion), which is most probably caused by the near-field effect of the transducer. The results of the  $\text{SNR}_e$  and  $\text{CNR}_e$  analysis are shown in figure 5.11. Although the  $\text{SNR}_e$  and  $\text{CNR}_e$  are approximately 15 dB lower, probably caused by the experimental conditions that are less ideal than the simulations, the results are in good correspondence with the simulation results and lead to similar conclusions as drawn from the simulation data.



## DISCUSSION

In this study, the common 1D least-squares strain estimator was evaluated when applied on phased array data of an inhomogeneous phantom. Vertical and horizontal strains were reconstructed using different kernel sizes. The 1D LSQSE was applied to a 2D plane fit of the correlation function (2D LSQSE), which outperformed the traditional approach, especially for larger steering angles.

In general, the 1D and 2D results showed that the axial and vertical strains have the lowest RMSE for moderate kernel sizes (< 11 pixels), whereas the lateral and horizontal strain require a larger, two-dimensional window (> 25 x 25 pixels). The under-sampling and the lack of phase information in the lateral direction are the main causes. Although most contour plots revealed an optimum, no conclusions should be drawn. For instance, the 'optimal' LSQSE window is highly dependent on the present strain and on the size and position of the region-of-interest. The largest kernel size is favorable for the right-background region, whereas the inclusion ROI required a more modest kernel length.

The 2D LSQSE resulted, in general, in lower RMSE values compared to the 1D LSQSE. Furthermore, the kernel size could be decreased in one direction when more data were used in the other direction. For instance, the lateral strain has the best quality at  $N_{\text{lat}} = 35$  pixels, whereas the 2D method required  $N_{\text{lat}} = 25$  pixels if  $N_{\text{ax}}$  was 3 to 9 pixels. The RMSE reduces from 40% to approximately 25% when using 2D instead

of 1D kernels. The use of median filtering also decreased the RMSE. However, the 2D results for unfiltered displacement data are better compared to the 1D LSQSE on filtered data. Filtering of displacement data can be avoided by using a 2D LSQSE. The advantage of filtered displacement data lies in a smaller optimal LSQSE size. The RMSE values were only slightly lower (Fig. 5.8). Still, larger 2D kernels are favored for the in-plane strains and for the right background ROI (the outer regions). Besides, the median filter is especially useful in filtering outliers. The median filter is a non-linear operation, whereas the LSQSE is a linear operation.

In the inclusion larger RMSE values were found for all strain components than in the background material. This can be explained by the smoothing effect of the LSQSE, which causes a loss in resolution. The absolute strain values in the inclusion were normally lower compared to the background, but over-smoothing resulted in the contribution of higher surrounding strain values to the new, filtered strain estimate. The strain value in the inclusion increased for larger kernels, decreasing the contrast between the inclusion and background material. Consequently, the resolution of the elastogram decreases significantly<sup>29;30</sup>. Figure 5.6b also illustrates the noise reduction and the decrease in resolution. This effect is not depicted by figure 5.9, which illustrates the fact that the trade-off between SNRe and resolution is not mirrored in the CNRe. However, the RMSE of the inclusion does reveal the loss of resolution, especially of the vertical strain images. The RMSE in the inclusion

will increase from 13% to 35% for the 1D LSQSE and up to 45% in the 2D case (see Fig. 5.8). However, the ranges of horizontal RMSEs were similar in the inclusion for the 1D and 2D LSQSE (25% - 45%). It must be noted that a separate resolution analysis was performed, but the results were similar to the RMSE in the inclusion and therefore not included in this paper.

The calculated CNRe shows an improvement for larger kernel sizes in both directions. A possible explanation could be a larger decrease in variance, present in the denominator of the CNRe equation, compared to the decrease in strain difference in the numerator (Bilgen and Insana 1997). This would lead to a higher CNRe, while the actual resolution is lower. The SNRe and CNRe prove to be unreliable quality measures and the RMSE analysis seems to be more useful and accurate. This is illustrated by the fact that based on SNRe and CNRe in both simulation and phantom experiments, different conclusions could be drawn. For instance that the largest kernel size does improve contrast and precision. It must be noted, that quantitative comparison of RMSE values with different phantoms is cumbersome, since RMSE values depend on the strains present and these strains should be known *a priori*. A good alternative would be an analysis of resolution using different phantoms (Alam et al 2000; Righetti et al 2002).

## CONCLUSION

In conclusion, the 2D least-squared plane fit is a robust strain estimator that can handle unfiltered displacement data. The 2D LSQSE outperforms the traditional 1D LSQ strain estimator. The technique can be applied to phased array data and enhances both axial / lateral and vertical / horizontal strain images. In particular, the horizontal or lateral strain components benefit from the 2D LSQSE. The loss in resolution or contrast does not outweigh the gain in precision. However, it must be noted that different applications require different settings. For instance, resolution is favored over precision when the goal is detection of small tumors. Extension of this method to three dimensions is straightforward and easy. The 2D approach allows simultaneous estimation of the shear strains in either the axial/lateral or the vertical/horizontal direction. However, the SNRe and CNRe of the shear strain images were beyond the scope of this study. The difference in performance in a phased array configuration when using LSQSE kernels with a fixed size in pixels and a kernel size in mm was not examined in this study.

## APPENDIX

The general equation of a linear plane is given by:

$$\delta = \alpha x + \beta y + \gamma \quad (5.1)$$

where  $\delta$  is the displacement,  $\alpha$  and  $\beta$  are directional coefficients,  $\gamma$  is the offset and  $x$ ,  $y$  are the spatial coordinates.

The directional coefficients  $\alpha$  and  $\beta$  are the least-squares strain estimates in the  $x$  and  $y$ -direction, respectively. The least-squares solution for parameter vector  $\eta$  is given by:

$$\bar{\eta} = (A^T A)^{-1} A^T \bar{u} \quad (5.2)$$

with  $A$  being defined as:

$$A = \begin{bmatrix} \sum_{i=1}^M x_i^2 & \sum_{i=1}^M x_i y_i & \sum_{i=1}^M x_i \\ \sum_{i=1}^M x_i y_i & \sum_{i=1}^M y_i^2 & \sum_{i=1}^M y_i \\ \sum_{i=1}^M x_i & \sum_{i=1}^M y_i & M \end{bmatrix} \quad (5.3)$$

and vector  $u$  :

$$\bar{u} = \begin{pmatrix} \sum_{i=1}^M x_i \delta_i \\ \sum_{i=1}^M y_i \delta_i \\ \sum_{i=1}^M \delta_i \end{pmatrix} \quad (5.4)$$

where  $M$  is the total amount of pixels for a  $N_{ax} \times N_{lay}$  window. It may be noted that this approach can be easily be extended to higher order functions (polynomials) or higher dimensions (hyper-planes).



---

# CHAPTER 6

## CORRELATION-WEIGHTED TRACKING OF TISSUE

---

*Richard G.P. Lopata, Maartje M. Nillesen, Inge H. Gerrits, Hendrik (Rik)  
H.G. Hansen, Livia Kapusta, Johan M. Thijssen & Chris L. de Korte*

---

Based on: **A Novel Tracking Method for Three-Dimensional Cardiac Strain Imaging.**  
R.G.P. Lopata, M.M. Nillesen I.H. Gerrits, H.H.G. Hansen, L. Kapusta, J.M. Thijssen  
and C.L. de Korte. *Proceedings 4th European Conference of the International Federation for  
Medical and Biological Engineering, Antwerp, Belgium 2008*; 22: 697-700.

---

## ABSTRACT

Current developments in 3D ultrasound imaging are boosting research in 3D strain imaging. 3D cardiac strain imaging seems promising considering the complex 3D structure and deformation of the heart. Segmentation and tracking of the tissue-of-interest is necessary for proper strain imaging. This study focuses on tracking of myocardial tissue using displacements and strain, derived from radio frequency ultrasound data. A novel tracking method was implemented to reconstruct strain from inter-frame strain measurements (i.e. strain rate). A region-of-interest (ROI) was deformed using displacement measurements and regularized using the behavior of neighbouring pixels. The forces were weighted using the difference between theoretical and measured cross-correlation values. The tracking method was tested using a tube phantom, which was heavily translated and dilated using a pressure column. Displacements and strain rate were estimated using the radio frequency data. Next, Biplane images of a canine heart were acquired. The strain algorithm was applied on the data. ROIs in the lateral wall in both the short and long axis view were manually segmented and subsequently tracked. In the phantom, each pixel within the ROI was tracked separately. The local strains were reconstructed correctly after tracking, despite large translations and deformations. Using the translational behavior of neighbouring pixels was favored over mesh regularization. In the animals, the strain curves were consistent with other animal and human studies on strain imaging. Furthermore, the strain curves showed less drift and higher peak strains after tracking.

## INTRODUCTION

Elastography is an imaging technique for the estimation of mechanical properties and deformation of tissues. Ultrasound elastography, or strain imaging, has been adapted for a variety of clinical applications (Ophir et al. 1991; Bohs and Trahey 1991; Langeland et al. 2004; Lopata et al. 2006; Cespedes et al. 1999). In addition to traditional speckle-tracking (envelope-based) techniques (Bohs and Trahey 1991), methods using the radio frequency data (RF) are commonly used, for instance in cardiac applications (Langeland et al. 2004; Chapter 7). In general, RF-based methods are more sensitive than envelope-based methods (Chapter 2 and 4). The availability of commercial 3D systems has enabled research on 3D strain imaging and segmentation (Chapter 7-9). However, the addition of the third (spatial) dimension results in a significant decrease in temporal resolution (*i.e.* frame rate). The movement (and deformation) of the tissue-of-interest will become larger in between frames. Consequently, this will decrease the accuracy of displacement estimates due to extensive decorrelation. Furthermore, the estimated strain rate has to be integrated over time if the total strain is desired (Langeland et al. 2004).

Accumulation of strain rate measurements is not trivial in cardiovascular applications, since the tissue is moving in all directions. Normally, speckle tracking techniques are used and only the outer contour of a tissue or object is tracked. However, contour tracking is not sufficient when assessment of local strain is desired. Each pixel within a

region-of-interest (ROI) needs to be tracked separately for proper accumulation of the local strain rate estimates in order to obtain local strain. This is not trivial, considering the aforementioned issues.

In this chapter, a tracking algorithm is introduced, using RF-based displacement and strain estimates, to follow the translational movement of each pixel for subsequent frames. The approach was tested on experimental phantom data and applied on *in vivo* cardiac data.

## MATERIALS

A thick-wall tube phantom was constructed using a solution of 9% polyvinyl-alcohol in water with 1.0% scattering particles (diameter 40 - 63  $\mu\text{m}$  SiC). The PVA gel was poured into a cylindrical mold with an outer diameter of 13 mm and an inner diameter of 3 mm. The gel was subjected to three freeze/thaw cycles ( $-20^\circ\text{C}$ ) to solidify and stiffen the PVA gel. The tube was attached to a pressure column, that was rapidly elevated and lowered. This resulted in an increased intra-luminal pressure, deformation and translational movement of the tube.

Linear array images of the phantom were acquired with a SONOS 7500 real-time 3D system (Philips Medical Systems, Bothell, USA), equipped with a linear array transducer (11-3L, center frequency  $f_c = 7.5$  MHz) at a frame rate of 30 Hz.

ECG-triggered BiPlane data of the heart of a dog were acquired with an X4 matrix array transducer ( $f_c = 3.5$  MHz) at a frame

rate of 100 Hz. BiPlane imaging was chosen since this semi-3D technique captures left ventricular movement in both the short axis (Sax) and long axis view (Lax) allowing strain estimation in three orthogonal directions. These experiments were approved by the local ethical animal committee .

## METHODS

### *Strain Imaging*

The translation and deformation of the phantom was measured using a 2D strain algorithm (Chapter 2). 2D kernels of radio frequency data were cross-correlated. The location of the peak of the cross-correlation function (CCF) indicates the displacements along the ultrasound beam (axial direction) and perpendicular to the ultrasound beam (lateral direction). 2D parabolic interpolation of the CCF peak yields sub-sample resolution displacement estimates in both directions. The strain rate was derived from the measured displacements using a least-squares strain estimator (Chapter 2 - 5).

Frame-to-frame displacements and strain rate were estimated using the aforementioned algorithm and acquired RF-data. The resulting strain rate images had an axial resolution of 2 mm with an overlap of 75%. The lateral resolution in the linear array images is 135  $\mu\text{m}$ . The lateral resolution of phased array data decreases with depth. The angle between the RF-lines was 0.75°.

The axial and lateral displacements measured in linear array data are the vertical

(z) and horizontal (x) displacements, respectively. In sector scan data, the data obeys a polar grid and the displacements and strains in the axial and lateral direction correspond to the radial and circumferential direction of the heart, respectively.

### *Local Tracking*

An initial region-of-interest (ROI) was drawn in the first image (Fig. 6.1c and Fig. 6.3a). For each point (or pixel) within the initial ROI,  $p_i = (x_i, z_i)$ , the measured displacements in both the lateral ( $\delta x_i$ ) and axial direction ( $\delta z_i$ ) were used as an external force,  $F_{ext}$ , to find the coordinates in the subsequent frame. However, corrupted displacement estimates due to signal decorrelation or low signal intensity will result in erroneous tracking of pixels which yields discontinuous ROI shapes and drift. Two internal forces were tested and compared for regularization. First, the smoothness of the pixel traces was controlled by taking the position of neighbouring pixels into account:

$$F_{int} = \sum_{n=1}^N (x(p_{n,i+1}), z(p_{n,i+1})) / N \quad (6.1)$$

where  $p_{n,i+1}$  are the coordinates of the N neighbors of  $p_{i+1}$ . Secondly, the movement of neighbouring pixels was used:

$$F_{int} = \sum_{n=1}^N (\delta_x(p_{n,i}), \delta_z(p_{n,i})) / N \quad (6.2)$$

These forces are similar except at the boundaries of a ROI. The resulting coordinates of  $p_i$  in the next frame are a combination of the external and (one of the) internal forces:



$$p_{i+1} = \gamma(p_i + F_{ext}) + (1 - \gamma)F_{int} \quad (6.3)$$

where  $\gamma$  is a weighting factor. The weighting factor was coupled to the maximum cross-correlation value (MCC). The MCC is a measure for the quality of the displacements. A low MCC value implies bad displacement estimates and requires more influence of  $F_{int}$ . However, the MCC also decreases for higher strain levels. The theoretical MCC can be computed for a certain strain using:

$$\rho_{max}(p_i) = \text{sinc}(Tf_c\varepsilon(p_i)) \quad (6.4)$$

with  $T$  the axial kernel length in seconds and  $\varepsilon$  the local strain for position  $p_i$ . The absolute difference between the theoretical and the measured MCC,  $\Delta\rho$ , was chosen to assess the accuracy of the measured displacements without any influence of strain. Estimates with  $\Delta\rho > 0.2$  were denoted as erroneous estimates. Hence,  $\gamma$  was defined as:

$$\gamma = \begin{cases} 1 - 5\Delta\rho, & \Delta\rho \leq 0.2 \\ 0, & \Delta\rho \geq 0.2 \end{cases} \quad (6.5)$$

After tracking all pixels of the ROI, the strain images were generated.

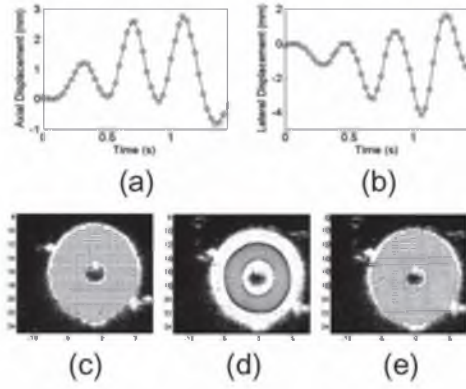


Figure 6.1 The axial (a) and lateral displacements (b) of the centre of the vessel phantom as a function in time; c) The initial grid of the ROI within the phantom; d) The resulting grid using coordinate regularization e) The resulting grid using displacement regularization.

## RESULTS

The vessel phantom was subjected to relatively large translations (up to 5.0 mm, Fig. 6.1a-b). The initial mesh (Fig. 6.1c) was compared with the resulting mesh after the entire cycle. Regularization using equation 6.2 revealed a high amount of region implosion (Fig. 6.1d). The use of neighbouring

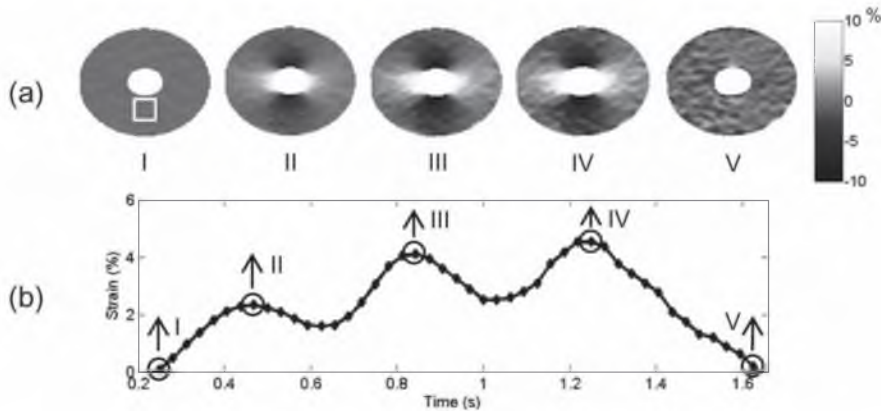


Figure 6.2 Axial elastograms for five different time points during the translation and deformation cycle (I-V) and b) the mean axial strain for the box-shaped area (white dashed line in a-I).

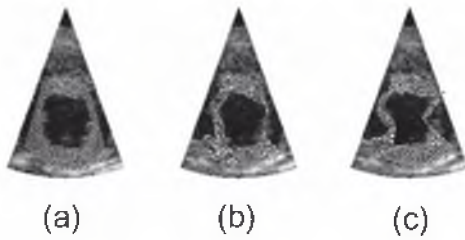


Figure 6.3. The initial grid of a ROI in the left ventricle (Sax-view); b) The resulting grid without any regularization; c) The resulting grid using displacement regularization as internal force.

displacement values resulted in almost no implosion of the region but a less uniformly distributed mesh after 64 frames (Fig. 6.1e). The results revealed high MCC-values, so little regularization was necessary.

The resulting axial elastograms are shown in figure 6.2a. The mean strain curve in figure 6.2b corresponds to a square ROI (Fig. 6.2a-I, white dashed line). The elastograms correspond with the time points I-V, indicated by circles. The axial strain patterns are in correspondence with previous studies (Ribbers et al. 2007). The peak strain ranged from -10 to 10%. After removing the pressure, the resulting strain should be zero. The final strain image revealed almost no strain and little strain residue. In addition, no trend is observed in the curve.

Figure 6.3 shows the Sax-view of the left ventricle of a canine heart. The initial ROI is again divided into an equally spaced mesh (Fig. 6.3a). To demonstrate the necessity of regularization, the resulting mesh after one entire cardiac cycle without the use of an internal force is shown in figure 6.3b. The mesh had an irregular shape and the mesh is non-uniformly distributed. The mesh with displacement regularization (Fig. 6.3c) revealed a smoother shape and a more uniform distribution of mesh points. The

use of equation 6.1 resulted again in severe implosion (results not shown).

Figure 6.4 shows both the short-axis (a) and the long-axis images (b) of the left ventricle for one cardiac cycle. The captured ECG-signal is shown (Fig. 6.4c) and the black-dashed lines indicate the time points at which the images I to V were acquired. In both the Sax and Lax view, the meshes return to their initial position although with altered appearance. A region was indicated in the starting frame of the Sax-view (white line). The mean strain in both the axial both directions was calculated. The three resulting strain curves for this ROI are shown in figure 6.4d-f after cumulation with (solid) and without tracking (dashed).

## DISCUSSION

Tracking is necessary when estimating strain in actively deforming tissue. A pixel-based approach is needed to assess local strain. The proposed approach uses RF-based displacement estimates. RF-based displacement estimation has the advantage of a higher sensitivity, but may lack robustness. Unreliable displacement estimates can be caused by either large deformations or by low echogenicity. Hence, regularization of the tracked mesh is favored.

The preliminary findings of this current study show that an additional regularization force based on the behavior of neighbouring pixels improved mesh uniformity and smoothness without implosion of the ROI. The main advantage of the MCC-coupled

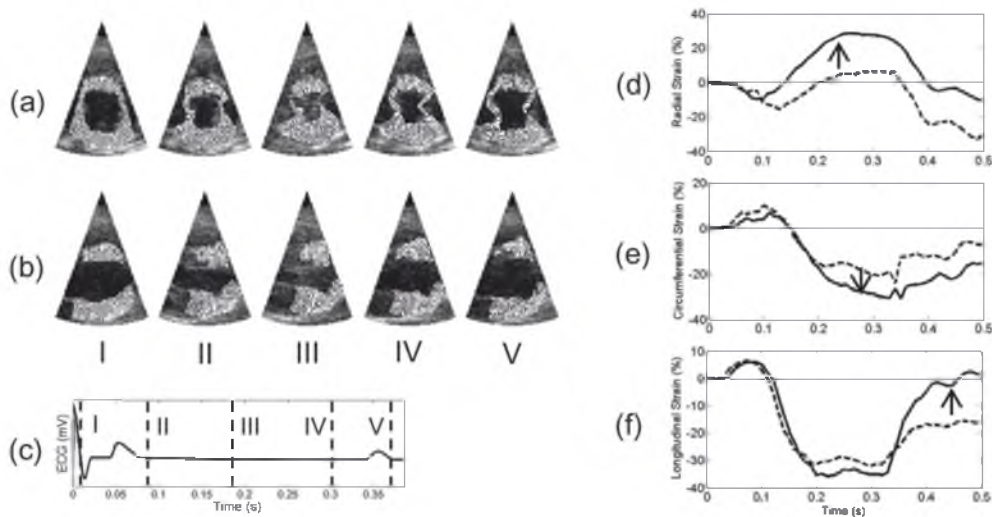


Figure 6.4. a) Sax images of the left ventricle with the tracked region for several time points during the cardiac cycle (I-V); b) Lax images of the left ventricle with tracked region; c) The captured ECG-signal with the time points indicated by black dashed lines; d) The mean radial (axial) strain with (solid) and without tracking (dashed); e) The mean circumferential (lateral) strain; f) the mean longitudinal strain.

weighting factor lies in the fact that translations were not over-smoothed, since reliable displacement estimates were maintained. Since the linear data of the tube phantom had a high echogenicity and the maximum strain rate was moderate ( $\pm 0.5\%$ ), MCC-values were high (0.9 – 1.0) and little regularization was necessary.

In the cardiac data, high local strain rate ( $\pm 5 - 10\%$ ), low echogenicity and out-of-plane motion can be a significant source of error and could very well be the cause of the problems at 3 and 9 o'clock in the Sax view (Fig. 3a). Especially the measured lateral movement seemed to be underestimated. Besides, the mesh shape had altered, probably due to the aforementioned problems and the fact that the last acquired image was not exactly equal to the initial frame. However, the resulting strain curves were in accordance with previous studies. The strain curves with tracking showed higher

maximum strain values and less trend, although considerable trend was still present in the circumferential strain (Fig. 6.4e).

For further improvement of tracking, a detrend or a two-way approach can be used (Langeland et al. 2004). A detrend of each pixel's coordinates results in final meshes that are equal to the initial grids. This may result in a tracking-lag during the systolic phase. In two-way tracking, tracking is repeated in reverse and the average of the forward and backward tracking is used. In our opinion, the latter is favored.

## CONCLUSION

In conclusion, pixel-based tracking and assessing local strain in actively deforming tissue is feasible using RF-based techniques.

---

# Part - II

---

---

# 3D CARDIAC IMAGING

---

Handwritten text in a box, possibly a list or notes.



---

# CHAPTER 7

## CARDIAC BIPLANE STRAIN IMAGING

---

*Richard G.P. Lopata, Maartje M. Nillesen, C. (Kiek) N. Verrijp  
Sandeep K. Singh, Martin M.Y. Lammens, Jeroen A.W.M. van der Laak,  
Herbert. B. van Wetten, Johan M. Thijssen, Livia Kapusta & Chris L. de Korte*

---

Based on: **Cardiac BiPlane Strain Imaging: Initial *In Vivo* Experience.** R.G.P. Lopata, M.M. Nillesen, C.N. Verrijp, S.K. Singh, M.M.Y. Lammens, J.A.W.M. van der Laak, H.B. van Wetten, J.M. Thijssen, L. Kapusta and C.L. de Korte, *Physics in Medicine & Biology* 2010; 55, pp. 963-979.

---

## ABSTRACT

In this chapter, we propose a biplane strain imaging method using a commercial ultrasound system, yielding estimation of the strain in three orthogonal directions. Secondly, an animal model of the children's heart was introduced that is suitable to simulate congenital heart disease and was used to test the method *in vivo*. The proposed approach can serve as a framework to monitor the development of cardiac hypertrophy and fibrosis. A 2D strain estimation technique using radio frequency (RF) ultrasound data was applied. Biplane image acquisition was performed at a relatively low frame rate (<100 Hz) using a commercial platform with an RF-interface. For testing the method *in vivo*, biplane image sequences of the heart were recorded during the cardiac cycle in four dogs with an aortic stenosis. Initial results reveal the feasibility to measure large radial, circumferential and longitudinal cumulative strain (up to 70%) at a frame rate of 100 Hz. Mean radial strain curves of a manually segmented region-of-interest in the infero-lateral wall show excellent correlation between the measured strain curves acquired in two perpendicular planes. Furthermore, the results show the feasibility and reproducibility of assessing radial, circumferential and longitudinal strains simultaneously. In this preliminary study, three beagles developed an elevated pressure gradient over the aortic valve ( $\Delta p$ : 100 – 200 mmHg) and myocardial hypertrophy. One dog did not develop any sign of hypertrophy ( $\Delta p = 20$  mmHg). Initial strain (rate) results showed that the maximum strain (rate) decreased with increasing valvular stenosis (-50%), which is in accordance with previous studies. Histological findings corroborated these results and showed an increase in fibrotic tissue for the hearts with larger pressure gradients (100, 200 mmHg), as well as lower strain and strain rate values.



## INTRODUCTION

Congenital malformations of the heart may lead to a reduced function of the myocardium. Resulting non-ischemic heart failure is already described in childhood and adolescence. In children with a valvular aortic stenosis a pressure overload in the left ventricle will be present. In time, this pressure overload is an important factor that may lead to myocardial hypertrophy, followed by fibrosis (Sasayama et al. 1976). Consequently, non-invasive diagnostic methods for monitoring myocardial damage might be an important tool to evaluate therapies that are aiming at reducing the risk of chronic heart failure. Although echocardiography is a well established clinical tool in pediatric cardiology (Kiraly et al. 1997; Sahn & Vick 2001; Lang et al. 2006), it does not provide quantitative information on locally disturbed functional properties of the myocardium. Currently, the pressure gradient across the stenotic valve as assessed with Doppler ultrasound is used as a diagnostic standard. However, this technique only yields information on the severity of the flow gradient and provides neither quantitative information on cardiac function nor on the functional composition of the heart muscle (Pacileo et al 2003; Khalid et al. 2006). Hence, it is of crucial importance to obtain quantitative information about the heart function.

Cardiac ultrasound strain imaging is a technique that uses two-dimensional (2D) echo data to estimate the local deformation of the heart. Cardiac tissue velocity and strain can be quantified using various approaches.

In general, the displacement of signal segments is tracked using a pattern matching algorithm. Cardiac strain can be quantified using Tissue Doppler Imaging (TDI) based strain imaging (Heimdahl et al. 1998) or 2D speckle tracking (Kaluzynski et al. 2001; Leitman et al. 2004). The first approach has a high sensitivity in the axial direction, but it is a one-dimensional technique. The second approach, *i.e.* speckle tracking, provides strain values in two dimensions. Two-dimensional data windows were used to estimate the displacements in both directions (Bohs and Trahey 1991; Chaturvedi et al. 1998). Recent studies revealed that 2D cardiac strain imaging is feasible using 2D speckle tracking (Kaluzynski et al. 2001; Leitman et al. 2004). Speckle tracking yields robust displacement and strain estimation. However, robustness is gained at the cost of sensitivity to changes in the ultrasound data caused by small deformations (Cho et al. 2006).

One can also use the raw, radio frequency data (RF). This approach has proven to yield enhanced performance compared to 2D speckle tracking techniques (Chapter 2). RF-based strain imaging is used for a wide variety of clinical purposes, for instance for detecting tumors and lesions (Céspedes et al. 1993a), atherosclerotic plaques (de Korte et al. 2000a) and blood clots (Xie et al. 2004). In most of these applications, quasi-static or external compression of tissues is used. However, the tissue deformation in the heart is caused by an active contraction/relaxation process repeating itself each heart cycle. One-dimensional strain imaging was successfully applied in actively deforming tissue like skeletal muscle (Kallel

et al. 1998) and the heart (D'hooge et al. 2000, Konofagou et al. 2002). Several 2D methods using RF-data have been proposed (Konofagou and Ophir 1998; Chen et al. 2004; Langeland et al. 2004; Chapter 4) and were applied to cardiac data (Langeland et al. 2006; Lee et al. 2007).

A limitation of 2D cardiac imaging is simply the lack of the third dimension. The orientation of muscle fibers is not confined to one single plane and the heart has a complex 3D structure and geometry. The “out-of-plane motion” is therefore an important source of error in 2D strain measurements (Konofagou and Ophir 1998; Konofagou et al. 2002) and the full three-dimensional (3D) strain tensor cannot be estimated from 2D data. In other words, the available 2D information is not sufficient for a full assessment of heart geometry and dynamic function. Since 3D ultrasound imaging is on the rise, new techniques became available for estimating strain in more than two dimensions (Yoshikawa et al. 2005; Chen et al. 2005). However, one of the established problems in this field is the sub-optimal temporal resolution of 3D + time datasets.

Adequate spatial information and resolution are obtained at the cost of the temporal resolution. This issue results in contradictory interests. On one hand, adequate spatial information and resolution are required for accurate strain imaging within the entire 3D volume of the heart. At the same time, temporal resolution is also required because high deformation rates decrease the signal correlation significantly. High de-correlation of post-deformation signals may cause inaccuracies and biased strain estimates (Alam and Ophir 1997). Besides, large

translations of signal segments will cause problems for smaller search windows. Therefore, a relatively high frame rate is required to be able to solve these issues. Several publications indicated that a frame rate of 200 to 300 Hz is required (Kanai et al. 1997, Langeland et al. 2007). Also Konofagou and coworkers based their results on data with a high temporal resolution system using a non-standard ECG gated acquisition protocol (Luo et al 2007). Recently, Chen et al (2009) reported that the frame rate should be ten times higher than the heart rate when using RF-data. However, this seems optimistic and the maximum applied strains in the phantom study were relatively low (< 5%).

Insufficient spatial and temporal resolution has prohibited widespread application of 3D RF-based strain imaging, although some studies report (preliminary) results using either 3D speckle tracking (Saito et al. 2007, Crosby et al 2009), RF-data (Patil et al. 2007, Lopata et al. 2007), or registration (Elen et al 2008). A first step towards full 3D strain imaging is biplane strain imaging. This commercially available technique enables the measurement of cardiac strain in two orthogonal planes simultaneously. Hence, the strain can be measured in two orthogonal directions for a segment of the left ventricle in both the short-axis and long-axis view. It must be noted, that the full 3D strain tensor can only be estimated along the line that is formed by the boundary between the planes and that out-of-plane motion is still present.

In the present chapter, the feasibility of cardiac strain imaging using biplane RF-data was examined. Phased array biplane imaging was used as a fast technique to



Figure 7.1 Biplane image of a canine heart: (a) short-axis view (Sax) of the left ventricle; (b) long-axis view (Lax) of the left ventricle and (c) the total biplane image.

image two orthogonal planes in the myocardium simultaneously (Fig. 7.1). Contrary to previous studies using mechanical semi-3D arrays (Yoshikawa et al. 2005), a matrix array transducer was available and used. However, the system allows biplane acquisition at a maximum frame rate of only 100 Hz. As stated before, this is considered to be relatively low for RF-based strain imaging, but it is two to three times higher than the frame rate available for 3D full volume data.

The aims of this study were two-fold. First, the technical challenge was to perform RF-based 2D displacement and strain estimation by 2D kernel matching using a commercial ultrasound system with a matrix array transducer and get reproducible results *in vivo* in subjects with a wide range of heart rates. The system's temporal and spatial resolutions were limited and it was examined whether cardiac strain imaging would be feasible. The second aim was to evaluate the method *in vivo* in subjects with different pathology of the heart muscle. Both aims were achieved using data acquired in a canine model of a child's heart. This particular animal model was chosen because the geometry and size of the heart

resemble that of a small child (Willmann et al. 2009). A valvular aortic stenosis was surgically induced in the beagles. The effects of an elevated pressure gradient were studied using biplane ultrasound (strain) imaging. Histological evaluation of the myocardial tissue was performed. The animal model and imaging technique are proposed as a framework to monitor the development of hypertrophy in the heart due to valvular aortic stenosis using strain imaging. The preliminary findings are reported.

## MATERIALS

In a pilot animal study, four dogs (beagles) with a surgically induced valvular aortic stenosis were studied. Early and recent reports in literature revealed that pathological effects developed during growth in this animal model, caused by a valvular aortic stenosis (Sink et al. 1980; Hori et al. 2008). During the intervention, one of the three cusps of the aortic valve was plicated, resulting in a bicuspid valve. As a result, a pressure

gradient ( $\Delta p$ ) of approximately 30 mmHg over the stenotic valve was present in all dogs directly after the intervention. This pressure gradient normally develops progressively in the young dogs, yielding a chronic pressure overload of the left ventricle. Consequently, the heart muscle becomes hypertrophic. As a result of this chronic condition, fibrosis gradually develops.

All four dogs of this pilot animal study were used for demonstrating the feasibility of the proposed strain estimation technique *in vivo*. In one particular animal, the surgical creation of a valvular aortic stenosis failed to develop a chronic pressure overload. This was demonstrated using Doppler echocardiography that revealed that the pressure gradient over the valve reduced from 30 mmHg (immediately after the intervention) to 20 mmHg within two months. It remained at this level during the follow up and the geometry of the heart also showed no signs of hypertrophy. This animal was considered to be a valid “reference” model. The other dogs developed a mean pressure gradient of 100, 120 and 200 mmHg, respectively. The dogs were followed for nine months and terminated after the last examination for histological analysis. All the animal experiments were performed according to the national ethical rules and permission was obtained from the local animal ethics committee.

## METHODS

### *Two-Dimensional Strain Estimation*

When using 3D ultrasound techniques, large volumes of the heart are imaged. Therefore, vast amounts of data are generated. Also for biplane imaging, the amount is enormous when the deformation of the heart is followed during several heartbeats. To decrease the computational load significantly, a fast correlation and interpolation algorithm is required. For 2D strain estimation, an iterative correlation-based coarse-to-fine strain algorithm (Shi and Varghese 2007) was developed using a 2D parabolic approximation with an additional step of local aligning and local axial stretching (Chapter 2 - 4).

The coarse-to-fine algorithm estimates displacements parallel and perpendicular to the ultrasound beam simultaneously, using the cross-correlation function of 2D pre- and post-compression kernels. First, large kernels of demodulated RF-data (so-called signal ‘envelope’) are correlated and the cross-correlation is used to find a coarse 2D displacement field by detecting its peak (Fig. 7.2). In consecutive iterations, RF-data are used and the kernel size is decreased. This results in higher precision and resolution of the displacement estimates. Smaller data kernels can be used, since the initial displacement field is used as an initial guess. For all steps, the pre-compression kernel was correlated with a larger kernel in the post-compression area, automatically defining and limiting the possible measured axial and lateral displacements (Fig. 7.2). To obtain sub-sample resolution in both the axial and lateral direction, a 2D parabolic function was fitted to the peak of the 2D cross-correlation function. It was shown that this method performed equally

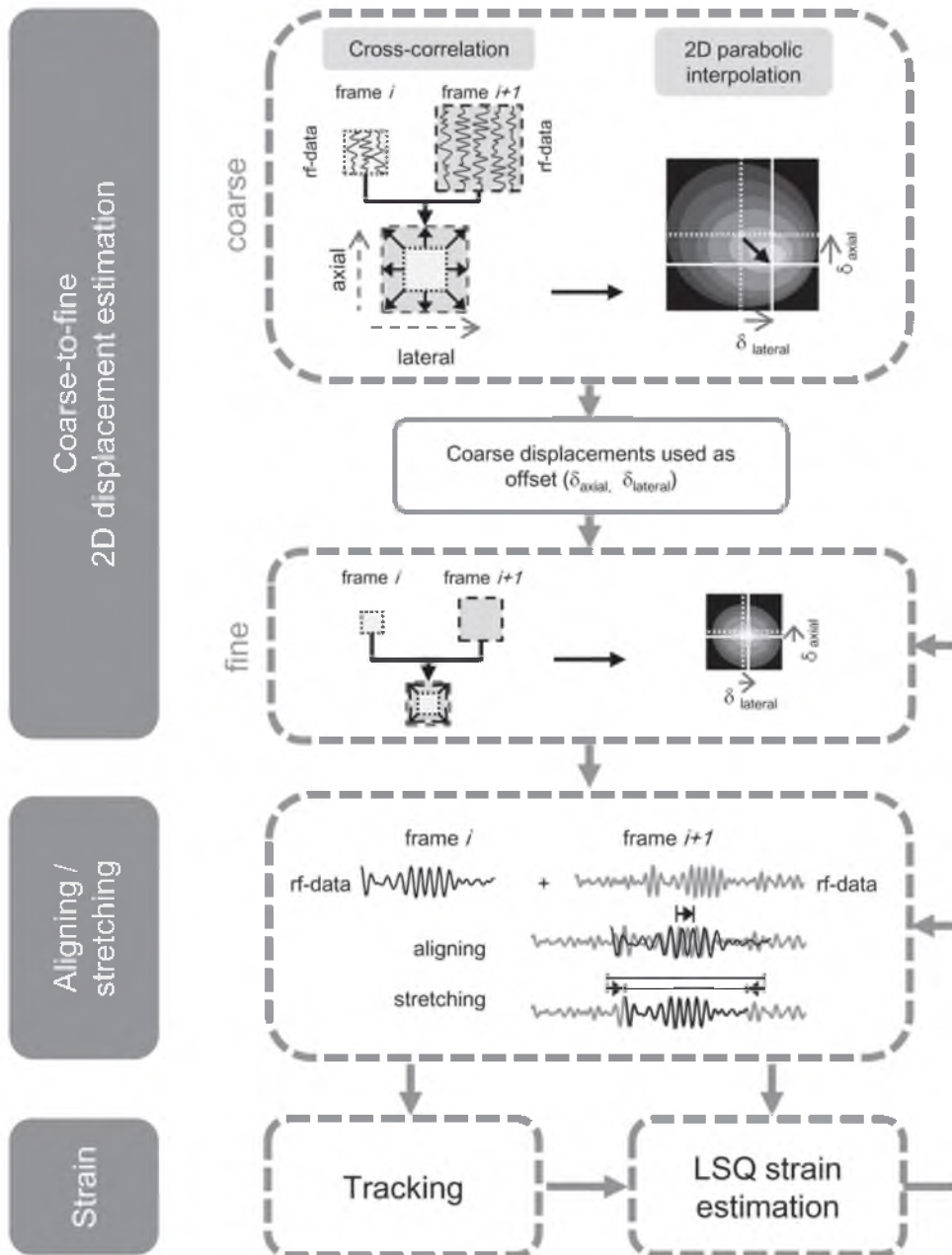


Figure 7.2 Schematic overview of the 2D (biplane) strain method. This iterative procedure starts off at coarse scale, using large 2D kernels of envelope data. During consecutive steps the axial kernel size is decreased and radio-frequency data is used to increase both resolution and precision. Finally, the data is re-correlated using so-called aligning and stretching for further improvement of the 2D displacement fields. After obtaining the displacement estimates, the myocardial tissue is tracked using these data and the cumulative strain images are generated

**Table 7.1 Used settings of the strain estimation method for each iteration.**

|                         | Coarse   | Middle   | Fine              | Aligning | Stretching |
|-------------------------|----------|----------|-------------------|----------|------------|
| Axial window (pre)      | 6 mm     | 3 mm     | 1 mm              | 1 mm     | 1 mm       |
| Axial window (post)     | 12 mm    | 6 mm     | 2 mm              | 2 mm     | 2 mm       |
| Used data               | Envelope | RF-data  | RF-data           | RF-data  | RF-data    |
| Lateral window (pre)    | 5 lines  | 5 lines  | 5 lines           | 5 lines  | 5 lines    |
| Lateral window (post)   | 11 lines | 11 lines | 11 lines          | 11 lines | 11 lines   |
| Median filter (axial)   |          |          | 5.0 mm x 5 lines  |          |            |
| Median filter (lateral) |          |          | 5.0 mm x 11 lines |          |            |

well or even better than other interpolation techniques and also proved to be a fast alternative to interpolation of RF-lines (Chapter 2). To enhance the correlation between pre- and post-compression windows, the signal kernels were “re-correlated” by aligning the windows on sub-sample level in both the axial and lateral direction using interpolation (Fig. 7.2). Finally, the data is compressed or stretched using strain estimates of the previous iteration (“stretching”) in order to increase correlation in areas with high strain (Chapter 2 and 4).

The performance of this method was previously evaluated using linear array ultrasound data in phantoms (Chapter 2). However, 2D and biplane echocardiographic data are often acquired with phased array transducers. The resulting sector scan data are stored in a polar coordinate system and have non-equidistant line spacing in the Cartesian system. The applicability of the method on phased array data was demonstrated and its performance was quantified using simulations and phantom studies (Chapter 4). This study revealed that strain estimation using 2D data kernels outperformed 1D kernel matching for sector scan

data. The strain quality was quantified in a commonly used inhomogeneous tissue phantom. The signal-to-noise ratio (SNR) of the strain images was found to be 30 dB (axial) and 20 dB (lateral) in a simulation study, but was 5 to 7 dB lower in experimental data. Furthermore, it was shown that the use of local aligning and stretching improved the SNR of the strain images by 5 to 20dB for a range of strains of 0.5 – 5.0%. Again, phased array sector scans operate in a polar coordinate system and strains are not measured in the vertical or horizontal direction. The axial displacements and strains are measured along the direction of beam propagation. The so-called in-plane displacements and strains are measured perpendicular to the ultrasound beam and are the lateral displacements and strains. Since biplane data consist of two perpendicular planes, the lateral strain is measured in two directions, the azimuth and elevational direction.

The 2D strain algorithm used a decreasing radial pre-compression kernel size from coarse (6.0 mm) to fine scale (1.0 mm) with a fixed pre- and post-compression lateral kernel size of 5 scan lines. The post-

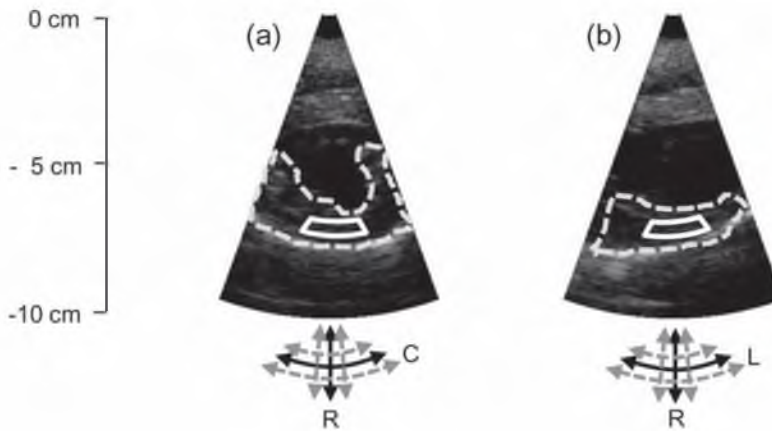


Figure 7.3 Biplane image of a canine heart in short- and long-axis view. The total tracked region-of-interest in the lateral wall is indicated with the grey line (dashed) in both images. The used region for strain analysis is the region within the white line (solid). The direction of the measured strain components is indicated in the lower part (arrows).

compression kernels (*i.e.* search area in the next frame) were two times larger in both directions (see Table 7.1). After coarse-to-fine displacement estimation, aligning and stretching were performed. The axial displacements were smoothed with a sliding-window median filter of (5.0 mm x 5 lines). The lateral displacement estimates are noisier because of under-sampling and the lack of phase information in this direction. Hence, a filter of 5.0 mm x 11 lines was used for the lateral displacements. The spatial derivatives of the axial and lateral displacements were calculated in the axial and lateral direction, respectively, using a 1D least-squares (LSQ) strain estimator (Kallel and Ophir 1997) with a kernel size of 11 displacement estimates.

### Experimental Data Acquisition

Data were acquired with a Philips SONOS 7500 live 3D US system and an X4 matrix

array transducer with a center frequency of 2.5 MHz and a bandwidth of 1-4 MHz (Philips Medical Systems, Bothell, USA). The system was equipped with an RF-interface that transferred the radio frequency data to a regular PC work station. The RF-data were digitized at 19.5 MHz. The compression and gain settings did not change or influence the RF-data. Using a smaller imaging plane (angle of 40° instead of 90°, imaging depth of 10 cm) in the parasternal view, a frame rate in the order of 100 Hz (96-104 Hz depending on echo depth) was achieved. The sector was large enough to image the total region of interest in the infero-lateral wall of the myocardium (Fig. 7.3). The electrocardiographic (ECG) signal was captured during the acquisition. RF-acquisition was triggered on the R-wave of the ECG signal.

Each animal was imaged monthly over a period of six months. Depending on the heart rate of the animals (70 – 140 bpm) and due to the limited data storage capacity

of the system (200 images), this resulted in at least one complete cardiac cycle. In retrospect, the experiments yielded four suitable datasets for each animal. Using biplane imaging and the proposed strain estimation method, frame-to-frame deformations of the infero-lateral wall in the short-axis plane (Sax) and the long-axis plane (Lax) were obtained over the heart-cycle (Fig. 7.3). Considering the orientation of the myocardium in the image sector, the measured axial strains within the infero-lateral wall were assumed to be parallel to the radial strains (R). The lateral strains in the Sax- and Lax-planes were relatively parallel to the circumferential (C) and longitudinal (L) strain, respectively (Fig. 7.3). Combination of these two views with 2D strain estimation and with the previous assumptions yielded the deformation of the heart muscle in radial, circumferential and longitudinal directions for the middle segment of the left ventricle. The myocardial tissue was manually segmented by a trained observer (Fig. 7.3). Instead of tracking the contour of the ROI, all windows within the segmented ROI were tracked using the measured displacements (Chapter 6). The least squares strain estimator was used again to estimate the radial (Sax and Lax), circumferential (Sax) and longitudinal (Lax) strains. The cumulative strain values were determined for all pixels within the ROI for all strain components during the heart cycle. For comparison between dogs, a small region within the myocardium was defined (Fig. 7.3, white solid lines). The cumulative strain curves, the maximum strain rate and maximum strain were measured.

### *Histopathological Examination and Statistics*

After removal of the heart, the left and the right ventricle were opened to allow free drainage of blood. The hearts were cut in slices (thickness = 1 cm) perpendicular to the long axis. The slice originating at one centimeter below the aortic valve and corresponding to the short axis view echo data (Fig. 7.1) was removed for histological examination and fixed in 10 % buffered formalin solution. After 5 days of fixation this slice was photographed, divided in anatomically marked portions and completely embedded in paraffin. Tissue samples (thickness = 5  $\mu\text{m}$ ) were stained with Haematoxylin/Eosin (HE) and Masson Trichrome for histopathological examination. The HE staining was used for general histological evaluation of the tissue and Masson to evaluate the fibrotic component. However, the latter stain was also used for digital image analysis as it permits to quantify the fibrotic component.

For quantitative measurement, the paraffin blocks including the lateral wall were selected, and 5  $\mu\text{m}$  thick sections were stained with 1% acid Fuchsin. The percentage fibrosis was assessed by digital image analysis, as described by Van der Steen et al (1994). For each beagle, 100 microscopic fields of view of the lateral wall with exclusion of the papillary muscle and 35 fields of the papillary muscle were measured, with pixel size 1.3  $\mu\text{m}$  x 1.3  $\mu\text{m}$  (image size = 0.7  $\text{mm}^2$ ).

Quantification of the area occupied by fibrosis was performed fully automatically, using a KS400 image analysis work station



(Carl Zeiss, Germany). Collagen belonging to blood vessels was interactively excluded from the analysis, whereas ischemic infarction zones in the papillary muscle were included. All statistics were performed using SPSS for Windows (SPSS Inc, Chicago, Ill, USA, version 16.0.2). Because data from histometry show a skewed distribution, deviating from the normal distribution, log-conversion was also applied. To study differences between different beagles, ANOVA was used with Dunnett post-hoc testing in case of a significant main effect. Statistical differences were considered significant for  $p < 0.05$ .

## RESULTS

An example of the deformation (*i.e.* strain) of the heart during the cardiac cycle can be appreciated in figure 7.4. The biplane cardiac strain images are shown (Fig. 7.4a-d). Furthermore, the cumulative strain was determined for a region in the infero-lateral wall for all three components of the strain (Fig. 7.4f-g). The strain range for this particular example is from -30 to 30%. The positive radial strains reveal thickening of the myocardial wall in the systolic phase and thinning in the diastolic phase (Sax and Lax, Fig. 7.4a-b). The circumferential and longitudinal strain components are negative, representing shortening of the muscle during contraction, followed by lengthening in the diastolic phase (Fig. 7.4c-d). Radial strain images as determined for both planes (Fig. 7.4a-b) show similar

behavior and ‘match’ at the intersection of the biplane. It may be noted that the radial strain images roughly return to their initial value in diastole, but a small residue of strain remains (see Discussion). This residue is higher for the components C and L due to noise accumulation.

In figure 7.4f-g the mean cumulative strain curves are shown for a central ROI in the myocardial wall (Fig. 7.3, white solid line). Again, both radial strain curves are similar in magnitude and shape. The radial strain has a maximum expansion value of approximately 50% in both curves. The circumferential and longitudinal strain curves have a maximum contraction value of -14% and -33% respectively. This corresponds to figure 7.4c and figure 7.4d, where the level of contraction in the Lax view is higher.

As an example, all four strain curves for the beagle with the lowest pressure gradient are shown in figure 7.5. Here the error bars are added to indicate the variance of the strain measurements within the ROI for each phase of the cardiac cycle. Again, the radial strain curves of both planes are similar and also the error bars have an almost equal magnitude. The error on circumferential and longitudinal strain is higher as can be expected. This is caused by the lower spatial resolution and absence of phase information in this direction.

The four beagles developed pressure gradients over the aortic valve of 20, 100, 120 and 200 mmHg, respectively. The radial strain curves, obtained in the beagles with 20 and 200 mmHg, are shown to illustrate that the difference in shape is reproducible (Fig. 7.6a-b, Fig. 7.6d-e). The radial

strain of the pathological dog ( $\Delta p = 200$  mmHg) shows a different shape and lower maximum strain values. Furthermore, the images of the myocardial tissue revealed more fibrosis for this beagle (Fig. 7.6f). A more extensive analysis of the differences between the four beagles is given in figure 7.7 and figure 7.8. In figure 7.7, the mean maximum, end-systolic, strain (left) and the maximum systolic strain rate (right) for all three directions are shown for the four beagles. The strain and strain rate traces were averaged for all pixels within the ROIs. The median values are also indicated (black horizontal lines). The maximum radial strain rate decreases for dogs with a higher pressure gradient. The trend in maximum radial strain seems less evident but the measurements are less scattered. The longitudinal strain and strain rate also decreases in magnitude. However, the circumferential strain shows little difference and no distinct correlation with the present pressure gradient can be depicted.

Histological analysis of the dog with the lowest pressure gradient revealed no signs of hypertrophy nor of dilation of the left ventricle. No formation of fibrosis was found (see Fig. 7.6c), except for some sub-endocardial fibrosis in a papillary muscle and in the septum and in a microscopic old infarction at the junction of the septum and the posterior wall. Still, this dog may be considered to be a reference model, as in the lateral wall no fibrosis was observed. The other dogs with an elevated pressure gradient revealed diffusely increased fibrotic tissue in the myocardium, both interstitial and in the perivascular spaces. The beagle with a  $\Delta p = 200$  mmHg had a more intense, sometimes

multifocal interstitial fibrosis in the papillary muscles. This beagle presented several small, partly fibrotic ischemic infarctions. One of them, lying in the posterior wall, was already partly calcified. On morphometric examination the variance of the fibrosis seemed to increase with the  $\Delta p$ .

The dogs with an elevated pressure gradient of 100 and 200 mmHg revealed a higher percentage of fibrotic tissue in the myocardium (see Fig. 7.8). Log-conversion of the data facilitated comparison. Again, the variance of fibrotic tissue seems to increase with the pressure gradient. However, the amount of fibrosis in the beagle with a  $\Delta p = 120$  mmHg seems relatively low compared to the other dogs, especially the dog with  $\Delta p = 100$  mmHg. Statistically, a significant lower amount of collagen was found in the dog with  $\Delta p = 20$  mmHg compared to the dog with 200 mmHg ( $p < 0.001$ ). The beagle with  $\Delta p = 100$  mmHg also had less collagen compared to the dog with  $\Delta p = 200$  mmHg ( $p = 0.003$ ). However, the fibrotic tissue present in the beagle with  $\Delta p = 120$  mmHg was surprisingly lower compared to the other dogs ( $p < 0.001$ ).

## DISCUSSION

In this chapter, the feasibility of biplane cardiac strain imaging was investigated. The primary objective was to investigate if three orthogonal strain components can be measured using a commercial ultrasound machine with a standard acquisition protocol. The technique was evaluated *in vivo*

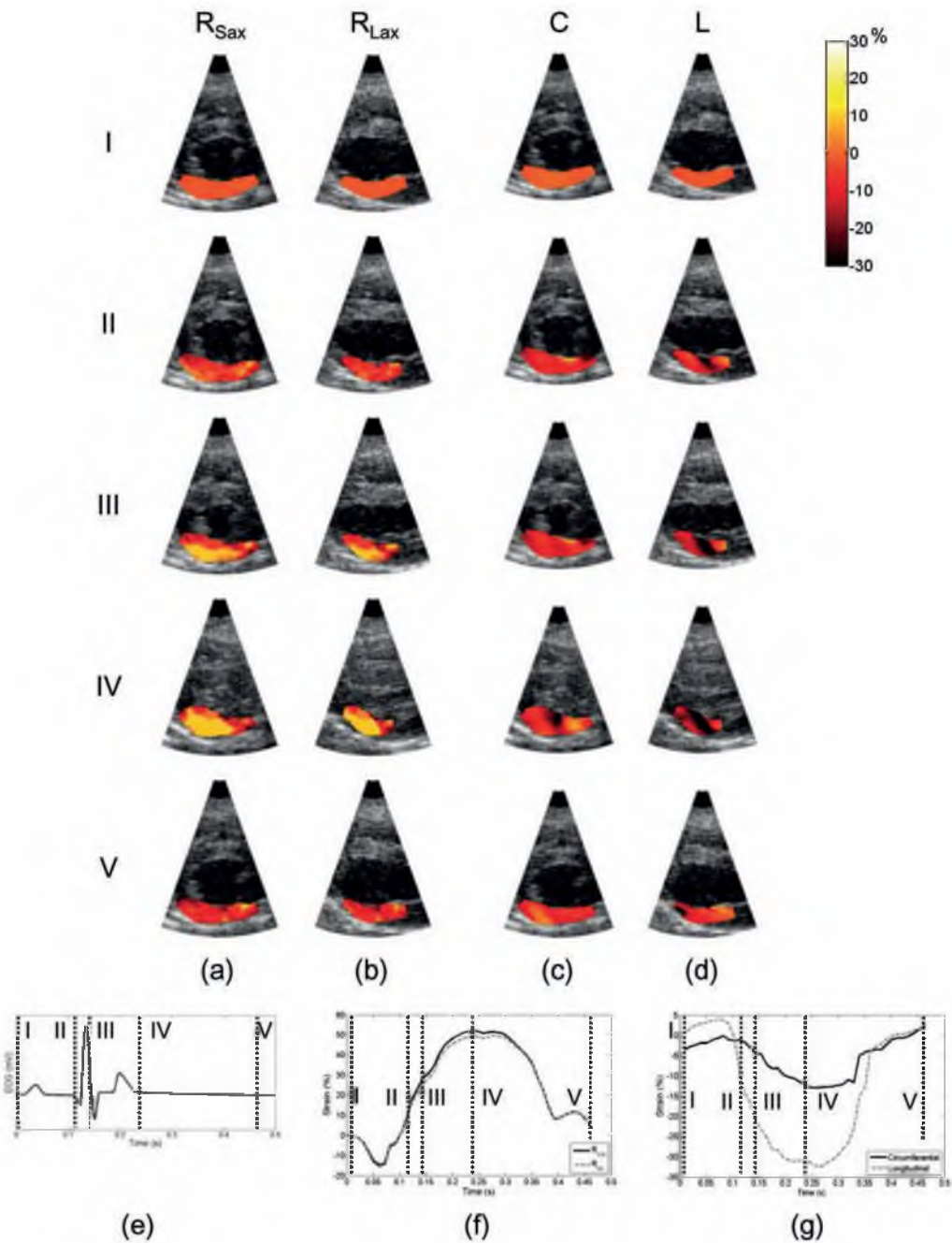


Figure 7.4 Cumulative strain in the animal model at several time points (I – V) of the cardiac cycle within the ROIs in the infero-lateral wall of the left ventricle. The strains are projected on the B-mode images (a) Short-axis radial strain, (b) Long-axis radial strain; (c) Circumferential strain and (d) Longitudinal strain; (e) the measured ECG-signal, the vertical dashed lines indicate the time points I - V; (f) the cumulative radial strain curves; (g) the cumulative mean circumferential and longitudinal strain curves.

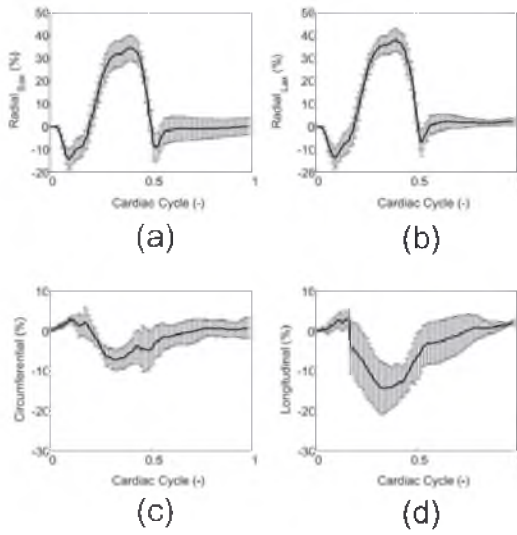


Figure 7.5 Example of all four mean strain curves (with error bars) for the beagle with the lowest pressure gradient ( $\Delta p = 20$  mmHg): (a) Short-axis radial strain, (b) Long-axis radial strain; (c) Circumferential strain and (d) Longitudinal strain. The strain was averaged for all pixels within the ROI (white line, see Fig. 2).

in four different beagles and preliminary findings of a pilot animal study on valvular aortic stenosis were reported.

The strain images in figure 7.4 provide a good overview of cardiac deformation of the infero-lateral wall during the cardiac cycle. The strain images provide local information of myocardial contraction and relaxation in semi-3D space and time. The independently measured radial strain images in both planes reveal a good similarity. This is even more clearly shown in the mean cumulative strain curves in figure 7.4f and figure 7.5 and figure 7.6. The shape of the presented radial strain curves is in accordance with previous studies in humans (Kowalski et al. 2003) and animals (Langeland et al. 2006). The results show that cardiac strain estimation from biplane imaging is feasible and reveal the reproducibility of the method (Fig.

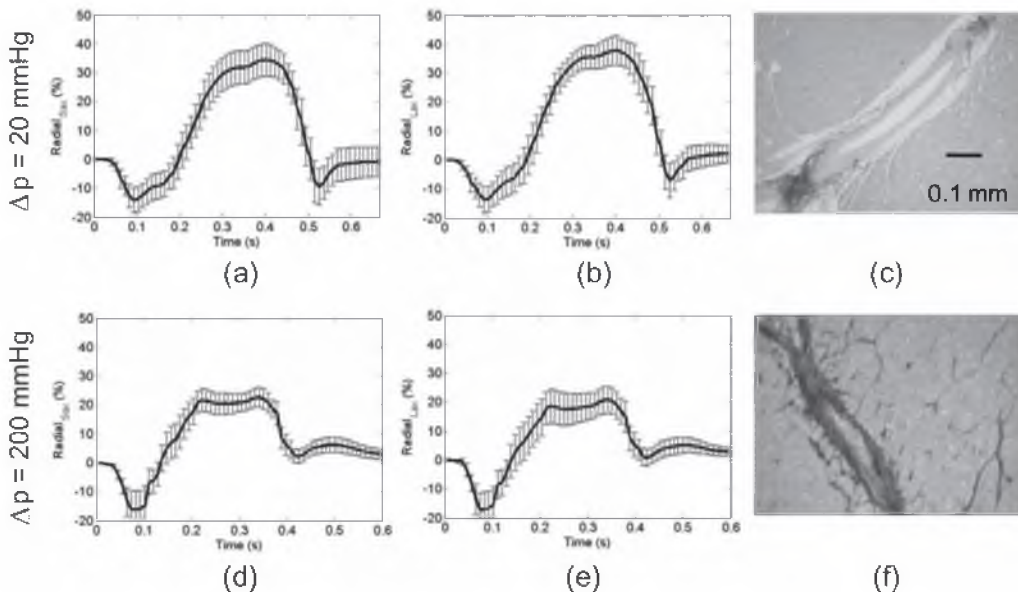


Figure 7.6 Both short-axis (a) and long-axis mean radial strain curves (b) for the beagle with the lowest pressure gradient ( $\Delta p = 20$  mmHg); (c) A tissue sample of the myocardium is shown after staining of fibrosis (black structures). The mean radial strain curves (d-e) and histology (f) for the beagle with the highest pressure gradient ( $\Delta p = 200$  mmHg).

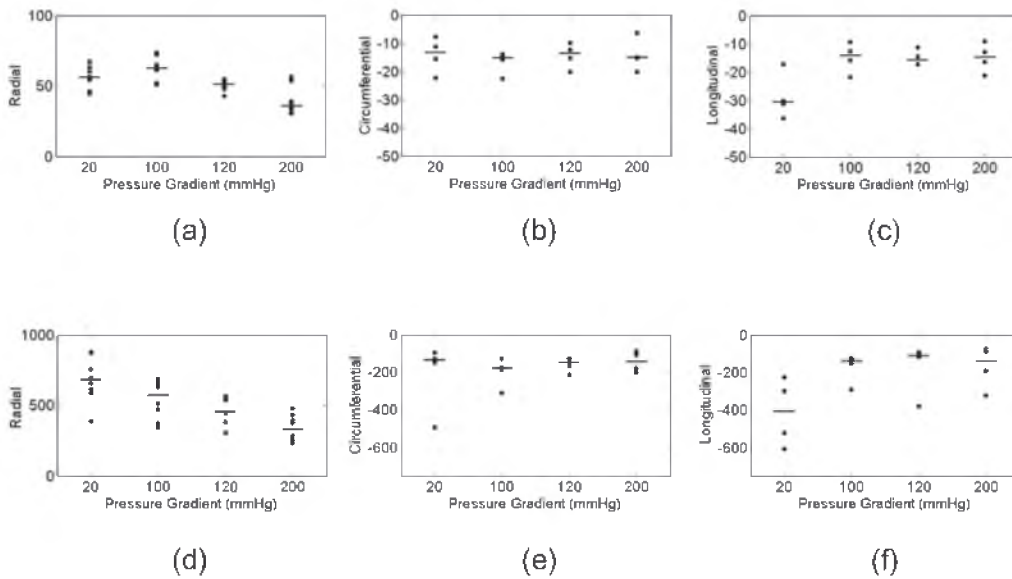


Figure 7.7 Plots of the average maximum strain (top row) and maximum strain rate (lower row) for all strain components (R, C, L) of four measurements in all four dogs. The median values are indicated by the horizontal dashes.

7.4-Fig. 7.7) in the three directions within the encountered range of heart rates and for the different pathologies.

However, the time-dependent behavior and translational and rotational movement of the infero-lateral wall make it difficult to interpret these strain images in terms of local contraction and relaxation. Furthermore, the noisy character of the circumferential and longitudinal strain images makes analysis even more complex. Despite the loss of information after averaging of the strain values, the mean strain curves of a fixed ROI in the infero-lateral wall demonstrated to reveal information of myocardial function in time during contraction and relaxation of the heart. These curves are useful in assessing hypertrophy or cardiac failure (Weidemann et al. 2002, Ganame et al. 2003). The differences in circumferential and longitudinal strain are not fully understood yet, but

corroborate the need for the extension of current techniques to a full 3D approach. The choice of ROI will influence the shape and magnitude of the strain curves. Hence, a region in the middle of the myocardium was chosen. However, this choice of ROI might have caused the low circumferential strain values.

One could question whether normalization of the measured strain curves is necessary for comparison of strain measurements in time. No significant correlation between strain (rate) and heart rate was found in this study. However, heart rate, cardiac output, and pressure determine the functional and mechanical properties of the heart during contraction and relaxation and thus the strain profiles. Therefore, a more parametrical approach for the interpretation of strain images is unavoidable.

The maximum strain values showed a

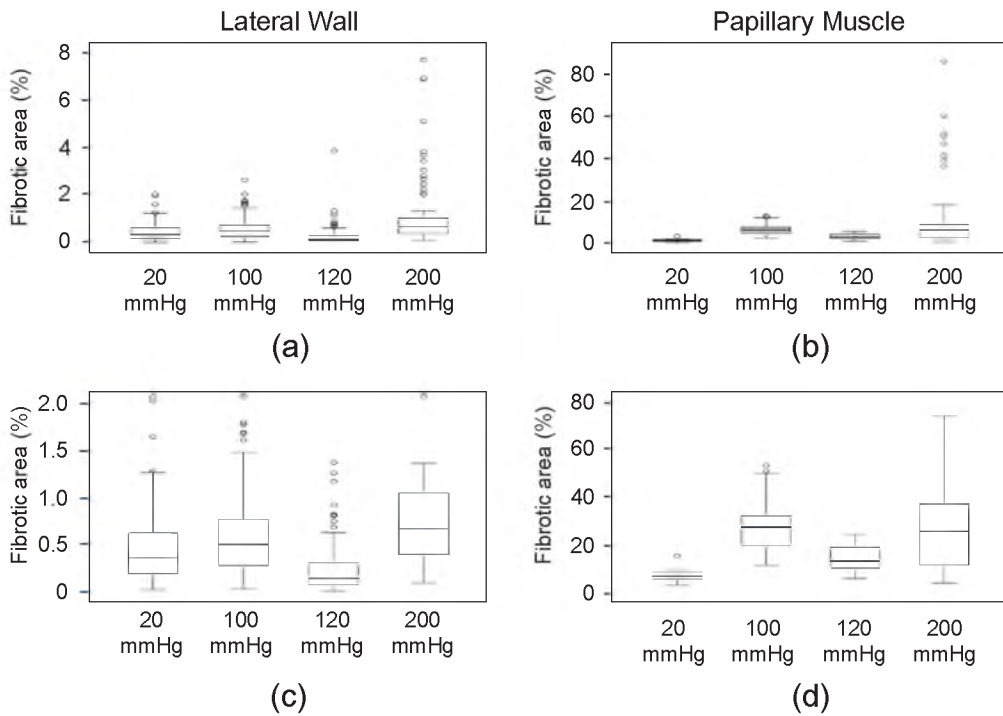


Figure 7.8 Histology results of the four dogs: Box-and-whisker plots of the amount of fibrotic tissue within short-axis slice of myocardial tissue (a) and of the papillary muscle (b). The box-and-whisker plots of the log-converted data are also shown for the myocardial tissue (c) and the papillary muscle (d).

decrease for higher pressure gradients but the reference animal ( $\Delta p = 20$  mmHg) had relatively average radial strain values (56 %) compared to the other dogs (36 - 62 %). However, the strain rate results revealed a negative correlation between maximum systolic strain rate and pressure gradient, which could be an indication of myocardial stiffening. The systolic radial strain decreased from 675 to 330 %/s (median values, see Fig. 7.7). The longitudinal strain was halved and the strain rate decreased from -410 to -140 %/s, although the values were more dispersed. However, the circumferential strain and strain rate did not reveal any significant trends or correlation with the pressure gradient. These results are in accordance with previous studies (Ganame

et al. 2003, Kowalski et al. 2003), that also found a large decrease in radial/longitudinal strain and strain rate in different pathologies. Ganame et al. found that the radial strain in control subjects was 60-65% and the strain rate was 500%/s. In patients with concentric hypertrophic cardiomyopathy, the radial strain and strain rate dropped to 40-45% and 300%/s, respectively. In these studies it was also shown that the longitudinal strain (-rate) decreased significantly. However, the strain was measured by acquiring data from a different position.

Although the pressure gradient is a good measure of the development of hypertrophy, the left ventricular pressure would be ideal for normalization purposes. However, measuring the LV pressure in patients (or animals)

is too invasive and stresses in the myocardial wall cannot be measured. Furthermore, the range of heart rates was quite large, since the animal's heart rate is not easily controlled. The impact of the pressure gradient correlated with the percentage of fibrosis as measured on histological examination of the lateral wall of the left ventricle. There was no perfect correlation however, probably partly due to the presence of more ischemic lesions that were seen as infarctions in the papillary muscle. Another reason could be an increased perivascular fibrosis both in the papillary muscle and in the external part of the lateral wall of the ventricle. The effect of the pressure gradient was better detectable in the papillary muscles (Fig. 7.8b) than in the outer part of the ventricle wall (Fig. 7.8a). Although in the lateral wall of the dog with the lowest pressure gradient no obvious fibrosis was found, it remains debatable if this dog can be considered to be an ideal reference model due to the presence of a small infarction.

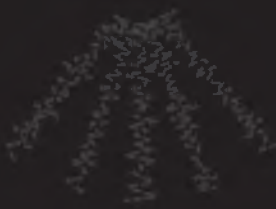
The authors are aware of the limitations of this study. First of all, a follow-up, large scale study is needed, including a control group of healthy dogs for reference. Secondly, only four suitable measurements were available for each dog due to numerous practical reasons and problems. In a follow-up study, the echo exams have to be extended, including reproducibility measurements per date. The lack of multiple measurements makes it more difficult to assess the influence of growth on the strain analysis and to monitor the development of hypertrophy and the formation of fibrosis in time.

Extension of the current technique to a full 3D approach is still desirable, considering the ability to measure the full 3D strain tensor within 3D space and following the tissue in 3D space. Since these datasets have a reduced frame rate compared to biplane imaging, the low frame rate limit will determine the feasibility of 3D strain imaging. However, full 3D strain imaging will enable the algorithm to account for out-of-plane motion and will allow 3D tracking. The advantage of 3D strain estimation might also lie in the possibility to measure torsion during the contraction of the heart muscle. Torsion may become an important parameter to characterize local heart function (van der Toorn et al. 2002).

## CONCLUSION

Cardiac strain imaging is feasible using the biplane phased array RF-data on a commercial US system. The algorithm allowed strain imaging in both orthogonal planes simultaneously at moderate frame rates. The feasibility of the technique was evaluated in an animal model. Preliminary results of this pilot study indicated that different strain values were found in animals with a severe stenosis with respect to a reference animal. However, a large scale animal study is required to further validate the animal model. In a follow-up study, a large group of patients will be imaged to demonstrate the clinical applicability of the proposed method.

Handwritten text in a box, possibly a list or notes.





---

# CHAPTER 8

## CARDIAC THREE-DIMENSIONAL STRAIN IMAGING

---

*Richard G.P. Lopata, Maartje M. Nillesen,  
Johan M. Thijssen, Livia Kapusta & Chris L. de Korte*

---

Based on: **3D Cardiac Strain Imaging in Young Children using RF-data.** R.G.P. Lopata, M.M. Nillesen, J.M. Thijssen, L. Kapusta and C.L. de Korte; *Ultrasound in Medicine & Biology* 2010; *Submitted*

---

## ABSTRACT

In this study, a new RF-based, three-dimensional (3D) strain imaging technique is introduced and applied to 3D full volume ultrasound data of the hearts of healthy children. Continuing advances in performance of transducers for 3D ultrasound imaging have boosted research on 3D strain imaging. In general, speckle tracking techniques are used for strain imaging. However, RF-based strain imaging techniques are known for their better performance, but such a system output is not commercially available. Furthermore, the relatively low frame rate of 3D ultrasound data has limited broad application of RF-based cardiac strain imaging. In this study, the previously reported 2D strain methodology was extended to the third dimension. 3D RF-data were acquired in eight healthy children, in the age of 6–14 yrs, at a relatively low frame rate of 38–51 Hz. A 3D, free-shape, coarse-to-fine displacement and strain estimation algorithm was applied to the RF-data. The heart was segmented using 3D ellipsoid fitting. Strain was estimated in the radial (R), circumferential (C) and longitudinal directions (L). Preliminary results revealed the applicability of the 3D strain estimation technique on full volume 3D RF-data. The technique enabled 3D strain images of all three strain components. The average strains for all children in the lateral wall were  $R = 32 \pm 13 \%$  (infero-lateral) and  $R = 41 \pm 15 \%$  (antero-lateral),  $C = -11 \pm 4 \%$  (antero-lateral) and  $C = -9 \pm 2 \%$  (infero-lateral),  $L = -17 \pm 6 \%$  (antero-lateral) and  $L = -14 \pm 5 \%$  (infero-lateral). In the septum, strains were found to be  $R = 16 \pm 14 \%$  (antero-septal) and  $R = 13 \pm 9 \%$  (infero-septal),  $C = -11 \pm 4 \%$  (antero-septal) and  $-17 \pm 1 \%$  (infero-septal) and  $L = -16 \pm 3 \%$  (antero-septal) and  $L = -13 \pm 3 \%$  (infero-septal). Strain in the anterior and inferior walls seemed underestimated, probably caused by the low (in-plane) resolution and poor image quality. The field-of-view and image quality were not always sufficient to image the entire left ventricle. It is concluded that 3D strain imaging using RF-data is feasible, but validation with other modalities and with conventional 3D speckle tracking techniques will be necessary.

## INTRODUCTION

Echocardiography is a well established clinical tool in pediatric cardiology and is often the method of choice for its non-invasive nature, low cost and bed-site applicability. Two-dimensional (2D) and three-dimensional (3D) ultrasound (US) are used to image the heart from several viewing angles to visualize its geometry (see Figs. 8.1 and 8.2), to estimate the heart's dimensions and calculate cardiac output and ejection fraction. US is used to assess the function of both the myocardium and the valves and to detect eventual valvular regurgitation. The velocity of the blood flow within the ventricles, as well as the velocity of movement of the myocardial tissue, can be measured with Doppler based US techniques. Hence, echocardiography can be used to detect congenital heart disease at an early stage (Sahn & Vick 2001; Kiraly et al. 2003). Currently, the application of 3D imaging technology becomes more and more clinically useful (Lang et al. 2006).

Strain imaging, or elastography, is a well-known and widely adopted technique to quantify tissue deformation. At first, the application was limited to so-called 'quasi-static' deformation, where a tissue is deformed externally by the US transducer or by an applied load (Ophir et al. 1991; Céspedes et al. 1993a). Over the years, strain imaging was also performed with dynamic data, acquired in 'actively' deforming tissues such as arterial wall (de Korte et al. 2000b), skeletal muscle (Kallel et al. 1998) and the heart (D'hooge et al. 2000; Konofagou et al. 2002). Parallel to this progression, the

technique was extended from a 1D approach to 2D image data and, more recently, to 3D volume datasets.

In general, one can use all available ultrasound data for strain imaging, *i.e.*, the conventional scan-converted B-mode data, the so-called signal 'envelope' or demodulated data and, most prominently, the radio-frequency (RF) data. The latter are in particular useful because of the available phase information in addition to the signal amplitude that is used in the other two applications. Techniques that use solely the signal amplitude are generally known as 'speckle tracking techniques', referring to the speckle patterns in the ultrasound images of tissue (Bohs and Trahey 1991; Chaturvedi et al. 1998), whereas tracking and strain estimation using RF-data is referred to as 'strain imaging' (Ophir et al. 1991; Konofagou and Ophir 1998; Chen et al. 2004; Chapter 2). However, RF-based strain imaging is in fact also a speckle tracking technique but it achieves a higher level of accuracy and precision by using the phase information as well. Its use in the heart is limited by the magnitude of the present strain and the available frame rate (Varghese et al. 1997; Alam and Ophir 1997, Céspedes et al. 1999). Inherently, amplitude-based speckle tracking is capable of measuring higher strain values and therefore favored when frame rate is low or frame-to-frame deformation is high, however, at the cost of sensitivity for small strains (Cho et al. 2006).

Several other approaches can be found in literature to quantify cardiac tissue velocity and strain. Tissue Doppler Imaging (TDI) is used to estimate local cardiac strain with a high sensitivity in the axial direction, *i.e.*,

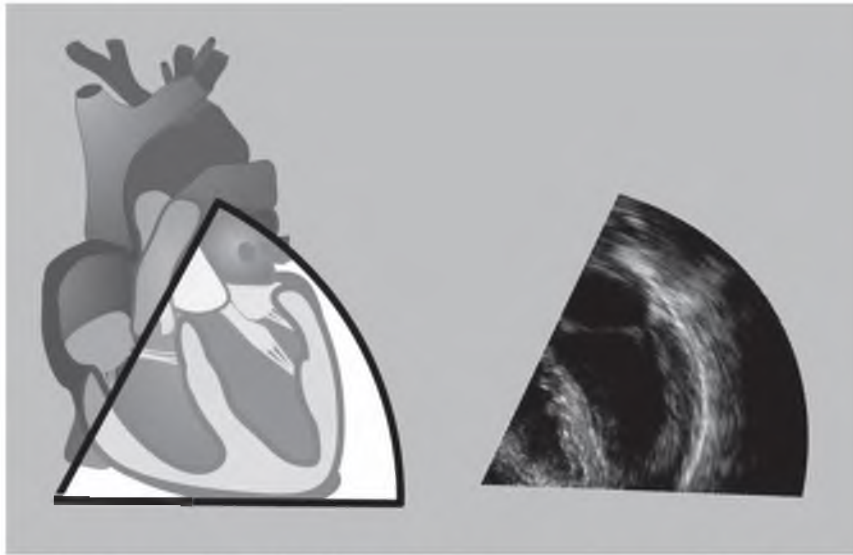


Figure 8.1. Schematic representation of the heart and the left-parasternal echo view (left) An example of a long-axis ultrasound images is given (right).

it is limited to one dimension (Heimdahl et al. 1998). Two-dimensional speckle tracking was proposed and shown to be feasible (Bohs and Trahey 1991; Chaturvedi et al. 1998), also in the heart (Kaluzynski et al. 2001; Leitman et al. 2004; Cho et al. 2006). RF-data were used for 1D strain imaging (D’hooge et al. 2000, Konofagou et al. 2002; Sutherland et al. 2004) and for 2D strain imaging (Langeland et al. 2005a; Lee et al. 2007). However, cardiac motion is not confined to a single 2D imaging plane and errors are introduced by so-called ‘out-of-plane motion’ (Konofagou and Ophir 1998; Konofagou et al. 2002). In order to obtain the strain in all three dimensions, one needs 3D data of the entire heart muscle and a 3D processing technique.

The introduction of three-dimensional ultrasound systems boosted research on 3D strain imaging. Biplane strain imaging was reported using RF-data acquired with

mechanical probes (Yoshikawa et al. 2005) and matrix array transducers (Chapters 7 & 12). Biplane data yield the deformation in two orthogonal planes, but not in full 3D space. Again, strain estimation using 3D full volume data is necessary to assess the full 3D strain tensor within 3D space.

Reports on 3D (cardiac) strain imaging are sparse. The frame rate of the commercial 3D ultrasound scanners is limited physically by the speed of sound: the volume scans require a considerable amount of scan lines, which lowers frame rate. By limiting the number of scan lines and at the same time maintain a reasonable field-of-view and frame rate, the in-plane resolution in both the azimuthal and elevational direction is relatively low. However, reasonable frame rate and resolution are required for accurate and precise tracking of tissue and for 3D strain estimation.

The effect of motion, deformation and

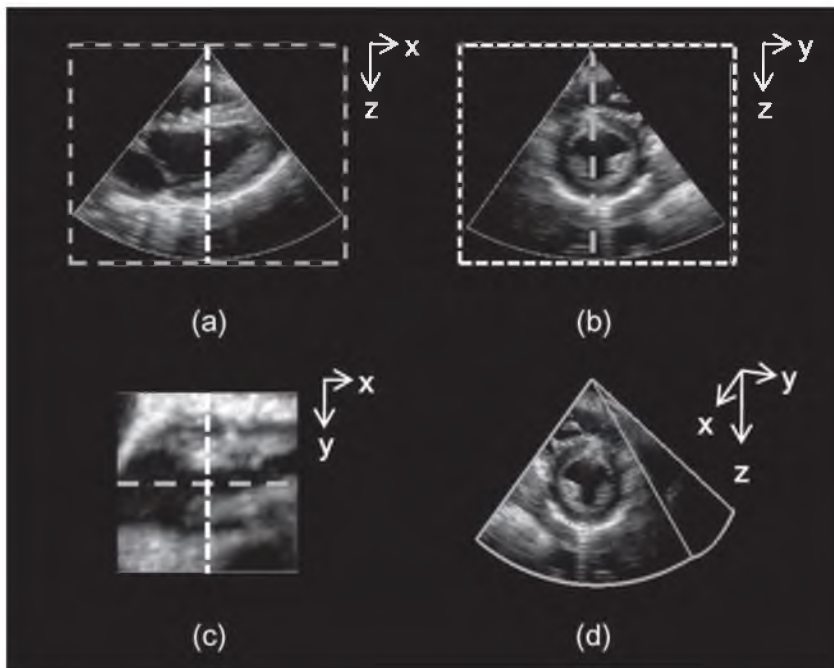


Figure 8.2. Example of 3D ultrasound data of the left ventricle; a) long-axis view; b) short-axis view; c) short/long-axis slice through the middle of the left ventricle; d) 3D volume rendering.

rotation on the precision of 3D speckle tracking and strain imaging was investigated in theoretical studies by means of simulations (Konofagou and Ophir 2000; Meunier 1998). Real three-dimensional B-mode data were processed to estimate tissue motion and deformation using reconstructive 3D TDI (Stoylen et al. 2003), 3D speckle tracking data (Chen et al. 2005; Crosby et al. 2009; Jia et al. 2007; Saito et al. 2008) and image registration (Elen et al. 2008). Crosby reported a fast and robust 3D speckle tracking algorithm, using simulated 3D envelope data. Three in vivo cases were examined, including patients with a myocardial infarction. Elen et al. applied a 3D spatio-temporal elastic registration algorithm to simulated and real 3D volume B-mode data of the left ventricle (Elen et al. 2008).

A few studies reported the first, prelimi-

nary results on 3D RF-based strain imaging, mostly in phantoms or in quasi-static experiments (Lindop et al. 2006; Lopata et al. 2007; Patil et al. 2007; Said et al. 2006). Lindop et al. (2006) and Patil et al. (2007) reported 3D strain images in simulations and experimental data of phantoms with hard inclusions. Three-dimensional strain imaging was also performed on sector scan data (Lopata et al. 2007; Said et al. 2006). The sub-optimal temporal resolution of 3D (+ time) datasets remains a problem, in particular in cardiac applications (Lopata et al. 2007). However, new ultra-fast ultrasound imaging techniques are on the rise (Deffieux et al. 2008) and may relieve the present limitations to some extent.

In this study, 3D full volume RF-data were used to estimate 3D strain within the myocardium of the entire left ventricle

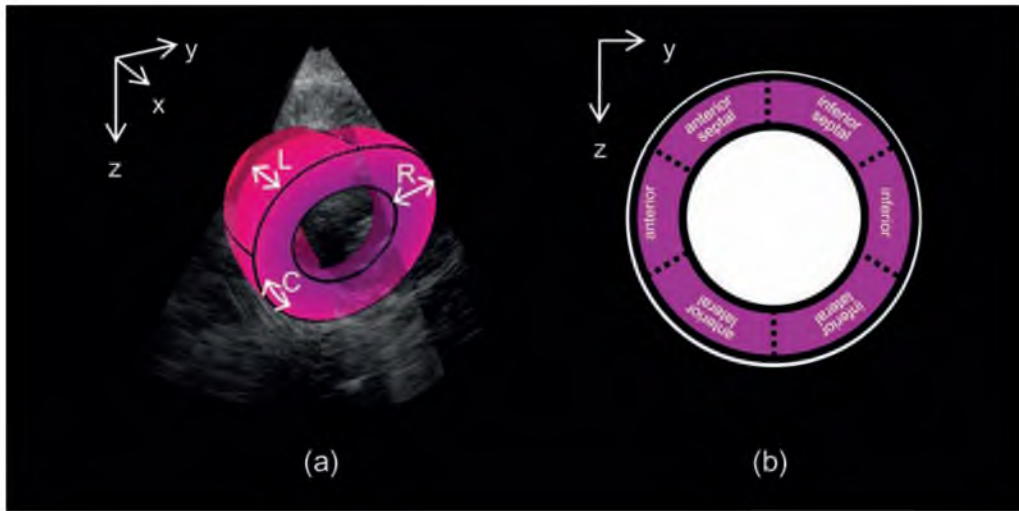


Figure 8.3. a) Schematic representation of the 3D ellipsoidal segmentation of the left ventricle and b) The division of the middle region of the myocardium in six regions as found in Cerqueira et al. (2002).

in healthy children, using a pediatric 3D probe and a commercial ultrasound system equipped with an RF-interface. The in-plane resolution and frame rate were limited with respect to conventional 2D imaging systems. Preliminary results show the feasibility of RF-based 3D strain imaging in the heart.

## MATERIALS

Three-dimensional, full volume data were acquired in eight healthy children in the age range of 6 – 14 years. The image protocol was approved by the local medical ethics committee. The parents and children gave their informed consent. Data were acquired with an iE33 ultrasound system (Philips Medical Systems, Bothell, USA), equipped with an X7 pediatric matrix array probe (2 – 7 MHz) and a custom designed RF-interface ( $f_s = 16$  MHz). The scanning angle between the image lines was either  $1.25^\circ$  or  $1.5^\circ$ .

The heart was imaged intercostally in the left parasternal view (Figs. 8.1 – 8.2). The 3D full volume data were acquired during four to seven consecutive heartbeats using ECG triggering, resulting in a frame rate of 38 – 51 Hz. During the acquisition, the children were asked to hold their breath to prevent a different position of the heart with respect to the transducer for the different heart beats resulting in so-called ‘stitching’ artifacts. Data were checked for stitching artifacts and the measurement was repeated if a stitching artifact was found.

## METHODS

The methodology as described in Chapters 2 – 5 was extended to three dimensions. A coarse-to-fine, ‘free-shape’ (Chapter 3), 3D strain algorithm was used to estimate the 3D displacement field. The procedure started at

**Table 8.1** Used settings of the 3D strain estimation method for each iteration.

|                           | Coarse   | Middle            | Fine     |
|---------------------------|----------|-------------------|----------|
| Used data                 | Envelope | RF-data           | RF-data  |
| Axial window (pre)        | 4,9 mm   | 2,5 mm            | 1,25 mm  |
| Axial window (post)       | 19,3 mm  | 4,9 mm            | 2,5 mm   |
| Overlap                   | 80%      | 80%               | 80%      |
| Lateral window (pre)      | 11 lines | 5 lines           | 5 lines  |
| Lateral window (post)     | 21 lines | 11 lines          | 11 lines |
| Elevational window (pre)  | 11 lines | 5 lines           | 5 lines  |
| Elevational window (post) | 21 lines | 11 lines          | 11 lines |
| Median filter (axial)     |          | 5.0 mm x 5 lines  |          |
| Median filter (lat/elev)  |          | 5.0 mm x 11 lines |          |

coarse scale, using cross-correlation of 3D kernels demodulated RF-data (so-called ‘envelope data’) to estimate global motion in all three directions simultaneously. A 3D parabolic interpolation was used to obtain sub-sample displacement estimates. In consecutive iterations, the RF-data were used for displacement estimation. The initial displacement estimates of previous iterations were used to align the RF-data.

The rough axial displacement estimates were also used to warp the 3D kernels of RF-data in the axial direction (‘free-shape’, see also Chapter 3) to increase correlation in regions where large shearing or rotational movement occurred. The 3D displacement fields were median filtered. All parameters of the 3D displacement estimation procedure are listed in Table 8.1. The final resolution of the displacement images was 0.5

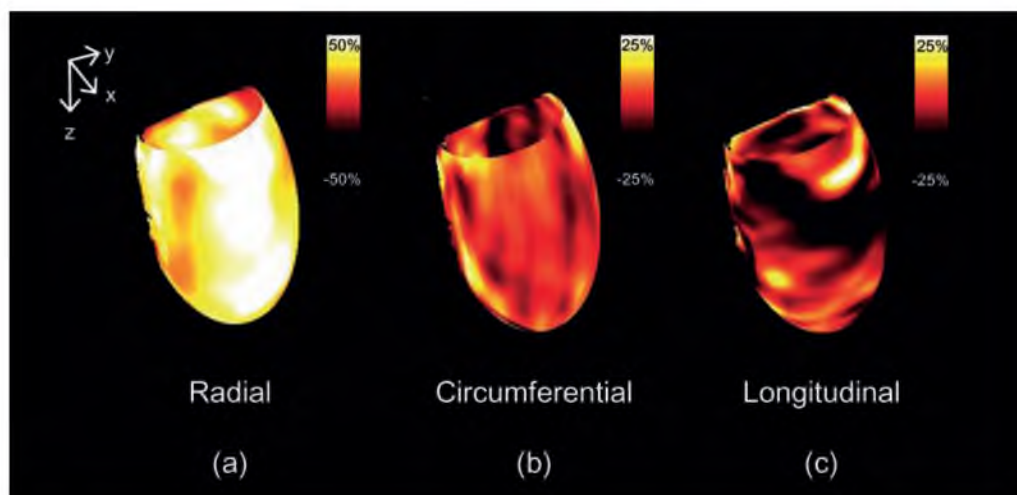


Figure 8.4 End-systolic radial (a), circumferential (b) and longitudinal strain (c), averaged over the myocardial wall in the radial direction.

mm x 1.25 ° x 1.25 ° or 0.5 mm x 1.5 ° x 1.5 °, depending on the used azimuth/elevational angle. No re-correlation techniques (Chapter 2) were used because of the high computational load of such interpolation-based techniques.

For proper tracking of the myocardium, segmentation is required. The heart was segmented by manually drawing contours along the endocardium using several short- and long-axis 2D slices of the 3D dataset. The drawn contours were used to establish the 3D orientation of the endocardium. A three-dimensional ellipsoid was fitted through these data (Fig. 8.3a). The 3D ellipsoid was expanded in its normal directions, resulting in an approximation of the shape of the myocardium. By choosing a simple shape, such as an ellipsoid, its mathematical formulation can be used to define and sample the points within the region-of-interest (ROI) in the directions of the heart, *i.e.*, the radial (R), circumferential (C) and longitudinal direction (L). The resulting ellipsoid consists of 181 points in both the longitudinal and circumferential direction and 21 points in the radial direction.

All points within the ROI were tracked using the estimated and subsequently filtered 3D displacement fields. In order to reconstruct tissue movement during the entire cardiac cycle. However, accumulation errors are likely to occur. Linear detrending was used to regularize the tracking results. and the accumulated displacements were derived from the tracked coordinates. A 3D least-squares-error strain estimator (LSQSE) technique was used to estimate the radial, circumferential and longitudinal strains (Lopata et al. 2007) using the

accumulated displacements. The size of the LSQSE kernel was 5 x 11 x 11 samples (R x C x L). The total ROI was divided in the standard 16 areas that are generally used in cardiac deformation analysis and bulls eye visualization (Cerqueira et al. 2002). The heart is subdivided in a basal, mid and apical region in the long-axis direction. The basal and mid-section are subdivided in six regions, whereas the apical region is divided in four regions. The six areas in the mid-section of the heart are shown in figure 8.3. Three-dimensional strain images were generated by superimposing the strain over the B-mode data. For this purpose, the strains were averaged in the radial direction over the myocardium. The mean strain curves for these regions were calculated for all subjects.

## RESULTS

Figure 8.4 shows an apical 3D rendering of the end-systolic, 3D strain data obtained in the left ventricle and projected on the ellipsoid middle surface. In this figure, the lateral wall is facing the reader. The radial, circumferential and longitudinal strain, averaged in the radial direction over the myocardium, are shown. The radial strain corresponds with wall thickening, whereas the longitudinal and circumferential strains reveal systolic shortening of the myocardium in these two directions, respectively.

Figure 8.5 shows an example of the 3D strain in the normal transverse view. The radial, circumferential and longitudinal



strain over the myocardial wall are superimposed on a biplane cross-section of the 3D B-mode data. The images are shown for six time points during the cardiac cycle, as indicated on the ECG-signal.

Inspection of the tracking results revealed that not all points in the basal and apical regions of the heart were properly tracked. In several cases, these regions were not fully visualized or image quality was poor. Therefore, strain analysis for all subjects was limited to the mid-area of the heart (Cerqueira et al. 2002). Figure 8.6 shows the individual R, L and C strain curves for all subjects and the grouped mean curved (black solid lines). The highest radial strains were found in the lateral wall, with  $R = 32 \pm 13 \%$  (infero-lateral) and  $R = 41 \pm 15 \%$  (antero-lateral). As expected, the strains in the septum are considerably lower,  $R = 16 \pm 14 \%$  (antero-septal) and  $R = 13 \pm 9 \%$  (infero-septal). However, inferior ( $R = 10 \pm 5 \%$ ) and anterior strain ( $R = 15 \pm 7 \%$ ) were lower compared to others and therefore considered to be underestimated (see Discussion).

The shape of the measured longitudinal and circumferential strains (Fig. 8.5) were similar to those found in other studies (Crosby et al. 2009; Elen et al. 2008), including our own (Chapter 7). The longitudinal strain ranged from  $-16 \pm 3 \%$  (antero-septal) and  $-13 \pm 3 \%$  (infero-septal), respectively, to  $-17 \pm 6 \%$  (antero-lateral) and  $-14 \pm 5 \%$  (infero-lateral). The lateral circumferential strain was found to be  $-11 \pm 4 \%$  (antero) and  $-9 \pm 2 \%$  (infero) whereas the septal strain was  $-11 \pm 4 \%$  (antero) and  $-17 \pm 1 \%$  (infero), respectively.

## DISCUSSION

In this study, an RF-based 3D strain estimation technique was applied to RF-data obtained in the heart of healthy children. The preliminary results on 3D cardiac strain imaging are reported. Previous reports on 3D RF-based strain imaging are mostly limited to simulation and phantom studies. Most in vivo 3D applications use signal envelope (B-mode) data, *i.e.*, speckle tracking. However, it was shown that RF-data have the potential of outperforming B-mode speckle tracking since the available phase information results in an overall higher sensitivity in the axial and in-plane directions (Chapter 2 & 4). This higher precision and accuracy is obtained at the cost of robustness and is affected by a low frame rate of the data acquisition. The coarse-to-fine approach uses both envelope and RF-data, thereby combining the advantage of measuring large translation and deformation (using envelope data) with the ability of obtaining high precision strain estimates in subsequent iterations (RF-data).

The matrix array pediatric probe was advantageous for this study because of its small footprint and high center frequency. However, apical image acquisition was still cumbersome as well as imaging the apex in the transverse orientation as was used in this paper. The ECG-gated protocol allowed a frame rate of 38 to 51 Hz, which seems relatively low compared to 2D ultrasound techniques, but it was in fact at least two times higher compared to our previous study in which we used an older system (SONOS 7500 with X4 matrix array result-

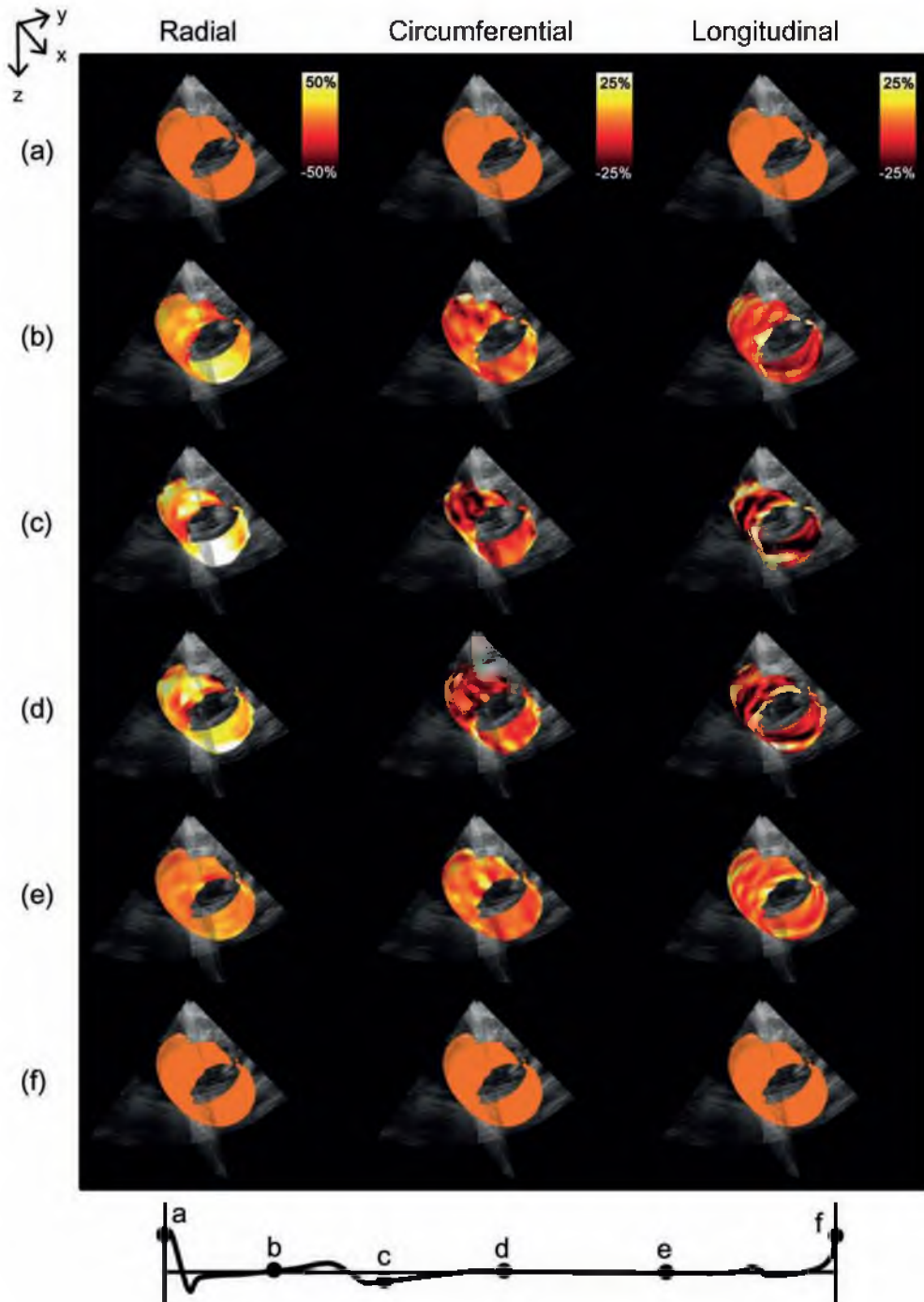


Figure 8.5 Radial, circumferential and longitudinal strain for the entire left ventricle for six time points during the cardiac cycle (a-f). Please note that the strain was averaged over the myocardial wall in the radial direction for visualization purposes.

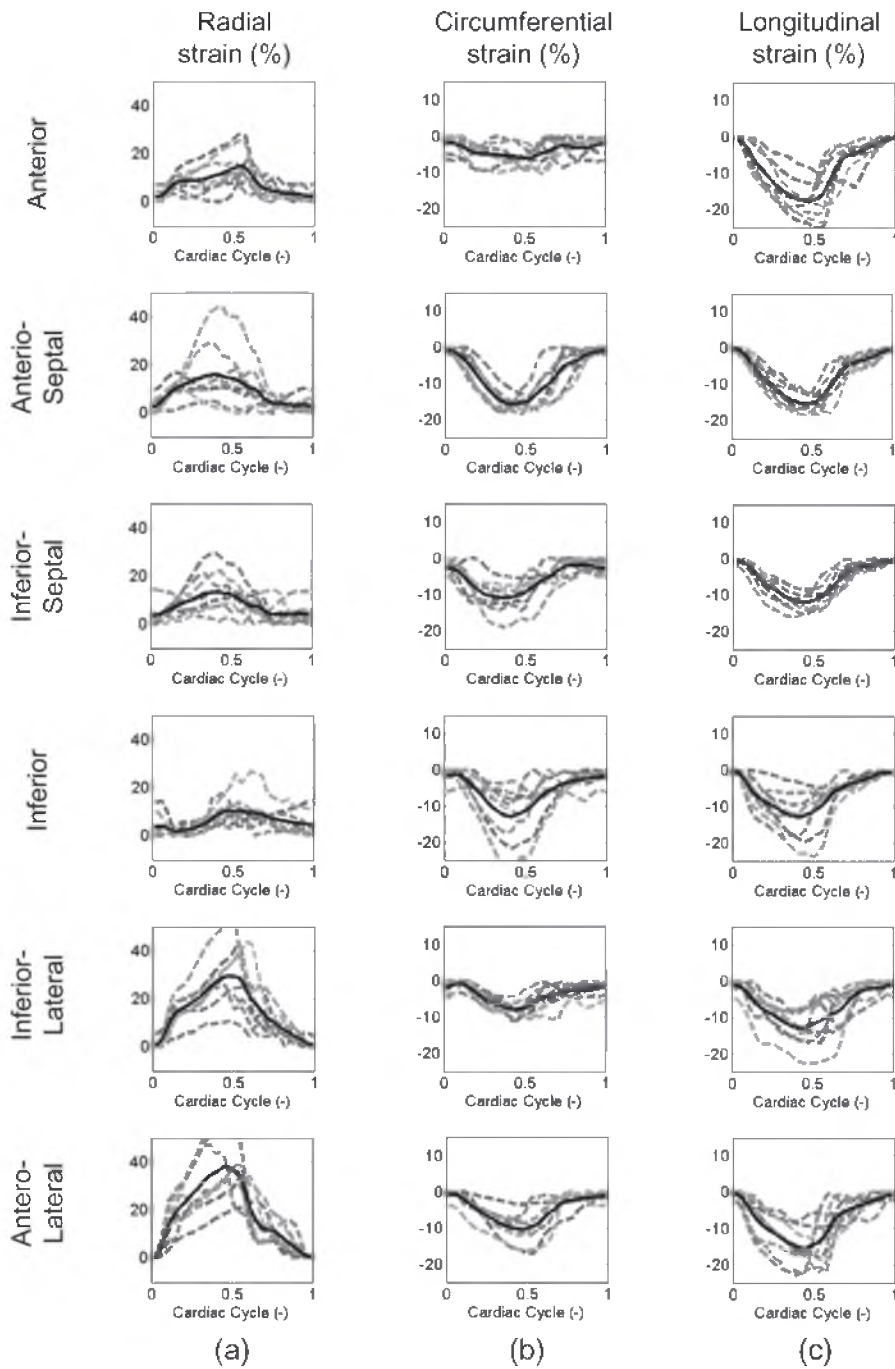


Figure 8.6 Radial, circumferential and longitudinal strain curves for six regions in the middle section of the left ventricle for all subjects (grey) and averaged over all subjects (black).

ing in a frame rate of 19 Hz, (Lopata et al. 2007)). A consequence of ECG gating is the possible occurrence of stitching, caused by a variable heart rate and movement artefacts. Especially with the younger children, breath holding during image acquisition tended to arouse the child and consequently increase heart rate. However, we succeeded in obtaining high quality datasets without stitching artifacts in these eight healthy children.

The image quality of the anterior and inferior walls was relatively poor. This could explain the observed underestimation of the strain components in these regions. In these regions, the direction of the ultrasound beam is practically parallel to the myocardial wall. This results in a lower image quality. Besides, in these regions, the radial strain is mainly based on lateral displacement and strain information, which is of lower quality due to the lack of phase information and resolution. Higher in-plane resolution might overcome these issues, but will not increase overall image quality. Image acquisition from several positions and/or angles and fusion of both image and strain data might overcome these problems (Rajpoot et al. 2009).

In addition, the field-of-view was limited and did not comprise the entire left ventricle in some cases. Figure 8.4 shows strain in the entire left ventricle, but these data were not available for all children. Hence, 3D strain was measured and compared in the middle part of the left ventricle for all subjects, which is a limitation of this study.

Obviously, increased frame rate will enhance both accuracy and precision of the measured strain components. However, the physical properties of sound prohibit frame

rate increase when a matrix array configuration with line-by-line transmit/receive technology is used. This problem has been partially tackled by using multiple receive lines per transmission pulse. New ultra-fast ultrasound technology using plane wave transmission and synthetic aperture reception could be used to improve frame rate (Deffieux et al. 2008), but at the cost of a degradation in lateral resolution and image quality.

The authors are aware of several other limitations of this study. First of all, RF-acquisition was limited to one full volume dataset for one entire heart cycle. Since the storage of the RF-data took around five minutes, only one complete 3D dataset was available for each child in both the transverse and the apical view. However, the quality of the apical datasets was inferior compared to the transverse data. In future studies, only the transverse data will be acquired multiple times. Secondly, the computational load of the Matlab (Mathworks Inc, Natick, MA, USA) based 3D strain estimation algorithm was relatively high. Especially the first step of the strain algorithm, when no prior estimates are available and therefore the search area has to be sufficiently large, was computationally intensive ( $\approx 4$  hours). Consecutive steps were significantly faster but still slow ( $\approx 1$  hour). Besides, since no *a priori* segmentation over the entire heart cycle was available, displacement estimation was performed within a large portion of the entire volume. To speed things up, replacing the first iteration by a fast speckle tracking algorithm is recommended as well as Graphics Processing Unit (GPU) programming of the coarse-to-fine algorithm.

Further improvement of the strain results could be accomplished by means of 3D re-correlation techniques (see Chapters 2 & 4). Secondly, the segmentation could be improved using image envelope data and correlation based automatic segmentation (Chapter 9). In the future, an integrated approach could be both more robust and faster.

The 3D strain technique should be validated: simulation data of the left ventricle could be used to assess the performance of the 3D displacement and strain estimation (Elen et al. 2008; Crosby et al. 2009). Secondly, an evaluation of RF-based strain imaging vs. speckle tracking can give insight in the actual benefit of using RF-data. However, speckle tracking is not evidently the golden standard. A recent study in which 2D speckle tracking was compared with sono-micrometry in sheep, revealed a quite low correlation between the two techniques (Ishizu et al. 2010). In a future patient studies, tagged MR imaging could be performed and compared to the ultrasound tracking results. After validation, a large scale normal and patient study has to be executed to assess the use of 3D strain imaging for the detection and monitoring of congenital heart disease.

## CONCLUSION

In conclusion, the feasibility of using 3D RF-data for 3D (+t) cardiac strain imaging was shown. Preliminary results are in accordance with other studies. In the future, 3D ultrasound data and strain analysis will be compared with MRI tagging. Advances in transducer design will hopefully enhance both the spatial and temporal resolution of the 3D ultrasound data, which is indispensable for both accurate and robust RF-based strain imaging.

### *Acknowledgements*

The authors would like to thank Bob Rijk and Imke Tomasouw-Janssen for their assistance with the echographic image acquisitions and Tim Idzenga for his help with C-implementation of the 3D tracking algorithm.

Handwritten text in a rectangular box, possibly a list or notes.



---

# CHAPTER 9

## SEGMENTATION OF THE HEART USING TEMPORAL INFORMATION

---

*Maartje M. Nillesen, Richard G.P. Lopata, Henk-Jan Huisman  
Johan M. Thijssen, Livia Kapusta & Chris L. de Korte*

---

Based on: **Correlation Based 3D Segmentation of Echocardiographic Images using Radio Frequency data.** M.M. Nillesen, R.G.P. Lopata, H.J. Huisman, J.M. Thijssen, L. Kapusta and C.L. de Korte, *IEEE Transactions on Medical Imaging* 2010; *Submitted*

---

## ABSTRACT

Clinical diagnosis of heart disease might be substantially supported by automated segmentation of the myocardium in 3D echographic images. Because of the poor echogenicity contrast between blood and myocardial tissue in some regions and the inherent speckle noise, automated analysis of these images is challenging. A priori knowledge on the shape of the heart cannot always be relied on, e.g., in children with congenital heart disease, segmentation should be based on the echo features solely. The objective of this study was to investigate the merit of using temporal cross-correlation of radio frequency (RF) data for automated segmentation of 3D echocardiographic images. Maximum temporal cross-correlation (MCC) values were determined locally from the RF-data using an iterative 3D technique. MCC values as well as a combination of MCC values and adaptive filtered, demodulated RF-data were used as an additional, external force in a deformable model approach to segment the endocardial surface and were tested against manually segmented surfaces. Results on 3D full volume images of 10 healthy children demonstrate that incorporation of MCC improves the segmentation results significantly.



## INTRODUCTION

Ultrasound is a reliable and fast imaging modality that is pre-eminent in cardiac imaging of children because of its non-invasiveness and high temporal resolution. The introduction of real-time 3D echographic imaging techniques has been a major step forward for quantitative analysis of the heart as these techniques provide rich information about the whole structure and 3D motion of the heart. 3D echocardiography enables the estimation of clinically important parameters such as cardiac output and ejection fraction without the necessity of making 2D geometrical assumptions. These geometrical assumptions generally include a simplified shape of the left ventricle which may lead to inaccurate estimation of the ventricular function (Gopal et al. 1995; Jacobs et al. 2006). 3D ultrasound imaging might also facilitate simultaneous estimation of strain in radial, circumferential and longitudinal direction in the heart muscle. Furthermore, inaccurate strain estimates due to out of plane motion (Konofagou and Ophir 2000) can be prevented.

The availability of 3D echocardiography has also boosted the urge for automated segmentation methods since manual segmentation of 3D ultrasound image sequences is very time-consuming. Moreover, manual segmentation by an expert is subject to inter-and intra-expert variability. Many approaches for segmenting the endocardial wall in adult echocardiographic images have been proposed. An overview can be found in Noble and Boukerroui (2006).

The inherent speckle noise from randomly backscattered echoes and the poor echogenicity contrast between blood and myocardium in some regions impose strong demands on the segmentation algorithm. If the orientation of the muscle fibers is mainly parallel to the propagation direction of the ultrasound beam, myocardial echogenicity is reduced to within the range of blood echogenicity. Automatic segmentation purely based on differences in echogenicity will lead to erroneous segmentation in these low echogenicity regions as the contrast between blood and myocardial tissue is absent. To overcome segmentation errors in these regions, methods using shape and appearance models have been proposed (Bosch et al. 2002; Hansegard et al. 2007). These models incorporate knowledge about the shape and appearance of, for example, the left ventricle by using an average shape and appearance model of the adult heart. These methods rely on implicit knowledge that is also used by expert cardiologists during manual segmentation and are successful in normal adult heart geometries in standardized (apical) views. However, echocardiography in children often aims at detection of congenital deformities of the heart. The use of *a priori* knowledge about the average shape of the ventricle may lead to incorrect segmentation in these images.

Segmentation in pediatric echocardiographic images faces some additional difficulties. Due to the relatively small intercostal spaces, image quality might be affected negatively by the ribs, causing shadowing and clutter artifacts. Compared to adults, the position of the heart within the thorax is different in such a way that in

most 3D apical images in young children the lateral wall (compare the standard 2D two-chamber view) is difficult to visualize. Three-dimensional transthoracic short-axis (Sax) and long-axis (Lax) views lead to much better image quality as the largest part of the muscle fibers is now perpendicular to the ultrasound beam. However, in this different view it is challenging to visualize the entire left ventricle and often the apex is missing or has a very low echogenicity. Furthermore, most commercial segmentation methods require a standardized apical view and no accurate segmentation is obtained in this different viewing angle with these methods.

In order to obtain more accurate segmentations in problematic low contrast regions without the necessity of making *a priori* assumptions on shape/appearance and viewing angle, the addition of temporal information using cross-correlation techniques might be helpful. These techniques build on the underlying principle that echographic data of two successive time frames will correlate less for fast moving blood than for the myocardial tissue. For the analysis of echocardiographic images, an expert cardiologist mentally incorporates the movement of the heart throughout the cardiac cycle to determine the exact geometry of the heart and uses the temporal coherence of structures to resolve ambiguities. In this chapter, we propose the use of temporal cross-correlation techniques that utilize the rich phase information available in the radio frequency (RF) signal.

In the field of ultrasound segmentation, most methods are based on using conventional B-mode images (amongst others, (Angelini et al. 2001; Corsi et al.

2002; Gerard et al. 2002; Lin et al. 2003; van Stralen et al. 2005)), whereas only a few studies are dedicated to segmentation based on the radio RF-data. Davignon et al. (Davignon et al. 2005) used statistical parameters, derived from the envelope of the RF-data, representative of the scattering conditions in the tissue in a multi-parametric segmentation process and they evaluated these parameters in simulated ultrasound data. Boukerroui et al. (Boukerroui et al. 2001) computed the mean central frequency (MCF) and integrated backscatter (IBS) from the local frequency spectra of the RF-signal and used these parameters in a multi-parametric and multi-resolution segmentation algorithm. Dydenko et al. (Dydenko et al. 2003) proposed the use of spectral autoregressive parameters and velocity-based parameters and tested these on 2D simulated and cardiac RF-data. Gerrits et al. (Gerrits et al. 2007) used the temporal decorrelation of Doppler RF-signals for 3D region based-segmentation of the left ventricle. Yan et al. (Yan et al. 2007) investigated several RF-derived parameters as the IBS, the MCF and the maximum cross-correlation coefficient (MCC). In the latter study, segmentation based on parametric images obtained from the MCC using phase sensitive speckle tracking was promising.

This study aims at three-dimensional (3D) automated segmentation of the endocardial surface in 3D pediatric echocardiographic images. We propose the use of temporal cross-correlation values of subsequently acquired 3D volumes. Cross-correlation values were derived from an iterative coarse-to-fine displacement algorithm that was originally developed for strain estima-

tion. These values were included as external force in a deformable model. The effect of incorporating the cross-correlation values in the segmentation method has been investigated by evaluating the obtained results.

## MATERIALS

Echocardiographic image sequences of the left ventricle were obtained in ten healthy children (6-15 years old). The protocol was approved by the local ethics committee and both parents and children gave their informed consent. ECG-gated, transthoracic full volume image sequences (3D + t) were obtained in long/short axis views. All children were in sinus rhythm ( $79 \pm 12.6$  (mean  $\pm$  SD) beats per minute) and the volume rate varied between 41 and 56 Hz, depending on the image depth. RF-data were acquired directly after receive beam forming using an iE33 ultrasound system (Philips Medical Systems, Bothell, WA, USA), equipped with an RF-interface and a pediatric X7-2 matrix array transducer (2-7 MHz). RF-data were sampled at 16 MHz and transmitted to an external hard disk. The data were band-pass filtered to prevent disturbance by clutter and noise from frequencies outside the frequency band of the transducer. The data were amplitude demodulated using the Hilbert transform method and log-compressed for visualizing the echograms. Since the frame rate of the used echo system for full volume imaging is still limited, a cardiac phase (end-systole) with low deformation rate of the heart muscle

was chosen for evaluation and validation of the segmentation method.

## METHODS

### *Maximum cross-correlation computation*

Since the blood flow velocity in the ventricles is predominantly higher than the velocity of the surrounding myocardial tissue, temporal correlations between successive ultrasound volumes might be used as a feature to distinguish between blood and myocardial tissue. For 3D strain imaging purposes, the cross-correlation function (CCF) of 3D windows of RF-data was calculated (Chen et al. 2005; Lopata et al. 2007; Chapter 8). We used a 3D coarse-to-fine displacement estimation algorithm (Lopata et al. 2007; Chapter 8) that was based on an earlier developed 2D algorithm (Shi and Varghese 2007, Chapter 2) to estimate axial, lateral and elevational displacements iteratively. For strain estimation, the position of the peak of the cross-correlation function is used since this position corresponds to the displacement of the tissue. In this study, we used the magnitude of the peak, *i.e.*, the maximum of the cross-correlation function (MCC) as driving force for the segmentation model.

Three-dimensional windows were cross-correlated for two subsequent time frames and the MCC was determined. The 3D normalized CCF for the two successive RF-data frames  $I_t$  and  $I_{t+1}$  was defined as:

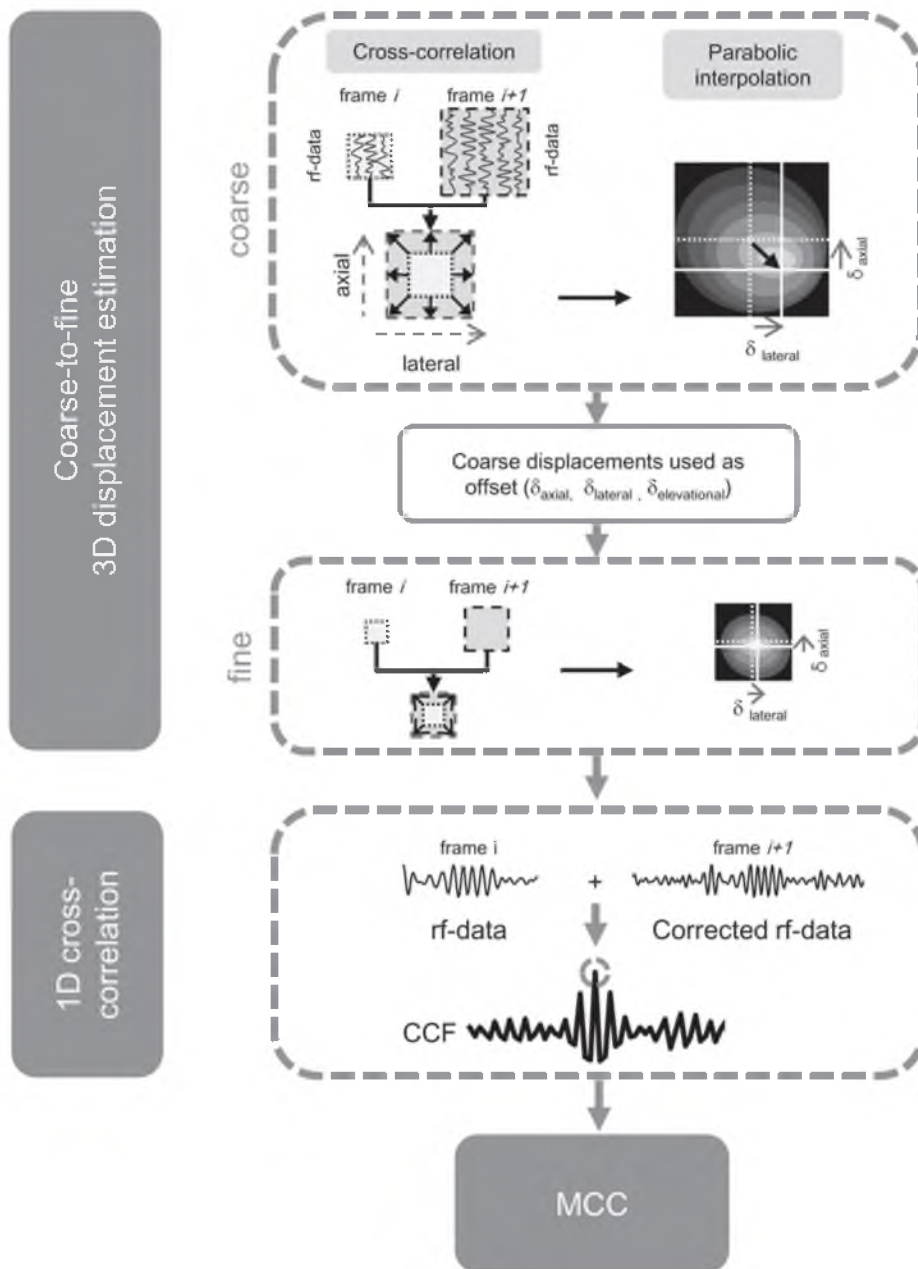


Figure 9.1 Schematic overview of the maximum cross-correlation computation method using a coarse-to-fine displacement algorithm. Three dimensional windows of data are cross-correlated between two consecutive echo volumes. Starting with a coarse window the maximum of the cross-correlation function yields global displacement estimates. These (coarse) displacement estimates are used iteratively as an offset to compute cross-correlations and displacement estimates at a finer scale. In the final step, the maximum of the cross-correlation in 1D is computed to obtain more accurate maximum cross-correlation values. It should be noted that in this schematic overview all 3D computations are depicted in 2D for clearness' sake.

**Table 9.1 Settings and window sizes used in the coarse-to-fine MCC estimation algorithm.**

|  | Coarse<br>(3D MCC)              | Middle<br>(3D MCC)             | Fine<br>(3D MCC)               | Fine<br>(1D MCC)                 |
|--|---------------------------------|--------------------------------|--------------------------------|----------------------------------|
| Used data  | Envelope                        | Envelope                       | RF-data                        | RF-data                          |
| Axial window<br>(frame $t$ )                     | 5 mm                            | 2.5 mm                         | 2.5 mm                         | 2.5 mm                           |
| Axial window<br>(frame $t + 1$ )                 | 19 mm                           | 3.7 mm                         | 3.7 mm                         | 3 mm                             |
| Used data  | Envelope                        | Envelope                       | RF-data                        | RF-data                          |
| Lateral / Elevational<br>window (frame $t$ )     | 11 lines                        | 3 lines                        | 3 lines                        | 1 line                           |
| Lateral / Elevational<br>window (frame $t + 1$ ) | 21 lines                        | 11 lines                       | 11 lines                       | 1 line                           |
| Median filter<br>displacement<br>estimates       | 11 mm<br>x 7 lines<br>x 7 lines | 8 mm<br>x 7 lines<br>x 7 lines | 8 mm<br>x 7 lines<br>x 7 lines | None                             |
| Median filter<br>MCC estimates                   | None                            | None                           | None                           | 4.5 mm<br>x 3 lines<br>x 3 lines |

$$CCF(w, t, \tau) = \frac{\sum_{w \in K_w} [I_t(w) - \bar{I}_t][I_{t+1}(w + \tau) - \bar{I}_{t+1}]}{\sqrt{\sum_{w \in K_w} [I_t(w) - \bar{I}_t]^2 [I_{t+1}(w + \tau) - \bar{I}_{t+1}]^2}} \quad (9.1)$$

where  $w = (w_{ax}, w_{lat}, w_{elev})$  denotes the axial, lateral and elevational index and  $\tau = (\tau_{ax}, \tau_{lat}, \tau_{elev})$  denote the spatial shift between frames  $I_t$  and  $I_{t+1}$ . The maximum absolute shift  $\tau$  was limited, hereby limiting the maximum axial and lateral and elevational displacements that could be measured.  $K_w$  defines a symmetrical window centered around  $w$  and  $\bar{I}_t$  and  $\bar{I}_{t+1}$  indicate the mean values for the specified windows for  $I_t$  and  $I_{t+1}$  used in the CCF computation. Table 9.1 provides a detailed overview of all window dimensions

used in the CCF computations. The peak of the cross-correlation function within the search window revealed the displacement estimate  $\delta = (\delta_{ax}, \delta_{lat}, \delta_{elev})$  of a 3D segment of RF-data in the next time frame in 3D space:

$$\delta_{iter}(w, t) = \arg \max_{\tau} CCF(w, t, \tau) \quad (9.2)$$

The displacement estimation  $\delta_{iter}$  was further improved by parabolic interpolation of the CCF around the peak (Fig. 9.1).

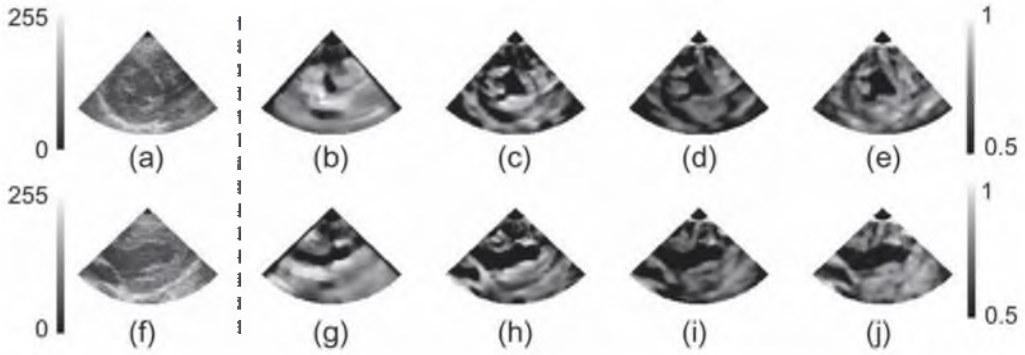


Figure 9.2 Maximum cross-correlation (MCC) images for the four iteration steps as described by the iterative 3D cross-correlation refinement algorithm. From left to right: Envelope data (log-compressed demodulated RF data, (a), (f)) and MCC values (median filtered) for iteration step 1 to 4: (b)-(e) (short axis view) and (g)-(j) (long axis view). The 2D planes shown are selected from a 3D full volume data set.

$$CCF_{1D}(w, t, \tau_{ax}, \delta) = \frac{\sum_{w \in K_w} [I_t(w) - \bar{I}_t][I_{t+1}(w + \tau + \delta_{iter-1}) - \bar{I}_{t+1}]}{\sqrt{\sum_{w \in K_w} [I_t(w) - \bar{I}_t]^2 [I_{t+1}(w + \tau + \delta_{iter-1}) - \bar{I}_{t+1}]^2}} \quad (9.3)$$

### *Iterative cross-correlation refinement*

Now we have obtained an initial displacement estimate, this displacement can be compensated for in the CCF computation in an iterative manner. By doing this, the cross-correlation values can be optimized and further refined. The displacement field  $\delta$  estimated in the previous iteration was used as an offset for the CCF computation: The iterative displacement estimation method was applied using a coarse-to-fine algorithm, as illustrated by figure 9.1 and 9.2. In the first iteration, the envelope data (*i.e.*, demodulated RF-data using the Hilbert transform) were cross-correlated using large windows (coarse) to obtain a coarse displacement field. In the second iteration, the window size was decreased (fine), enabling more precise displacement estimates at a higher resolution. The third iteration used the RF-data at a fine scale

enabling even more accurate displacement estimations because of the use of high-resolution phase information (Chapter 2 and 4). All displacement estimates were smoothed using a median filter. Detailed information on window sizes is given in Table 9.1. As a final step, the peak of the one-dimensional CCF in the axial direction (based on RF-data) was estimated. After compensation for the 3D local displacement field using 3D cross-correlations in the first three iterations, we used the 1D cross-correlation in the fourth iteration since this is a better representation of the actual correlation between the two consecutive volumes. Therefore, more precise and higher cross-correlation values are achieved using the 1D CCF. The maximal absolute axial shift was limited between -5 and +5 samples. The maximum of this 1D CCF was defined as the MCC parameter that was used as a novel feature in the segmentation process.

Finally, the MCC values were median filtered. Figure 9.2 illustrates the iterative cross-correlation refinement algorithm by showing MCC values for the four iteration steps in short and long axis views of the left ventricle.

### *3D Adaptive filtering*

Besides estimation of the maximum cross-correlation values, adaptive filtering was used as a more conventional method to optimize the distinction between blood and myocardium. 3D Adaptive Mean Squares filtering of the amplitude demodulated data was applied in the spatial domain (Nillesen et al. 2007b). The 3D filter window size was related to image speckle size and contained approximately  $5 \times 2 \times 2$  (axial x lateral x elevational) speckles. The AMS filter incorporates knowledge about speckle statistics (Nillesen et al. 2008) of blood and myocardium in an adaptive manner: homogeneous regions are filtered strongly, *i.e.* speckle noise is reduced, whereas in inhomogeneous regions the degree of filtering is low, such that transitions between blood and myocardium are preserved. The AMS filter has been proven

to enhance the difference between echo-levels originating from blood and myocardial wall (Nillesen et al. 2007a), and to be effective for segmentation of 3D echocardiographic images when using gradient based deformable models (Nillesen et al. 2009).

### *Deformable Model*

A gradient-based deformable simplex mesh model (Delingette 1999) was used for segmentation of the left ventricle. A simplex mesh consists of a set of vertices that forms a discrete non-parametric representation of a surface in  $\mathbb{R}^3$ . In this model, each vertex of the mesh  $p_i = (x_i, y_i, z_i)$  is displaced in an iterative manner according to the discrete approximation of the Newtonian law of motion:

$$p_{i+1} = p_i + \alpha F_{int} + F_{ext} \quad (9.4)$$

$F_{int}$  is a regularization force and controls the smoothness of the surface (Delingette 1999).  $F_{ext}$  is an external force derived from the image data that steers the simplex mesh onto boundary structures. In this study,  $F_{ext}$  consists of an adaptive filtering based component (AMS) and the newly defined maximum cross-correlation component:

$$F_{ext} = \beta F_{gradAMS} + \nu F_{gradMCC} + \kappa F_{speedAMS} + \lambda F_{speedMCC} \quad (9.5)$$

Both AMS and MCC values were used to compute gradient and speed forces. The gradient force  $F_{grad}$  is defined as:

$$F_{grad\ force}(p_i) = \nabla \frac{1}{1 + \exp\left(-\frac{|\nabla G_\sigma * I_{force}(x_i, y_i, z_i)| - \zeta_{grad}}{\eta_{grad}}\right)} \quad (9.6)$$

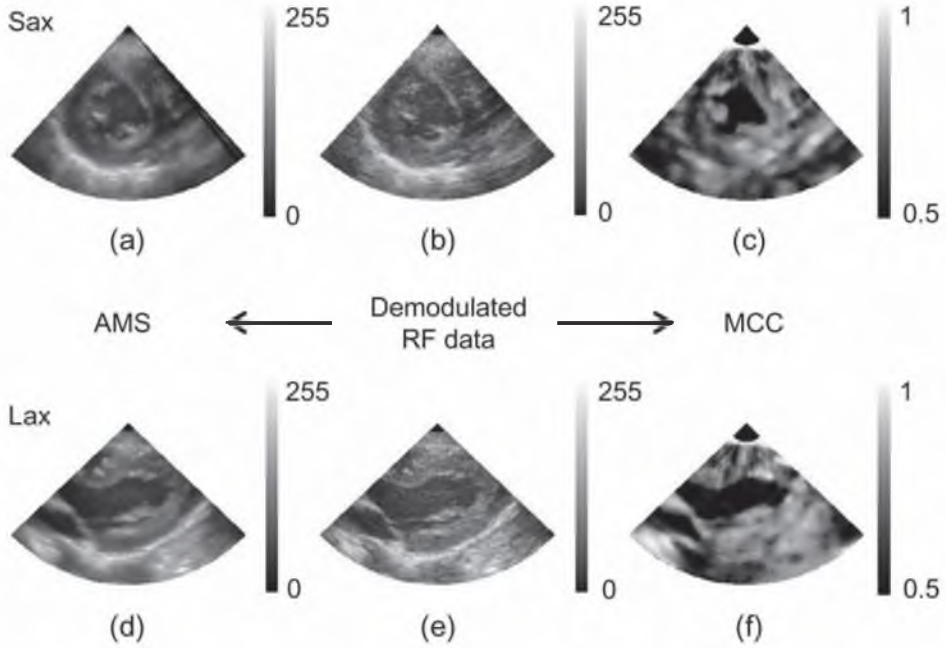


Figure 9.3 Short (upper panel, a-c) and long (lower panel, d-f) axis views from a full volume dataset. The demodulated RF-data (b,e) is used to compute the adaptive filtered data (a,d) and the maximum cross-correlation values (c f). Both AMS and MCC are used as external force in the deformable model.

where  $I_{force}$  stands for image intensity (echo level) of either the AMS image (force = AMS) or the MCC image (force = MCC). The parameters  $\zeta_{grad}$  and  $\eta_{grad}$  are used to scale the gradient magnitude to the interval  $[0, 1]$  by sigmoidal intensity mapping and are based on the minimum and average gradient magnitude value (Ibanez et al. 2003). Gaussian smoothing ( $G_\sigma$ ) with a relatively small  $\sigma$  (0.5 mm) is applied to increase the width of the attraction potential and to smooth undesired small gradients inside the left ventricular cavity.

$F_{speed}$  is a complimentary, inflating force, into the vertex normal direction and is defined as (Bottger et al. 2007):

$$F_{speed,force}(p_i) = \frac{1}{1 + \exp\left(-\frac{|\nabla G_\sigma * I_{force}(x_i, y_i, z_i)| - \zeta_{speed}}{\eta_{speed}}\right)} \quad (9.7)$$

The parameters  $\zeta_{speed}$  and  $\eta_{speed}$  are chosen such that  $F_{speed}$  has high values in regions with no gradient information and has low values at boundaries and lies between 0 and 1, in order to reduce the need for close-to-boundary initialization of the mesh.

Weighting factors  $\alpha$ ,  $\beta$ ,  $\nu$ ,  $\kappa$  and  $\lambda$  were used to balance the different forces. Whereas adaptive filtering and computation of the cross-correlation was performed by processing the data along the scan-lines, computation of the external and internal forces, as well as the deformation of the simplex mesh was performed on the data in scan-converted (*i.e.*, sector) format. Initialization of the mesh was done by interactive



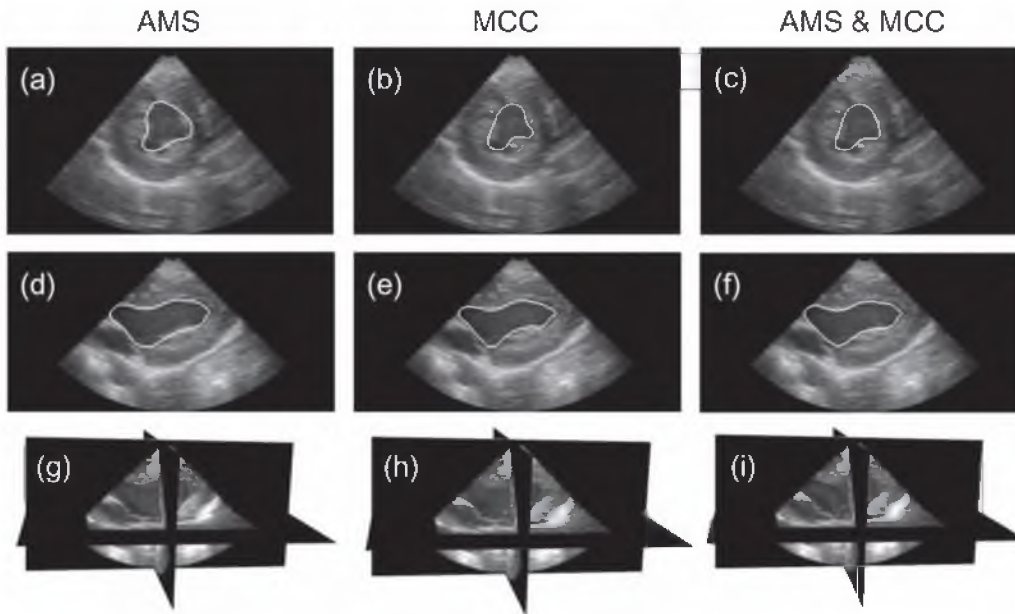


Figure 9.4 Segmentation results for a full volume dataset. Short axis (upper panel, a-c), long axis (middle panel, d-f) and 3D views (lower panel, g-i) are shown for the three different settings of the deformable model. From left to right: echographic data overlaid with contours of the segmented endocardial surface using 1) AMS, 2) maximum cross-correlation (MCC) and 3) an equally weighed combination of AMS and MCC force.

placement of a small spherical mesh in the center of the left ventricle. Figure 9.3 shows long and short-axis views from a full volume dataset for the two external force types of the model. In this figure, the original demodulated RF-data, the data after adaptive filtering and the maximum cross-correlation image are shown. Image data were visualized in scan-converted format, in order to obtain realistic anatomical views.

### *Evaluation*

The method was evaluated by comparing left ventricular cavity contours as obtained from the segmentation method with contours obtained from manual segmentation. Segmentation results of three different force types were compared: using AMS force

only (original model,  $\beta$  and  $\kappa \neq 0$ ,  $\nu = \lambda = 0$ ), using cross-correlation force only ( $\beta = \kappa = 0$ ,  $\nu$  and  $\lambda \neq 0$ ), and the combined model ( $\beta$  and  $\kappa$  and  $\nu$  and  $\lambda \neq 0$ ). In the combined model, AMS and MCC are equally weighed forces. For each dataset, the same initial position of the mesh in the center of the left ventricle was used for all three methods.

Contours were extracted from the 3D volume segmented by the deformable model and compared to manual segmentation for long-axis views and short-axis cross sections. The endocardial surface was segmented manually by a trained observer for all data sets by drawing 2D contours for each axial-elevational plane (short-axis view). The observer was unaware of the automatically segmented contours. Papillary muscles were excluded from the left ventricular cavity. For each data set, a set of relevant Sax and Lax

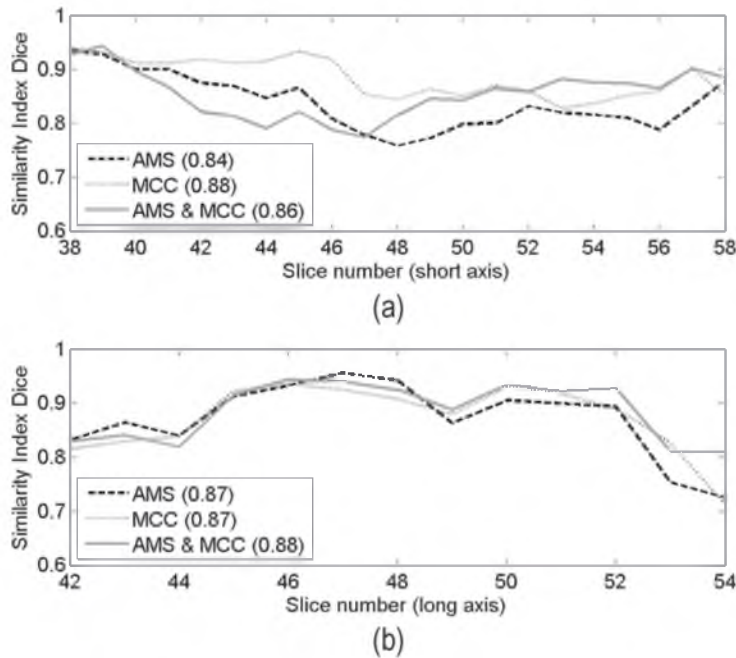


Figure 9.5 Similarity indices (SI) between automated and manual segmentation for the three different force types (AMS (solid), MCC (dotted), AMS & MCC (dashed)). 2D SI's for the relevant short axis planes (Fig. 4a) and long axis planes (Fig. 4b) are shown for a single dataset, cf. figure 3. Average SI's over all relevant planes are denoted within the brackets.

planes was defined. A plane was considered 'relevant' if it contained (part of) the left ventricle. Planes on the periphery of the left ventricle, where it was not possible to draw reliable contours, were left out. 2D similarity indices were computed for all relevant planes in the axial-lateral (Lax) and axial elevational (Sax) planes. The Dice coefficient (Dice 1945) was computed between manual ( $Ref$ ) and automatic segmentation ( $Seg$ ) to express similarity:

$$SI_{Dice} = \frac{2(Ref \cap Seg)}{Ref + Seg} \quad (9.8)$$

It should be mentioned that this similarity index was applied to 2D contours as well as to 3D volumes. Statistical analysis (Wilcoxon signed rank test) was performed

to test whether the 2D SI's for all relevant planes of all data sets were significantly different for the three force types.

## RESULTS

3D segmentation of the left ventricle was performed in full volume images obtained from ten healthy children in the end systolic phase of the heart cycle. Three different force types were tested using the deformable model for each dataset: AMS, MCC and an equally weighed combination of both.

Figure 9.3 shows characteristic Sax and Lax views from a full volume dataset for

**Table 9.2 Average 2D similarity indices (Dice) over relevant planes of the long axis and short axis views for the three different force types. For each data set the method with the highest average SI is denoted in bold.**

| Volunteer | Average 2D Similarity Index relevant short axis views (Sax) |             |             | Average 2D Similarity Index relevant long axis views (Lax) |             |             |
|-----------|---|-------------|-------------|--|-------------|-------------|
|           | AMS   | MCC         | AMS & MCC   | AMS  | MCC         | AMS & MCC   |
| 1         | 0.80  | 0.78        | <b>0.82</b> | 0.71   | 0.83        | <b>0.85</b> |
| 2         | 0.84  | <b>0.88</b> | 0.86        | 0.87   | 0.87        | <b>0.88</b> |
| 3         | 0.72  | 0.83        | <b>0.88</b> | 0.75   | 0.78        | <b>0.83</b> |
| 4         | <b>0.83</b>   | 0.82        | 0.80        | 0.77   | <b>0.81</b> | 0.74        |
| 5         | 0.72  | 0.67        | <b>0.82</b> | <b>0.81</b>  | 0.67        | 0.81        |
| 6         | 0.82  | 0.81        | <b>0.83</b> | <b>0.83</b>  | 0.78        | 0.82        |
| 7         | 0.83  | 0.78        | <b>0.86</b> | 0.83   | 0.78        | <b>0.84</b> |
| 8         | 0.80  | 0.81        | <b>0.83</b> | <b>0.79</b>  | 0.78        | 0.79        |
| 9         | 0.88  | 0.86        | <b>0.89</b> | <b>0.86</b>  | 0.85        | 0.84        |
| 10        | 0.78  | 0.73        | <b>0.79</b> | 0.76   | 0.77        | <b>0.79</b> |

the two external forces of the deformable model. In general the contrast between blood and the myocardium is higher for the maximum cross-correlation values than for the adaptive filtered data. MCC values also seem to yield better contrast between blood and myocardium in low echogenicity regions of the heart muscle, for example in the region where the muscle fibers are parallel to the ultrasound beam (cf. Sax view, compare Fig. 9.3a and 9.3c).

Figure 9.4 shows segmentation results for the three force types, AMS, MCC, and AMS combined with MCC. This figure depicts the scan-converted demodulated RF-data overlaid with contours of the segmented endocardial surface in Sax, Lax views as well as a 3D volume representation.

In order to perform a more thorough evaluation of the influence of the MCC on the segmentation results, 2D and 3D Dice

similarity indices (SI's) between automatic and manual segmentation were computed. 2D SI's for one data set (cf., Fig. 9.4) are given in figure 9.5. Average 2D SI's over all relevant planes are denoted in brackets for all three force types. Table 9.2 summarizes the average 2D similarity indices over all relevant planes of Lax and Sax views for AMS, MCC and the combination of AMS and MCC. As can be appreciated from this table, the most accurate segmentation was obtained by the combination of AMS and MCC. Especially in the Sax views, in 80% of the cases the combination of AMS and MCC outperforms segmentation based on AMS or MCC alone. In the Lax view, in 60% of the cases the segmentation using the combination is equally or more accurate than segmentation based on AMS alone.

A Wilcoxon signed rank test on the 2D SI's over all relevant planes of all datasets

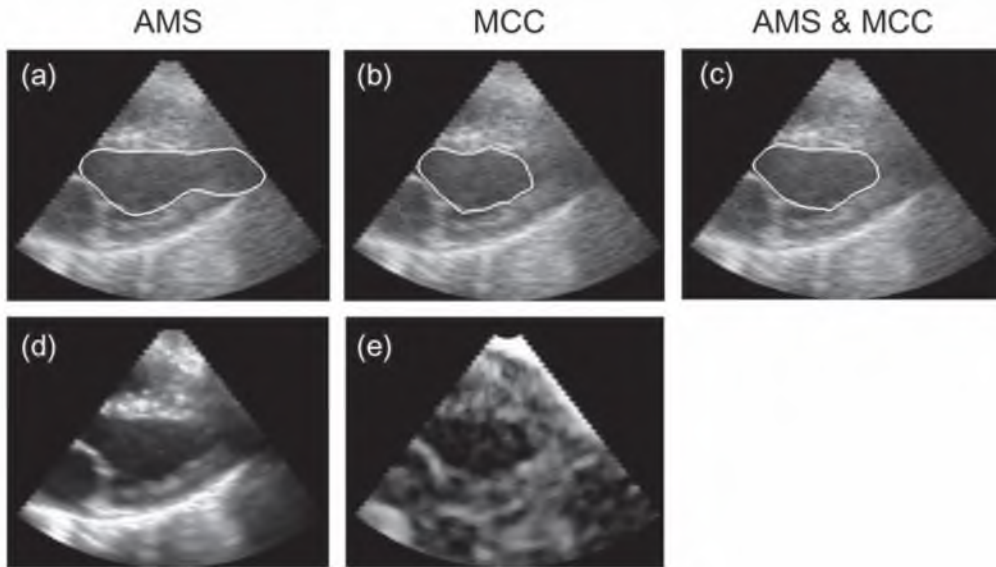


Figure 9.6 Typical example of oversegmentation of the left ventricle when only AMS values are used for segmentation (a). Addition of temporal information by using the MCC leads to improved segmentation in the apical region (b,c). The lower panel shows the AMS (d) and MCC (e) force to explain the differences in segmentation.

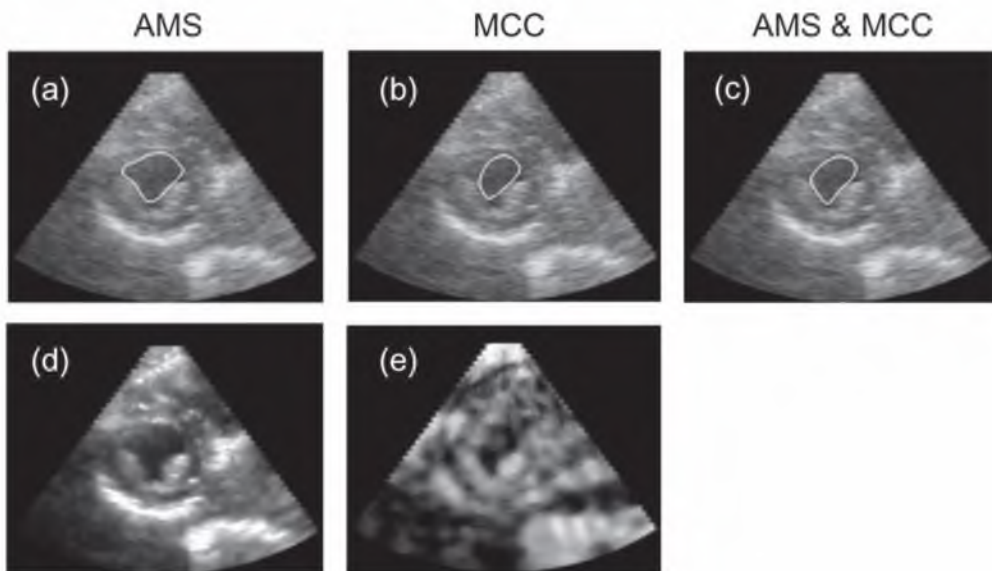


Figure 9.7 Typical example of inaccurate segmentation of the left ventricle when only MCC values are used for segmentation (a). In this case, addition of temporal information by using the MCC (b) does not improve the segmentation of the endocardium. The lower panel shows the AMS (d) and MCC (e) force to explain the differences in segmentation.

**Table 9.3 Average 3D similarity indices (Dice) for the three different force types. For each data set the method with the highest SI is denoted in bold**

| Volunteer | AMS         | MCC         | AMS & MCC   |
|-----------|-------------|-------------|-------------|
| 1         | 0.65        | <b>0.82</b> | 0.80        |
| 2         | 0.84        | <b>0.88</b> | 0.84        |
| 3         | 0.76        | 0.79        | <b>0.83</b> |
| 4         | 0.73        | <b>0.79</b> | 0.68        |
| 5         | 0.71        | 0.67        | <b>0.81</b> |
| 6         | 0.80        | 0.77        | <b>0.80</b> |
| 7         | 0.80        | 0.76        | <b>0.85</b> |
| 8         | 0.75        | <b>0.76</b> | 0.73        |
| 9         | <b>0.87</b> | <b>0.87</b> | <b>0.87</b> |
| 10        | 0.72        | <b>0.79</b> | 0.76        |

reveals significant improvement for the combination of AMS and MCC compared to segmentation based on AMS alone, as well for Sax views ( $n = 269$ ,  $p < 0.001$ ) as for Lax views ( $n = 131$ ,  $p < 0.05$ ). The combined force also significantly ( $p < 0.001$ ) outperforms segmentation based on the MCC force alone for both short and Lax views.

Furthermore, we compared the entire manually segmented 3D surface with the automatically segmented surface by calculating the 3D similarity index. Results are shown in Table 9.3. The 3D SI shows that compared to the use of the AMS force solely, the use of MCC values is advantageous, either as a force on its own or in combination with the AMS force. It should be noted that also planes that are very difficult to analyze are included within the 3D similarity measure and reference contours might be less reliable for these planes.

In figure 9.6 an illustrative example for segmentation of the Lax view is given that shows the additional value of the MCC in low echogenicity regions. It can be clearly

seen that for this dataset, segmentation exclusively based on the AMS data resulted in crossing boundaries at the apical side of the Lax view and thus led to overestimation of the left ventricular cavity. Addition of the MCC feature improved the segmentation results and yielded correct dimensions of the left ventricle. It can be concluded from this figure that the MCC (Fig. 9.6e) is still distinctive in the case of blood vs. myocardium in the apical region whereas the AMS filtered data is not (Fig. 9.6d). Similarity indices also reflect improved segmentation when using MCC values (SI AMS: 0.73, SI MCC: 0.87, SI AMS & MCC: 0.88).

Segmentation based on maximum cross-correlation can in some cases lead to incorrect results and underestimation of the endocardial dimension. This is illustrated by the MCC segmentation in figure 9.7 and reflected by the corresponding SI values (AMS: 0.91, MCC: 0.75, AMS & MCC: 0.81). Also in the combined force setting (AMS and MCC) the endocardial cavity is still underestimated.

## DISCUSSION

In this study, we investigated a method that enables segmentation of anatomical structures in pediatric hearts by incorporating temporal information. Temporal cross-correlation using the phase information present in the RF-signal was used as an additional feature to distinguish between blood and myocardium. The method was tested on 3D echocardiographic image sequences of ten healthy children and compared to a more conventional method that only uses echo-amplitude information.

Using the 3D iterative displacement estimation algorithm, the maximum temporal cross-correlation values were optimized and refined by each iteration step as illustrated by figure 9.2. This optimization procedure was necessary to obtain the deformation of the heart muscle in 3D and, after compensation for this 3D deformation field, to obtain accurate MCC values.

According to the preliminary results, maximum temporal cross-correlation values based on the RF-signal have additional value for the segmentation of cardiac tissue. Since correlation can still be high in (myocardial) regions with low echogenicity (and thus low contrast with blood), inclusion of this parameter in the deformable simplex model as an extra feature in general improves segmentation. Quantitative analysis using 2D image planes reveals that in the majority of cases the combination of the MCC and AMS outperforms segmentation using MCC or AMS only. Especially in the short-axis view, the combination is beneficial. This is probably related to the fact that in

short-axis views the ultrasound beams and the muscle fiber orientation are parallel in a significant part of the myocardium, resulting in low echogenicity. On the contrary, in the long-axis view only the apical region suffers from this artifact. As a result, only in 50% of the cases the combination improves the segmentation in the long-axis view.

A deformable model that only uses the cross-correlation force underestimated the blood pool region in some cases (Fig. 9.6). This is most likely caused by the larger windows used in the calculation of correlation values and because of the blood close to the heart wall 'adhering' to the moving tissue, leading to a higher correlation values, *i.e.*, lower MCC contrast, in blood regions close to the endocardial border.

In high quality images (without low contrast regions), segmentation exclusively based on the AMS force already yielded accurate results. In these images, the MCC force did not have additional value or even led to slightly lower similarity indices in some planes, see for example the SI's for data set 9 in Tables 9.2 and 9.3. However, from the 2D and 3D similarity indices as shown already in Tables 9.2 and 9.3, we might conclude that on average, the MCC force does improve the segmentation results. It should be noted that these tables show only average SI's, while improvement of the SI for individual planes demonstrates greater differences between the three force types (*e.g.* see Fig. 9.5a, short-axis views).

Presently, the MCC parameter has been tested in the end-systolic phase because of the limited frame rate of the used echomachine while imaging the entire left ventricle. The limited frame rate results in a limited

accuracy of cross-correlation in phases of the heart cycle with fast deformation of the heart muscle. Consequently, we firstly evaluated the performance in cardiac phases with small deformation of the heart muscle, *i.e.*, in the end-systolic or end-diastolic phase. However, with the introduction of the latest real-time 3D echocardiographic scanners increased frame rates seem to be a matter of time. For now, the cross-correlation based model could be used in the end-diastolic and end-systolic phases as a more robust initialization for segmentation of the other frames in the cardiac cycle. In future, the method will be extended to more frames during the cardiac cycle. Since the temporal behavior of blood is also not constant over the heart cycle, incorporation of this knowledge might be beneficial to improve the proposed approach.

The ECG gated full volume data sets used in this study comprise four to seven cardiac cycles to build up a complete volume. So-called stitching artefacts may occur due to inaccurate synchronization between two consecutive heart beats, because of heart rate variation or motion of the patient due to respiration. It is clear that this inaccurate synchronization between cardiac cycles will have a severe influence on the temporal cross-correlation values since these are calculated using 3D volumes. For this reason, full volume datasets that contain severe stitching artefacts are less suitable for MCC based segmentation. It should be mentioned that these stitching artefacts often cause disturbance of the geometry and outcome of these data cannot be used for quantitative analysis anyway.

Further research is required to investigate the optimal combination of echo-level and temporal information. In the combined force model that is currently used, AMS and MCC forces are equally weighed. A more sophisticated balance between these two forces might improve the segmentation results. This could be done by implementing a quality measure for transitions between blood and myocardium. For example, in high quality images with high contrast borders, the AMS force should dominate over the MCC force. In contrast, MCC values close to one should be relied on stronger than lower MCC values. Additionally, location specific weighting might be applied. For example in the apical region, the AMS based segmentation is generally worse than the MCC based one, in contrast to the septal wall that is normally better segmented using AMS values as external force. This information might be beneficial for improving the overall performance of a segmentation method using both MCC and AMS.

## **CONCLUSION**

In conclusion, temporal information present in the RF-signal yields a useful parameter to distinguish between blood and endocardial border in regions with low contrast in echogenicity. The MCC value improves segmentation in these regions but further investigation of this parameter is required to exploit the full benefit of it for automated segmentation.

---

# Part - III

---



---

# NON-CARDIAC APPLICATIONS

---

Handwritten text in a box, possibly a list or notes.



---

# CHAPTER 10

## 2D STRAIN IMAGING IN VESSELS

---

*Richard G.P. Lopata, Hendrik (Rik) H.G. Hansen, Maartje M. Nillesen,  
Johan M. Thijssen, Livia Kapusta & Chris L. de Korte*

---

Based on: **Non-invasive Carotid Strain Imaging Using Angular Compounding at Large Beam Steered Angles: Validation in Vessel Phantoms.** H.H.G. Hansen, R.G.P. Lopata and C.L. de Korte, *IEEE Transactions on Medical Imaging* 2009; 28(6), pp. 872-880.

---

## ABSTRACT

Stroke and myocardial infarction are initiated by rupturing vulnerable atherosclerotic plaques. With non-invasive ultrasound elastography, these plaques might be detected in carotid arteries. However, since the ultrasound beam is not aligned with the radial direction in which the artery pulsates, radial and circumferential strains need to be derived from axial and lateral data. Conventional techniques to perform this conversion have the disadvantage that lateral strain is required. Since the lateral strain has relatively poor accuracy, the quality of the radial and circumferential strains is reduced. In this chapter, the radial and circumferential strain estimates are improved by combining axial strain data acquired at multiple insonification angles. Adaptive techniques to correct for grating lobe interference and other artifacts that occur when performing beam steering at large angles are introduced. Acquisitions at multiple angles are performed with a beam steered linear array. For each beam steered angle, there are two spatially restricted regions of the circular vessel cross-section where the axial strain is closely aligned with the radial strain and two spatially restricted regions (different from the radial strain regions) where the axial strain is closely aligned with the circumferential strain. These segments with high quality strain estimates are compounded to form radial or circumferential strain images. Compound radial and circumferential strain images were constructed for a homogeneous vessel phantom with a concentric lumen subjected to different intraluminal pressures. Comparison of the elastographic signal-to-noise ratio (SNRe) and contrast-to-noise ratio (CNRe) revealed that compounding increases the image quality considerably compared to images from 0° information only. SNRe and CNRe increase up to 2.7 dB and 6.6 dB, respectively. The highest image quality was achieved by projecting axial data, completed with a small segment determined by either principal component analysis or by application of a rotation matrix.

## INTRODUCTION

Strain imaging is a well known ultrasound technique for estimating the elastic properties of tissue (Ophir et al. 1991). One of the fields in strain imaging research that gained a lot of interest during the last decade is vascular strain imaging, with a focus on atherosclerosis (van der Steen et al. 1998; de Korte and van der Steen 2002b). Atherosclerosis is a systemic disease that causes arteries to thicken, due to the deposition of atherogenic lipoproteins in the vessel wall. Most people in Western society suffer from atherosclerosis when they age, however, atherosclerosis in itself is not dangerous (Davies 1996). Atherosclerosis becomes life-threatening when a plaque ruptures, and a blood clot is formed as part of the body's healing process. In most of the cases this blood clot does not occlude the artery at the site of rupture, but is transported distally by the blood flow towards the heart, or brain, where it might occlude a smaller artery, resulting in a cardiac infarct, or in a stroke, respectively. Therefore, the vulnerability of a plaque is a measure for the risk caused by atherosclerosis. Vulnerable plaques are characterized by a large lipid pool, that often contains large amounts of macrophages, surrounded by a thin fibrous cap (Schaar et al. 2004). The pulsating blood pressure exerts forces on the thin cap, which can lead to rupture. This usually happens at the spots of highest strain (Cheng et al. 1993), which makes ultrasound elastography a very promising candidate for detection of the vulnerable plaque.

Carotid atherosclerosis is strongly related

to coronary and cerebrovascular disease (O'Leary et al. 1999). Previous studies, in which an intravascular catheter is used to perform strain imaging, have confirmed the high sensitivity and specificity of ultrasound elastography for detecting vulnerable plaques *in vitro* (Schaar et al. 2003) and *in vivo* (de Korte et al. 2002a). The intravascular approach however has some large practical drawbacks: it is invasive, expensive and can only be applied to patients that already undergo surgical intervention. If it would be possible to convert this technique into a non-invasive technique, all of these disadvantages would be overcome, allowing the technique to be applied on a broad scale, perhaps even for screening purposes. Hence, a non-invasive technique for detection of vulnerable plaques in the carotids will have a high clinical impact.

In recent studies (Maurice et al. 2004; Ribbers et al. 2007), the feasibility of transcutaneous ultrasound strain imaging of the carotids has been investigated. It was shown (Maurice et al. 2004; Ribbers et al. 2007) that non-invasive strain imaging of the carotids is feasible. However, in contrast to intravascular strain imaging, in the non-invasive case the ultrasound beam is not aligned with the radial strain for the complete vessel cross-section. Therefore, the axial and lateral strains need to be estimated and converted into radial and circumferential strains afterwards. Axial and lateral strains can be estimated in a number of ways; by cross-correlation of pre- and post-compression data (Ribbers et al. 2007), or by application of a Lagrangian speckle motion model estimator (Maurice and Bertrand 1999; Maurice et al. 2004). In both approaches,

the relatively poor quality of the lateral estimates, due to the lower resolution and the lack of phase information, restricts the image quality of the reconstructed radial and circumferential strains.

This study investigates a new approach to obtain radial and circumferential strain images of higher quality by combining strain data non-invasively obtained at large beam steered angles. The approach is based on the fact that there are regions (circle segments) of a vessel cross-section in which the radial strain and the ultrasound beam, or the circumferential strain and the ultrasound beam, are closely aligned. In those regions the radial or circumferential strain estimates are mainly dependent on axial strain input. In other words, the distortion caused by lateral strain input in these circle segments is small. With beam steering techniques (Rao et al. 2006), it is possible to change the ultrasound beam direction and thereby the segments in which the ultrasound beam and radial or circumferential strain estimates are aligned. By combining these circle segments of high quality strain estimates, obtained at different angles, it should be possible to construct radial and circumferential images of high quality for the entire vessel cross-section. A number of studies can be found that also perform angular compounding to improve the signal-to-noise ratio as well as the contrast-to-noise ratio of ultrasound images (Lacefield et al. 2004) as well as of strain images (Techavipoo and Varghese 2005; Rao et al. 2006). However, usually only small angles up to 15° of steering are used to construct compound strain images, whereas the proposed approach uses beam steering at larger angles up to 45 degrees.

Furthermore, the proposed compounding technique consists of combining different regions of strain data acquired at multiple angles, whereas the aforementioned studies image a single region from multiple angles and combine the data to improve the image quality in that region. One of the major difficulties that arises when performing beam steering at large angles, are artifacts caused by grating lobes. Grating lobes are secondary ultrasound beams caused by diffraction of the array transducer, when the element pitch of the array is larger than half the wavelength. The reflection and scattering generated by the secondary beam is interpreted as if it originated from the main beam, which causes the generation of artifacts on the ultrasound image. In clinical images the artifact is present in the entire image, whereas in a simple phantom experiment the artifact appears local.

This chapter describes and compares various methods to construct full 360° radial and circumferential strain images from non-invasively obtained radio frequency (RF) data at large insonification angles by means of a vessel phantom experiment.

## **MATERIALS**

A homogeneous vessel phantom was made of a 8% gelatin (Dr. Oetker, Ede, The Netherlands) solution with 3% Agar (Agar Agar CMN, Boom, Meppel, The Netherlands), and 1% SiC scatterers (9 to 15  $\mu\text{m}$ , E. Merck, Darmstadt, Germany). To create the solution, water was heated to 60°C, and

8 grams of gelatin, 3 grams of Agar and 1 gram of scatterers were added. The mixture was boiled and stirred until a homogeneous solution of 100 grams remained. During cooling to room temperature, the resulting solution was degassed by a vacuum pump and poured into a cylindrical mold with an outer radius of 6.5 mm. The 'lumen' was created by central placement of a metal rod with a radius of 1.5 mm. The resulting wall thickness of 5 mm is equal to the wall thickness of the vessel phantom used in intravascular experiments performed earlier by our group (de Korte et al. 1997a). The mould with solution was placed in a refrigerator at 6 °C for one night.

The next day, the phantom was placed in a tank filled with a 2.95% saline solution. The lumen of the phantom was attached to a pressure column filled with the same saline solution on one side, and to a closed valve on the other side as illustrated previously (Ribbers et al. 2007). Remaining air bubbles in the lumen were removed by opening of the valve and flushing with the solution. The pressure column was used to impose different intraluminal pressures on the phantom. The room temperature was 21.6 °C during the experiment. The saline solution was used to reduce previously reported artifacts (Ribbers et al. 2007) caused by refraction of the ultrasound beam at the liquid-phantom transition areas due to speed of sound differences between the two media (Thompson et al. 2004). The speed of sound in gelatin at 21.6 °C is about 1520 m/s (de Korte et al. 1997b), which also is the speed of sound in a saline solution of 2.95% at 21.6 °C (Kleis and Sanchez 1990).

## METHODS

### *Data Acquisition*

RF-data of the phantom were obtained with a Philips Sonos 7500 ultrasound machine equipped with an RF interface (Bothell, WA, USA). Measurements were performed with a linear array transducer (Philips, 11-3L) with a central transmit frequency of 7 MHz and a bandwidth of 3 to 11 MHz. The RF-data were sampled at 39 MHz. Cross-sectional data were obtained with the transducer mounted facing downwards to the phantom. Measurements were carried out starting at a 10 mmHg intraluminal overpressure. At this intraluminal pressure, RF-data were recorded at the followinginsonification angles; 45, 30, 15, 0, -15, -30, and -45 degrees. Next, the pressure difference was increased with 4 mmHg and post-compression images were recorded at the mentioned beam steered angles. This procedure was repeated for eight different cross-sections of the vessel phantom, resulting in eight datasets with a pressure difference of 4 mmHg between pre- and post-compression. A pressure difference of 4 mmHg was applied, since it results in strains ranging from -1.5% to +1.5%, which corresponds to the interframe strain range measured *in vivo* in the carotid (Schmitt et al. 2007). Furthermore, the pressure step applied and the strain range achieved also correspond to the intravascular vessel phantom experiments (de Korte et al. 1997a). This enables us to compare the current non-invasive experiments with the previous intravascular experiments. The procedure took approxi-

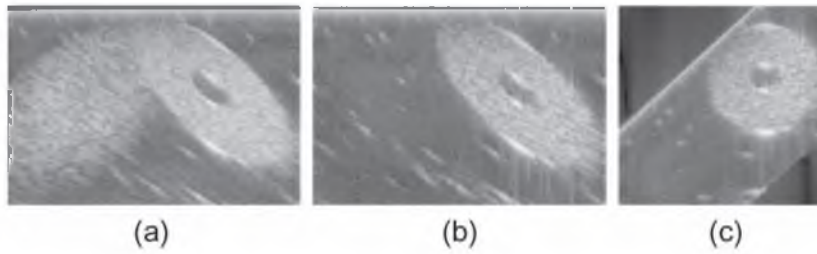


Figure 10.1 Artifacts in B-mode echogram due to large beam steered angle. (a) unfiltered skewed B-mode echogram obtained at a  $45^\circ$  insonification angle showing a grating lobe artifact, (b) same image after application of a low-pass filter for the removal of grating lobes, (c) same image as (b) with correction for skewness.

mately 16 minutes ( $\sim 2$  minutes for each cross-section).

### *Pre-processing*

Before the strain algorithm was applied to the pre- and post-compression datasets a number of corrections were carried out on the RF-data:

- In general, in ultrasound imaging an average speed of sound in tissue of 1540 m/s is assumed. This has several consequences, especially when compounding images obtained at various insonification angles. When the speed of sound in the examined tissue is lower than 1540 m/s, as is the case for this phantom material, each RF pulse will have a longer traveling time, which will be interpreted as an echo coming from a larger depth. Over- or underestimation of the speed of sound also gives rise to another artifact that appears when beam steering is performed. To transmit the ultrasound beam at a certain angle, a specific delay is calculated for each transducer element. This delay is inversely proportional to the assumed speed of sound. Overestimation of the speed of sound, *i.e.*, a lower speed of sound in reality, results in an underestimation of the time delays. This means, that the ultrasound beam will be transmitted at a smaller angle in reality, than the imposed angle. The larger the angle, the larger the mismatch caused by the speed of sound difference (Krucker et al. 2004). Since the real sound speed is known for the used setup, the data were scaled accordingly, and the angle was corrected (Hansen et al. 2009).
- Grating lobes are secondary ultrasound beams emitted in directions other than the electronically steered direction. The scattering caused by this secondary beam is received by the transducer and interpreted as originating from the main beam, which gives rise to the appearance of artifacts. An example of a grating lobe artifact for the used setup is shown in figure 10.1a. Each line of RF-data of the phantom measurements was low-pass filtered with an angle dependent cut-off frequency, of course at the cost of spatial resolution. The larger the insonification angle, the lower the cut-off frequency of the applied low-pass filter (Hansen et al. 2009). The effect of low-pass filter-



ing for the removal of the grating lobe artifacts at 45° beam steering can be appreciated from figure 10.1b

- Finally, an additional processing step is required before strain estimation techniques are applicable. This processing step only applies to the RF-data acquired at non-zero beam angles. Normally, when measuring without beam steering, the sample points of each RF-line form a rectangular grid with the sample points of the next RF-line. However, due to the beam steering, the RF-data is stored in a rectangular grid, while it contains sample points acquired at an angle. This causes the image to be a skewed representation of reality, as can be observed in figures 10.1a and 10.1b. To reshape the skewed data to right-angled data, each RF-line is shifted by a certain number of points, compared to the next RF-line. Because the shift is usually not an integer, a spline interpolation is performed (Hansen et al. 2009). This interpolation is carried out in one dimension (1D) instead of two dimensions (2D), to preserve RF phase information. The result of unskewing the data is shown in figure 10.1c.

### *Strain Estimation*

Before applying the strain algorithm, a region of interest (ROI) is selected with the same inner radius as the phantom, but with a slightly smaller outer radius, to avoid possible boundary artifacts. This ROI is rotated for each insonification angle to make sure that the same region is selected for the data

measured at all insonification angles.

The lateral and axial displacements are calculated in an iterative coarse-to-fine process, as described in (Chapter 2). Per iteration, the displacements are globally estimated by 2D cross-correlation of windows of the pre- and post-compression data. The ‘coarsest’ pre-compression window length used was 128 points and the ‘finest’ 16 points. Each window had an overlap with the next window of 50%. For a window length of 16 points this results in a resolution of approximately 150  $\mu\text{m}$ . By fitting a 2D parabola through the cross-correlation peak value and its nearest neighbors, the displacements can be more precisely estimated. In an additional iteration the displacement estimates are used to align the pre- and post-compression windows at sub-sample and sub-line level to obtain even better displacement estimates. The lateral displacements resulting from each iteration were filtered with a 2D median filter of 7x7 data points. Displacement values in the axial direction were filtered with a median filter of 5x5 points. Lateral and axial strain values were obtained using a 1D least-squares strain estimator (LSQSE, Kallel and Ophir 1997) with a window length of 9 samples. In a final step, local temporal stretching is applied (Chapter 2): RF signals of the ‘finest’ post-compression windows are rescaled according to the previously determined strain values and then the displacement and strain estimation is repeated. Due to the stretching of the post-compression windows, the cross-correlation peak can be detected more accurately, and as a consequence, the accuracy of the displacements and strains also increases.

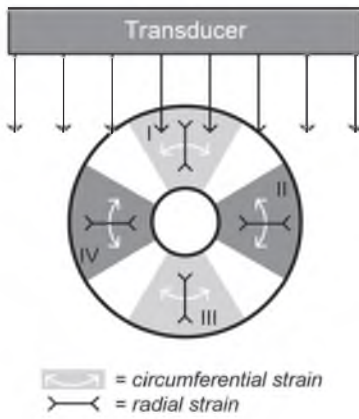


Figure 10.2 Schematic overview of the vessel cross-section and the radial and circumferential strain directions relative to the ultrasound beam at a zero degree insonification angle. In regions I and III the radial strain is approximately directed in the axial direction and the circumferential strain in the lateral direction. In regions II and IV exactly the opposite is the case.

Lateral and axial strains need to be converted to radial and circumferential strains since the latter two are rotationally symmetric for a cylindrical structure: for a certain distance to the lumen centre the radial strain will be equal for all angles, whereas the axial and lateral strain values change from positive to negative or vice versa for each quarter of the cross-section (Ribbers et al. 2007). Three methods for calculating radial and circumferential strains from axial and lateral strains are investigated. The first method is principal component analysis (Waldman et al. 1985). Principal strains are defined as normal strains along the axes of deformation, where shear strains are zero. For a concentrically deforming isotropic homogeneous cylinder, these axes are in the radial and circumferential direction. To obtain the principal strains, the estimated strain tensor is transformed into a symmetrical tensor. The positive and negative eigen values of this symmetrical tensor represent the circumferential and radial strain, respectively.

The second method (Lee et al. 2007) makes use of a rotation matrix to rotate the symmetrical strain tensor,  $E_{xy}$ , into the polar strain tensor,  $E_{rc}$ :

$$E_{rc} = \begin{bmatrix} \epsilon_{rad} & \epsilon_{shear} \\ \epsilon_{shear} & \epsilon_{circ} \end{bmatrix} = M^T E_{xy} M \quad (10.1)$$

with: 
$$M = \begin{bmatrix} \cos \theta & -\sin \theta \\ \sin \theta & \cos \theta \end{bmatrix}$$

where  $\theta$  is the angle between the ultrasound beam and the radial strain, which is calculated with respect to a manually selected reference point that corresponds to the center of the lumen. The diagonal values of  $E_{rc}$  represent the radial and circumferential strains.

The third method estimates the radial and circumferential strain by projection of the axial and lateral strains. A plane strain condition is assumed, which was shown to be a valid assumption for a concentric homogeneous vessel phantom and seems to be a reasonable assumption for the *in vivo* case, regarding the low strains measured *in vivo* in the direction of the vessel axis (Ribbers et al. 2007). In regions I and III (Fig. 10.2) the radial strain is closely aligned with the ultrasound beam and therefore, the axial strain is a fair approximation of the radial strain. In these regions the lateral strain is equivalent to the circumferential strain. In regions II and IV it is exactly the opposite. The projection results in an underestimation of the actual radial and circumferential strains, which can be corrected for (de Korte et al. 1999).

Regions I and III:

$$\epsilon_{rad,xx} = \frac{\epsilon_{xx}}{2 \cos^2 \theta - 1}$$

and

$$\epsilon_{circ,yy} = \frac{\epsilon_{yy}}{2 \cos^2 \theta - 1} \quad (10.2)$$

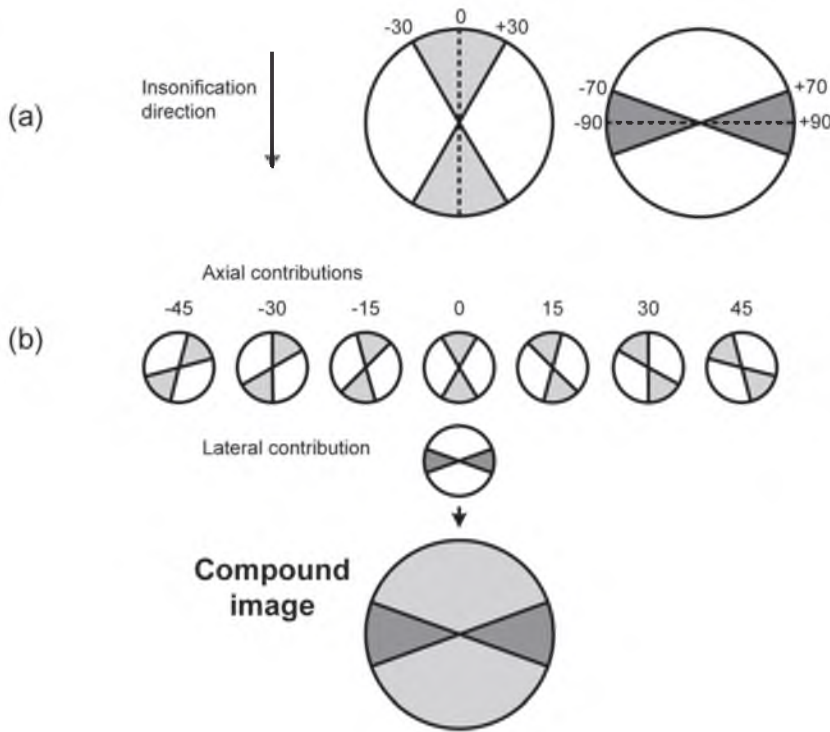


Figure 10.3 Schematic overview of the construction of a compound radial strain image from radial strain data obtained at multiple insonification angles. From all insonification angles the radial strain in the region between  $-30^\circ$  and  $+30^\circ$  with respect to the ultrasound beam is used for the construction of the compound image. Because it is not possible to construct a full  $360^\circ$  compound image from this information, smaller segments calculated from mainly lateral strain data obtained at  $0^\circ$  steering are added.

Regions II and IV:

$$\epsilon_{circ,xx} = \frac{\epsilon_{xx}}{2 \sin^2 \theta - 1}$$

and

$$\epsilon_{rad,yy} = \frac{\epsilon_{yy}}{2 \sin^2 \theta - 1} \quad (10.3)$$

where  $\epsilon_{i,j}$  are the estimated strains. The first index of  $\epsilon$  indicates whether the radial or circumferential strain is estimated, the second index explains whether the axial,  $\epsilon_{xx}$ , or the lateral strain,  $\epsilon_{yy}$ , was used for the projection.

### Compounding

Once the circumferential and radial strains are determined, compound images of the radial and circumferential strains obtained at multiple insonification angles are constructed. The compounding method for a radial strain image is visualized in figure 10.3. For each insonification angle, the radial strain data in circle segments of  $-30^\circ$  to  $+30^\circ$  with respect to the insonification direction are selected for contribution (Fig. 10.3a).

As pointed out in the previous section, the radial strain closely resembles the axial strain in these segments and is, therefore, more accurately approximated than in segments which require

more lateral strain input to construct radial strains. The segments acquired at the multiple angles are all reoriented as if they were obtained at a  $0^\circ$  insonification angle. For instance, the segments selected at the maximum insonification angle of  $+45^\circ$  will contribute data from  $+15^\circ$  to  $+75^\circ$  to the compound image, and the segments selected at  $+30^\circ$  will contribute from  $+0^\circ$  to  $+60^\circ$ . In the regions where the segments overlap, the strain values are averaged. Figure 10.3a shows the compounding schematically. Figure 10.3b also shows that it is not possible to construct a full  $360^\circ$  compound image from the described segments. The compound image is completed by adding two smaller segments ( $40^\circ$  opening angle) of radial strain estimates determined from  $0^\circ$  data. It should be remarked that the radial strain estimates in these segments are of poorer quality because they are mainly determined by the lateral strain. For the construction of the compound circumferential strain images, segments perpendicular to the segments chosen for the radial strain image are selected.

For each dataset a reference radial and circumferential strain image is constructed from data acquired at the  $0^\circ$  insonification angle only. Principal component analysis is used to obtain these images (Ribbers et al. 2007), thus enabling a comparison between the present multi angle and previous single angle approach. For each dataset also five compound radial and circumferential strain images are constructed using different methods. Compound images are constructed from segments calculated by; principal component analysis, the rotation formula, projection of axial and lateral

strains, a combination of projection of axial strains and principal component analysis, and a combination of projection of axial strains and the rotation formula.

Due to the cylindrical geometry and homogeneity of the phantom, theoretically the radial strain values are negative and equal at equal distances,  $r$ , from the centre of the lumen. The circumferential strain values are positive and equal at equal distances  $r$ . Furthermore, the absolute strain decays proportionally to  $1/r^2$ , as described by (de Korte et al. 1997a). Due to this circle symmetric decay it is possible to calculate elastographic signal-to-noise, SNRe, and contrast-to-noise ratios, CNRe, in decibels for the reference and compound images, using points located on circles around the lumen centre. The circles are located at 3 and 5 mm with respect to the lumen centre for the CNRe, and 3 mm for the SNRe. The strain values on the circle were estimated by 2D linear interpolation of the data.

The SNRe and CNRe values of the various compounding methods were compared with one another, with the reference images and with the previous intravascular experiments (de Korte et al. 1997b). Paired t-tests were performed to confirm the difference and statistical significance was defined as  $P < 0.05$ .

CNRe is usually used to quantify target detectability in elastography (Techavipoo and Varghese 2005). A more general definition of CNRe is used in this study: the ability of a technique to distinguish two homogeneous regions with different levels of strain, in this case a circle with high strain values close to the lumen, and a circle with lower strain values more distal to the lumen.

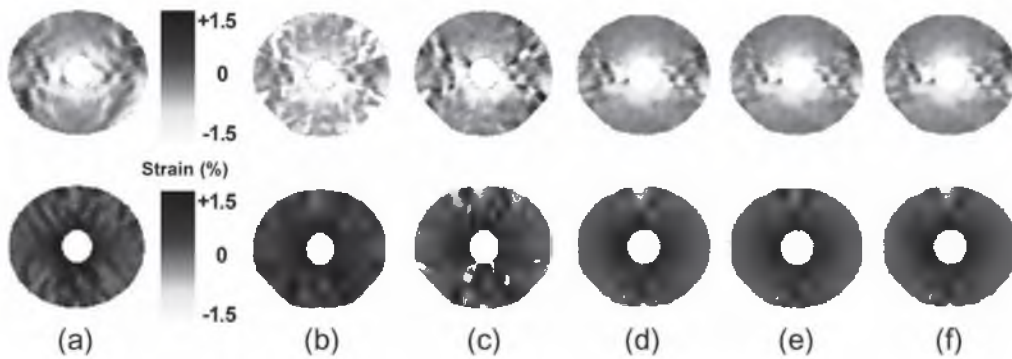


Figure 10.4 Radial (top row) and circumferential (bottom row) strain images for a concentric homogeneous vessel phantom. (a) the radial, and circumferential strain images calculated by principal component analysis from  $0^\circ$  data only. (b)-(f) the compound radial and circumferential strain images constructed by; principal component analysis, application of the rotation matrices, projection of axial and lateral strain, projection of axial strain completed with a segment of principal component analysis, projection of axial strain completed with a segment obtained from the rotation matrices.

## RESULTS

The constructed radial and circumferential strain images for the first dataset are shown in figure 10.4. In figure 10.4a the reference images are shown. On the right of the color bar are the compounded images. Figure 10.4b represents the compound images estimated by combining segments of principal strain data. The other subplots are constructed by using the rotation matrix (c), by projecting axial and lateral strain (d), and by projecting axial strain and adding a segment of principal strain (e), or rotational strain (f). It should be recalled that projecting strain is only an option for small projection angles and is therefore useful only, when constructing a compound image. As can be observed, the radial strain is negative and the circumferential strain is positive, corresponding to compression and expansion of the tissue in these regions, respectively. The increase in intraluminal pressure

causes the phantom to be compressed from the inside to the outside, in other words, negative strain values will be resulting in the radial direction. The diameter is increasing by the increased intraluminal pressure, causing extension of the material in circumferential direction. Due to the plane strain assumption, the circumferential strain has to be the opposite of the radial strain.

The circular symmetry, as predicted by theory, is also clearly visible. Although a small area with unexpected strain values is present between 5 and 7 o'clock in the circumferential strain images. It should be noticed that the size of this erroneous area is smaller for the compound images. The three rightmost radial and circumferential compound images that were constructed by projection of mainly axial data, show a much better circular symmetry than the reference images.

Mean and standard deviations of the SNRe and CNRe values for the reference images calculated from the eight datasets

**Table 10.1 SNRe and CNRe values for the reference images and the compound strain images constructed with the five methods.**

|                               | <b>Method</b>          | <b>SNRe (dB)<br/>mean ± std</b> | <b>CNRe (dB)<br/>mean ± std</b> |
|-------------------------------|------------------------|---------------------------------|---------------------------------|
| <b>Radial strain</b>          | Ref. principal         | 7.7 ± 1.8                       | 6.6 ± 4.2                       |
|                               | Principal strain       | *5.1 ± 3.5                      | *-1.5 ± 3.6                     |
|                               | Rotation matrix        | *4.9 ± 2.8                      | 6.7 ± 5.2                       |
|                               | Projection only        | 8.4 ± 1.9                       | *12.0 ± 4.3                     |
|                               | Projection & principal | *8.9 ± 1.8                      | *13.1 ± 4.2                     |
|                               | Projection & rotation  | *8.8 ± 1.9                      | *13.2 ± 4.0                     |
| <b>Circumferential strain</b> | Ref. principal         | 7.0 ± 1.7                       | 6.4 ± 3.2                       |
|                               | Principal strain       | 5.9 ± 1.8                       | *-8.4 ± 5.9                     |
|                               | Rotation matrix        | *3.4 ± 2.0                      | *-4.2 ± 7.1                     |
|                               | Projection only        | *9.1 ± 1.7                      | *10.5 ± 4.0                     |
|                               | Projection & principal | *9.7 ± 1.4                      | *11.6 ± 3.4                     |
|                               | Projection & rotation  | *9.6 ± 1.4                      | *11.6 ± 3.5                     |

\*Outcome of paired t-test <0.05 when compared to reference image

using 0° data only, are shown in Table 10.1. The mean and standard deviations of the SNRe and CNRe values of the compound strain images are also shown in Table 10.1. Improvements or reductions in SNRe or CNRe of the compound images compared to the reference images that were found to be significant are marked with an asterisk.

In general, the images of highest quality are obtained when the projection formula is used to construct the major part of the image. Significant contrast-, and signal-to-noise ratio increases up to 2.7 dB, and 6.6 dB are observed respectively. SNRe and CNRe increase significantly when instead of projecting lateral strains, principal component analysis, or the rotation method is used to complete the compound radial strain image (paired t-test,  $P < 0.05$ ). The differences in SNRe and CNRe between the

images completed with principal component analysis and the rotation method, are not significant (paired t-test,  $P > 0.05$ ). The compound images constructed by the rotation matrix and by principal component analysis are of poorer quality than the reference images.

## DISCUSSION

Compounding allows the construction of radial strain images with higher quality than can be determined from zero degree information only. Primarily, the higher quality is obtained because the images are mainly based on axial strain, instead of on axial and lateral strain. The lateral strain

estimate has a lower SNRe than the axial strain estimate (Chapter 2; Konofagou et al. 2000a). Furthermore, in this circular geometry, erroneous lateral strain values are found in some regions (at 5 and 7 o'clock in this phantom) due to the aforementioned refraction artifact (Thompson et al. 2004). The ultrasound lines are redistributed in space due to this effect, and this redistribution changes when the intraluminal pressure increases. Since the lateral strain estimate assumes a non-changing distribution of ultrasound lines, an artifact is observed in the lateral strain images in these regions. Despite of the use of the saline solution to limit the acoustic impedance mismatch between liquid and gelatin, the artifact is still present, however, to a lesser amount than in case water would have been used (Ribbers et al. 2007).

Because the artifact is mainly observed in the 5 to 7 o'clock area of the lateral strain image and not in the axial strain image, the artifact is primarily present in the circumferential strain images. In contrast to the compound radial strain images, the artifact is also present in the compound circumferential strain images, since these are completed by adding circumferential strain values that are determined mainly from the erroneous lateral strain values in the 5 to 7 o'clock area. The artifact is also present in the not compounded radial and circumferential strain images. This is probably because these images were estimated by principal component analysis, which uses lateral as well as axial strain input to reconstruct the radial and circumferential strains for the entire cross-section.

As aforementioned, the SNRe and CNRe

values of the compound circumferential strain images that are calculated by principal component analysis or the rotation method, are lower than the SNRe and CNRe values of the reference images. This reduction in SNRe and CNRe is probably due to the fact that not only lateral strains obtained without beam steering, but also at up to  $45^\circ$  and  $-45^\circ$  degrees steering are contributing to the image. At these large insonification angles an increased amount of filtering is required to remove the grating lobes, which results in a lower resolution. Hence, these lateral strain estimates are probably less accurate than those obtained without beam steering. Furthermore, the 5 and 7 o'clock artifact, that was observed in the lateral strain image of the 0 degree situation, rotates when the beam steered angle is changed. Consequently, the artifact is distorting the entire bottom half of the circumferential, but also of the radial compound strain images obtained by principal component analysis or application of the rotation matrix (Fig. 10.4).

Since the images constructed by application of the projection formula require much less lateral strain input than the images constructed by principal component analysis, the rotation matrices, and the reference images, it makes sense that the image quality is best for those images.

The increase in SNRe and CNRe when principal component analysis or the rotation method is used to complete the compound radial strain image, instead of projecting lateral strains (Table 10.1), might be explained by the fact that in the latter case pure lateral information is used, whereas in the other cases also axial information is

added to estimate the radial strains. It is disputable whether principal component analysis or the rotation method should be used to complete the compound image. The rotational method requires the selection of a center of reference with respect to which a rotation is carried out, which is not required for principal component analysis. Therefore, the use of the rotational formula ascertains that the calculated radial strain is really the strain in the radial direction with respect to the chosen center. The minimum eigen value obtained by the principal component analysis does however not necessarily represent the strain in the (exact) radial direction. An artifactual negative strain value in circumferential direction could easily be regarded as radial strain by the principal component analysis. This incorrect 'attenuation' of artifacts is probably the reason why the SNRe and CNRe are higher for the images that were completed by principal component analysis.

For *in vivo* application, which implies that mainly inhomogeneous and asymmetrical structures are investigated, the use of principal strains is discouraged. The principal strain directions would then also differ from the radial and circumferential directions.

Rao et al. (Rao et al. 2006) described angular compounding of axial strain data obtained at various beam steered angles for a cylindrical inclusion phantom, and reported increases in SNRe and CNRe of 3 dB and 10 dB respectively. Although smaller increases were found in the current study, the value of the comparison is to be doubted, because of essential differences between both techniques, and because

different phantoms were used in the studies. Rao et al. uses angular compounding to improve the quality of the axial strain image for one part of the phantom, whereas the current study combines radial or circumferential strain estimates in different phantom regions, calculated from acquisitions at different angles, to construct a compound radial or circumferential strain image of high quality for a larger region. The image quality does not improve further when performing beam steering at angles larger than 10° when using the first technique (Rao et al. 2006), due to increasing decorrelation of the pre- and post-compression RF-data. Because the regions of interest in the current study are chosen in such a way that the investigated strain rotates with the beam steering angle, the decorrelation effect is counteracted, and it is possible to increase image quality by adding data obtained at beam steering angles of more than 10 degrees.

Using an intravascular transducer de Korte et al. found SNRe and CNRe values of +6.3 dB and -2.3 dB respectively. These values were calculated from figure 1 in (de Korte et al. 1997a). Thus, the current multiple angle approach even outperforms the intravascular approach that was performed with a transducer with a center frequency of 20 MHz. The large increase in CNRe of about 9 dB, when comparing the intravascular results to our results, can probably be ascribed to the more sophisticated strain algorithm and the improved quality of the ultrasonic equipment. The strain algorithm has been improved by implementing a 2D instead of 1D cross-correlation, a coarse-to-fine approach, an aligning procedure, and local temporal stretching. Finally, it



should be noticed that although the current phantom contained more Agar than the phantom used intravascularly, the measured strains were in the same range. The Young's modulus of the phantom was also similar to that of the intravascular experiments. By fitting a  $1/r^2$  curve through the strain data and then solving the theoretical relation for the strain as function of the radius (Ryan and Foster 1997) a Young's modulus of 32 kPa was found. The Young's modulus of the intravascular phantom was reported to be about 30 kPa. The agreement of the Young's moduli despite of the differences in Agar content is probably due to differences in preparation and the used measurement method.

The compounding of segments is now performed by straightforward averaging in the regions of overlap. Making use of the fact that the strain estimate quality diminishes when the angle increases, due to the increased amount of filtering applied, the application of weight functions to the various contributions will probably increase the quality of the compound strain images further. The reduction in frequency band for larger angles could also be taken into account by adapting window sizes of the 1D LSQSE, and the median filters.

For the compounding technique to be applicable *in vivo*, it would be ideal if the same cross-section could be measured at the multiple insonification angles before and after compression. However, since the carotid is moving and pulsating this is probably not possible. ECG or blood pressure triggering to obtain images of the cross-section at similar moments at different angles during subsequent heartbeats would be required.

Tracking of the deforming tissue might also be useful to reduce movement errors. Of course, it can be expected that not all motion artifacts can be corrected for, which will result in less improvement in SNRe and CNRe than observed in the current *in vitro* study. However, it is likely that the reduction in improvement is rather small, since IVUS elastography has shown that it is possible to construct strain images of a cross-section of a pulsating artery with an ultrasound probe that was mounted on a freely moving catheter (de Korte et al. 2002a).

The selection of the region of interest and of the point of reference, with respect to which the projections are carried out, was currently performed manually. However, automated segmentation of the boundary between lumen and arterial wall seems feasible (Brusseau et al. 2004). Segmentation of the peri-adventitia might be performed using this method, or using similar approaches such as currently developed for cardiac imaging (Chapter 9). Automatic calculation of the center of gravity from this segmented luminal contour (Shapo et al. 1996) could then serve as point of reference for the projections.

Recently, we could show (Hansen et al. 2007), that the quality of the strain images increased, when more angles were added to the compounding. Due to the non-stationarity *in vivo*, it will only be possible to perform the acquisitions for one angle per heartbeat. Investigation of the minimum selection of angles that enables the construction of compound strain images with acceptable quality and whether the radial strain profile remains reproducible during those acquisitions is required. Furthermore, due

to the different imaging depth of the carotid artery *in vivo*, there will probably be a limit on the maximum beam steering angle that can be used. The maximum angle will have to be determined, and if required segment sizes will have to be increased. Additionally, dedicated transducers might be developed for imaging deeper arteries.

The speed of sound was homogeneous in the used setup. However, *in vivo* this will not be the case. Presumably, this will necessitate assuming (based on anatomy) or determining regions of equal sound speed within the tissue, which might even be possible in an automated manner (Napolitano et al. 2006). The RF corrections for skewness, grating lobes, and speed of sound, would then have to be carried out separately for all different regions. Dividing the image in two regions of homogeneous sound speed: one corresponding to the fat layer between skin and artery, and one corresponding to the vessel wall and lumen, might perhaps be sufficient to deal with most of the speed of sound problems.

Finally, it should be noticed, that with IVUS elastography it is only possible to estimate circumferential strains by deriving them from lateral information (*i.e.* perpendicular to the ultrasound beam), since the ultrasound beams are transmitted in the radial direction. With the non-invasive compounding approach, radial as well as circumferential strains can be reconstructed from mainly axial data. A proper estimation of radial as well as circumferential strain is expected to enable a more correct reconstruction of elastic moduli (Baldewsing et al. 2004a-b).

## CONCLUSION

It is possible to construct compound radial and circumferential strain images from RF-data obtained at multiple large beam steered angles ranging from  $-45^\circ$  to  $45^\circ$ . Compounding increased image quality with approximately 2 dB in SNRe and 6 dB in CNRe compared to the radial and circumferential strain images obtained without beam steering. The compound images of highest quality are constructed when mainly axial strain that is projected in radial or circumferential direction is used.



1. 2. 3. 4. 5. 6. 7. 8. 9. 10. 11. 12. 13. 14. 15. 16. 17. 18. 19. 20. 21. 22. 23. 24. 25. 26. 27. 28. 29. 30. 31. 32. 33. 34. 35. 36. 37. 38. 39. 40. 41. 42. 43. 44. 45. 46. 47. 48. 49. 50. 51. 52. 53. 54. 55. 56. 57. 58. 59. 60. 61. 62. 63. 64. 65. 66. 67. 68. 69. 70. 71. 72. 73. 74. 75. 76. 77. 78. 79. 80. 81. 82. 83. 84. 85. 86. 87. 88. 89. 90. 91. 92. 93. 94. 95. 96. 97. 98. 99. 100.



---

# CHAPTER 11

## 2D STRAIN IMAGING IN MUSCLES: THE CLEFT LIP

---

*Chris L. de Korte, Nancy van Hees, Richard G. P. Lopata,  
Gert Weijers, Christos Katsaros & Johan M. Thijssen*

---

Based on: **Quantitative Assessment of Oral Orbicular Muscle Deformation after Cleft Lip Reconstruction: An Ultrasound Elastography Study.** C.L. de Korte, N. van Hees, R.G.P. Lopata, G. Weijers, C. Katsaros and J.M. Thijssen, *IEEE Transactions on Medical Imaging* 2009; 28(8), pp. 1217-1222.

---

## ABSTRACT

Reconstruction of a cleft lip leads inevitably to scar tissue formation. Scar tissue within the restored oral orbicular muscle might be assessed by quantification of the local contractility of this muscle. Furthermore, information about the contraction capability of the oral orbicular muscle is crucial for planning the revision surgery of an individual patient. In this chapter, we used ultrasound elastography to determine the local deformation (strain) of the upper lip and to differentiate contracting muscle from passive scar tissue. Raw ultrasound data (radio frequency format; RF) were acquired, while the lips were brought from normal state into a pout condition and back in normal state, in 3 patients and 3 normal individuals. During this movement, the oral orbicular muscle contracts and, consequently, thickens in contrast to scar tissue that will not contract, or even expand. An iterative coarse-to-fine strain estimation method was used to calculate the local tissue strain. Analysis of the raw ultrasound data allows estimation of tissue strain with a high accuracy. The minimum strain that can be assessed reproducibly is 0.1%. In normal individuals, strain of the orbicular oral muscle was in the order of 20%. Also, a uniform strain distribution in the oral orbicular muscle was found. However, in patients deviating values were found in the region of the reconstruction and the muscle tissue surrounding that. In 2 patients with a successful reconstruction, strain was reduced by 6 % in the reconstructed region with respect to the normal parts of the muscle (from 22% to 16% and from 25% to 19%). In a patient with severe esthetical and functional disability, strain decreased from 30% in the normal region to 5% in the reconstructed region. With ultrasound elastography, the strain of the oral orbicular muscle can be quantified. In healthy subjects, the strain profiles and maximum strain values in all parts of the muscle were similar. The maximum strain of the muscle during pout was 20%  $\pm$  1%. In surgically repaired cleft lips, decreased deformation was observed.

## INTRODUCTION

One out of 500 to 1000 babies is born with a facial cleft (Moss 2001). Cleft lip, with or without cleft palate, is the most common congenital malformation among facial clefts. The reconstruction of the upper lip and the restoration of the continuity of the circular muscle in the lip (oral orbicular muscle), which is performed at 2-6 months of age, is an important step in the treatment of these children. However, every surgical intervention leads inevitably to scar formation. The amount, position and appearance of the scar tissue strongly compromise the functional and esthetic outcome the primary lip repair. For this reason one or more revision operations are often necessary to improve esthetics and function of the upper lip. Residual deformities may vary from small esthetic irregularities such as slight asymmetry or scarring of the philtral area to major stigmata as shortening and flattening of the upper lip (Vegter et al. 1997). Furthermore, even residual malformation leading to functional disability may remain (Markus and Delaire 1993). The esthetic outcome of lip repair is usually judged clinically by visual inspection, while it is semi-quantitatively assessed using standardized photos in outcome studies (Nollet et al. 2007). Lip function is usually assessed subjectively by inspection, a method that has considerable drawbacks, since the extend of visible scarring influences the perception of impaired lip movement considerably (Ritter et al. 2002). The need for more objective measures to assess lip function is supported by a recent study, which showed poor agree-

ment among surgeons in judging the need for revision surgery of the cleft lip using photographs and videotapes (Trotman et al. 2007c). Mishima et al. (Mishima et al. 2004) and Trotman et al. (Trotman et al. 2007b) developed systems for three dimensional assessment of lip movements. However, these methods use information obtained from the outside of the lip and cannot give insight on the specific anatomical problem of the lip tissues. Therefore, a simple, convenient, and cost effective method to establish the quality of the reconstruction is required.

Ultrasound imaging, enables the visualization of different tissues in the healthy and reconstructed upper lip (Deng et al. 2000). The superficial epidermal layer yields a clear thin echo border and the loose connective tissue of the lip returns relatively bright echo values, whereas the deeper laying muscles are characterized by low echo levels. However, the characterization of the scar region and functionality of the muscle remains limited (Munshi et al. 2000), since the analysis is based on normal echograms. In particular, distinction between scar tissue and connective tissue or muscular tissue often remains difficult. The thickness of the muscle can be determined in both relaxed and contracted states, but published data show large variance in thickness increase and muscle size (Prabhu and Munshi 1995; Rasheed and Munshi 1996; van Hees et al. 2007).

Ultrasound elastography is a technique to quantify relative deformation of tissue using ultrasound and was first described in 1991 (Céspedes et al. 1993a; Ophir et al. 1991). Although in the first 10 years, this technique was mainly used for tumor detection, a tendency towards cardiac, vascular

and smooth muscular applications can be observed in the last decade (Céspedes et al. 2000; de Korte and van der Steen 2002b; Konofagou et al. 2002; Langeland et al. 2005a; Lee et al. 2007; Schaar et al. 2005). Elastography is based on acquiring multiple images of tissue while it is deforming. First the displacement is determined from subsequently acquired echo images. Next, the difference between two displacement estimates at different echo depths divided by the distance between these two depths is calculated for assessment of the strain (relative deformation). For an accurate estimation of the displacement, the raw ultrasound data containing both phase and amplitude information are used. The phase information is especially sensitive for minute displacements. A drawback of using the phase information is that only low deformation values can be measured. The maximum strain value that can be determined depends on the used frequency and required resolution, but is typically in the order of 2% between successive echo frames (Céspedes et al. 1999). Consequently, temporal resolution is an important issue. To properly track the tissue while it is contracting a frame rate of 30 to 100 images per second is required, depending on the rate of contraction. In contrast to most other diagnostic techniques, ultrasound offers this temporal resolution.

In this chapter, ultrasound elastography is used to assess the strain of lip tissue, especially of the oral orbicular muscle. The hypothesis is that scar tissue in surgically repaired cleft lips has a different strain pattern than the oral orbicular muscle of healthy subjects. Using elastography, the

absence of active contraction in parts of the oral orbicular muscle in reconstructed cleft lips, as well as reduced muscle function might be quantified.

## MATERIALS

Ultrasound data were acquired in three healthy volunteers (age range 24-30) and in 3 patients that underwent a surgical reconstruction of a unilateral (1 patient) or bilateral (2 patients) cleft lip. The patient with the reconstructed unilateral cleft had no functional disability and almost no esthetical malformation. One of the patients with the bilateral cleft had a successful repair with only moderate disability. The other patient had severe disability even after repeated surgical reconstruction procedures. All volunteers and patients signed an informed consent and the study was approved by the Ethical Committee of the Radboud University Nijmegen Medical Center.

## METHODS

Ultrasound data were acquired using a SONOS 7500 live 3D ultrasound system (Philips Medical Systems, Best, The Netherlands), equipped with an L3-11 (3-11 MHz) linear array transducer. The transmitted ultrasound pulse bandwidth was set at 7-11 MHz. The upper lip of the subjects was prepared by extruding approximately



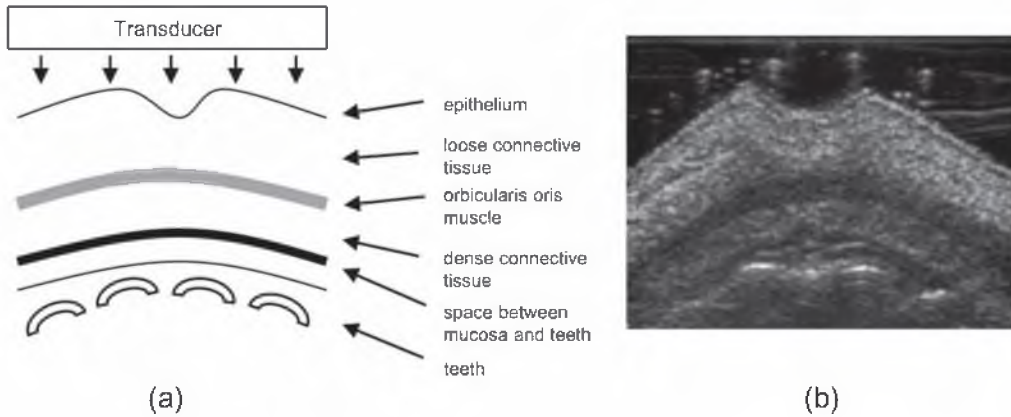


Figure 11.1 Scheme of application of ultrasound transducer on the upper lip. Left: scheme of the transversal image cross section. Right: Example of corresponding transversal ultrasound image of healthy subject.

a one-centimeter layer of commercial ultrasound coupling gel (Kendall Meditec, Mirandola (MO), Italy) over the full width of the upper lip. The transducer was carefully applied to this layer for making a transversal scanning plane while avoiding inclusion of air bubbles between transducer surface and gel (Fig. 11.1). In this way, the ultrasound beams are almost perpendicular to the muscle direction. The gel layer acted as an acoustic window and prevented direct contact between the lip and the ultrasound transducer.

The acquisition of ultrasound data started with the lip in a non-contracted state. During the acquisition, the subject was asked to slowly contract the lips by smoothly moving them into a pout condition and from this condition back to the initial non-contracted state without moving the lips forward or backward. A full acquisition took 3 seconds. The deformation of the lip is caused by contraction of the oral orbicular muscle, which is positioned in the upper and lower lip as a circular struc-

ture. Due to the contraction, this muscle will change its length and thickness. This deformation of the muscle and surrounding tissue is determined using ultrasound elastography.

The raw (RF) ultrasound data were sampled at 39 MHz in the ultrasound machine and transmitted using a USB 2.0 interface to a workstation using a custom made module (AFLINK, Philips Medical Systems). The frame rate while acquiring the ultrasound data was 40 images per second.

The strain was calculated between subsequent echo frames to prevent strain values larger than 2%. In this way, the decorrelation was kept low. For calculating the strain, the ultrasound data were divided into windows. In conventional strain estimation algorithms, first the displacement of tissue is determined from the time shift between two congruent ultrasound data window pairs taken from consecutive echo images and additionally the strain is calculated using these displacement estimates (Ophir et al. 1991). This time shift can be calcu-

**Table 11.1 Maximum strain values (%) in the different regions of the lip**

| Region | Normal 1 | Normal 2 | Normal 3 | Unilateral | Bilateral 1 | Bilateral 2 |
|--------|----------|----------|----------|------------|-------------|-------------|
| left   | 18.5     | 25.6     | 17.7     | 21.8       | 25.1        | 25.1        |
| middle | 19.6     | 22.3     | 17.8     | 22.0       | 19.7        | 5.7         |
| right  | 18.2     | 23.1     | 19.6     | 16.3       | 19.1        | 6.4         |
| scar   |          |          |          | 11.7       |             |             |
| mean   | 18.8     | 23.7     | 18.4     |            |             |             |
| sd     | 0.7      | 1.7      | 1.1      |            |             |             |

lated by using cross-correlation analysis. The position of the peak of the cross-correlation function represents the shift between the two windowed data. In this study, the displacement of the tissue was determined using a coarse-to-fine strain estimation method (Chapter 2). This method is based on initially calculating the displacement using a large window (2.5 mm). For an RF-based technique, an accurate displacement estimate using a relatively large window can only be determined if the strain is in the order of 1 to 2%, depending on the window size and ultrasound frequency used (Céspedes et al. 1999). However, by using the envelope of the ultrasound data, a reliable displacement estimate for larger strain values can be calculated (Varghese and Ophir 1998b). Therefore, initially, an envelope based correlation is applied using a relatively large window. In this way, the chance is minimized that the wrong peak of the cross-correlation function is taken, a problem frequently occurring using this technique. This coarse estimate is used as input for a displacement estimate using a smaller window and an RF-based technique. Since the tissue is not only moving along the ultrasound beams (axial direction) but also perpendicular to that (lateral direction),

the displacement is determined in axial as well as in lateral direction (2D). Although no lateral strain is calculated in this study, the lateral displacement estimate is used to improve the axial strain estimate (Chapter 2). The resolution of the coarse displacement estimate is increased by interpolating the peak of the correlation function with a parabola. By iteratively repeating this step in which the window size is decreased, a final window size of 0.6 mm is obtained with an error of the displacement estimate of 15  $\mu\text{m}$  (Chapter 2 - 4). Since the overlap between windows was taken 50%, a strain estimate for each 300  $\mu\text{m}$  was determined. Strain was calculated from the final displacement estimate using a least squares strain estimation (LSQSE) algorithm (Kallel and Ophir 1997). Finally, the deformation of tissue over the full cycle was constructed by cumulatively summing the strain data determined from subsequent echo images.

Quantitative analysis of the relative muscle deformation was performed by manually selecting the left, middle and right part. The average accumulated strain in these regions was plotted as a curve as function of time.

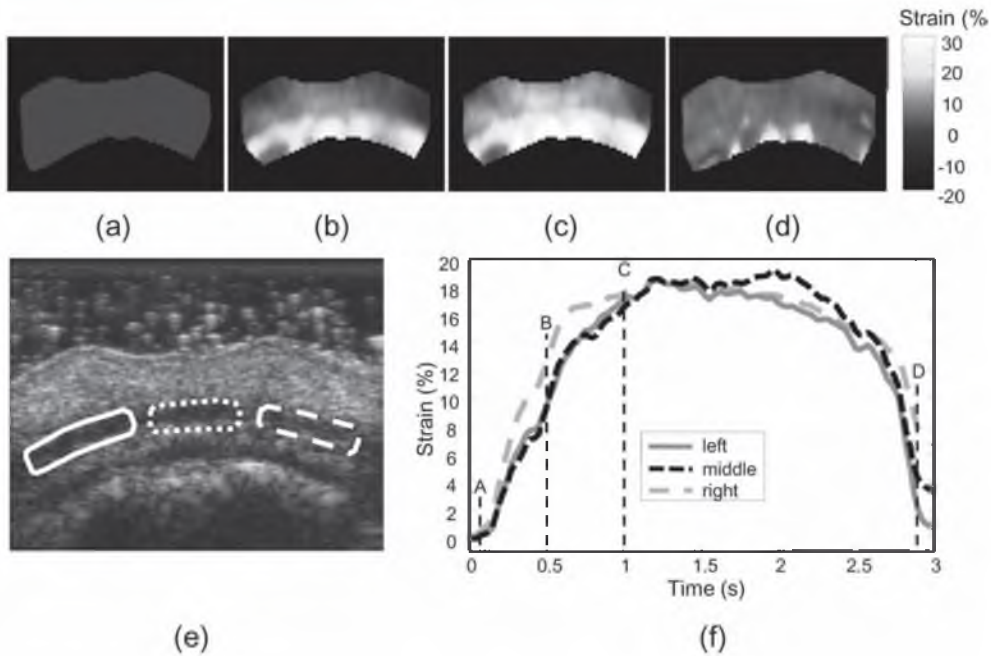


Figure 11.2 A-D: Strain images of a healthy lip during a contraction-relaxation sequence. The strain is color coded from zero (yellow) to 30% thickening (blue), and to 20% thinning (red). The thickening of the muscle is clearly visible. E: On the echogram three regions-of-interest (red, green, and blue) are selected within the orbicular oral muscle. F: The strain vs. time curves show similar thickening (up to 20%) for all three regions.

## RESULTS

The cumulative strain images acquired over the full cycle show positive strain values in the oral orbicular muscle from initial state to pout condition and strain values returning to zero after release of the pout condition and going back to initial state (Fig. 11.2). Positive strain values represent a thickness increase and this increase is related to the contracting oral orbicular muscle. While contracting, the muscle is getting shorter and consequently getting thicker.

Initially, the surrounding tissue is almost not deforming as illustrated by the low strain values (Fig 11.2b). However, the pout

condition also results in a smaller circumference of the mouth. This shortening of the tissue in the direction perpendicular to the strain estimate results in thickening of the tissue in the direction parallel to the strain estimate. This is visualized by the positive strain values in later stages of the cycle (Fig. 11.2c). Especially in the central part of the lip these positive strain values are found. In normal lips, similar deformation patterns and levels in the left, middle and right part of the muscle were observed (Fig. 11.2e). The strain profile and the maximum value of strain values were similar. In all normal subjects, a maximum strain value of around 20 % was found in all three parts of the lip (Table 11.1). The high correspondence between the three curves is demonstrated

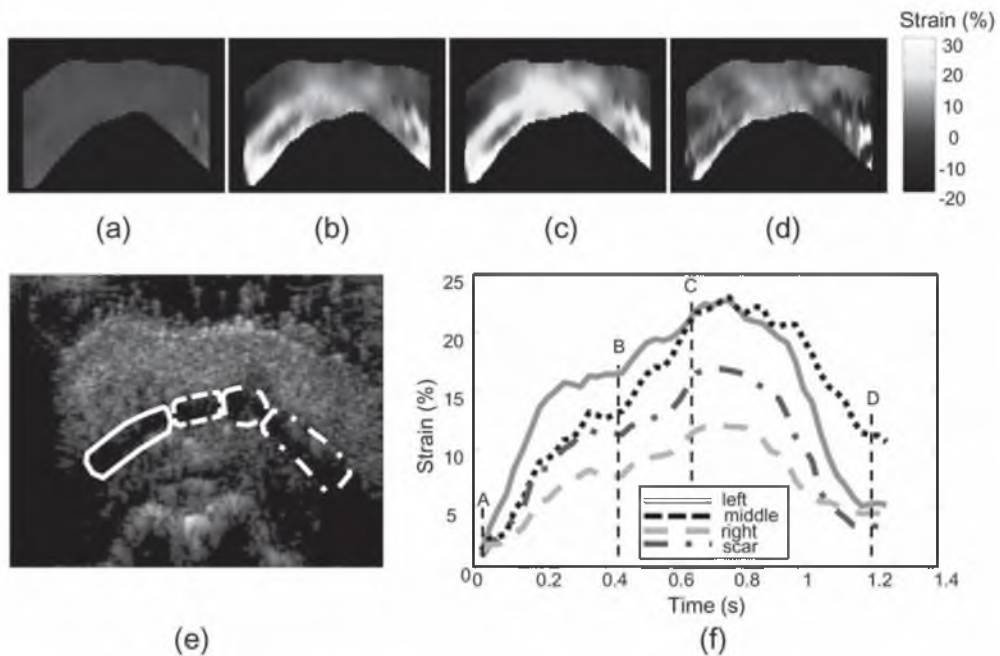


Figure 11.3 A-D: Strain images of a repaired cleft lip during a contraction-relaxation sequence. The strain is color coded from zero (yellow) to 30% thickening (blue), and to 20% thinning (red). E: On the echogram four regions-of-interest (red, green, purple and blue) are selected within the orbicular oral muscle. F: The strain vs. time curves show thickening (up to 30%) in the left (red) and middle (green) part of the lip, whereas reduced thickening (17%) is found in the right part of the lip (blue). In the scar region (purple) is even more decreased (12%).

by the similarity of the shape (Fig. 11.2e) and by the low standard deviation of the maximum strain value (Table 11.1)

In patients, strain patterns different from the normal strain patterns were obtained, depending on the rate of success of the surgical procedure. In a patient with a successful repair of a unilateral cleft lip, only a small deviation of the strain pattern was observed (Fig. 11.3). The region where this deviation was found was co-localized with a region with different echogenicity in the conventional echogram. However, in a patient with a surgically repaired bilateral cleft lip (bilateral 1), different strain patterns were found. The left side of the lip showed strain values of the oral orbicular muscle similar to normal

patients. However, it is clear that the middle and right part have lower strain values with respect to the left part. Although the repair seems to have succeeded in creating a united oral orbicular in this patient, the functionality of the muscle in these regions appears to be decreased.

In a patient with residual deformities and reduced functional properties (bilateral 2), no strain was observed in the middle and right side of the lip (Fig. 11.4). The left part showed a properly functioning oral orbicular muscle: strain values up to 25 % were found. However, the middle and right part of the muscle showed no deformation at all, except from a small drift up to 6 % strain.

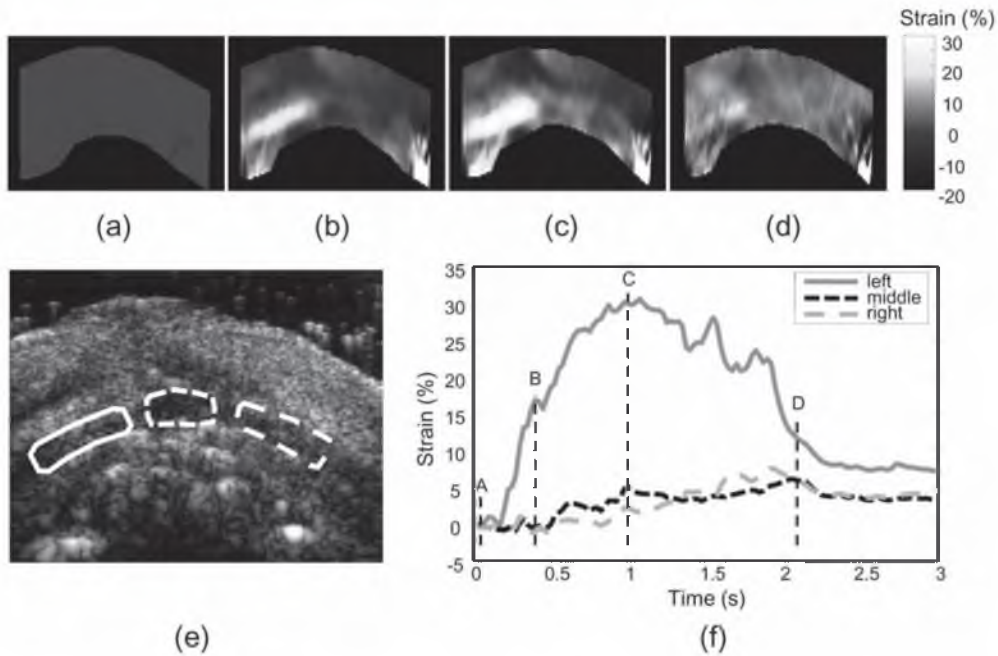


Figure 11.4 A-D: Strain images of a repaired left lip during a contraction-relaxation sequence. The strain is color coded from zero (yellow) to 30% thickening (blue), and to 20% thinning (red). E: On the echogram three regions-of-interest (red, green, and blue) are selected within the orbicular oral muscle. F: The strain vs. time curves show thickening (up to 30%) in the left part (red) of the lip, whereas reduced thickening (5%) is found in the middle and right part (green and blue) of the lip.

## DISCUSSION

In this study, an image of the strain of a cross-section of the lip was made. Using ultrasound elastography, the strain of the oral orbicular muscle was quantitatively determined. In contrary to conventional standardized photographs and films, information of the structures within the lip was obtained instead of information from the outside only. The principal findings of this study are:

1) Ultrasound elastography provides local quantitative information of the different parts of the oral orbicular muscle. In healthy volunteers, the strain profiles are similar for

all areas and the maximum strain was found to be around 20 %.

2) In patients with a reconstructed cleft lip, different strain profiles and different maximum strain values were found. In this pilot study, the deviation and the size of the area in which these deviating strain values were measured seemed related to the quality of the reconstruction.

Local quantitative strain information of the oral orbicular muscle was previously not available. Using conventional echography, changes in the thickness of the various tissues could be measured. In our previous study based on conventional ultrasound data (van Hees et al. 2007), the thickness of the oral orbicular muscle changed by 50 %

(from 2 to 3 mm). However, the standard deviation of the increase was 0.7 mm, indicating a large variance in the thickness estimate between subjects. Also, in other studies in which the thickness change of the muscle during contraction was investigated using conventional ultrasound, values ranging from -2% (Prabhu and Munshi 1995) to 37% (Rasheed and Munshi 1996) and even 50% (Vinkka-Puhakka et al. 1989) were reported. In all these studies, different methods for deformation of the muscle were used in subjects with different malformations. In the present study, all normal volunteers showed maximum strain values around 20% in the right, left and middle part of the muscle, although this number is based on a limited number of subjects. The small standard deviation ranging from 0.7 to 1.7 % strain illustrates the high quality of the estimate and the potential of ultrasound elastography to quantitatively determine the relative deformation. A thickness measurement is based on the outline of the muscle that can be easily obscured by out of plane motion and echo pattern changes, whereas the deformation of the whole cross-section of the muscle is used in elastography. Because a 2D imaging technique was used in this study, special care was taken to prevent out of plane motion during contraction and relaxation of the lip. In acquisitions of the volunteers with large in plane motion, strain images were deteriorated. In these acquisitions, the position of the different tissues was not stable and consequently the cumulative strain values did not correspond to a particular region but a region composed of muscle and connective tissue. This problem can be solved by automati-

cally tracking the tissue over the deformation cycle. Since displacement is already estimated, this information can be used to automatically track the tissue. The current progress in 3D echography allows even to compensate for out of plane motion.

The strain values are dependent on the angle between muscle fiber orientation and ultrasound beam direction. However, in this study no difference between the left, middle, and right regions of the muscle was found in healthy lips. A large scale prospective study currently performed will provide data on the difference between these regions and the necessity to correct for this.

The strain images provide information on the presence and absence of a thickening oral orbicular muscle. Where in the normal volunteers, the oral orbicular muscle can be identified throughout the lip from left though right, this pattern is not always apparent in patients with a reconstructed cleft lip. Although this study is a feasibility study based on a limited amount of patients, a relation between the severity of disability and the deviation of strain pattern from the normal situation is found. In a patient with a very successful unilateral cleft lip reconstruction, only a small deviation is present. In a small part, a less deforming region is present. So, although the repair of the muscle was successful and a closed structure was obtained, full recovery of the function was not achieved. In the patient with the repaired bilateral cleft, larger areas with reduced functionality were found. The right and middle parts of the oral orbicular muscle showed reduced deformation. However, also in this patient, partial recovery of the functionality of the muscle was

achieved. This is in contradiction to the patient with severe malformations who had reduced function of the lip even after repeated surgeries to correct esthetic malformations.

Our results explain the findings of Trotman et al. (Trotman et al. 2007c) who showed, using a video-based tracking system, that patients with a cleft lip exhibit less upper lip movements and greater asymmetry of mean upper lip movements relative to non-cleft individuals. The decreased strain locally observed in our cleft patients might be also associated with the greater contraction instability of the upper cleft lip measured by Trotman et al. (Trotman et al. 2007a). Using standardized photos or films, the effect of the reduced muscle function was measured previously (Trotman et al. 2007c), but no information on the actual function of the oral orbicular muscle was provided. In a follow up of this study, the force generated by the upper and lower lips was measured (Trotman et al. 2007a). Although reduced force was found in cleft lip patients, it is hard to determine the location with the reduced function. Using elastography, the absence of muscle function can be directly related to a specific region. In the study by Trotman and coworkers a compensatory force from the lower lip was found in cleft lip patients. In our study also a compensatory increased deformation of the non diseased side of the lip was found in the patient with almost no deformation in the diseased side.

Elastography of the lip may contribute to the objective assessment of treatment outcome as well as in the decision making procedure of the surgeon who is confronted with a compromised lip repair. Currently,

the esthetic and functional outcome of lip repair is usually judged clinically by visual inspection, a method that has considerable drawbacks, since the extent of visible scarring influences the perception of impaired lip movement considerably [5]. Because elastography yields information about the non-visible part of the lip, it will allow the surgeon to identify the in-depth location and the amount of the scar and it can give an objective picture of local tissue deformation. This information will help the surgeon to decide whether a lip revision might improve lip function, as well as to choose the least invasive operation technique for the specific patient. Since this study only describes the technique and first evaluation in a relative small number of people, larger scale prospective and retrospective studies are required to assess the full potential of the ultrasound elastography technique to aid the physician in evaluating the reconstruction and to improve the surgical technique.

## CONCLUSION

With ultrasound elastography the local relative deformation of the oral orbicular muscle can be quantified. In healthy subjects, the strain profiles in all parts of the muscle are similar. The maximum strain of the muscle is 20% +/- 1%. In surgically repaired cleft lips decreased strain was locally observed relative to 20% strain in healthy parts. In this preliminary study, the decreased strain values were related to the success of the reconstruction.





---

# CHAPTER 12

## BIPLANE STRAIN IMAGING IN MUSCLES: THE BICEPS

---

*Richard G.P. Lopata, Johannes P. van Dijk, Sigrid Pillen, Maartje M. Nillesen,  
Huub Maas, Johan M. Thijssen, Dick F. Stegeman & Chris L. de Korte*

---

Based on: **Dynamic Imaging of Skeletal Muscle Contraction in Three Orthogonal Directions.** R.G.P. Lopata, J.P. van Dijk, S. Pillen, M.M. Nillesen, H. Maas, J.M. Thijssen, D.F. Stegeman and C.L. de Korte, *Journal of Applied Physiology* 2010; *in press*

---

## ABSTRACT

In this study, a multi-dimensional strain estimation method using biplane ultrasound is presented to assess local relative deformation (i.e., local strain) in three orthogonal directions in skeletal muscles during induced and voluntary contractions. The method was tested in the m. biceps brachii of five healthy subjects for three different types of muscle contraction: 1) excitation of the muscle with a single electrical pulse via the musculocutaneous nerve, resulting in a so-called 'twitch' contraction; 2) a train of five pulses at respectively 10 Hz and 20 Hz to obtain a sub-maximum tetanic contraction; 3) voluntary contractions at 30, 60, and 100% of maximum contraction force. Results show that biplane ultrasound strain imaging is feasible. The method yielded adequate performance using the radio frequency (RF-) data in tracking the tissue motion and enabled the measurement of local deformation in both the vertical direction (orthogonal to the arm) and in the horizontal directions (parallel and perpendicular to direction of the arm) in two orthogonal cross-sections of the muscle. The twitch experiments appeared to be reproducible in all three directions and high strains in vertical (25 to 30%) and horizontal (-20% to -10%) directions were measured. Visual inspection of both the ultrasound data as well as the strain data revealed a relaxation that was significantly slower than the force decay. The pulse train experiments nicely illustrated the performance of our technique: (i) Similar patterns of force and strain waveforms were found; (ii) Each stimulation frequency yielded a different strain pattern, e.g., peak vertical strain was 40% during 10 Hz stimulation and 60% during 20 Hz stimulation. The voluntary contraction patterns were found to be both practically feasible and reproducible, which will enable muscles and more natural contraction patterns to be examined without the need of electrical stimulation.

## INTRODUCTION

For a long time, studying dynamic muscle properties in humans was the exclusive domain of mechanical measurements (external force and movement) and electrophysiology (electromyography, EMG). Imaging of skeletal muscles has been applied for more than three decades using different modalities, including MRI and ultrasonography (Mercuri et al. 2005; Peetrons 2002; Pillen et al. 2008). Apart from imaging of muscle anatomy, also quantification of translational movement and local deformation of muscle tissue will be of interest in fundamental and clinical questions. For these purposes, the high temporal resolution of more recent ultrasound equipment enables the investigation of dynamic image sequences, which provides information on the changes that occur within the muscle during contraction (Loram et al. 2006; Pillen et al. 2008). Hence, ultrasound imaging of muscles may give more insight in the process of force production and its dependency on muscle structure. This might be of use when studying force generation in primary muscle disorders such as muscular dystrophies, but also in connective-tissue diseases in which changes of the mechanical properties of muscle and connective tissue could influence force transmission.

Muscle contraction is known for its anisotropic behavior, *i.e.*, the deformation of the muscle is different in different directions. The complexity of skeletal muscle strain has been examined and shown with two-dimensional (2D) and three-dimensional (3D) finite element

modeling (Blemker et al. 2005; Chi et al. 2010; Oomens et al. 2003; Tang et al. 2009). However, most reports on strain imaging in skeletal muscles are limited to one or two dimensions and are, therefore, unable to reveal the 3D anisotropic behavior of the muscle. A multi-dimensional imaging modality is needed for a comprehensive mapping of muscle contraction. Since the distribution of muscle strain is known to be non-uniform (Blemker et al. 2005), such imaging should yield estimates of tissue strain locally.

Ultrasound “elastography” was introduced by Ophir et al. (Ophir et al. 1991) as a technique to estimate the mechanical properties of biological tissues and organs from the relative deformation, *i.e.*, strain. Local displacement is assessed by correlating segments of ultrasound data acquired sequentially (Ophir et al. 1991; Ophir et al. 1999). By calculating the first order spatial derivative of the displacement field(s), ‘strain images’ are obtained. Initially, the technique was used to visualize the distribution of strain within tissue under external compression in order to estimate the mechanical properties of tissues and organs (Céspedes et al. 1993; Krouskop et al. 1998; Ophir et al. 1999), *i.e.*, a passive deformation. More recently, strain imaging was also applied to data acquired in actively deforming tissue, such as the heart, to assess its function (D’hooge et al. 2000; Konofagou et al. 2002). A limited number of studies reports on strain imaging in skeletal muscles. One of the first *in vivo* efforts was performed with Doppler-based techniques (Grubb et al. 1995). Speckle tracking methods using the raw, radio frequency (RF) data were

applied to skeletal muscles, both *ex vivo* (Witte et al. 2004) and *in vivo* (Lopata et al. 2006; Witte et al. 2007). Several studies can be found on the ultrasonic measurement of aponeurosis strain (Maganaris and Paul 2000; Magnusson et al. 2003). A recent study by Deffieux et al. (2009) reported on 1D strain imaging, *i.e.* strain in the direction of the ultrasound beam, in 2D and 3D images of electrically stimulated muscles using an ultrafast (frame rate > 1000 Hz) ultrasound technique. Also in the field of MRI, both tracking of displacement as well as elastography of skeletal muscle have been reported (Dresner et al. 2001; Zhong et al. 2008). A study by Pappas et al. revealed the non-uniform shortening of the *m. biceps brachii* using cine phase contrast MRI (Pappas et al. 2002).

Ultrasound has several advantages over MRI, such as the bed side applicability, cost effectiveness and the high spatial and temporal resolution. However, there is a trade-off between spatial resolution, field-of-view and temporal resolution, which is especially evident in 3D applications. RF-based techniques have an optimal performance for strains between 0.1% and 5.0%. Consequently, the frame-rate has to be high to keep the frame-to-frame tissue deformation within that range. If the strain rate becomes too high, the accuracy and precision of the strain estimates will decrease rapidly due to significant de-correlation of the ultrasound data (Céspedes et al. 1999). Since the motion of the muscle and the deformation within skeletal muscles will be large, a relatively high frame rate of the equipment is required for ultrasound strain imaging. “Biplane” imaging is a fast

semi-3D imaging technique (frame rate = 25 - 120 Hz) that is commercially available. Besides that a relatively high frame rate can be achieved, the major advantage is the ability of acquiring data from two orthogonal planes simultaneously, yielding both a cross-sectional and longitudinal view of the muscle. Hence, the deformation can be assessed in three orthogonal directions during muscle contraction.

The primary goal of this study was to develop a multi-dimensional, non-invasive technique to track rapid muscle motion and to measure local tissue deformation (*i.e.*, strain) accurately in three orthogonal directions. A biplane strain imaging method is proposed that uses the RF echo-data to estimate tissue deformation. The method is applied to the human *m. biceps brachii* during both voluntary and electrically-induced contraction. The latter will result in a controlled reproducible contraction, whereas the former will be easier to perform and be less demanding in clinical practice.

## MATERIALS

### *Experimental Setup*

Five healthy male subjects, free of any neurological complaints, were recruited (age 22 – 44 years) and gave their informed consent to participate in the study. The study conformed to the Declaration of Helsinki and to the local ethics committee.

Each subject was asked to lie down on a bed, with the left arm flexed in a 45 degree

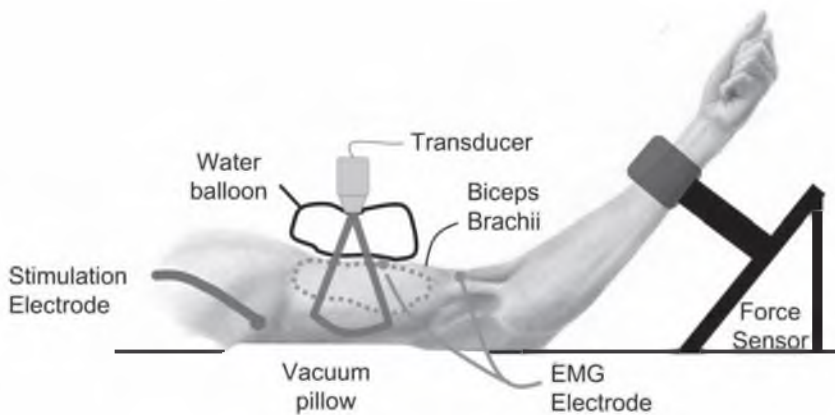


Figure 12.1 Schematic representation of the experimental set-up. This set-up enabled simultaneous excitation of the muscle, measurement of the exerted force and EMG as well as ultrasound data acquisition of the *m. biceps brachii*. The *m. brachialis* is not visible in this figure. The upper arm was fixed in a vacuum pillow and the echo transducer was placed in a clamp. The force sensor and wrist brace were fixed on the table. The musculocutaneous nerve was stimulated electrically, resulting in muscle contraction.

angle as shown in Fig. 12.1. The wrist was cuffed and attached to a force sensor. The force sensor and the wrist clamp were fixed onto a table. To minimize movements, the entire arm was supported by a vacuum pillow, which is a large synthetic bag containing small Styrofoam balls that becomes rigid after removing the air content with a vacuum pump. To record surface EMG of the *m. biceps brachii*, two electrodes were placed in a so-called belly-tendon montage; the active electrode was placed at about the middle of the muscle belly, the reference electrode was placed on the distal tendon (Kincaid et al. 1993). The ultrasound transducer was positioned on top of the *m. biceps brachii*, orthogonal to the muscle surface (see Fig. 12.1). A water balloon was placed between the transducer and the skin to provide an offset for the transducer and to prevent transducer motion during muscle contraction. This offset was necessary to include a larger area of the *m. biceps brachii* in the imaged sector.

To be able to record reproducible muscle contractions, the musculocutaneous nerve innervating the *m. biceps brachii* and *m. brachialis* was stimulated electrically in part of the experiments. A single, square, electric current pulse of 100  $\mu$ s was given in the axilla using a hand-held electrode. It elicited a so-called twitch in the muscle. The current strength was increased until the compound muscle action potential, recorded by the EMG electrodes, no longer increased in amplitude, indicating complete recruitment of all muscle fibers in the muscle.

Biplane ultrasound images and force exerted at the forearm were measured for three different types of muscle contraction:

1. Excitation with a single electrical pulse on the musculocutaneous nerve as described above. This twitch contraction was repeated three times for reproducibility analysis.
2. Excitation of the elbow flexors with a train of five such pulses at a rate of 10 Hz and 20 Hz.
3. Voluntary contractions at 30, 60, and 100% of maximum voluntary contraction

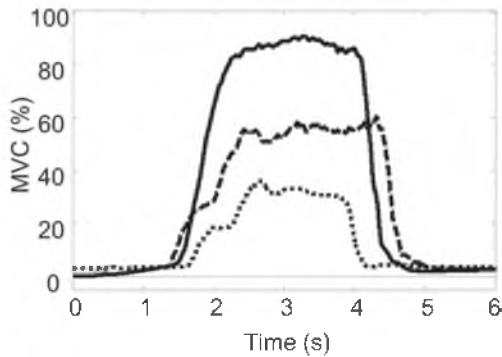


Figure 12.2 Typical example of the resulting force curves during voluntary contraction at 30, 60 and 100% MVC for one volunteer.

(MVC). First, the MVC force was determined for each person by asking the subject to fully contract the muscle twice for one second with one minute rest in-between. If the two contractions were similar, the maximum was taken as the MVC. After a short period of rest, the subjects were asked to follow a block shaped curve of two seconds that was shown on a monitor (Fig. 12.2). The force exerted by the subject was drawn on top of the predefined pattern for visual feedback. The subjects were familiarized with the procedure until they were capable of following the block-shaped curves on screen at 30%, 60%, and 100% of their MVC. Each subject practiced the predefined pattern at 30% MVC at least three times prior to the recording.

As stated above, results from voluntary contractions are less reproducible than stimulated contractions, but they might become clinically more relevant since they can be performed in virtually any skeletal muscle.

The *m. biceps brachii* was chosen because it mainly flexes the forearm during stimulation of the musculocutaneous nerve, which

produces a force that can easily be measured. We looked also at the tibialis anterior muscle as an alternative, but this muscle produces both dorsiflexion and inversion of the ankle, making it difficult to measure exerted force. Furthermore, we choose the *m. biceps brachii* for its superficial location and good accessibility for ultrasound imaging.

### Data Acquisition

Surface EMG data were digitized at 2000 Hz (Refa 64, 22 bits, 71.5 nV/bit, TMSi, The Netherlands). Force data were recorded using a force transducer (AST, KAP-E 2KN, 2.5 mV/N), digitized (2000 Hz) using a data acquisition board (National Instruments, DAQpad 6015, 16 bits, 0.3 mV/bit), and stored on the hard-disk of a PC. An externally generated synchronization signal was recorded simultaneously with the EMG and force data and was fed into the ECG input of the ultrasound machine for off-line synchronization.

The ultrasound data were acquired using a real time 3D ultrasound system (Philips iE33, Philips Medical Systems, Bothell, USA) equipped with an X7 matrix array transducer and an RF-interface. The matrix array transducer, with a bandwidth of 2-7 MHz, was used in biplane mode at a frame rate of 38-50 Hz, depending on the size of the image sector. The RF-data were sampled at 32 MHz and transported to an external hard disk using a USB 2.0 connection. With biplane imaging over a separate longitudinal or cross-sectional view, two orthogonal images in both the cross-sectional and longitudinal direction of the muscle were

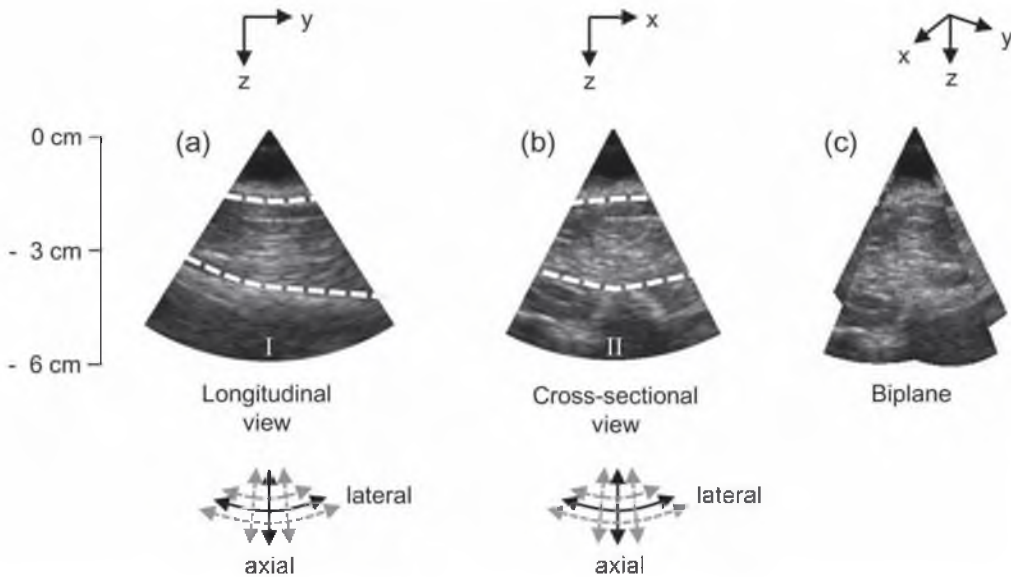


Figure 12.3 Example of Biplane ultrasound data of the upper arm. A: Longitudinal view (parallel to muscle/arm direction). B: Cross-sectional plane (orthogonal to muscle/arm direction). C: Biplane view. The m. biceps brachii is indicated by the dashed white lines. Segmentation was performed by a trained observer. The axial and lateral directions of the ultrasound data are shown (bottom figure) as well as the Cartesian coordinate system (top figure)

measured simultaneously (Fig. 12.3). This has the advantage that such semi-3D data can be used to evaluate tissue deformation in three orthogonal directions. The position of the ultrasound probe was carefully chosen to minimize out-of-plane motion in both views. All data were checked during post-processing for large translational movement by comparing the first and final frame of each dataset. The 2D tracking algorithm corrected for the remaining translational movement within the image plane.

### *Biplane Strain Imaging*

The RF-data were processed using a 2D displacement estimation and tracking algorithm that was tested on phantoms and applied successfully *in vivo* on cardiac data

(Chapter 2- 8). This algorithm uses cross-correlation of 2D segments of RF-data to measure the displacement in two directions simultaneously. Within a 2D ultrasound sector scan image, the direction parallel to the ultrasound beam is called the axial direction, whereas the direction orthogonal to the ultrasound beam is known as the lateral direction (Fig. 12.3).

The algorithm comprises a so-called coarse-to-fine approach (Shi and Varghese 2007). The algorithm starts at coarse scale using the demodulated RF-data ('signal envelope') to find the global motion of the tissue. A large segment of echo-data of frame  $f$  (7.2 mm x 11 lines) is cross-correlated with a larger search area within the next frame  $f+1$  (17.0 mm x 21 lines). The position of the peak of the cross-correlation is detected and 2D parabolic interpolation of this peak

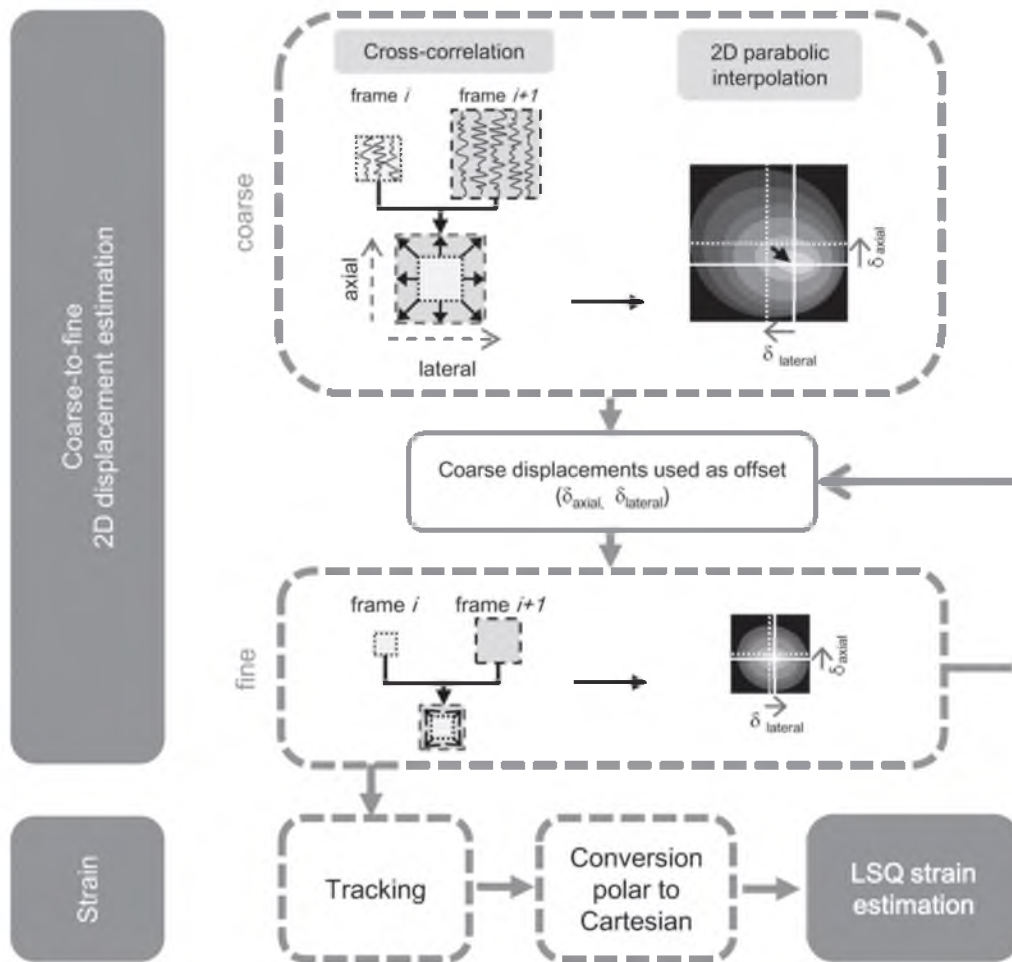


Figure 12.4 Schematic overview of the two-dimensional displacement estimation procedure. The graph shows all necessary steps to obtain 2D strain images from the rf-data. Please see the Methods section for a detailed explanation of the used method.

is performed to obtain sub-sample displacement estimates. The resulting 2D displacement fields are up-sampled to higher resolution and used in the next iteration (Fig. 12.4).

In the next two iterations, smaller pre-compression windows of RF-data are used (2.4 mm x 5 lines and 1.2 mm x 5 lines respectively) with an overlap of 80%. By stepwise decreasing the axial window size and using the RF-data, both resolution

and precision of the displacement estimates are enhanced (Chapter 4). The use of smaller data windows also enables accurate RF-based displacement estimation in high strain areas (Céspedes et al. 1999). Hence, the used window size is reduced significantly for the next iteration. The post-compression window sizes were also decreased (7.3 mm x 11 lines and 3.7 mm x 11 lines), thereby limiting the search area. It must be noted that lateral window size and resolution



cannot be expressed in units such as millimeters, since it is depth dependent due to diverging distance between image lines. Strain values were obtained every 0.3 mm in the axial direction and for each RF-line (*i.e.* lateral direction), corresponding to a horizontal resolution ranging from 0.15 mm for superficial structures and 1.0 mm for structures at maximum depth. The axial and lateral displacement data were filtered with a median filter of 3.0 mm x 5 lines and 3.0 mm x 11 lines, respectively.

After the third and final iteration, the axial and lateral displacements are used to track the tissue yielding the coordinates of each pixel for all consecutive frames (Chapter 6).

The resulting coordinates are transformed to Cartesian coordinates (see Fig. 12.4). Two-dimensional, least-squares strain estimators with a window size of 11 x 5 and 3 x 15 pixels are used to obtain the strains ( $\epsilon$ ) in the vertical ( $z$ ) and horizontal ( $x$ ,  $y$ ) direction (Chapter 5). In the longitudinal plane, the vertical strain,  $\epsilon_{zz}$  (I), and the horizontal strain,  $\epsilon_{yy}$ , are measured. The vertical strain ( $\epsilon_{zz}$  (I)) is the strain orthogonal to the arm and parallel to the US probe, and the horizontal strain ( $\epsilon_{yy}$ ) is the strain parallel to the arm. In the cross-sectional plane, the vertical strain,  $\epsilon_{zz}$  (II), and the horizontal strain,  $\epsilon_{xx}$ , are measured. The vertical strain ( $\epsilon_{zz}$  (II)) is again the strain orthogonal to the arm and parallel to the US probe, whereas the horizontal strain ( $\epsilon_{xx}$ ) is the strain orthogonal to the arm and orthogonal to the US probe. It may be noted that along the central line, theoretically,  $\epsilon_{zz}$  (I) and  $\epsilon_{zz}$  (II) should be equal.

### Statistics

The mean strain curves as a function of time for the *m. biceps brachii* were calculated as well as the strain values during maximum contraction within the entire *m. biceps brachii*. The intra- and inter-subject variability of the average maximum strain values was calculated. The Pearson's linear correlation coefficient was used to assess the similarity between the twitch contraction curves of the three acquisitions for all volunteers. The increase and decay in both force and strain curves were determined as the mean half time and the Student's t-test was applied to determine possible significant differences between force and strain half times. Furthermore, the Student's t-test was used for comparison of the maximum vertical strains, individually measured in both planes, during twitch contraction. For the voluntary contractions, linear regression analysis was performed on the vertical strain estimates (from both planes) during the plateau phase vs. the measured MVC using a 95% confidence interval.

## RESULTS

Examples of resulting strain data for a single twitch contraction are shown in Figure 12.5. For a large region within the *m. biceps brachii* (Fig. 12.5a), the strain curves are given (Fig. 12.5b). The strain curves show the global deformation behavior of the muscle as a function of time. The strain images visualize the local strain distribu-

tion within the muscle at several moments in time (Fig. 12.5c-f). The longitudinal images of the *m. biceps brachii* reveal that the maximum vertical strain is in the centre of the muscle. Vertical strain values up to 50% were measured. The cross-sectional view reveals different local regions of high strain. The horizontal strain reveals shortening up to -20% in the *m. biceps brachii*. The horizontal strain images,  $\epsilon_{xx}$  and  $\epsilon_{yy}$ , have a noisier appearance than  $\epsilon_{zz}$  (Fig. 12.5e-f).

Figure 12.6 shows the mean strain curves for a standard ROI in the *m. biceps brachii* as well as the force for all three twitch contractions in a single subject. For this subject, the average maximum vertical strain is  $27.4\% \pm 2.3\%$  during twitch contraction and the horizontal components revealed an average maximum strain of  $-20.5 \pm 4.1\%$  ( $\epsilon_{yy}$ ) and  $-5.99 \pm 2.0\%$  ( $\epsilon_{xx}$ ). There is a high level of similarity between contractions for the four different strain directions (Fig. 12.6a-d).

The plots in Figure 12.7 show the mean values of the vertical and horizontal strain components during the phase of maximum strain during twitch contraction within the *m. biceps brachii* for all five subjects. For all subjects, the intra-subject variability of the vertical strains was found to be 3.1% ( $\epsilon_{zz}(I)$ ) and 2.1% ( $\epsilon_{zz}(II)$ ). The inter-subject vertical strain was  $\epsilon_{zz}(I) = 19.7 \pm 6.9\%$  and  $\epsilon_{zz}(II) = 18.8 \pm 5.4\%$ . A Student's t-test revealed no significant difference in  $\epsilon_{zz}$  during the phase of maximum contraction between the cross-sectional and longitudinal strain images ( $p < 0.12$ ). The mean Fisher z-transformed correlation of the vertical strain curves was 0.97 ( $\epsilon_{zz}(I)$ , 95% confidence interval = 0.59 – 1.0) and 0.97 ( $\epsilon_{zz}(II)$ , 95% confidence interval = 0.79 – 1.0) for all subjects.

Since the correlation data were not normally distributed, the Fisher z-transformation was used to calculate the mean and 95% confidence interval of the correlation values. The inter-subject horizontal strains and variability were estimated to be  $\epsilon_{yy} = -9.2 \pm 5.9\%$  and  $\epsilon_{xx} = -5.9 \pm 3.1\%$ , whereas the intra-subject variability was 3.5% ( $\epsilon_{yy}$ ) and 1.8% ( $\epsilon_{xx}$ ). For the horizontal strain curves, the correlations were 0.66 ( $\epsilon_{yy}$ , 95% confidence interval = -0.67 – 0.98) and 0.86 ( $\epsilon_{xx}$ , 95% confidence interval = -0.63 – 1.0), revealing a lower precision of the horizontal strain estimates.

Results for all volunteers reveal that the strain increases approximately at the same rate (mean half time,  $t_{1/2, \text{mean}} = 18.4 \pm 23.1$  ms) as the measured force ( $t_{1/2, \text{mean}} = 18.5 \pm 4.1$  ms) during contraction (Student's t-test,  $p < 0.02$ ). However, the mean force curve decays considerably faster (mean half time,  $t_{1/2, \text{mean}} = 69 \pm 24$  ms) than the vertical strain ( $t_{1/2, \text{mean}} = 214 \pm 161$  ms). The difference was found to be significant (Student's t-test,  $p < 0.01$ ).

The comparison of the three different types of electric nerve stimulation is illustrated in Figure 12.8. The strain curves in all four directions are shown for single pulse stimulation, a pulse train at 10 Hz and for pulse train stimulation at 20 Hz for one volunteer (see Discussion). At 10 Hz, the force profile dropped slightly prior to the next pulse so that an alternating wave shape profile becomes visible (Fig. 12.8e). The strain curves nicely follow this pattern (Fig 12.8a-d). At 20 Hz, this profile is no longer visible as the next pulse arrives before the relaxation phase starts. The mean strains at 20 Hz are approximately 30-50% higher

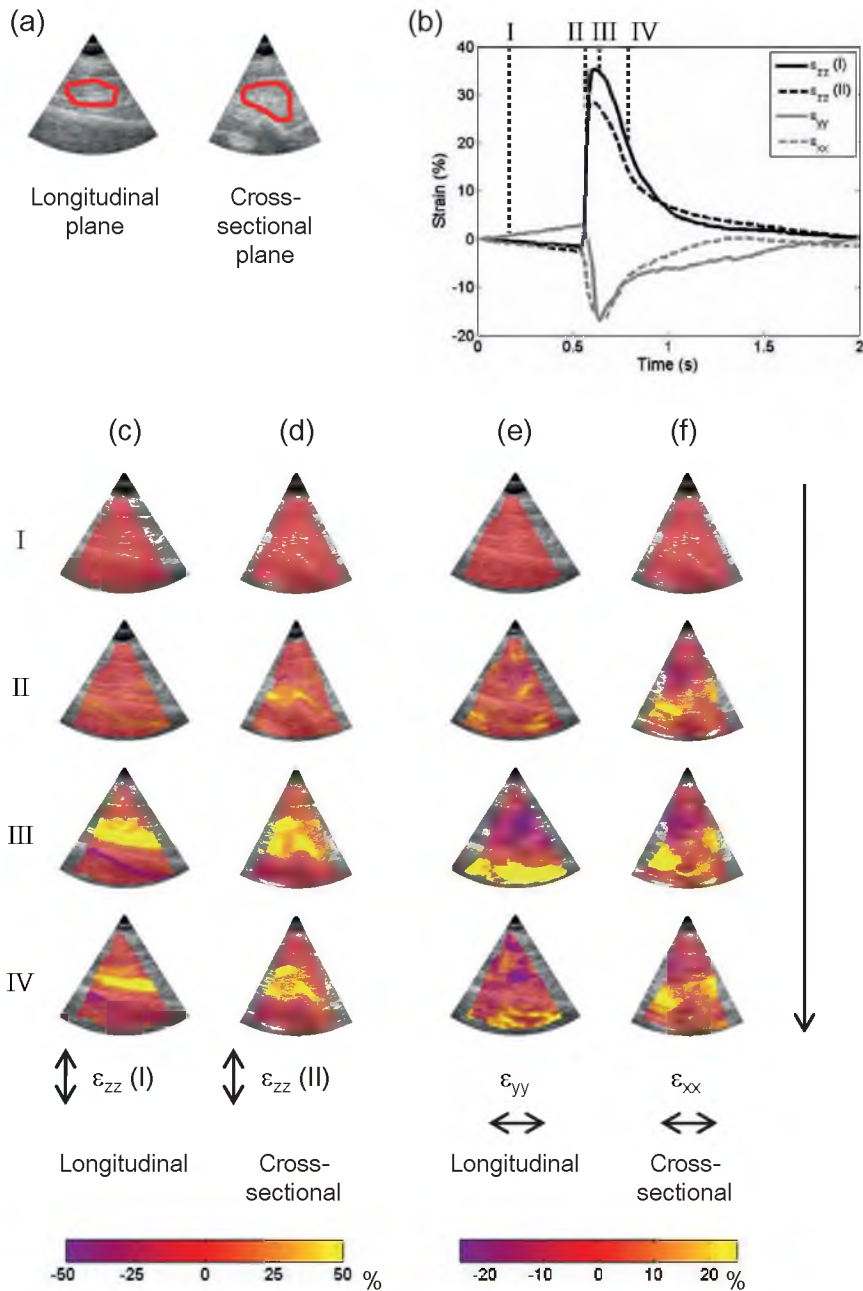


Figure 12.5 A: B-mode Biplane images of the upper arm. The red solid areas indicate the region-of-interest in the m. biceps brachii. The mean strain curves for the regions drawn in A are shown as a function of time (B). Four time points are indicated (I-IV, black dashed lines). These correspond with the typical biplane strain images of the upper arm (C - F). C: The vertical strain in the longitudinal plane,  $\epsilon_{zz}$  (I). D: The vertical strain in the cross-sectional plane,  $\epsilon_{zz}$  (II). E: The horizontal strain in the longitudinal plane,  $\epsilon_{yy}$ . F: The horizontal strain in the cross-sectional plane,  $\epsilon_{xx}$ .

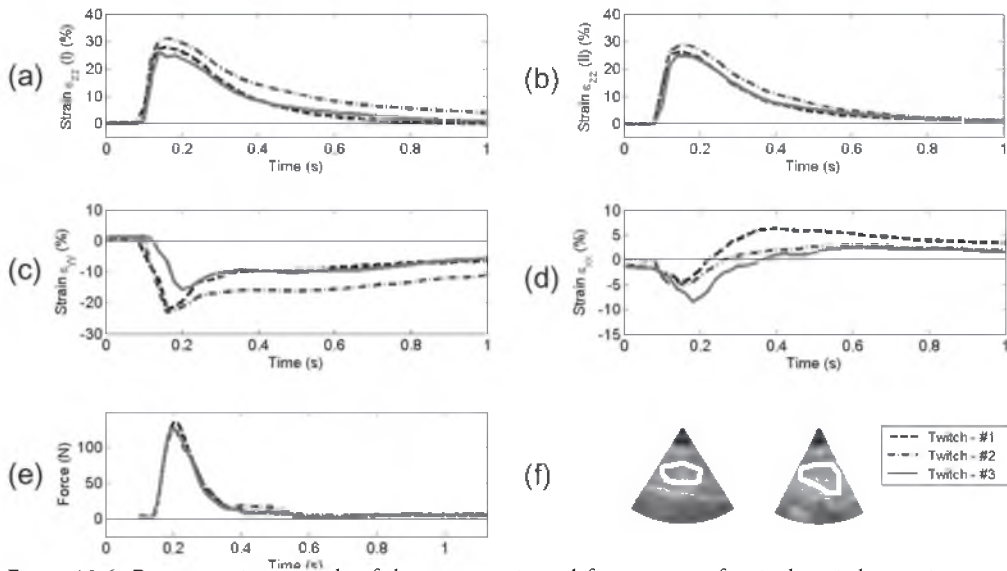


Figure 12.6 Representative example of the mean strain and force curves of a single twitch experiment as a function of time, performed three times in each subject. A: Vertical strain in the longitudinal plane ( $\epsilon_{zz}$  (I)). B: Vertical strain in the cross-sectional plane ( $\epsilon_{zz}$  (II)). C: Horizontal strain in the longitudinal plane ( $\epsilon_{yy}$ ). D: Horizontal strain in the cross-sectional plane ( $\epsilon_{xx}$ ). E: Measured force. F: B-mode data and ROIs indicating the region in which the strain was analyzed (white solid curves).

compared to the 10 Hz pulse strain. No distinct strain peaks related to the subsequent pulses can be found in the curves, which is in accordance with the measured smooth developing force profile.

An example of the voluntary contraction experiment is shown in Figure 12.9. The measured force (Fig. 12.9a) and verti-

cal strain curves (Fig. 12.9b) show a good resemblance. The mean vertical strain is already relatively high for 30% of the MVC and the increase is moderate for higher force levels (Fig. 12.9b). The strain images captured during the plateau phase show an increase in strain and different patterns for increasing force (Fig. 12.9c). The measured

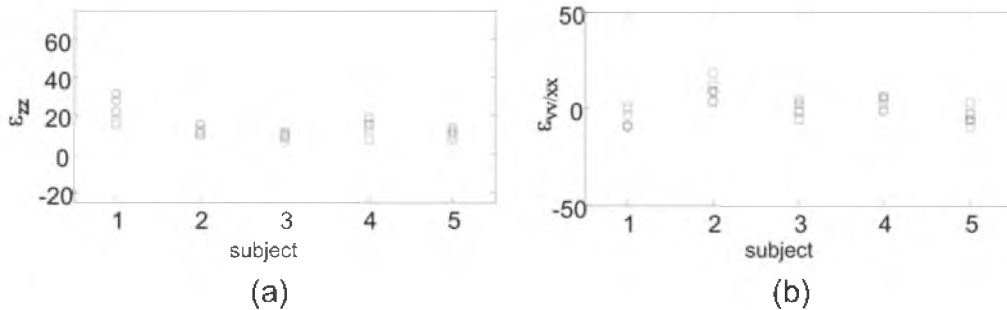


Figure 12.7 Mean values of the various strains within the m. biceps brachii during twitch contraction for each subject. The measurements were repeated three times in each subject ( $n = 5$ ). The strains were measured in the frame at which maximum contraction was reached. A: Mean vertical strain in the longitudinal plane  $\epsilon_{zz}$  (I, circles) and in the cross-sectional plane  $\epsilon_{zz}$  (II, squares). B: Mean horizontal strain in the longitudinal plane  $\epsilon_{yy}$  (circles) and in the cross-sectional plane  $\epsilon_{xx}$  (squares).

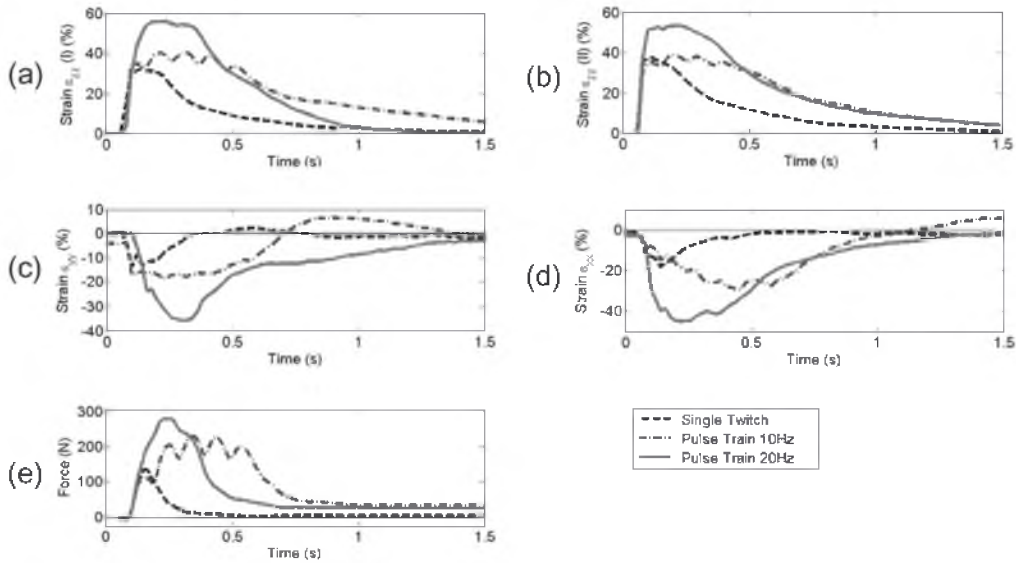


Figure 12.8 Example of the mean strain curves and force measurements in the m. biceps brachii for three different types of nerve stimulation (single twitch, pulse train at 10 Hz, pulse train at 20 Hz) for one volunteer. A: Vertical strain in the longitudinal plane ( $\epsilon_{zz}(I)$ ) as a function of time. B: Vertical strain in the cross-sectional plane ( $\epsilon_{zz}(II)$ ). C: Horizontal strain in the longitudinal plane ( $\epsilon_{yy}$ ). D: Horizontal strain in the cross-sectional plane ( $\epsilon_{xx}$ ). E: Measured force as a function of time.

mean vertical strain estimates (from both planes) during the plateau phase of are also shown as a function of the exerted force (Fig. 12.10). Results of linear regression are provided ( $R = 0.75$ ), including the 95% confidence intervals. Strain increases with force as expected.

## DISCUSSION

We presented a method to measure strain in contracting skeletal muscles using biplane ultrasound. The use of biplane ultrasound enabled dynamic imaging and estimation of local muscle deformation in multiple directions for different types of induced muscle contraction patterns.

Using the proposed method, 2D strain

was measured locally within two orthogonal planes in skeletal muscle, revealing the deformation in both the cross-sectional and longitudinal direction. The 2D displacement algorithm was able to properly track the tissue displacement and estimate the strain using the RF-data, despite the high strain (and thus strain rates) that occurred during muscle contraction and despite the observed rotation of the muscle tissue. Because of the lower sampling density in the lateral direction and the lack of adequate phase information in that direction., the horizontal strain images and curves are of less quality. This is corroborated by the measured range of strain values and the correlation and similarity of the strain curves. Below we discuss the feasibility of the biplane method for each of the different muscle contraction types:

1. The twitch experiments led to a controlled contraction and were used to demonstrate

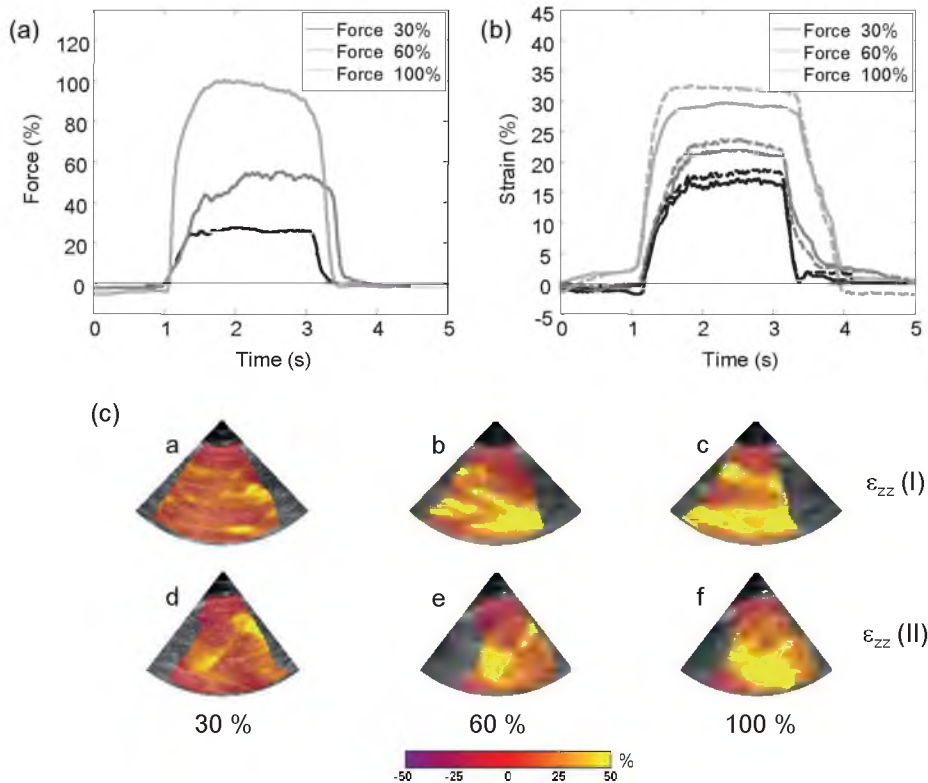


Figure 12.9 Results of the voluntary contraction experiment for one volunteer. A: Measured force during voluntary contraction while following a block-shaped force curve at 30, 60 and 100 % of the subject's maximum possible force. B: Measured vertical strain in the longitudinal (*solid*) and cross-sectional planes (*dashed*) for 30, 60 and 100 % of exerted force. C: Vertical strain images at the three different force levels in both the longitudinal plane (a-c) and the cross-sectional plane (d-f). The vertical line in B indicates the time point corresponding with the strain images (C).

the reproducibility of the strain measurements. The maximum strain values showed a fair reproducibility. The shape of the strain curves also showed good similarity in all three directions for each subject (see Results). The observed range of strains during twitch contraction was already quite high (10 – 30%), thereby already showing the need for a technique, that is capable of measuring high strains. This induces the need of using a coarse-to-fine algorithm. Large signal windows are required to track the large global motion, whereas small

signal windows are required when high strain is present. The muscle data contain both features.

2. The pulse train example nicely illustrates the performance of our technique in following a submaximal-tetanic contraction. The shape of the strain curves clearly revealed the difference between the different stimuli. However, electrical nerve stimulation with a train of pulses is not very comfortable and in the *m. biceps brachii* it is not easily performed. The induced contraction after a train of pulses resulted into relative large

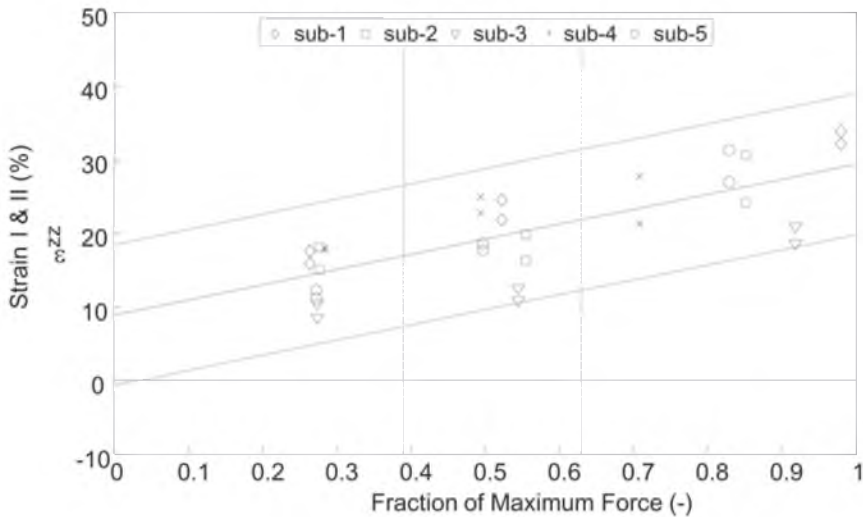


Figure 12.10 Results of the voluntary contraction experiment for all five subjects. The measured average vertical strain in the m. biceps brachii during the plateau is shown as a function of exerted force for both planes. The regression curve is given (*solid*) as well as the 95% confidence interval (*dashed*).

motion of the entire arm, moving away from both the stimulation electrodes and the ultrasound transducer (even though it was fixated). This movement is not expected to have affected the results substantially, but obtaining the reproducibility of the stimulus train was not trivial.

3. The feasibility and reproducibility of measuring strain during voluntary contraction was also examined. The reproducibility appears to be better for the lower force values (Fig. 12.10), which can be explained by the fact that lower strains can be measured more accurately. However, the tracking method was able to trace the strain at 60% and 100% MVC despite the fast contraction and relaxation of the muscle. Hence, this study reveals that strain measurements during voluntary contraction are indeed possible. Further research is needed to determine the relation between muscle excitation, force, and strain in more detail. For instance, the vertical strain at 30% MVC was relatively

high (Fig. 12.9) and increased moderately for higher MVC values. This might be explained by opposing forces, caused by the stiffness of the surrounding connective tissue. In addition, other parameters could be of interest, such as the average strain rate during contraction, or the relaxation time.

Intra- and inter-subject reproducibility is not easily quantified, considering the wide range of strain values during contraction and the noise level. However, the intra- and inter-subject variability and the similarity of the strain curves (see Results and Fig. 12.6-12.7) indicate that the measurements are consistent between (and within) subjects. Especially the resemblance between the vertical strain in the longitudinal and in the cross-sectional plane is promising (Fig. 12.6a-b, 12.7a). The intra-subject variability (1.8 – 3.5%) was found to be lower than the inter-subject variability analysis (3.1 – 6.9%), revealing that the largest variance exists between the different

subjects but with a good reproducibility for each individual subject. Although the force and strain curves of the twitch experiment showed a high resemblance, no distinct relationship between force and strain was found for this experiment. This was not the case for the voluntary contraction experiment, where a linear correlation between force and strain was found (Fig. 12.10) and each subject could serve as his own reference. However, the high observed strains at 30% MVC suggest that force and strain are not directly proportional.

We found that relaxation of muscle tissue measured with strain is significantly prolonged compared to the reduction of force in all different types of muscle contraction (Fig. 12.6, 12.8 and 12.9). The motion was also visible in the M-mode image (data not shown). A possible explanation may be that the subject slightly contracted the muscle immediately after the stimulus or that a delay between force and movement is present. Measurement errors, such as the accumulation of tracking errors, use of a large ROI and out-of-plane motion, could have led to an overestimation of this finding. However, this seems unlikely, since the five stimulus pulses (10 Hz) were followed accurately by the strain algorithm.

Other techniques may be applied also for deformation measurements. Conventional ultrasound B-mode data can be analyzed by 2D speckle tracking techniques to obtain 2D strain. The advantage of B-mode speckle tracking is its robustness. However, the resolution of B-mode data is much lower compared to RF-data and the sensitivity of RF-based strain imaging is higher in the axial direction and approximately equal in

the lateral direction (Chapter 4). Secondly, the use of three-dimensional techniques should be considered. Full 3D volume imaging is currently available, including 3D RF-data (Lindop et al. 2006; Lopata et al. 2007). Obviously, 3D data would yield the full 3D strain tensor within 3D space, which is necessary to characterize the heterogeneous and anisotropic properties of the muscle locally. However, sufficient temporal resolution is required and can only be obtained at the cost of a limited image view angle or of spatial resolution. This is not an attractive option when examining skeletal muscle contraction, since multiple (triggered) contractions are required to obtain RF-data at a sufficient frame rate when using a standard 3D system. For instance, 3D cardiac data are normally acquired using ECG-triggering in four to seven consecutive heart beats, resulting in a frame rate of 35-50 Hz. Since fatigue may be induced and reproducibility is not high enough for voluntary contractions, this acquisition scheme is not preferred. Moreover, 3D imaging will increase both experiment time (and patient's burden) and computational load. Finally, the field of view of ultrasound data is limited compared to MR imaging (Pappas et al. 2002). However, ultrasound data acquisition has the primary advantages of being cost effective as well as its ease of use. Another benefit to point out is that the temporal and spatial resolution are higher compared to MRI. Besides, the so-called 'speckle' appearance of the ultrasound images enables displacement estimation without the use of tagging.

The vertical and horizontal strain images have shown the advantage of displaying local



information of the strain, whereas mean strain curves only reveal the global deformation of the tissue and are limited to one dimension (comparable to force curves and the work on aponeurosis strain measurements (Magnusson et al. 2003)). The fact that strain differs locally can be seen in the strain images (Figs. 12.5 and 12.9) during maximum contraction. Such non-uniform strain distributions have been reported also by others. The experimental MRI findings of Pappas et al. (2002) showed a homogeneous strain distribution over the anterior fascicles, but a heterogeneous deformation pattern along the centerline of the *m. biceps brachii*. It was hypothesized that this heterogeneity might be caused by the presence of the aponeurosis and tendons and the difference in stiffness of these two with respect to the muscle tissue. These experimental findings were corroborated by the simulation work of Blemker et al. (2005). However, the field-of-view of the biplane ultrasound images is too small to measure the strain variation over the entire muscle as performed by Pappas et al (2002). Besides, in those experiments, a lower MVC of 15% was used and muscle shortening was examined in the fiber direction but not in the orthogonal direction (= vertical strain), which makes a direct comparison with our results difficult. We have shown that our method can identify non-uniform strain distributions also at higher activation levels.

The clinical applications of measuring local skeletal muscle strain are diverse. Measurement of the time and amount of strain in relation to force could be of use in studies regarding force transmission. This could be of special interest in disorders of

connective tissue such as Ehlers Danlos Syndrome. Also force generation in primary muscle disorders such as muscle dystrophies could be studied using strain - force patterns. As strain appears to diminish slower than force, it might be a more sensitive method to detect disorders with delayed relaxation such as myotonic disorders. Using the presented method, one can assess local multi-dimensional strains and strain differences within a muscle. This can be of interest in disorders with focal muscle involvement, such as inflammatory muscle diseases (Reimers et al. 1993). Also disorders affecting peripheral nerves would be interesting to study using skeletal muscle strain. However, further research is needed to investigate whether skeletal muscle strain measurement can detect differences on a motor unit level as this could be used to monitor disease progression such as amyotrophic lateral sclerosis (Al-Chalabi and Leigh 2000).

## CONCLUSION

In conclusion, we introduced a multi-dimensional strain method using biplane imaging in skeletal muscles during induced and voluntary contraction. The method revealed good performance using RF-data in tracking the tissue motion and enabled the measurement of local deformation, even despite the large displacement and strain between the subsequently acquired echo frames and despite the moderate frame rate of the ultrasound equipment in biplane mode.



---

# CHAPTER 13

## GENERAL DISCUSSION & PERSPECTIVE

---



## I. METHODS

### *Summary*

In the first part of this thesis, several methods for 2D ultrasound strain imaging of deforming tissues and structures were examined. A coarse-to-fine technique was developed, enhancing both resolution and precision of strain images in two directions. It was found that the use of RF-data outperformed that of envelope-data in terms of precision and contrast with higher resolution and for larger deformation (Chapter 2). Two-dimensional kernel matching was favored, especially using axial warping of the 2D post-compression kernels. Image warping, or companding, has been reported before (Chaturvedi et al. 1998), but this study showed the true merit for shearing and rotating structures (Chapter 3). The latter enhanced strain measurements when large axial shearing and considerable rotation was present in the data. Other techniques were used to enhance correlation between pre- and post-compression data. This so-called local aligning and stretching improved correlation and, therefore, yielded better displacement and strain estimates in both axial and lateral direction (Chapter 2 & 4). This method differs from earlier reports on global stretching (Varghese et al. 1996) and adaptive strain imaging (Alam et al. 1998), because it uses local *a priori* knowledge, derived from previous iterations. The techniques proved to be applicable on both linear array (Chapter 2 - 3) and phased array data (Chapter 4 - 5) in a quasi-static setup and were applied to actively deforming

tissue using 2D, Biplane and 3D ultrasound data in the remainder of this thesis.

### *Limitations*

One of the limitations of the proposed methodology is the computational load. The processing time of the strain algorithm is long, depending on the type of data and experiment time. Besides, real-time application of the coarse-to-fine approach and additional re-correlation techniques also seems troublesome. However, the use of 2D parabolic interpolation on 2D cross-correlation data proved to perform equally well as RF-data interpolation (Konofagou et al. 1998), reducing the computational load considerably (Chapter 2). It must be noted that the image acquisition was not in real-time either, since ECG-triggering was necessary in the case of 3D full volume imaging and 2D compounding (Chapter 7-9, 10).

The strain methods require a rough, though accurate, initial estimate of the 2D and 3D tissue displacement. The coarse-to-fine, free-shape algorithms require these prior estimates to enhance strain precision and accuracy in subsequent iterations. The analysis cannot be performed when the algorithm fails in the first iteration. The signal envelope is used to increase the success of this first step.

Another limiting factor is the fact that the choice of the optimal window size actually depends on the present strain (Céspedes et al. 1999), which is not *a priori* known in most *in vivo* data. This is especially an issue at relatively low frame rates when imaging largely deforming structures, such as the

heart. This leads to significant de-correlation of the ultrasound data, which will decrease the accuracy and robustness of the method.

### *Future work*

For future work, a fast and robust registration technique of B-mode envelope data (Chen et al. 2008; Elen et al. 2008; Crosby et al. 2008) could probably be adapted to provide the input for the RF-based strain imaging techniques. The strain estimation method could also be reconfigured to a hybrid approach, using both the RF-data and envelope data. The choice of the used data could be based on prior strain estimates, i.e. use envelope data for large strain.

The possibility of lateral warping and stretching was not examined in the presented work. Although no phase information is present in the lateral direction (Chen et al. 2004), stretching and warping in this direction could improve 2D strain estimation when high lateral strains are present.

### *Scope*

Several developments will help in a real-time realization of the proposed techniques. Large internal memory chips are currently available, which already enable retrospective RF-data acquisition and possibly also semi real-time strain imaging. Smart use of parallel memory boards and graphic processing units (GPU) might support these purposes. The latter could be programmed in order to develop dedicated strain imaging hardware.

Conventional ultrasound scanners

have frame rates in the range of 15 – 150 frames/s, depending on transducer type and imaging mode. Higher frame rates would result in a lower relative deformation between two subsequent images. However, new techniques such as ultrafast ultrasound imaging (frame rate of 1000-6000 frames/s) are on the rise and will tackle the problem of de-correlation (Deffieux et al. 2008). However, this fast frame rate is achieved at the cost of lateral resolution, since the ultrasound beams are not focused during transmission (only in receive mode).

## **II. 3-D CARDIAC STRAIN IMAGING**

### *Summary*

Recently, several studies report on 3D strain measurements in the heart using 3D ultrasound systems and 3D speckle tracking (Papademetris et al. 1999; Chen et al. 2005; Song et al. 2007; Elen et al. 2008; Crosby et al. 2008; Seo et al. 2009). However, only few studies report findings on 3D RF-based strain imaging, mostly on non-cardiac applications (Lindop et al. 2006; Patil et al. 2007; Lopata et al. 2007). In this thesis, RF-based strain imaging and segmentation techniques were applied in the heart using biplane and full 3D ultrasound data. Both the biplane and 3D methods revealed good performance. Coarse-to-fine strain imaging enabled the use of RF-data, thereby enhancing both strain resolution and precision,

although this depended on the phase of the heart cycle. The *in vivo* results revealed the applicability and performance of these methods (Chapter 7-8). In a pilot *in vivo* study on (semi-3D) biplane strain imaging, differences in strain were observed between dogs with different degrees of hypertrophy, correlating with the present pressure gradient. The 2D/biplane methodology was extended to 3D and tested on 3D full volume data of the left ventricle in young, healthy children (Chapter 8). Results were in accordance with previous studies (Crosby et al. 2009). Besides tracking and strain analysis of the heart muscle, measured cross-correlation values were used to improve segmentation of the left ventricle in the healthy children, clearly revealing the merit of RF-data (Chapter 9).

### *Limitations*

Only a small number of animals were available for the study on hypertrophy and fibrosis for several reasons, since only a pilot with four animals was conducted first (Chapter 7). A larger study, including 3D ultrasound and strain data, has recently been performed including a considerable number of healthy young children (see also chapter 8). In this thesis, strain estimation was not validated within the entire heart *in vivo*. MR imaging and tagging is required to validate the techniques. In the animal study, the strain was estimated in only a limited segment of the left ventricle and not in full 3D. In the children study, full 3D images were acquired, but the apex was often not visible. Strain is often measured in apical views of

the heart (Elen et al. 2008; Crosby et al. 2008). The image quality in children in the apical view was not sufficient for accurate strain imaging and segmentation. It might be of interest to image the heart from different angles, to visualize the entire heart and map the 3D strain. Hence, for a more extensive performance validation of the biplane and 3D strain imaging and segmentation techniques, an *ex vivo* beating-heart setup could be considered for this purpose (see next section). One could even include the right ventricle, which is of interest for clinical research on pulmonary hypertension (Arnould et al. 2009; Cacciapuoti 2009).

As noted in one of the previous sections, a coarse-to-fine approach is limited by the requirement that the first rough displacement estimates have to be accurate within a reasonable range to guarantee precise and accurate results in consecutive iterations. Hence, a robust technique is required for proper initialization of the proposed methodology. Especially in fast contracting tissue such as the heart, this can be a problem. Conventional B-mode speckle tracking or image registration (Elen et al. 2008) could be used to obtain a robust and fast initial estimate of tissue motion to facilitate the RF-based methods.

### *Future work*

In general, the work in the beagles and healthy children was promising but still preliminary. The pilot studies should be extended to a large patient population with cardiological disorders affecting both muscle function (strain imaging) and geometry

(segmentation). A large study on healthy volunteers is required to assess the normal values of cardiac strain. Monitoring children over a number of years would enable the assessment of growth-related strain changes.

The author believes that considerable progress could be made in the future by adapting so-called 'fusion techniques'. Fusion of ultrasound images, acquired at different angles with respect to the heart geometry, was shown by the group of prof. A Noble (Rajpoot et al. 2009; Gooding et al. 2010). The fused data reveals enhanced image quality and a larger sector of the heart, both improving segmentation results. This technique could also be used to fuse the 3D displacement and strain data, acquired from different imaging positions, using the image fusion as guidance. In several regions, strain estimates will improve due to enhanced image quality, an enlarged contribution of axial strain estimates to the full 3D strain tensor, or simply by averaging.

Furthermore, integration of the strain and segmentation results could improve both techniques. A first step was made by using the cross-correlation data to improve segmentation. However, one could also use the measured displacements for segmentation or for tracking the end-diastolic and end-systolic meshes through the cardiac cycle. Vice versa, the segmentation of the heart muscle could be used to speed up strain-calculations and, more importantly, provide a rough initial estimate of both position and strain of the heart muscle.

It must be noted that the availability of 3D ultrasound and strain in 3D space and time require sophisticated imaging and visualization tools. One could use a

dedicated 3D stereoscopic viewing station for offline analysis (PS-Tech, NL), which is now used for data. However, considering the recent advances in 3D movies (e.g. 'Avatar') and the recent availability of 3D LCD monitors, real-time viewing in 3D becomes feasible (Siemens, GE Healthcare).

Validation of cardiac strain imaging and segmentation techniques remains a cumbersome task. As a golden standard, MR imaging is often used for non-invasive validation of segmentation techniques (Lee et al. 2008). CT and MR images have a less noisy appearance and direction-independent in-plane resolution, although slice thickness is comparable to, or worse than, B-mode imaging. Hence, segmentation of these images is more robust. CT imaging, however, is considered to be too invasive for such purposes and would never be used in studies of healthy volunteers. Additionally, MR tagging could be used to validate the strain imaging techniques. MR tagging yields global strain for a coarse grid. Another, invasive, technique would be sonomicrometry (Langeland et al. 2004), but this technique is not applicable in healthy subjects and patients. Finally, a comparison of the proposed methods with commercially available techniques should be performed to assess the possible differences in performance, accuracy, specificity and sensitivity. Nowadays, several systems are equipped with 3D tracking, strain estimation and segmentation software (Aloka, Philips, Toshiba).



*Scope*

Besides improved tracking and segmentation algorithms, computational efficiency and method validation, several hardware improvements might be expected to become available in the near future. Transducer design is still an evolving branch of ultrasound research, resulting in higher frame rates and higher transmission frequencies and, therefore, better temporal and spatial resolution. Furthermore, fast techniques such as ultra fast plane wave imaging are on the rise, which might also be applied in the heart.

### III. NON-CARDIAC APPLICATIONS

*Summary*

In the final part of this thesis, the possibility of RF-based strain imaging was investigated in several actively deforming structures and tissues. The technique was applied in vessel phantoms and muscles (lip, skeletal muscles). The vessel phantom study (Chapter 10) was devised to investigate the feasibility and performance of beam steering techniques to improve non-invasive strain estimation in circular structures in the radial and circumferential directions. It was shown that the proposed method improved both precision and contrast of the strain images

A good contrast of the local strain was also found in the cleft lip study (Chapter

11). RF-based 2D strain imaging, without beam-steering, was applied to data of the contracting orbicular muscle. The preliminary but unique results showed that several patients had decreased muscle function in regions with presumable scar tissue, not found by inspection of the echogram.

In Chapter 12, biplane strain imaging was performed in skeletal muscles, in this case the biceps muscle. Only few reports were found on strain in skeletal muscles (Witte et al. 2007; Deffieux et al. 2009). In this study, the deformation was measured in the three principal directions of the muscle and was investigated for three types of muscle contraction, both induced and voluntary. It was found that large strains could be measured for each type of muscle contraction. The feasibility of measuring strain during voluntary contraction might lead to a less invasive experiment without electrical stimulation.

*Limitations*

The major limitation of these studies is the lack of extensive volunteer and patient studies. In fact, the beam steering techniques were only tested in vessel phantoms, but not *in vivo* (Chapter 10). The image quality will be significantly lower in patients caused by the presence of surrounding tissue. Besides, the vessel wall will be much thinner ( $< 1.0$  mm) compared to the relatively thick wall of the vessel phantoms (5.0 mm). In case of the lip and muscle studies (see Chapter 11 & 12), a small number of volunteers (lip  $N = 3$ , muscle  $N = 5$ ) and patients (lip  $N = 3$ ) were examined. These numbers may

be sufficient to show the feasibility in pilot studies, but should be extended for proper validation. No patients were investigated in the skeletal muscle study.

### *Future work & Scope*

The application of beam-steering and 2D strain imaging in the carotid arteries is currently under investigation. More recently, non-invasive 2D strain imaging was applied in the abdominal aorta by the author. Strain imaging in the lip is applicable for the detection of decreased muscle function of the orbicular muscle. A large study in patients and volunteers is required to quantify the specificity and sensitivity of this technique. This will help the surgeon to determine whether a new operation has to be performed to reconstruct the lip and improve muscle function.

Similar conclusions can be drawn for strain imaging in the skeletal muscles. Several patient groups are of interest to study with ultrasound strain imaging. Patients with myotonic disorders are known for their slow muscle relaxation (Hogrel 2009). Both muscle contraction and relaxation can be quantified with the proposed method in any arbitrary, superficial muscle. Considering the non-invasive nature of this technique, it could also be used to monitor patients with a progressive decrease in muscle function (amyotrophic lateral sclerosis). Furthermore, patients with mitochondrial disorders might be of interest. Mitochondrial disease has a negative influence on muscle development and function and results in muscle fatigue and degeneration.

---

# CHAPTER 14

## SUMMARY

---



Ultrasound (US) imaging is a well-established tool for non-invasive imaging of biological tissue and organs. Despite the acoustical limitations of ultrasound imaging, the applications are numerous. The spatial and temporal resolutions of ultrasound are still superior to those of CT and MR imaging, although the US images are known for their somewhat noisy appearance due to “speckle” formation. US is practically unable to image (beyond) hard structures, such as bone.

Doppler-based techniques and speckle tracking can be used to estimate blood flow velocity, as well as tissue motion and deformation, respectively. The raw ultrasound radio frequency (RF) data contains valuable phase information, besides the normally used amplitude information, that can enhance tissue motion and deformation measurements. Unfortunately, RF-data is generally not available in commercial equipment. In this thesis, several aspects of RF-based motion and deformation imaging were explored and the proposed methodology was applied to *in vivo* data.

Most techniques determine 1D strain in the direction of the ultrasound beam, although more and more reports on 2D displacement and strain estimation are published. However, determination of the in-plane strain is still difficult and challenging. In **chapter 2**, the performance of 2D displacement and strain estimation was investigated. Simulation and experimental studies on accuracy, precision and contrast of both axial and lateral displacement and strain estimates were performed with a linear array transducer. The use of coarse-to-fine displacement estimation improved

strain estimation when large displacements occurred and allowed the use of small data windows to measure higher strains. Two-dimensional parabolic interpolation proved to be a good alternative for time-consuming RF-interpolation to obtain sub-sample displacement estimates without the loss of precision. Further improvement was achieved by local 2D aligning and axial stretching of the RF-data. As a result, higher strains could be measured at both high resolution and precision. This methodology was further improved by allowing the 2D search window to be deformed in the axial direction, using prior axial displacement estimates (**chapter 3**). This so-called free-shape 2D displacement estimation technique was especially beneficial for structures where large shearing and rotation occurred. It was found that both shearing and rotation reduce the accuracy and precision of strain estimates significantly. Using the proposed approach, axial shear strains up to 6.0% were measured accurately, rotation was adequately measured up to 5.0 degrees. The vertical and horizontal strains present were measured more accurately as compared to methods without using free-shaped kernels.

In many applications, sector scan data is acquired using phased and curved array transducers. The advantage of a sector scan, opposed to a linear array, is the large( $r$ ) image view and the smaller footprint. However, the lateral spacing increases for larger image depths, and therefore, the spatial sampling degrades over depth. In **chapter 4**, the use of 2D kernels of RF-data acquired with a phased array transducer was examined and the performance of local

aligning and stretching was investigated. It was found, that the proposed methodology was applicable to phased array data. The use of 2D pre-compression kernels was favored over the 1D case. Furthermore, the strain estimates showed a fair improvement when local aligning and stretching of the sector scan RF-data were applied. In general, the accuracy, precision and contrast of the displacement and strain estimates were lower compared to the linear array data. This was caused by the lateral sampling and spacing issues and by the lower center frequency.

To obtain strain estimates, the use of 1D least-squared strain estimators (LSQSE) is widely adopted. It was investigated for phased array data whether a 2D LSQSE would improve strain estimation (**chapter 5**). The 2D LSQSE was preferred over the 1D case and was able to produce both the axial and lateral strains, as well as the vertical and horizontal strains. Especially the lateral/horizontal strain improved significantly. Higher strain precision was obtained at the cost of resolution, making its application not trivial.

After testing the different techniques, several *in vivo* applications were explored, mostly actively deforming tissue. To obtain the accumulated strain during a complete cardiac deformation cycle, a tracking method was devised using the calculated cross-correlation values to determine the amount of regularization needed (**chapter 6**). The regularization was necessary to avoid drift of the tracked mesh and resulting strain curves.

In the next part of this thesis, cardiac applications were investigated and reported. In **chapter 7**, the methods were applied to

biplane data of the canine heart. Biplane data are acquired in two orthogonal planes, which enables the measurement of strain in three orthogonal directions. Four beagles with an induced valvular aortic stenosis were examined at regular intervals. Using a 2D matrix array transducer, biplane RF-data were acquired. The radial, circumferential and longitudinal strains were determined over the entire cardiac cycle at a relatively low frame rate of 100 Hz. Results revealed that the various beagles developed a different degree of stenosis and hypertrophy. The strain results revealed a decrease in contractility (lower strain rate) and stiffer muscle (lower strain) as a function of the developed pressure gradient over the aortic valve. Histology corroborated these findings, which were promising and suggested a future use in the clinic to monitor hypertrophy. However, a full 3D construction of the strain in the entire left ventricle was not achieved. As a first step towards full 3D strain imaging of the heart, the proposed methodology of chapters 2 – 7 was extended to 3D space and applied to ultrasound data of the left ventricle in young healthy children (**chapter 8**). It appeared that the data enabled a full 3D reconstruction of the cardiac strain. The measured strain curves were in accordance with those obtained in previous studies, despite the low image quality as well as frame rate (35 - 50 Hz). Proper validation is necessary, for instance with MRI, before applying the method to patient data. The 3D method could also be used in the future to assess rotation and torsion of the heart. In **chapter 9**, it was shown that the maximum cross-correlation values could be used as an additional feature in the segmentation of

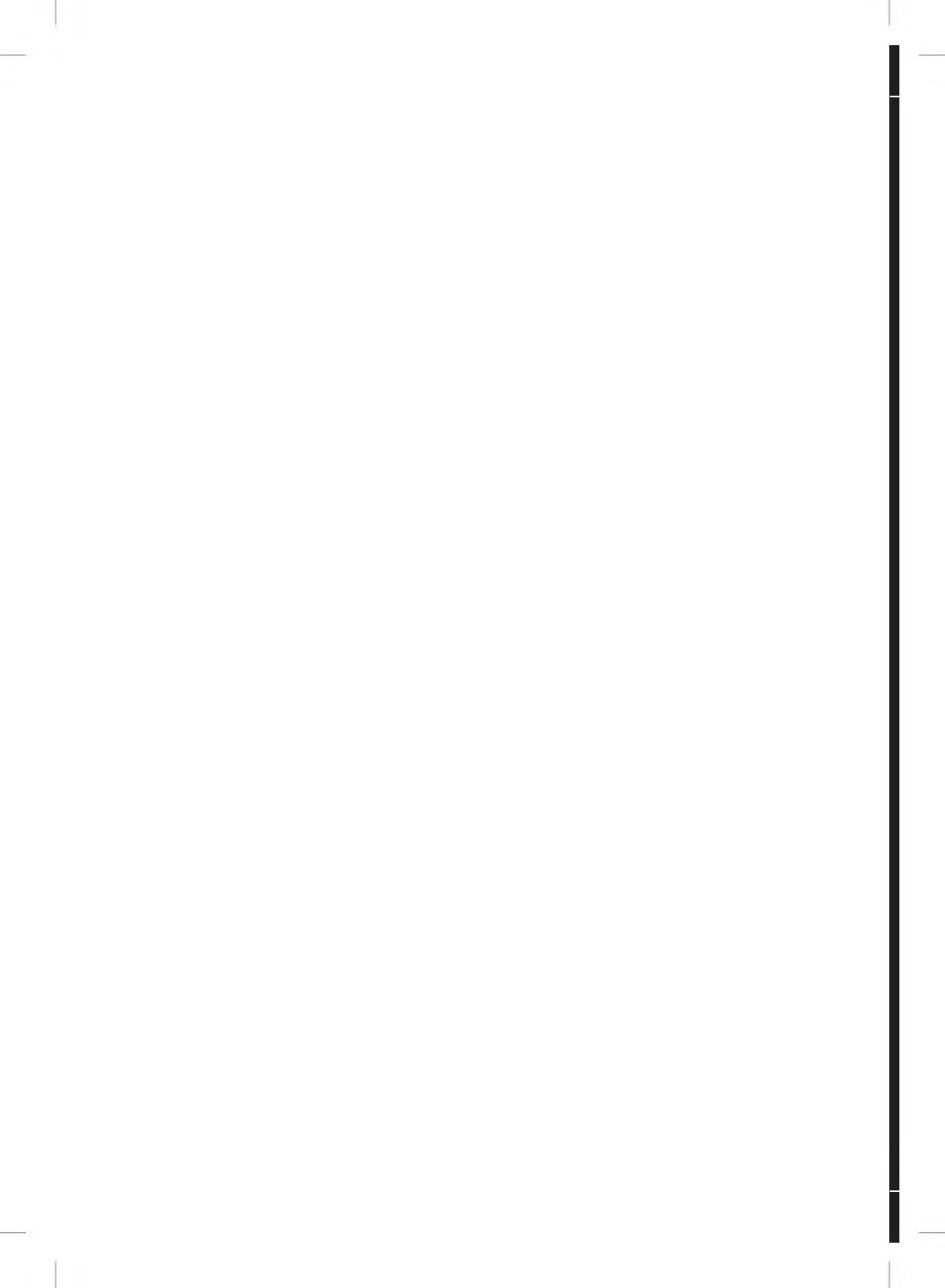
the endocardium. The method was tested on data obtained in 10 healthy children in the end-diastolic and end-systolic phases of the heart cycle. Results revealed improved segmentation results when cross-correlation values were used as an extra feature. Besides the measured cross-correlation values, the estimated displacements could be used to track the segmented inner (and eventually outer) borders of the tissue over the entire cardiac cycle.

In the final part of this thesis, three other applications of 2D and biplane strain imaging were demonstrated. First, the 2D strain algorithm was applied to beam-steered data of vessel phantoms in **chapter 10**. The axial and lateral displacements were estimated and compounded to yield a 360 degree radial and circumferential strain image. The prospects for this method are great and the *in vivo* applicability is already under investigation. Secondly, 2D strain imaging of the cleft lip was explored in **chapter 11**. This pilot study revealed that in normal volunteers, similar strain profiles were found in the different areas of the upper lip. Also, the maximum strain value found appeared to be similar in all volunteers. In a small patient group, it could be shown that non-contractile scar tissue, invisible on regular B-mode images, can be easily detected using strain imaging.

Finally, the method was applied in actively deforming, skeletal muscle tissue (**chapter 12**). Biplane imaging and strain estimation were performed in the biceps muscle, yielding the strain in both the cross-sectional and longitudinal directions of the muscle. Three different types of induced and voluntary contraction

patterns were examined. Biplane strain was measured during a) single twitch contraction; b) tetanic contraction and c) voluntary contraction. The latter makes the technique suitable for clinical application, since no electrical stimulation was required. Preliminary results revealed the reproducibility and feasibility of the technique. The shape of the strain curves resembled the measured force curves, although the relaxation of the strain was significantly slower than muscle force decay. This technique could be used to diagnose and monitor the process of muscle disease progression, for instance in patients with amyotrophic lateral sclerosis.

**In conclusion**, RF-based 2D and 3D strain techniques can be used to measure strain in actively deforming tissue and are suitable for a large variety of applications. Since echographic systems with RF-data are becoming more and more available, the prospects of the techniques are excellent, as well as various. Nevertheless, additional research is considered to be necessary, especially for the final development of full 3D applications.





---

# CHAPTER 15

NEDERLANDSE  
SAMENVATTING

---



Ultrageluid (UG) is een alom gebruikte diagnostische techniek voor de, niet-invasieve, beeldvorming van biologische weefsels en organen. Ondanks de bekende fysische limieten van akoestiek binnen het menselijke lichaam, zijn er zeer veel verschillende toepassingen van ultrageluid in de geneeskunde. De spatiële en temporele resoluties van ultrageluid zijn nog altijd superieur ten opzichte van CT en MRI, hoewel de beelden bekend staan om het ruizige karakter, ook wel “speckle” patroon genoemd. Daarnaast is het nauwelijks mogelijk om harde structuren zoals bot en de hierachter liggende weefsels in beeld te brengen. Doppler technieken en ‘Speckle Tracking’ kunnen gebruikt worden om respectievelijk bloedstroomsnelheid, weefselbeweging en weefselvervorming (rek) te meten. De ruwe ultrageluiddata, de zogenaamde radio frequentie (RF) data, bevat, naast de signaal amplitude die op het scherm wordt afgebeeld, waardevolle fase informatie die de meting van weefselbeweging en vervorming kan verbeteren. Echter, RF-data is niet altijd in commerciële UG apparatuur beschikbaar. In dit proefschrift worden verschillende aspecten onderzocht van het in beeld brengen en meten van beweging en vervorming van weefsels met gebruikmaking van RF-data. De ontwikkelde en voorgestelde methoden werden daarnaast toegepast op een grote variëteit aan *in vivo* data.

Veel technieken zijn ontwikkeld voor het bepalen de vervorming in de richting van de ultrageluidbundel en zijn 1D, in de richting van de ultrageluidbundel, hoewel steeds meer 2D en 3D technieken gerapporteerd worden. Echter, de bepaling van rek in de

richtingen loodrecht op de ultrageluidbundel blijft vaak zowel moeilijk als uitdagend. De werking en prestaties van een ontwikkeld algoritme voor het meten van 2D verplaatsing en rek werden tot in detail onderzocht in **hoofdstuk 2**. Een simulatie studie en verschillende experimenten werden uitgevoerd om de nauwkeurigheid, precisie en het contrast te kwantificeren van zowel de verticale (axiale) als de horizontale (laterale) verplaatsingen en rekken, dit met behulp van een “linear array” transducer. Een iteratief algoritme voor 2D verplaatsing en rek bepaling werd ontwikkeld. Deze methode schat eerst de verplaatsingen op grove schaal (lage resolutie) en verbeterde daarna deze benadering op fijne(re) schaal (hoge resolutie). Deze methode verbetert de schatting van rek aanzienlijk in structuren waar grote verplaatsingen voorkomen en laat het gebruik van kleine segmenten RF-data toe, wat het meten van hogere rekken ten goede komt. Het gebruik van een 2D parabolische interpolatie van de kruis-correlatie functie voor het bepalen van subresolutie (sub sample) verplaatsingswaardes bleek een goed alternatief te zijn voor de tijdrovende interpolatie van RF-data zonder dat hierbij precisie verloren ging. Verdere verbetering werd bereikt door lokale 2D uitlijning en uitrekking van de vervormde RF-data. Deze vorm van data “registratie” resulteerde in de mogelijkheid om hoge rekken te meten met zowel een hoge resolutie als een hoge mate van precisie en nauwkeurigheid. Deze methodologie werd verder verbeterd door vervorming van het 2D zoekgebied toe te staan in de axiale (verticale) richting, gebruikmakende van eerdere geschatte axiale verplaatsingen (**hoofdstuk 3**). Deze

zogenaamde ‘vrije vorm’ 2D techniek voor het meten van verplaatsingen en rekken is vooral voordelig voor structuren waarin grote afschuifrekken en rotaties voorkomen. Uit de resultaten bleek dat normaal afschuifrek en rotatie de nauwkeurigheid en precisie van verticale en horizontale rek bepaling aanzienlijk verminderen. Echter, met de voorgestelde techniek konden axiale afschuifrekken tot 6.0% en rotatie tot 5.0 graden gemeten worden. De bepaling van de verticale en horizontale rekken was significant beter in vergelijking tot de conventionele 1D en 2D technieken.

In veel toepassingen wordt zogenaamde sector scan data verkregen met “phased array” en “curved (convex) array” transducers. Het voordeel van een sector scan, in vergelijking tot een rechthoekige afbeelding, is de grote(re) beeldsector en de kleinere afmetingen van de transducer. Echter, de afstand tussen de lijnen neemt toe met de beelddiepte, dus de spatiële resolutie neemt af met de diepte. In **hoofdstuk 4** wordt het gebruik gedemonstreerd van 2D RF-data die werden opgenomen voor rek bepaling met een phased array transducer. Daarnaast werd wederom de verbetering door het gebruik van lokale uitlijning en vervorming van deze sector RF-data bepaald. De ontwikkelde methodes bleken toepasbaar op de sector scan data en de 2D techniek leverde betere resultaten dan de 1D methode. Een additionele verbetering in rek bepaling werd bewerkstelligd door het gebruik van lokale uitlijning en vervorming van de sector scan RF-data. Echter, de nauwkeurigheid, precisie en het contrast van de verplaatsing en rek bepaling waren lager in vergelijking tot de linear array data uit hoofdstuk 2 en 3.

Dit werd voornamelijk veroorzaakt door de slechtere laterale sampling (bemonstering) en de lagere zendfrequenties van de gebruikte transducers.

De bepaling van rek uit gemeten verplaatsingsvelden werd ook onder de loep genomen. Een veelgebruikte techniek voor het berekenen van de rek is de zogenaamde 1D “kleinste-kwadraten” rek schatter (LSQSE). In **hoofdstuk 5** werd onderzocht of een 2D variant van deze LSQSE de bepaling van rek in sector scan data zou verbeteren. Deze 2D LSQSE bleek beter te presteren dan de 1D LSQSE en kon zowel axiale en laterale rekken, alsmede de verticale en horizontale rekken bepalen. Vooral de laterale/horizontale rek bepaling verbeterde significant. Echter, hogere precisie werd behaald ten koste van resolutie. Dit maakt de toepassing van deze techniek niet triviaal.

Na uitvoerig testen van de diverse technieken, zijn verschillende *in vivo* toepassingen onderzocht, waarbij het rek bepaling in actief deformerend weefsel betrof. Daarbij is een accumulatie van verplaatsing en rek in de tijd nodig om *in vivo* de deformatie van het weefsel tijdens de gehele contractie/relaxatie cyclus te kwantificeren. Een eenvoudig tracking algoritme werd geïmplementeerd (**hoofdstuk 6**). Naast accumulatie van de verplaatsing in de tijd worden ook de berekende kruiscorrelatie (cross-correlation) waarden gebruikt tijdens tracking. Deze dienen als maat voor de benodigde regularisatie die vereist is om fout accumulatie en de resulterende drift in rek data te beperken.

In het tweede deel van deze thesis is de toepassing van de methodiek in het hart onderzocht. In **hoofdstuk 7** zijn de geïntro-

duceerde 2D methodes toegepast op biplane data van het hondenhart. Het voordeel van biplane is de beschikbaarheid van twee vlakken die loodrecht op elkaar staan, waardoor de vervorming in drie loodrechte richtingen gemeten kan worden. Het hart van vier beagles met een valvulaire aorta stenose werd op regelmatige tijdstippen met ultrageluid afgebeeld. Biplane RF-data werd met een matrix array transducer opgenomen (3D probe). De radiële, circumferentiële en longitudinale rek werden bepaald tijdens de gehele hart cyclus bij een relatief lage beeldfrequentie van 100 Hz. De resultaten toonden aan dat de vier beagles ieder een verschillende gradatie van stenose en hypertrofie ontwikkelden. De rek analyse onthulde een afname in contractiliteit (lagere rek toename tijdens systole) en een stijvere spier (lagere totale rek) bij een toename in de ontwikkelde druk gradiënt over de aortaklep. Histologische bevindingen bevestigden deze resultaten. De resultaten van deze biplane studie waren bemoedigend en suggereren een toepassing in de kliniek voor het monitoren van hypertrofie van het hart. Echter, een volledige 3D reconstructie van rek in het hele linker ventrikel bleef bij deze proefstudie uit. Als een eerste stap naar volledige 3D rek bepaling van het hart werd de 2D methodologie van de hoofdstukken 2 t/m 7 uitgebreid naar 3D en getest op 3D ultrageluiddata van het linker ventrikel bij jonge, gezonde kinderen (**hoofdstuk 8**). Een volledige 3D reconstructie van de rek in het linker ventrikel bleek mogelijk te zijn. De gemeten rekken waren vergelijkbaar met die gemeten in andere studies, ondanks de vaak lage beeldkwaliteit en de lage beeldfrequentie van de 3D volume data (35-50 Hz).

Een validatie van deze techniek met bijvoorbeeld MRI moet nog uitgevoerd worden, alvorens een grootschalige patiënten studie kan beginnen. De methodologie zou ook gebruikt kunnen worden om 3D rotatie en torsie van het hart te meten. In **hoofdstuk 9** werd de berekende 3D kruiscorrelatie van de 3D volume data voor aanverwante doeleinden gebruikt, namelijk voor segmentatie van het endocardium. Het gebruik van kruiscorrelatie als extra beeldeigenschap bij automatische segmentatie werd getest op 3D data van gezonde kinderen tijdens de eind-diastolische en eind-systolische fase van de hart cyclus, en verbetering in segmentatie werd waargenomen. Naast de berekende kruiscorrelatie waarden zouden ook de geschatte verplaatsingen gebruikt kunnen worden om de gesegmenteerde binnenwand (en uiteindelijk ook de buitenwand) van het hartweefsel te volgen tijdens de gehele hart cyclus.

In het laatste deel van dit proefschrift worden drie andere toepassingen van 2D en biplane rek bepaling met ultrageluid gedemonstreerd. Eerst werd het algoritme voor 2D rek bepaling toegepast op data in artificiële vaten, die onder verschillende hoeken in beeld gebracht zijn (**hoofdstuk 10**). Het 2D verplaatsingsveld werd geschat, waarna de beelden, onder verschillende hoeken werden opgenomen en samengevoegd tot een totaalbeeld van de in het vat aanwezig zijnde radiële en circumferentiële rek. De vooruitzichten van deze methode zijn zeer goed en de *in vivo* toepasbaarheid wordt momenteel onderzocht. Ten tweede werd 2D rek bepaling in de schisis (hazenlip) gedemonstreerd in **hoofdstuk 11**. Deze proefstudie toonde aan dat in

gezonde vrijwilligers gelijke rek profielen werden gemeten in verschillende gebieden van de bovenlip. Verder bleek de maximale rek gelijk te zijn in alle vrijwilligers. In een kleine groep schisis patiënten, die een lip reconstructie ondergaan waren, werd littekenweefsel ontdekt, dat niet contraheerde. Deze gebieden waren echter op de normale echobeelden niet te onderscheiden van het gezonde weefsel. Tenslotte werd de methode toegepast op data van actief samentrekkende skeletspieren (**hoofdstuk 12**). Biplane ultrageluid data werd opgenomen in de biceps tijdens spiercontractie. De rek werd vervolgens bepaald in een dwarsdoorsnede en lengtedoorsnede van de spier. Drie verschillende soorten samentrekking werden onderzocht en de rek en kracht werden bepaald voor een a) enkele 'twitch' contractie; b) tetanische contractie en c) vrijwillige contractie. Laatstgenoemde maakt deze techniek nog geschikter voor ruime toepassing in de kliniek, aangezien er geen elektri-

sche stimulatie voor nodig is. Voorlopige resultaten toonden de reproduceerbaarheid en haalbaarheid van deze techniek aan. De vorm van de rek curven was gelijk aan die van de kracht curven. Echter, de gemeten relaxatie van de spier in termen van rek was significant trager dan de kracht afname. Deze techniek zou gebruikt kunnen worden bij patiënten met progressieve spierziektes zoals amyotrofische laterale sclerose.

**Concluderend**, we hebben aangetoond dat technieken voor de bepaling van rek uit 2D en 3D ultrageluid RF-data in staat zijn rek te meten in actief vervormend weefsel en voor verschillende toepassingen aangevend kunnen worden. Inmiddels zijn UG systemen met toegang tot RF-data steeds beter verkrijgbaar, waardoor de vooruitzichten van deze technieken uitstekend zijn en de mogelijkheden talrijk. Desalniettemin is aanvullend onderzoek nog vereist, vooral op het gebied van de 3D toepassingen.

---

# REFERENCES

---

- Adler RS, Rubin JM, Bland PH, Carson PL. Quantitative tissue motion analysis of digitized M-mode images: gestational differences of fetal lung. *Ultrasound Med Biol* 1990; 16: 561-569.
- Ahlgren AR, Cinthio M, Steen S, Persson HW, Sjoberg T, Lindstrom K. *Effects of adrenaline on longitudinal arterial wall movements and resulting intramural shear strain: a first report*. *Clin Physiol Funct Imaging* 2009; 29: 353-359.
- Al-Chalabi A, Leigh PN. *Recent advances in amyotrophic lateral sclerosis*. *Curr Opin Neurol* 2000; 13: 397-405.
- Alam SK, Ophir J. *Reduction of signal decorrelation from mechanical compression of tissues by temporal stretching: applications to elastography*. *Ultrasound Med Biol* 1997; 23: 95-105.
- Alam S, Ophir J, Konofagou E. *An adaptive strain estimator for elastography*. *IEEE Trans Ultrason Ferroel Freq Contr* 1998; 45: 461-472.
- Alam SK, Ophir J, Varghese T. *Elastographic axial resolution criteria: an experimental study*. *IEEE Trans Ultrason Ferroel Freq Contr* 2000; 47: 304-309.
- Angelini ED, Laine AF, Takuma S, Holmes JW, Homma S. *LV volume quantification via spatiotemporal analysis of real-time 3-D echocardiography*. *IEEE Trans Med Imag* 2001; 20: 457-469.
- Angelini ED, Gerard O. *Review of myocardial motion estimation methods from optical flow tracking on ultrasound data*. *Conf Proc IEEE Eng Med Biol Soc* 2006; 1537-1540.
- Baldewsing RA, de Korte CL, Schaar JA, Mastik F, van der Steen AF. *A finite element model for performing intravascular ultrasound elastography of human atherosclerotic coronary arteries*. *Ultrasound Med Biol* 2004a; 30: 803-813.
- Baldewsing RA, de Korte CL, Schaar JA, Mastik F, van der Steen AF. *Finite element modeling and intravascular ultrasound elastography of vulnerable plaques: parameter variation*. *Ultrasonics* 2004b; 42: 723-729.
- Bilgen M, Insana M. *Predicting target detectability in acoustic elastography*. *Proc IEEE Ultrasonics Int Conf, Toronto, Canada* 1997; 1427-1430.
- Blemker SS, Pinsky PM, Delp SL. *A 3D model of muscle reveals the causes of nonuniform strains in the biceps brachii*. *J Biomech* 2005; 38: 657-665.
- Bohs LN, Trahey GE. *An efficient technique for two-dimensional ultrasonic velocity imaging*. *Ultrason Imag* 1989; 11:133.
- Bohs LN, Trahey GE. *A novel method for angle independent ultrasonic imaging of blood flow and tissue motion*. *IEEE Trans Biomed Eng* 1991; 38: 280-286.
- Bosch JG, Mitchell SC, Lelieveldt BP, et al. *Automatic segmentation of echocardiographic sequences by active appearance motion models*. *IEEE Trans Med Imag* 2002; 21: 1374-1383.
- Bottger T, Kunert T, Meinzer HP, Wolf I. *Application of a new segmentation tool based on interactive simplex meshes to cardiac images and pulmonary MRI data*. *Acad Radiol* 2007; 14: 319-329.
- Boukerroui D, Basset O, Baskurt A, Gimenez G. *A multiparametric and multiresolution segmentation algorithm of 3-D ultrasonic data*. *IEEE Trans Ultrason Ferroel Freq Contr* 2001; 48: 64-77.
- Brusseau E, de Korte CL, Mastik F, Schaar J, van der Steen AF. *Fully automatic luminal contour segmentation in intracoronary ultrasound imaging--a statistical approach*. *IEEE Trans Med Imaging* 2004; 23: 554-566.
- Brusseau E, Deprez JF, Duboeuf F, Basset O. *Locally regularized strain field estimation for freehand elastography*. *Conf Proc IEEE Eng Med Biol Soc* 2007; 75-78.
- Cerqueira M, Weissman N, Dilsizian V, Jacobs A, Kaul S, Laskey W, Pennell D, Rumberger J, Ryan T, Verani M. *Standardized myocardial*



- segmentation and nomenclature for tomographic imaging of the heart: A statement for healthcare professionals from the Cardiac Imaging Committee of the Council on Clinical Cardiology of the American Heart Association. *Circulation* 2002;105:539–542.
- Céspedes EI, Ophir J, Ponnekanti H, Maklad N. *Elastography: Elasticity imaging using ultrasound with application to muscle and breast in vivo*. *Ultrason Imag* 1993a; 17: 73-88.
- Céspedes I, Ophir J. *Reduction of image noise in elastography*. *Ultrason Imag* 1993b; 15, 89-102.
- Céspedes EI, Huang Y, Ophir J, Spratt S. *Methods for estimation of subsample time delays of digitized echo signals*. *Ultrason Imag* 1995; 17: 142-171.
- Céspedes EI, Ophir J, Alam SK. *The combined effect of signal decorrelation and random noise on the variance of time delay estimation*. *IEEE Trans Ultrason Ferroel Freq Contr* 1997; 44: 220-225.
- Céspedes EI, de Korte CL, van der Steen AF. *Echo decorrelation from displacement gradients in elasticity and velocity estimation*. *IEEE Trans Ultrason Ferroel Freq Contr* 1999; 46: 791-801.
- Céspedes, EI, de Korte, CL, van der Steen, AF. *Intraluminal ultrasonic palpation: assessment of local and cross-sectional tissue stiffness*. *Ultrasound Med Biol* 2000; 26: 385-396.
- Chaturvedi P, Insana M, Hall T. *2-D companding for noise reduction in strain imaging*. *IEEE Trans Ultrason Ferroel Freq Contr* 1998; 45: 179-191.
- Chen H, Shi H, Varghese T. *Improvement of elastographic displacement estimation using a two-step cross-correlation method*. *Ultrasound Med Biol* 2007; 33: 48-56.
- Chen H, Varghese T, Rahko PS, Zagzebski JA. *Ultrasound frame rate requirements for cardiac elastography: experimental and in vivo results*. *Ultrasonics* 2009; 49: 98-111.
- Chen X, Xie H, Erkamp R, et al. *3-D correlation-based speckle tracking*. *Ultrason Imag* 2005; 27: 21-36.
- Chen XC, Zohdy MJ, Emelianov SY, O'Donnell M. *Lateral speckle tracking using synthetic lateral phase*. *IEEE Trans Ultrason Ferroel Freq Contr* 2004; 51: 540-550.
- Cheng GC, Loree HM, Kamm RD, Fishbein MC, Lee RT. *Distribution of circumferential stress in ruptured and stable atherosclerotic lesions: a structural analysis with histopathological correlation*. *Circulation* 1993; 87: 1179-1187.
- Chi SW, Hodgson J, Chen JS, Reggie E, V, Shin DD, Roiz RA, Sinha S. *Finite element modeling reveals complex strain mechanics in the aponeuroses of contracting skeletal muscle*. *J Biomech* 2010; 43: 1243-1250.
- Chi-Fishman G, Hicks JE, Cintas HM, Sonies BC, Gerber LH. *Ultrasound imaging distinguishes between normal and weak muscle*. *Arch Phys Med Rehabil* 2004; 85: 980-986.
- Cho GY, Chan J, Leano R, Strudwick M, Marwick TH. *Comparison of two-dimensional speckle and tissue velocity based strain and validation with harmonic phase magnetic resonance imaging*. *Am J Cardiol* 2006; 97: 1661-6.
- Corsi C, Saracino G, Sarti A, Lamberti C. *Left ventricular volume estimation for real-time three-dimensional echocardiography*. *IEEE Trans Med Imag* 2002; 21: 1202-1208.
- Crosby J, Amundsen BH, Hergum T, Remme EW, Langeland S, Torp H. *3-D Speckle tracking for assessment of regional left ventricular function*. *Ultrasound Med Biol* 2009; 35: 458-471.
- Davies MJ. *Stability and instability: two faces of coronary atherosclerosis*. *Circulation* 1996; 94: 2013-2020.
- Davignon F, Deprez JF, Basset O. *A parametric imaging approach for the segmentation of ultrasound data*. *Ultrasonics* 2005; 43: 789-801.
- d'Hooge J, Heimdal A, Jamal F, et al. *Regional strain and strain rate measurements by*

- cardiac ultrasound: Principles, implementation and limitations. *Eur J Echocardiogr* 2000; 1: 154-170.
- d'Hooge J, Bijnens B, Thoen J, et al. *Echocardiographic strain and strain-rate imaging: a new tool to study regional myocardial function*. *IEEE Trans Med Imaging* 2002a; 21: 1022-1030.
- d'Hooge J, Konofagou E, Jamal F, et al. *Two-dimensional ultrasonic strain rate measurement of the human heart in vivo*. *IEEE Trans Ultrason Ferroelectr Freq Contr* 2002b; 49: 281-286.
- de Jong PGM, Arts T, Hoeks APG, Reneman RS. *Determination of tissue motion velocity by correlation interpolation of pulsed ultrasonic echo signals*. *Ultrason Imag* 1990; 12: 84-98.
- de Jong PGM, Arts T, Hoeks APG, Reneman RS. *Experimental evaluation of the correlation interpolation technique to measure regional tissue velocity*. *Ultrason Imag* 1991; 13: 145-161.
- de Korte CL, Céspedes EI, van der Steen AF, Lancée CT. *Intravascular elasticity imaging using ultrasound: feasibility studies in phantoms*. *Ultrasound Med Biol* 1997a; 23: 735-746.
- de Korte CL, Céspedes EI, van der Steen AF, Norder B, te Nijenhuis K. *Elastic and acoustic properties of vessel mimicking material for elasticity imaging*. *Ultrason Imag* 1997b; 19: 112-126.
- de Korte CL, Céspedes EI, van der Steen AF, Pasterkamp G, Bom N. *Intravascular ultrasound elastography: assessment and imaging of elastic properties of diseased arteries and vulnerable plaque*. *Eur J Ultrasound* 1998; 7: 219-224.
- de Korte CL, Céspedes EI, van der Steen AF. *Influence of catheter position on estimated strain in intravascular elastography*. *IEEE Trans Ultrason Ferroelectr Freq Control* 1999; 46: 616-625.
- de Korte CL, van der Steen AF, Céspedes EI, et al. *Characterization of plaque components and vulnerability with intravascular ultrasound elastography*. *Phys Med Biol* 2000a; 45: 1465-1475.
- de Korte CL, Pasterkamp G, van der Steen AF, Woutman HA, Bom N. *Characterization of plaque components using intravascular ultrasound elastography in human femoral and coronary arteries in vitro*. *Circulation* 2000b; 102: 617-623.
- de Korte CL, Siervogel M, Mastik F, et al. *Identification of atherosclerotic plaque components with intravascular ultrasound elastography in vivo: a Yucatan pig study*. *Circulation* 2002a; 105: 1627-1630.
- de Korte CL, van der Steen AF. *Intravascular ultrasound elastography: an overview*. *Ultrasonics* 2002b; 40: 859-865.
- Deffieux T, Gennisson JL, Tanter M, Fink M. *Assessment of the mechanical properties of the musculoskeletal system using 2-D and 3-D very high frame rate ultrasound*. *IEEE Trans Ultrason Ferroelectr Freq Control* 2009; 55: 2177-2190.
- Delingette H. *General object reconstruction based on simplex meshes*. *Intern J Comp Vision* 1999; 32: 111-146.
- Deng J, Newton NM, Hall-Craggs MA, et al. *Novel technique for three-dimensional visualisation and quantification of deformable, moving soft-tissue body parts*. *Lancet* 2000; 356: 127-131.
- Dice LR. *Measures of the Amount of Ecologic Association Between Species*. *Ecology* 1945; 26:2 97-302.
- Dickinson RJ, Hill CR. *Measurement of soft tissue motion using correlation between A scans*. *Ultrasound Med Biol* 1982; 8: 263-271.
- Dresner MA, Rose GH, Rossman PJ, Muthupillai R, Manduca A, Ehman RL. *Magnetic resonance elastography of skeletal muscle*. *J Magn Res Imag* 2001; 13: 269-276.
- Dydenko I, Friboulet D, Gorce JM, D'hooge J, Bijnens B, Magnin IE. *Towards ultrasound cardiac image segmentation based on the radio-frequency signal*. *Med Image Anal* 2003; 7:

353-367.

Elen A, Choi HF, Loeckx D, et al. *Three-dimensional cardiac strain estimation using spatio-temporal elastic registration of ultrasound images: a feasibility study*. IEEE Trans Med Imag 2008; 27: 1580-1591.

Emelianov SY, Lubinski MA, Weitzel WF, Wiggins RC, Skovoroda AR, O'Donnell M. *Elasticity imaging for early detection of renal pathology*. Ultrasound Med Biol 1995; 21: 871-83.

Emelianov SY, Chen X, O'Donnell M, et al. *Triplex ultrasound: elasticity imaging to age deep venous thrombosis*. Ultrasound Med Biol 2002; 28: 757-767.

Fung-Kee-Fung SD, Lee WN, Ingrassia CM, Costa KD, Konofagou EE. *Angle-independent strain mapping in myocardial elastography*. Proc IEEE Ultrasonics Int Conf, Rotterdam, The Netherlands, 2005; 516-519.

Ganame J, Pignatelli RH, Eidem BW, et al. *Myocardial deformation abnormalities in pediatric hypertrophic cardiomyopathy: are all etiologies identical?* Eur J Echocardiogr 2008; 9: 784-90.

Gao H, Choi HF, Claus P, et al. *A new convolution-based methodology to simulate ultrasound images in a 2D/3D sector format*. Proc IEEE Ultrasonics Int Conf, New York, USA, 2007; 2243-2246.

Garra BS, Céspedes EI, Ophir J, et al. *Elastography of breast lesions: Initial clinical results*. Radiology 1997; 202: 79-86.

Gerard O, Billon AC, Rouet JM, Jacob M, Fradkin M, Allouche C. *Efficient model-based quantification of left ventricular function in 3-D echocardiography*. IEEE Trans Med Imag 2002; 21: 1059-1068.

Gerrits IH, Nillesen MM, Lopata RGP, Rijk JPT, Thijssen JM, de Korte CL. *A robust deformable simplex mesh model with temporal signal decorrelation constraints in echocardiography*. Proc. IEEE Ultrasonics Int. Conf., New York,

USA, 2007; 1484-1487.

Gopal AS, Shen ZQ, Sapin PM, et al. *Assessment of cardiac-function by 3-dimensional echocardiography compared with conventional noninvasive methods*. Circulation 1995; 92: 842-853.

Grubb NR, Fleming A, Sutherland GR, Fox KA. *Skeletal muscle contraction in healthy volunteers: assessment with Doppler tissue imaging*. Radiology 1995; 194: 837-842.

Hall TJ, Zhu Y, Spalding CS. *In vivo real-time freehand palpation imaging*. Ultrasound Med Biol 2003; 29: 427-435.

Han W, Xie MX, Wang XF, et al. *Assessment of left ventricular torsion in patients with anterior wall myocardial infarction before and after revascularization using speckle tracking imaging*. Chin. Med J (Engl.) 2008; 121: 1543-1548.

Hansegard J, Urheim S, Lunde K, Rabben SI. *Constrained active appearance models for segmentation of triplane echocardiograms*. IEEE Trans Med Imag 2007; 26: 1391-1400.

Hansen HHG, Lopata RGP, de Korte CL. *Compounding of strain data non-invasively obtained at large beam steered angles*. Proc IEEE Ultrasonics Int Conf, New York, USA 2007; 1720-1723.

Hansen HHG, Lopata RGP, Holewijn S, Truijers M, de Korte CL. *Noninvasive vascular ultrasound strain imaging: different arteries, different approaches*. Proc IFMBE, Antwerp, Belgium 2008; 22: 298-302.

Heckman CJ, Perreault EJ, Sandercock TG, Maas H. *Muscle*. Encyclopedia of Neuroscience 2009; 2479-2487.

Heimdal A, Stoylen A, Torp H, Skaerpe T. *Real time strain rate imaging of the left ventricle by ultrasound*. J Am Soc Echocardiogr 1998; 11: 1013-1019.

Hori Y, Tsubaki M, Katou A, et al. *Evaluation of NT-pro BNP and CT-ANP as markers of concentric hypertrophy in dogs with a model of compensated aortic stenosis*. J Vet Intern Med

2008; 22: 1118-1123.

Hui L, Pemberton J, Hickey E, et al. *The contribution of left ventricular muscle bands to left ventricular rotation: assessment by a 2-dimensional speckle tracking method.* J Am Soc Echocardiogr 2007; 20(5): 486-491.

The ITK software guide (computer program). 2003.

Jacobs LD, Salgo IS, Goonewardena S, et al. *Rapid online quantification of left ventricular volume from real-time three-dimensional echocardiographic data.* Eur Heart J 2006; 27: 460-468.

Jensen JA, Svendsen NB. *Calculation of pressure fields from arbitrarily shaped, apodized, and excited ultrasound transducers.* IEEE Trans Ultrason Ferroel Freq Contr 1992; 3: 262-267.

Jensen JA. *Field: a program for simulating ultrasound systems.* Med Biol Eng Comp 1996; 35:1-353.

Jia C, Kim K, Koliass TJ, et al. *4D elasticity imaging of PVA LV phantom integrated with pulsatile circulation system using 2D phased array.* Proc IEEE Ultrasonics Int Conf, New York, USA 2007: 876-879.

Kallel F, Bertrand M. *Tissue elasticity reconstruction using linear perturbation method.* IEEE Trans Med Imaging 1996a; 15: 299-313.

Kallel F, Bertrand M, Ophir J. *Fundamental limitations on the contrast-transfer efficiency in elastography: an analytic study.* Ultrasound Med Biol 1996b; 22: 463-470.

Kallel F, Ophir J. *A least-squares strain estimator for elastography.* Ultrason Imag 1997; 19: 195-208.

Kallel F, Ophir J, Magee K, Krouskop T. *Elastographic imaging of low-contrast elastic modulus distributions in tissue.* Ultrasound Med Biol 1998; 24: 409-425.

Kallel F, Price RE, Konofagou EE, Ophir J. *Elastographic imaging of the normal canine*

*prostate in vitro.* Ultrason Imag 1999; 21: 201-215.

Kaluzynski K, Chen X, Emelianov SY, Skovoroda AR, O'Donnell M. *Strain rate imaging using two-dimensional speckle tracking.* IEEE Trans Ultrason Ferroel Freq Contr 2001; 48: 1111-1123.

Kanai H, Hasegawa H, Chubachi N, Koiwa Y and Tanaka M. *Noninvasive evaluation of local myocardial thickening and its color-coded imaging.* IEEE Trans Ultrason Ferroel Freq Contr 1997; 44: 752-768.

Khaled W, Reichling S, Bruhns OT, Ermert H. *Ultrasonic strain imaging and reconstructive elastography for biological tissue.* Ultrasonics 2006; 44(Suppl. 1): 199-202.

Khalid O, Luxenberg DM, Sable C, et al. *Aortic stenosis: the spectrum of practice.* Pediatr. Cardiol 2006; 27: 661-669.

Kincaid JC, Brashear A, Markand ON. *The influence of the reference electrode on CMAP configuration.* Muscle Nerve 1993; 16: 392-396.

Kiraly P, Kapusta L, van Lier H, Hofman AO, Daniels O. *Natural history of congenital aortic valvar stenosis: an echo and Doppler cardiographic study.* Cardiol Young 1997; 7: 188-193.

Kiraly P, Kapusta L, Thijssen JM, Daniels O. *Left ventricular myocardial function in congenital valvar aortic stenosis assessed by ultrasound tissue-velocity and strain-rate techniques.* Ultrasound Med Biol 2003; 29: 615-620.

Kleis SJ, Sanchez LA. *Dependence of speed of sound on salinity and temperature in concentrated NaCl solutions.* Solar Energy 1990; 45: 201-206.

Konofagou E, Ophir J. *A new elastographic method for estimation and imaging of lateral displacements, lateral strains, corrected axial strains and Poisson's ratios in tissues.* Ultrasound Med Biol 1998; 24: 1183-1199.

Konofagou EE, Varghese T, Ophir J, Alam SK.

- Power spectral strain estimators in elastography.* *Ultrasound Med Biol* 1999; 25: 1115-1129.
- Konofagou EE, Varghese T, Ophir J. *Theoretical bounds on the estimation of transverse displacement, transverse strain and Poisson's ratio in elastography.* *Ultrason Imag* 2000a; 22: 153-177.
- Konofagou EE, Ophir J. *Precision estimation and imaging of normal and shear components of the 3D strain tensor in elastography.* *Phys Med Biol* 2000b; 45: 1553-1563.
- Konofagou EE, d'Hooge J, Ophir J. *Myocardial elastography: a feasibility study in vivo.* *Ultrasound Med Biol* 2002; 28: 475-482.
- Kowalski M, Herbots L, Weidemann F, et al. *One-dimensional ultrasonic strain and strain rate imaging: a new approach to the quantitation of regional myocardial function in patients with aortic stenosis.* *Ultrasound Med Biol* 2003; 29: 1085-1092.
- Krouskop TA, Wheeler TM, Kallel F, Garra BS, Hall T. *Elastic moduli of breast and prostate tissues under compression.* *Ultrason Imaging* 1998; 20: 260-274.
- Krucker JF, Fowlkes JB, Carson PL. *Sound speed estimation using automatic ultrasound image registration.* *IEEE Trans Ultrason Ferroelectr Freq Control* 2004; 51: 1095-1106.
- Lacefield JC, Pilkington WC, Waag RC. *Comparisons of lesion detectability in ultrasound images acquired using time-shift compensation and spatial compounding.* *IEEE Trans Ultrason Ferroelectr Freq Control* 2004; 51: 1649-1659.
- Lang RM, Mor-Avi V, Sugeng L, Nieman PS, Sahn DJ. *Three-dimensional echocardiography: the benefits of the additional dimension.* *J Am Coll Cardiol* 2006; 48: 2053-2069.
- Langeland S, d'Hooge J, Torp H, Bijnens B, Suetens P. *Comparison of time-domain displacement estimators for two-dimensional rf tracking.* *Ultrasound Med Biol* 2003; 29: 1177-1186.
- Langeland S, d'Hooge J, Claessens T, et al. *RF-based two-dimensional cardiac strain estimation: a validation study in a tissue-mimicking phantom.* *IEEE Trans Ultrason Ferroelectr Freq Contr* 2004; 51: 1537-1546.
- Langeland S, d'Hooge J, Wouters PF, et al. *Experimental validation of a new ultrasound method for the simultaneous assessment of radial and longitudinal myocardial deformation independent of insonation angle.* *Circulation* 2005a; 112: 2157-2162.
- Langeland S, Wouters PF, Leather HA, Claus P, Bijnens B, d'Hooge J. *A parametric study on processing parameters for two-dimensional cardiac strain estimation: an in vivo study.* *Proc IEEE Ultrasonics Int Conf, Rotterdam, The Netherlands* 2005b. 1360-1363.
- Langeland S. *Multi-Dimensional Quantification of Myocardial Deformation using Echocardiographic Imaging: Development, Implementation and Validation.* *Katholic University of Leuven*; 2007.
- Ledesma-Carbayo M, Mahia-Casado P, Santos A, Perez-David E, Garcia-Fernandez MA, Desco M. *Cardiac motion analysis from ultrasound sequences using nonrigid registration: validation against Doppler tissue velocity.* *Ultrasound Med Biol* 2006; 32: 483-490.
- Lee WN, Ingrassia CM, Fung-Kee-Fung SD, Costa KD, Holmes JW, Konofagou EE. *Theoretical quality assessment of myocardial elastography with in vivo validation.* *IEEE Trans Ultrason Ferroelectr Freq Contr* 2007; 54: 2233-2245.
- Lee WN, Konofagou EE. *Angle-independent and multi-dimensional myocardial elastography: from theory to clinical validation.* *Ultrasonics* 2008; 48: 563-567.
- Leitman M, Lysyansky P, Sidenko S, et al. *Two-dimensional strain—a novel software for real-time quantitative echocardiographic assessment of myocardial function.* *J Am Soc Echocardiogr* 2004; 17: 1021-1029.
- Lin N, Yu W, Duncan JS. *Combinative multi-scale level set framework for echocardiographic*

## References

---

- image segmentation. *Med Image Anal* 2003; 7: 529-537.
- Lindop JE, Treece GM, Gee AH, Prager RW. *3D elastography using freehand ultrasound*. *Ultrasound Med Biol* 2006; 32: 529-545.
- Lopata RGP, Nillesen MM, Gerrits IH, Thijsen JM, Kapusta L, de Korte CL. *3D strain estimation for isotropic and anisotropic materials*. *Proc IEEE Ultrasonics Int Conf, Rotterdam, The Netherlands* 2005; 731-734.
- Lopata RGP, Nillesen MM, Gerrits IH, Thijsen JM, Kapusta L, de Korte CL. *In vivo 3D cardiac and skeletal muscle strain estimation*. *Proc IEEE Ultrasonics Int Conf, Vancouver, Canada* 2006; 744-747.
- Lopata RGP, Nillesen MM, Gerrits IH, Thijsen JM, Kapusta L, de Korte, CL. *4D Cardiac Strain Imaging: methods and Initial Results*. *Proc IEEE Ultrasonics Int Conf, New York, USA* 2007; 872-875.
- Lopata RGP, Nillesen MM, Gerrits IH, et al. *3D cardiac strain imaging using a novel tracking method*. *Proc IFMBE, Antwerp, Belgium* 2008; 22: 697-700.
- Loram ID, Maganaris CN, Lakie M. *Use of ultrasound to make noninvasive in vivo measurement of continuous changes in human muscle contractile length*. *J Appl Physiol* 2006; 100: 1311-1323.
- Lubinski MA, Emelianov SY, Raghavan KR, Yagle AE, Skovoroda AR, O'Donnell M. *Lateral displacement estimation using tissue incompressibility*. *IEEE Trans Ultrason Ferroel Freq Contr* 1996; 43: 247-256.
- Lubinski MA, Emelianov SY, O'Donnell M. *Speckle tracking methods for ultrasonic elasticity imaging using short-time correlation*. *IEEE Trans Ultrason Ferroelectr Freq Contr* 1999; 46: 82-96.
- Luo J, Bai J, He P, Ying K. *Axial strain calculation using a low-pass digital differentiator in ultrasound elastography*. *IEEE Trans Ultrason Ferroel Freq Control* 2004; 51: 1119-1127.
- Luo J, Fujikura K, Homma S, Konofagou EE. *Myocardial elastography at both high temporal and spatial resolution for the detection of infarcts*. *Ultrasound Med Biol* 2007; 33: 1206-1223.
- Luo J, Lee WN, Konofagou E. *Fundamental performance assessment of 2-D myocardial elastography in a phased array configuration*. *Proc IEEE Ultrasonics Int Conf, Beijing, China* 2008; 954-957.
- Luo X, Cao T, Li Z, Duan Y. *A preliminary study on the evaluation of relationship between left ventricular torsion and cardiac cycle phase by two-dimensional ultrasound speckle tracking imaging*. *Int J Cardiovasc Imaging*, 2009; 25: 559-568.
- Maas H, Baan GC, Huijting PA. *Intermuscular interaction via myofascial force transmission: effects of tibialis anterior and extensor hallucis longus length on force transmission from rat extensor digitorum longus muscle*. *J Biomech* 2001; 34: 927-940.
- Markus AF, Delaire J. *Functional Primary Closure of Cleft-Lip*. *British Journal of Oral & Maxillofacial Surgery* 1993; 31: 281-291.
- Madsen EL, Frank GR, Hobson MA, et al. *Spherical lesion phantoms for testing the performance of elastography systems*. *Phys Med Biol* 2005; 50: 5983-5995.
- Maganaris CN, Paul JP. *Load-elongation characteristics of in vivo human tendon and aponeurosis*. *J Exp Biol* 2000; 203: 751-756.
- Magnusson SP, Hansen P, Aagaard P, Brond J, Dyhre-Poulsen P, Bojsen-Moller J, Kjaer M. *Differential strain patterns of the human gastrocnemius aponeurosis and free tendon, in vivo*. *Acta Physiol Scand* 2003; 177: 185-195.
- Maurice RL, Bertrand M. *Lagrangian speckle model and tissuemotion estimation theory*. *IEEE Trans Med Imaging* 1999; 18: 593-603.
- Maurice RL, Ohayon J, Fretigny Y, Bertrand M, Soulez G, Cloutier G. *Noninvasive vascular*

- elastography: theoretical framework*. IEEE Trans Med Imaging 2004; 23: 164-180.
- McDicken WN, Sutherland GR, Moran CM, Gordan LN. Colour Doppler velocity imaging of the myocardium. *Ultrasound Med Biol* 1992; 18: 651-654.
- Meunier J, Bertrand M. *Ultrasonic texture motion analysis: theory and simulation*. IEEE Trans Med Imaging 1995; 14: 293-300.
- Meunier J. *Tissue motion assessment from 3D echographic speckle tracking*. *Phys Med Biol* 1998; 43: 1241-1254.
- Mercuri E, Jungbluth H, Muntoni F. *Muscle imaging in clinical practice: diagnostic value of muscle magnetic resonance imaging in inherited neuromuscular disorders*. *Curr Opin Neurol* 2005; 18: 526-537.
- Mishima K, Yamada T, Fujiwara K, Sugahara T. *Development and clinical usage of a motion analysis system for the face: preliminary report*. *Cleft Palate Craniofac J* 2004; 41: 559-564.
- Moss A. *Controversies in cleft lip and palate management*. *Ultrasound in Obstetrics & Gynecology* 2001; 18: 420-421.
- Munshi AK, Hegde AM, Srinath SK. *Ultrasonographic and electromyographic evaluation of the labial musculature in children with repaired cleft lips*. *J Clin Pediatr Dent* 2000; 24: 123-128.
- Napolitano D, Chou CH, McLaughlin G, et al. *Sound speed correction in ultrasound imaging*. *Ultrasonics* 2006; 44 (Suppl 1): 43-46.
- Nightingale KR, Kornguth PJ, Walker WF, McDermott BA, Trahey GE. *A novel ultrasonic technique for differentiating cysts from solid lesions: preliminary results in the breast*. *Ultrasound Med Biol*, 1995; 21: 745-751.
- Nillesen MM, Lopata RGP, Gerrits IH, et al. *Segmentation of the heart muscle in 3-D pediatric echocardiographic images*. *Ultrasound Med Biol* 2007; 33: 1453-1462.
- Nillesen MM, Lopata RG, Gerrits IH, Kapusta L, Thijssen JM, de Korte CL. *Modeling envelope statistics of blood and myocardium for segmentation of echocardiographic images*. *Ultrasound Med Biol* 2008; 34: 674-680.
- Nillesen MM, Lopata RG, de Boode WP, et al. *In vivo validation of cardiac output assessment in non-standard 3D echocardiographic images*. *Phys Med Biol* 2009; 54: 1951-1962.
- Noble JA, Boukerroui D. *Ultrasound image segmentation: a survey*. *IEEE Trans Med Imag* 2006; 25: 987-1010.
- Nollet PJ, Kuijpers-Jagtman AM, Chatzigianni A, et al. *Nasolabial appearance in unilateral cleft lip, alveolus and palate: a comparison with Eurocleft*. *J Craniomaxillofac Surg* 2007; 35: 278-286.
- Nottin S, Doucende G, Schuster-Beck I, Dauzat M, Obert P. *Alteration in left ventricular normal and shear strains evaluated by 2D-strain echocardiography in the athlete's heart*. *J Physiol* 2008; 586: 4721-4733.
- O'Donnell M, Skovoroda AR, Shapo BM, Emelianov SY. *Internal displacement and strain imaging using ultrasonic speckle tracking*. *IEEE Trans Ultrason Ferroel Freq Contr* 1994; 41: 314-325.
- O'Leary DH, Polak JF, Kronmal RA. *Carotid-artery intima and media thickness as a risk factor for myocardial infarction and stroke - Reply*. *New England Journal of Medicine* 1999; 340: 1763.
- Oomens CW, Maenhout M, van Oijen CH, Drost MR, Baaijens FP. *Finite element modelling of contracting skeletal muscle*. *Philos Trans R Soc Lond B Biol Sci* 2003; 358: 1453-1460.
- Oosterveld BJ, Thijssen JM, Verhoef WA. *Texture of B-mode echograms: 3-D simulations and experiments of the effects of diffraction and scatterer density*. *Ultrason Imag* 1985; 7: 142-160.
- Ophir J, Céspedes I, Ponnekanti H, Yazdi Y, Li X. *Elastography: a quantitative method for imaging the elasticity of biological tissues*. *Ultra-*

- son Imag 1991; 13: 111-134.
- Ophir J, Alam SK, Garra B, et al. *Elastography: ultrasonic estimation and imaging of the elastic properties of tissues*. Proc Inst Mech Eng [H] 1999; 213: 203-233.
- Pacileo G, Calabro P, Limongelli G, et al. *Left ventricular remodeling, mechanics, and tissue characterization in congenital aortic stenosis*. J Am Soc Echocardiogr 2003; 16: 214-220.
- Pappas GP, Asakawa DS, Delp SL, Zajac FE, Drace JE. Nonuniform shortening in the biceps brachii during elbow flexion. J Appl Physiol 2002; 92: 2381-2389.
- Parker KJ, Huang SR, Musulin RA, Lerner RM. *Tissue response to mechanical vibrations for "Sonoelasticity Imaging"*. Ultrasound Med Biol 1990; 16: 241-246.
- Patil AV, Garson CD, Hossack JA. *3D Prostate elastography: Algorithm, simulations and experiments*. Phys Med Biol 2007; 52: 3643-3663.
- Pettrons P. *Ultrasound of muscles*. Eur Radiol 2002; 12: 35-43.
- Pillen S, Arts IM, Zwarts MJ. *Muscle ultrasound in neuromuscular disorders*. Muscle Nerve 2008; 37: 679-693.
- Ponnekanti H, Ophir J, Huang Y, Céspedes I. *Fundamental mechanical limitations on the visualization of elasticity contrast in elastography*. Ultrasound Med Biol 1995; 21: 533-543.
- Prabhu NT, Munshi AK. *Ultrasonographic observation of the circumoral musculature: an in-vivo study*. J Clin Pediatr Dent 1995; 19: 195-203.
- Ramamurthy BS, Trahey GE. *Potential and limitations of angle-independent flow detection algorithms using radio-frequency and detected echo signals*. Ultrason Imag 1991; 13: 252-268.
- Rao M, Chen Q, Shi H, Varghese T. *Spatial-angular compounding for elastography using beam steering on linear array transducers*. Med Phys 2006; 33: 618-626.
- Rasheed SA, Munshi AK. *Electromyographic and ultrasonographic evaluation of the circumoral musculature in children*. J Clin Pediatr Dent 1996; 20: 305-311.
- Reimers CD, Fleckenstein JL, Witt TN, Muller-Felber W, Pongratz DE. *Muscular ultrasound in idiopathic inflammatory myopathies of adults*. J Neurol Sci 1993; 116: 82-92.
- Ribbers H, Lopata RGP, Holeyijn S, Pasterkamp G, Blankensteijn JD, de Korte CL. *Noninvasive two-dimensional strain imaging of arteries: Validation in phantoms and preliminary experience in carotid arteries in vivo*. Ultrasound Med Biol 2007; 33: 530-540.
- Righetti R, Ophir J, Ktonas P. *Axial resolution in elastography*. Ultrasound Med Biol 2002; 28: 101-113.
- Ritter K, Trotman CA, Phillips C. *Validity of subjective evaluations for the assessment of lip scarring and impairment*. Cleft Palate Craniofac J 2002; 39: 587-596.
- Rubin JM, Xie H, Kim K, et al. *Sonographic elasticity imaging of acute and chronic deep venous thrombosis in humans*. J Ultrasound Med 2006; 25: 1179-1186.
- Ryan LK, Foster FS. *Ultrasonic measurement of differential displacement and strain in a vascular model*. Ultrasonic Imaging 1997; 19: 19-38.
- Sahn DJ, Vick GW 3rd. *Review of new techniques in echocardiography and magnetic resonance imaging as applied to patients with congenital heart disease*. Heart 2001; 86: 1141-53.
- Said G, Basset O, Mari JM, Cachard C, Brusseau E, Vray D. *Experimental three dimensional strain estimation from ultrasonic sectorial data*. Ultrasonics 2006; 44 Suppl 1: 189-193.
- Saito K, Okura H, Watanabe N, et al. *Comprehensive evaluation of left ventricular strain using speckle tracking echocardiography in normal adults: comparison of three-dimensional and two-dimensional approaches*. J Am Soc Echocardiogr 2008; 22: 1025-1030.



- Sasayama S, Ross J, Franklin D, Bloor CM, Bishop S, Dilley RB. *Adaptations of the left ventricle to chronic pressure overload*. *Circ Res* 1976; 38: 172-178.
- Schaar JA, de Korte CL, Mastik F, et al. *Characterizing vulnerable plaque features by intravascular elastography*. *Circulation* 2003; 108: 2636-2641.
- Schaar JA, Muller JE, Falk E, et al. *Terminology for high-risk and vulnerable coronary artery plaques*. *European Heart Journal* 2004; 25: 1077-1082.
- Schaar JA, de Korte CL, Mastik F, et al. *Three-dimensional palpography of human coronary arteries: ex vivo validation and in-patient evaluation*. *Herz* 2005; 30: 125-133.
- Schmitt C, Soulez G, Maurice RL, Giroux MF, Cloutier G. *Noninvasive vascular elastography: toward a complementary characterization tool of atherosclerosis in carotid arteries*. *Ultrasound Med Biol* 2007; 33: 1841-1858.
- Shapo BM, Crowe JR, Skovoroda AR, Eberle M, Cohn NA, O'Donnell M. *Displacement and strain imaging of coronary arteries with intraluminal ultrasound*. *IEEE Trans Ultrason Ferroel Freq Contr* 1996; 43: 234-246.
- Shaw SM, Fox DJ, Williams SG. *The development of left ventricular torsion and its clinical relevance*. *Int J Cardiol* 2008; 130: 319-325.
- Shi H, Varghese T. *Two-dimensional multi-level strain estimation for discontinuous tissue*. *Phys Med Biol* 2007; 52: 389-401.
- Srinivasan S, Kallel F, Ophir J. *Estimating the elastographic signal-to-noise ratio using correlation coefficients*. *Ultrasound Med Biol* 2002; 28: 359-368.
- Sink JD, Attarian DE, Chitwood WR, Jr Hill RC, Pellom GL, Wechsler AS. *An improved technique for producing ventricular hypertrophy with a subcoronary valvular aortic stenosis model*. *Ann Thorac Surg* 1980; 30: 285-290.
- Skovoroda AR, Emelianov SY, O'Donnell M. *Tissue elasticity reconstruction based on ultrasonic displacement and strain images*. *IEEE Trans Ultrason Ferroel Freq Contr* 1995; 42: 747-765.
- Song X, Myronenko A, Sahn DJ. *Speckle tracking in 3D echocardiography with motion coherence*. In: *Computer Vision and Pattern Recognition*. Proc. IEEE Conf. on CVPR 2007: 1-7.
- to be missing after "conf. on Minneapolis, MN, 2007:1-7.
- Srinivasan S, Kallel F, Ophir J. *Estimating the elastographic signal-to-noise ratio using correlation coefficients*. *Ultrasound Med Biol* 2002; 28: 359-368.
- Srinivasan S, Ophir J. *A zero-crossing strain estimator for elastography*. *Ultrasound Med Biol* 2003; 29: 227-238.
- Støylen A, Ingul CB, Torp H. *Strain and strain rate parametric imaging. A new method for post processing to 3-/4-dimensional images from three standard apical planes. Preliminary data on feasibility, artefact and regional dyssynergy visualisation*. *Cardiovasc Res* 2003; 1:11
- Sühling M, Arigovindan M, Jansen C, Hunziker P, Unser M. *Myocardial motion analysis from B-mode echocardiograms*. *IEEE Trans Image Process* 2005; 14: 525-536.
- Sumi C, Sato K. *Regularization for ultrasonic measurements of tissue displacement vector and strain tensor*. *IEEE Trans Ultrason Ferroel Freq Contr* 2008; 55: 787-799.
- Sutherland GR, Di SG, Claus P, d'Hooge J, Bijnens B. *Strain and strain rate imaging: a new clinical approach to quantifying regional myocardial function*. *J Am Soc Echocardiogr* 2004; 17: 788-802.
- Takeuchi M, Nishikage T, Nakai H, Kokumai M, Otani S, Lang RM. *The assessment of left ventricular twist in anterior wall myocardial infarction using two-dimensional speckle tracking imaging*. *J Am. Soc. Echocardiogr* 2007; 20:

36-44.

Tang CY, Zhang G, Tsui CP. *A 3D skeletal muscle model coupled with active contraction of muscle fibres and hyperelastic behaviour.* J Biomech 2009; 42: 865-872.

Tanter M, Bercoff J, Sandrin L, Fink M. *Ultrafast compound imaging for 2-D motion vector estimation: application to transient elastography.* IEEE Trans Ultrason Ferroel Freq Contr 2002; 49: 1363-1374.

Techavipoo U, Chen Q, Varghese T, Zagzebski JA. *Estimation of displacement vectors and strain tensors in elastography using angular insonifications.* IEEE Trans Med Imaging 2004; 23: 1479-1489.

Techavipoo U, Varghese T. *Improvements in elastographic contrast-to-noise ratio using spatial-angular compounding.* Ultrasound in Medicine and biology 2005 ;31: 529-536.

Thitaikumar A, Ophir J, Krouskop TA. *Noise performance and signal-to-noise ratio of shear strain elastograms.* Ultrason Imag 2005; 27: 145-165.

Thitaikumar A, Krouskop TA, Garra BS, Ophir J. *Visualization of bonding at an inclusion boundary using axial-shear strain elastography: a feasibility study.* Phys Med Biol 2007; 25: 2615-2633.

Thitaikumar A, Mobbs LM, Kraemer-Chant CM, Garra BS, Ophir J. *Breast tumor classification using axial shear strain elastography: a feasibility study.* Phys Med Biol 2008; 53: 4809-4823.

Thompson RS, Macaskill C, Fraser VB, Farnell L. *Acoustic intensity for a long vessel with noncircular cross section.* IEEE Trans Ultrason Ferroel Freq Contr 2004; 51: 566-575.

Tournoux F, Chan RC, Handschumacher MD, et al. *Estimation of radial strain and rotation using a new algorithm based on speckle tracking.* J Am Soc Echocardiogr 2008; 21: 1168-1174.

Trahey GE, Allison JW, von Ramm OT. *Angle*

*independent blood flow detection by blood blow.* IEEE Trans Biomed Eng 1988; 34: 965-967.

Trotman CA, Barlow SM, Faraway JJ. *Functional outcomes of cleft lip surgery. Part III: measurement of lip forces.* Cleft Palate Craniofac J 2007a; 44: 617-623.

Trotman CA, Faraway JJ, Losken HW, van Aalst JA. *Functional outcomes of cleft lip surgery. Part II: Quantification of nasolabial movement.* Cleft Palate Craniofac J 2007b; 44: 607-616.

Trotman CA, Phillips C, Essick GK, et al. *Functional outcomes of cleft lip surgery. Part I: study design and surgeon ratings of lip disability and need for lip revision.* Cleft Palate Craniofac J 2007c; 44: 598-606.

van der Steen AF, Thijssen JM, van der Laak JA, Ebben GP, de Wilde PC. *Correlation of histology and acoustic parameters of liver tissue on a microscopic scale.* Ultrasound Med Biol 1994; 20: 177-186.

van der Steen AFW, de Korte CL, Céspedes EI. *Intravascular ultrasound elastography.* Ultraschall in Medizin 1998; 19: 196-201.

van der Toorn A, Barenbrug P, Snoep G, et al. *Transmural gradients of cardiac myofiber shortening in aortic valve stenosis patients using MRI tagging.* Am J Physiol Heart Circ Physiol 2002; 283: 1609-1615.

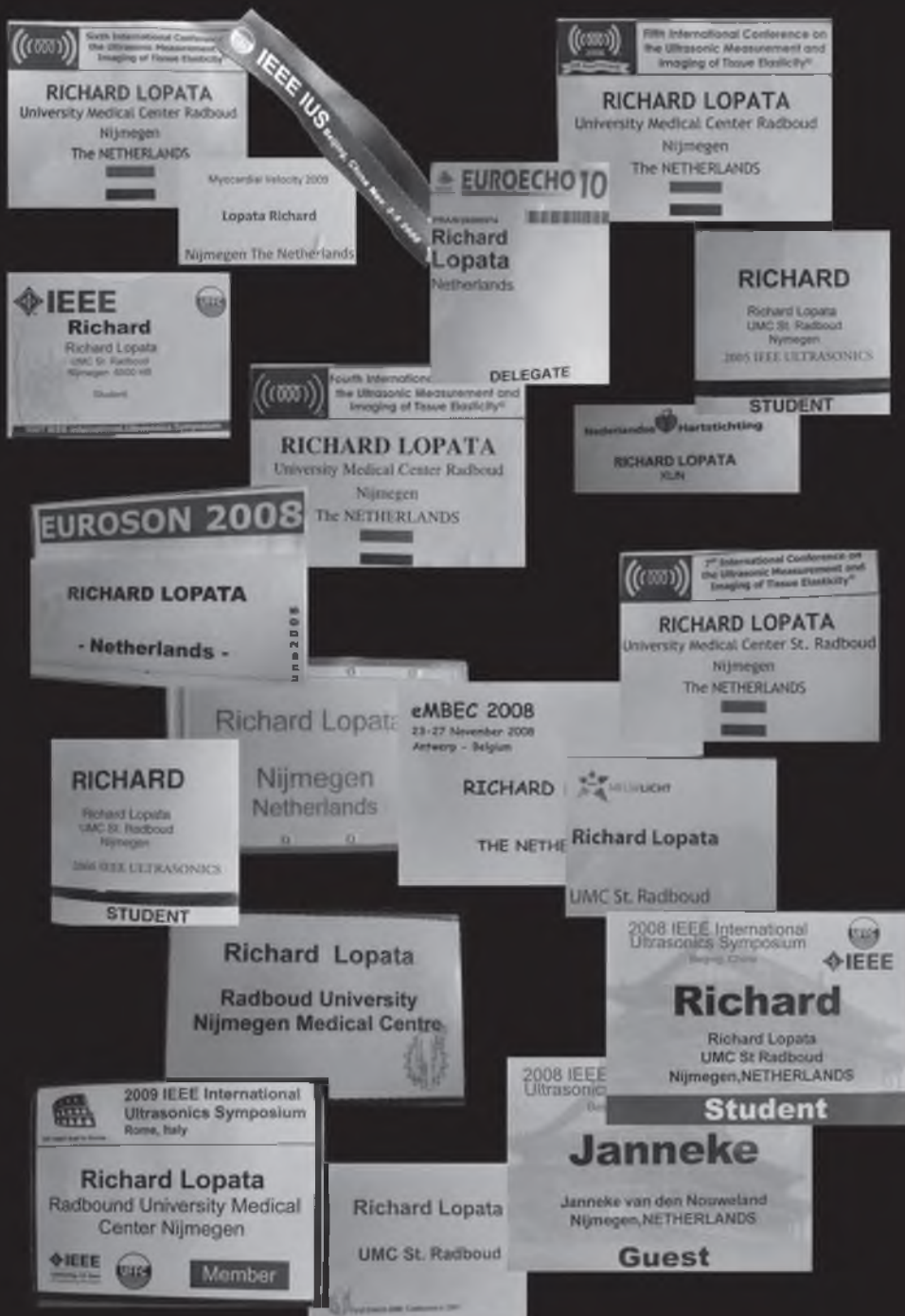
van Hees NJM, Thijssen JM, Huyskens RW, et al. *Quantitative Ultrasound Imaging of Healthy and Reconstructed Cleft Lip: a Feasibility Study.* Cleft Palate Craniofac J 2007; 44: 261-268.

van Stralen M, Bosch JG, Voormolen MM, et al. *Left ventricular volume estimation in cardiac three-dimensional ultrasound: a semiautomatic border detection approach.* Acad Radiol 2005; 12: 1241-1249.

Varghese T, Ophir J, Céspedes I. *Noise reduction in elastograms using temporal stretching with multicompression averaging.* Ultrasound Med Biol 1996; 22: 1043-1052.

Varghese T, Ophir J. *A theoretical framework for*

- performance characterization of elastography: the strain filter. *IEEE Trans Ultrason Ferroel Freq Contr* 1997; 44: 164-172.
- Varghese T, Bilgen M, Ophir J. *Multiresolution imaging in elastography*. *IEEE Trans Ultrason Ferroel Freq Contr* 1998a; 45: 65-75.
- Varghese T, Ophir J. *Characterization of elastographic noise using the envelope of echo signals*. *Ultrasound in Medicine and biology* 1998b; 24: 543-55.
- Vegter F, Mulder JW, Hage JJ. *Major residual deformities in cleft patients: a new anthropometric approach*. *Cleft Palate Craniofac J* 1997; 34: 106-110.
- Waldman LK, Fung YC, Covell JW. *Transmural myocardial deformation in the canine left ventricle. Normal in vivo three-dimensional finite strains*. *Circ Res* 1985; 57: 152-163.
- Weidemann F, Jamal F, Kowalski M, et al. *Can strain rate and strain quantify changes in regional systolic function during dobutamine infusion, B-blockade, and atrial pacing--implications for quantitative stress echocardiography*. *J Am Soc Echocardiogr* 2002; 15: 416-424.
- Willmann R, Possekel S, Dubach-Powell J, Meier T, Ruegg MA. *Mammalian animal models for Duchenne muscular dystrophy*. *Neuromuscul. Disord* 2009; 19: 241-249.
- Witte RS, Dow DE, Olafsson R, Shi Y, O'Donnell M. *High Resolution Ultrasound Imaging of Skeletal Muscle Dynamics and Effects of Fatigue*. *Proc IEEE Ultrasonics Int Conf, Montreal, Canada* 2004; 764-767.
- Witte RS, Kim K, Huang SW, Martin BJ, O'Donnell M. *Least-squares spline for reducing tracking error in muscle strain imaging*. *Proc 6th Intern Tissue Elasticity Conference, Santa Fe, NM, USA* 2007; 97.
- Xie H, Kim K, Aglyamov SR, et al. *Staging deep venous thrombosis using ultrasound elasticity imaging: animal model*. *Ultrasound Med Biol* 2004; 30: 1385-1396.
- Yagi S, Nakayama K. *Local displacement analysis of inhomogeneous soft tissue by spatial correlation of RF echo signals*. *Proc 1998 World Fed for Ultrasound Med Biol* 1988; 133.
- Yamakoshi Y, Sato J, Sato T. *Ultrasonic imaging of internal vibration of soft tissue under forced vibration*. *Proc Sec Joint Mtg of ASA and ASJ* 1998; Abstract RR-12.
- Yan P, Jia CX, Sinusas A, Thiele K, O'Donnell M, Duncan JS. *LV segmentation through the analysis of radio frequency ultrasonic images*. *Inf Process Med Imag* 2007; 20: 233-244.
- Yoshikawa H, Azuma T, Kawabata KTY, Umemura S. *Three-Dimensional Tracking Method of Tissue Motion with Biplane Images*. *Jap J Appl Physics* 2005; 44: 4561-4566.
- Yu W, Yan P, Sinusas A, Thiele K, Duncan J. *Towards pointwise motion tracking in echocardiographic image sequences - Comparing the reliability of different features for speckle tracking*. *Med Image Analysis* 2006; 10: 495-508.
- Zahiri-Azar R, Salcudean SE. *Time-delay estimation in ultrasound echo signals using individual sampletracking*. *IEEE Trans Ultrason Ferroel Freq Contr* 2008; 55: 2640-2650.
- Zhong X, Epstein FH, Spottiswoode BS, Helm PA, Blemker SS. *Imaging two-dimensional displacements and strains in skeletal muscle during joint motion by cine DENSE MR*. *J Biomech* 2008; 41: 532-540.



---

**PUBLICATIONS**  
**AWARDS**  
**&**  
**CONFERENCES**

---



---

## PEER-REVIEWED PAPERS IN INTERNATIONAL JOURNALS

- **Lopata RGP**, Nillesen MM, Thijssen JM, Kapusta L, de Korte CL. Three-dimensional cardiac strain imaging in healthy children using RF-data. *Ultrasound in Medicine and Biology*, 2010; *Submitted*.
- Nillesen MM, **Lopata RGP**, Huisman HJ, Thijssen JM, Kapusta L, de Korte CL. Correlation Based 3-D Segmentation of Echocardiographic Images using Radio Frequency Data. *IEEE Transactions on Medical Imaging*, 2010; *Submitted*.
- Hansen HHG, **Lopata RGP**, Idzenga T, de Korte CL. An angular compounding technique using displacement projection for noninvasive ultrasound strain imaging of vessel cross-sections. *Ultrasound in Medicine and Biology*, 2010; *In press*
- **Lopata RGP**, van Dijk JP, Pillen S, Nillesen MM, Maas H, Thijssen JM, Stegeman DF, de Korte CL. Dynamic imaging of skeletal muscle contraction in three orthogonal directions. *Journal of Applied Physiology*, 2010. *In press (E-pub)*.
- Hansen HHG, **Lopata RGP**, Idzenga T, de Korte CL. Full 2D displacement vector and strain tensor estimation for superficial tissue using beam-steered ultrasound imaging. *Physics in Medicine and Biology* 2010, 55(11); 3201-3218.
- **Lopata RGP**, Hansen HHG, Nillesen MM, Thijssen JM, de Korte CL. Methodical Study on the Measurement of Strain in Deforming Structures with Large Shearing and Rotational Movement using RF-based 1D and 2D Strain Estimation. *IEEE Ultrasonics, Ferro-electrics & Frequency Control*, 2010. 57(4); 855-865.
- **Lopata RGP**, Nillesen MM, Verrijp CN, Singh SK, Van Wetten HB, Lammens MMY, van der Laak JAWM, Thijssen JM, Kapusta L, de Korte CL. Cardiac Biplane Strain Imaging: Initial In Vivo Experience. *Physics in Medicine and Biology*, 2010. 55; 963-979.
- **Lopata RGP**, Nillesen MM, Hansen HHG, Gerrits IH, Thijssen JM, de Korte CL. Performance of Two-Dimensional Displacement and Strain Estimation Techniques Using a Phased Array Transducer. *Ultrasound in Medicine and Biology*, 2009; 35(12): 2031-2041.
- **Lopata RGP**, Hansen HHG, Nillesen MM, Thijssen JM, de Korte CL. Comparison of One-Dimensional and Two-Dimensional Least-Squares Strain Estimators for Phased Array Displacement Data. *Ultrasonic Imaging*, 2009; 31(1): 1-16.

- **Lopata RGP**, Nillesen MM, Hansen HHG, Gerrits IH, Thijssen JM, de Korte CL. Performance Evaluation of Methods for Two-Dimensional Displacement and Strain Estimation using Ultrasound Radio Frequency Data. *Ultrasound in Medicine & Biology*, 2009; 35(5): 796-812.
- Nillesen MM, **Lopata RGP**, de Boode WP, Gerrits IH, Huisman HJ, Thijssen JM, Kapusta L, de Korte CL. In Vivo Validation of Cardiac Output Assessment in Non-Standard 3D Echocardiographic Images. *Physics in Medicine & Biology*, 2009; 54(7): 1951-1962.
- Hansen HHG, **Lopata RGP**, de Korte CL. Non invasive carotid strain imaging using angular compounding at large beam steered angles: validation in vessel phantoms, *IEEE Transactions on Medical Imaging*, 2009; 28(6): 872-880.
- de Korte CL, van Hees N, **Lopata RGP**, Weijers G, Katsaros C, Thijssen JM. Quantitative Assessment of Oral Orbicular Muscle Deformation after Cleft Lip Reconstruction: an Ultrasound Elastography study. *IEEE Transactions on Medical Imaging*, 2009; 28(6): 1217-1222.
- Nillesen, MM, **Lopata RGP**, Gerrits, IH, Kapusta, L, Thijssen JM, de Korte C.L. Modeling Envelope Statistics of Blood and Myocardium for Segmentation of Echocardiographic Images. *Ultrasound in Medicine & Biology*, 2008; 34(4): 674-680.
- **Lopata RGP**, Backes WH, van den Bosch PPJ, Van Riel NAW. On the Identifiability of Pharmacokinetic Parameters in Dynamic Contrast-Enhanced Imaging. *Magnetic Resonance in Medicine* 2007; 58: 425-429.
- Nillesen MM, **Lopata RGP**, Gerrits IH, Kapusta L, Huisman HJ, Thijssen JM, de Korte CL. Segmentation of the heart muscle in 3-D pediatric echocardiographic images. *Ultrasound in Medicine and Biology* 2007; 33 (9): 1453-1462.
- Ribbers H, **Lopata RGP**, Holewijn S, Pasterkamp G, Blankensteijn JD, de Korte CL. Non-invasive two-dimensional strain imaging of arteries: validation in phantoms and preliminary experience in carotid arteries in vivo. *Ultrasound in Medicine & Biology* 2007; 33 (4): 530-540.



## AWARDS

### **Young Investigator Award 2009 - Best Student Paper**

‘On the Feasibility of Monitoring Cardiac Hypertrophy and Fibrosis using BiPlane Strain Imaging’,

The 8<sup>th</sup> International Conference on the Ultrasonic Measurement and Imaging of Tissue Elasticity 2009  
Vlissingen, The Netherlands.

### **Student Award BME 2009 (Best Oral Presentation)**

‘4D Cardiac Strain Imaging: Methods and Initial In Vivo Results’  
Second Dutch Biannual Conference on Biomedical Engineering 2009,  
Egmond aan Zee, the Netherlands

### **Young Investigator Award of the European Federation of Societies for Ultrasound in Medicine and Biology 2008**

‘4D Cardiac Strain Imaging for diagnosis of chronic heart failure’  
20<sup>th</sup> Euroson Congress 2008  
Timisoara, Rumania.

### **IEEE-UFFC Student Award 2006**

‘In Vivo 3D Cardiac and Skeletal Muscle Strain Estimation’  
IEEE International Ultrasonics Symposium 2006  
Vancouver, Canada.

## TRAVEL FUNDS

### **IEEE-UFFC Student Travel Award 2008**

‘BiPlane Cardiac Strain Imaging: A Study on Valvular Aortic Stenosis’  
IEEE Ultrasonics Symposium 2008  
Beijing, China.

### **Travel Award / Invited Oral Presentation**

‘In Vivo 3D Cardiac Elastography in an Animal Model and Human Heart’  
EuroEcho 2006  
Prague, Czech Republic.

## PROCEEDINGS

- **Lopata RGP**, Lindeboom L, Nillesen MM, de Korte CL, Bosboom EMH, van de Vosse FN. Fusion of 2D B-mode Images for Enhancement of the Abdominal Aorta. Proceedings IEEE Ultrasonics Symposium, San Diego, CA, USA, 2009. *In press*
- **Lopata RGP**, Hansen HHG, Schurink GW, van de Vosse FN, Bosboom EMH, de Korte CL. 2D RF-based Strain Imaging in the Normal and Diseased Aorta: A Feasibility Study. Proceedings IEEE Ultrasonics Symposium, San Diego, CA, USA, 2009. *In press*
- **Lopata RGP**, Nillesen MM, Kapusta L, Thijssen JM, de Korte CL. 4D RF-based Cardiac Strain IMaging in Healthy Children: Initial In Vivo Experience. Proceedings IEEE Ultrasonics Symposium, San Diego, CA, USA, 2009. *In press*
- Hansen HHG, **Lopata RGP**, Idzenga T, de Korte CL. Fast strain tensor imaging using beam steered plane wave ultrasound transmissions. Proceedings IEEE Ultrasonics Symposium, San Diego, CA, USA, 2009. *In press*
- **Lopata RGP**, Hansen HHG, Nillesen MM, Thijssen JM, de Korte CL. A Novel 2D Displacement Estimation Method using Free-shape Kernels of Radio Frequency Ultrasound Data in Rotating and Shearing Structures. Proceedings IEEE Ultrasonics Symposium, Rome, Italy, 2009; 2433-2436.
- **Lopata RGP**, van Dijk JP, Pillen S, Thijssen JM, Stegeman DF, de Korte CL. BiPlane Ultrasound Strain Imaging during Induced Contraction of Skeletal Muscles. Proceedings IEEE Ultrasonics Symposium, Rome, Italy, 2009; 455-458.
- Hansen HHG, **Lopata RGP**, Idzenga T, De Korte, C.L.: High quality non-invasive full 2D strain tensor imaging using a beam steered linear array ultrasound transducer, Proceedings of the IEEE International Symposium on Ultrasound, Rome, Italy, 2009; 1720-1723.
- Idzenga T, Hansen HHG, **Lopata RGP**, de Korte, C.L.: Non-invasive assessment of shear strain in the carotid arterial wall based on ultrasound radiofrequency data. Proceedings of the IEEE International Ultrasound Symposium, Rome, Italy, 2009; 2456-2460.
- Nillesen MM; **Lopata RGP**, Gerrits IH, Thijssen JM, Kapusta L, de Korte CL. 3D Cardiac Segmentation using Temporal Correlation of Radio Frequency Ultrasound Images. Med Image Comput Comput Assist Interv Lect Notes Comput Sc 2009; 5762: 927-934.

- Nillesen MM, **Lopata RGP**, Gerrits IH, Huisman HJ, Thijssen JM, Kapusta L, de Korte CL. Segmentation of 3D Cardiac Ultrasound Images using Correlation of Radio Frequency Data. Proceedings of the International Symposium of Biomedical Imaging, Boston, USA, 2009, 522-525.
- **Lopata RGP**, Nillesen MM, Gerrits IH, Hansen HHG, Kapusta L, Thijssen JM, de Korte CL. 3D Cardiac Strain Imaging using a Novel Tracking Method. Proceedings 4th European Conference of the International Federation for Medical and Biological Engineering, 2008; 22: 697-700.
- Nillesen MM, **Lopata RGP**, Gerrits IH, Kapusta L, Huisman HJ, Thijssen JM, de Korte CL. Segmentation of 3D Echocardiographic Images using Deformable Simplex Meshes and Adaptive Filtering. Proceedings 4th European Conference of the International Federation for Medical and Biological Engineering, 2008; 22: 550-554.
- Hansen HHG, **Lopata RGP**, Holewijn S, Truijers M, de Korte CL. Non-invasive Vascular Ultrasound Strain Imaging: Different Arteries, Different Approaches. Proceedings 4th European Conference of the International Federation for Medical and Biological Engineering, 2008; 22: 298-302
- **Lopata RGP**, Nillesen MM, Gerrits IH, Kapusta L, Thijssen JM, de Korte CL. BiPlane Cardiac Strain Imaging: A Study on Valvular Aortic Stenosis. IEEE International Ultrasonics Symposium, Beijing, China, 2008; 950-953.
- Nillesen MM, **Lopata RGP**, de Boode WP, Gerrits IH, Huisman HJ, Thijssen JM, Kapusta L, de Korte, CL. Cardiac output estimation in Non-Standard Echocardiographic Images. IEEE Int. Ultrasonics Symposium, Beijing, China, 2008; 1745-1748.
- de Korte CL, **Lopata RGP**, Nillesen MM, Weijers G, van Hees NJ, Gerrits IH, Katsaros C, Kapusta L, Thijssen JM. Ultrasound strain imaging: from nano-scale motion detection to macro-scale functional imaging. ISBI 2008. 5th IEEE International Symposium on Biomedical Imaging: From Nano to Macro, 2008; 544-547.
- de Korte CL, **Lopata RGP**, Hansen HHG, Nillesen MM, Gerrits IH, Kapusta L, Thijssen JM. Cardio Vascular Ultrasound Elastography. International Congress of Acoustics, Madrid, Spain, 2007; 394-395.
- **Lopata RGP**, Nillesen MM, Gerrits IH, Thijssen JM, Kapusta L, de Korte CL. 4D Cardiac Strain Imaging: Methods and Initial Results. IEEE International Ultrasonics Symposium, New York, NY, USA, 2007; 872-875.
- Nillesen MM, **Lopata RGP**, Gerrits IH, Kapusta L, Huisman HJ, Thijssen JM, de Korte CL. Three-dimensional Cardiac Image Segmentation using Adaptive Filtering and 3D Deformable Simplex Meshes. Proceedings of the IEEE International Ultrasonics Symposium, New York, NY, U.S.A., October 2007; 1468-1471.

- Gerrits IH, Nillesen MM, **Lopata RGP**, Rijk JPT, Thijssen JM, de Korte CL. A Robust Deformable Simplex Mesh Model with Temporal Signal De-correlation Constraints in Echocardiography. IEEE International Ultrasonics Symposium, New York, USA, 2007; 1484-1487.
- Hansen H.H.G., **Lopata RGP**, De Korte CL. Compounding of strain data non-invasively obtained at large beam steered angles. Proceedings of the IEEE International Ultrasonics Symposium, New York, NY, USA, 2007; 1720-1723.
- Maanders M, **Lopata RGP**, Bosboom EMH, van de Vosse FH, Lotgering FK, de Korte CL. Cervix Elastography: A preliminary study. EMBS Ann. Symp., NL 2007; 64-67.
- **Lopata RGP**, Nillesen MM, Gerrits IH, Thijssen JM, Kapusta L, de Korte CL. In Vivo 3D Cardiac and Skeletal Muscle Strain Estimation. IEEE Ultrasonics Symposium Vancouver, 2006; 744-747.
- Nillesen MM, **Lopata RGP**, Gerrits IH, Kapusta L, Huisman HJ, Thijssen JM, de Korte CL. 3D Segmentation of the Heart Muscle in Real-Time 3D Echocardiographic Sequences using Image Statistics. IEEE Ultrasonics Symposium 2006, Vancouver, Canada. 1987-1990.
- Nillesen MM, **Lopata RGP**, Gerrits IH, Kapusta L, Huisman HJ, Thijssen JM, de Korte CL. Three Dimensional Segmentation of the Heart Muscle using Image Statistics. SPIE Medical Imaging 2006, San Diego, CA, USA. Vol. 6147, p. 204-212.
- Nillesen MM, **Lopata RGP**, Gerrits IH, Kapusta L, Huisman HJ, Thijssen JM, de Korte CL. 3D Segmentation of the Heart Muscle in Real-Time 3D Echocardiographic Sequences using Image Statistics. Computers in Cardiology 2006, Valencia, Spain, 129-132.
- **Lopata RGP**, Nillesen MM, Gerrits IH, Kapusta L, Thijssen JM, de Korte CL. 3D Strain Estimation for Isotropic and Anisotropic Materials. IEEE International Ultrasonics Symposium, Rotterdam, NL, 2005; 731-734.
- Ribbers H, **Lopata RGP**, Holewijn S, Blankensteijn JD, de Korte CL. Non-invasive two dimensional elastography of the carotid artery. IEEE International Ultrasonics Symposium, Rotterdam, NL, 2005; 1113-1116.
- **Lopata RGP**, van Riel NAW. Identifiability Analysis of the Standard Pharmacokinetic Models in DCE MR Imaging of Tumours. Conf Proc IEEE Eng Med Biol Soc, 2004; 2: 1040-1043.

## CONFERENCE PRESENTATIONS

- **Lopata RGP**, Nillesen MM, Thijssen JM, Kapusta L, de Korte CL. 4D Cardiac Strain Imaging using RF-data in Young Children. 9th Int. Conf. on the Ultrasonic Measurement and Imag. of Tissue Elasticity, Snowbird, UT, USA, Oct 2009. Oral presentation.
- **Lopata RGP**, Hansen HHG, Schurink GW, de Korte CL, Bosboom EMH, van de Vosse FN. RF-based 2D Strain Imaging in the Normal and Diseased Abdominal Aorta. 9th Int. Conf. on the Ultrasonic Measurement and Imaging of Tissue Elasticity, Snowbird, UT, USA, Oct 2009. Oral presentation.
- **Lopata RGP**, Lindboom L, Nillesen MM, de Korte CL, Bosboom EMH, van de Vosse FN. Fusion of 2D B-mode Images for Enhancement of the Abdominal Aorta. IEEE Ultrasonics Symposium 2010, San Diego, CA, USA, Oct 2009. Poster presentation.
- **Lopata RGP**, Hansen HHG, Schurink, van de Vosse FN, Bosboom EMH, de Korte CL. 2D RF-based Strain Imaging in the Normal and Diseased Aorta: A Feasibility Study. IEEE Ultrasonics Symposium 2010, San Diego, CA, USA, Oct 2009. Oral presentation.
- **Lopata RGP**, Nillesen MM, Kapusta L, Thijssen JM, de Korte CL. 4D RF-based Cardiac Strain IMaging in Healthy Children: Initial In Vivo Experience. IEEE Ultrasonics Symposium 2010, San Diego, CA, USA, Oct 2009. Oral presentation.
- **Lopata RGP**, van Dijk JP, Pillen S, Thijssen JM, Stegeman DF, de Korte CL. BiPlane Ultrasound Strain Imaging during Induced Contraction of Skeletal Muscles. IEEE Ultrasonics Symposium 2009, Rome, Italy. Oral presentation.
- **Lopata RGP**, Hansen HHG, Nillesen MM, Thijssen JM, de Korte CL. A Novel 2D Displacement Estimation Method using Free-shape Kernels of Radio Frequency Ultrasound Data in Rotating and Shearing Structures. IEEE Ultrasonics Symposium 2009, Rome, Italy. Poster presentation.
- **Lopata RGP**, Nillesen MM, Kapusta L, Singh SK, Van Wetten HB, Lammens MMY, van der Laak JAWM, Thijssen JM, de Korte CL. On the Feasibility of Monitoring Cardiac Hypertrophy and Fibrosis using Biplane Strain Imaging. 8<sup>th</sup> Int. Conf. on the Ultrasonic Measurement and Imaging of Tissue Elasticity, Vlissingen, NL, Oct. 2009; Oral presentation.
- **Lopata RGP**, Hansen HHG, Nillesen MM, Thijssen JM, de Korte CL. Performance of RF-Based 2D Strain Imaging Techniques in Deforming Structures with Large Shearing and Rotational Movement. 8<sup>th</sup> Int. Conf. on the Ultrasonic Measurement and Imaging of Tissue Elasticity, Vlissingen, NL, Oct. 2009; Oral presentation.

- **Lopata RGP**, Nillesen MM, Gerrits, Gerrits IH, Kapusta L, Thijssen JM, de Korte CL. In Vivo 4D Cardiac Strain Imaging: Methods and Initial In Vivo Results. 2<sup>nd</sup> Dutch Conf. on Biomedical Engineering, Egmond aan Zee, the Netherlands, Jan. 2009; Oral presentation
- **Lopata RGP**, Nillesen MM, Gerrits IH, Hansen HHG, Kapusta L, Thijssen JM, de Korte CL. 3D Cardiac Strain Imaging using a Novel Tracking Method. 4<sup>th</sup> European Conference of the Intern. Fed. for Medical and Biological Engineering, Nov. 2008; Oral presentation.
- **Lopata RGP**, Nillesen MM, Gerrits IH, Kapusta L, Thijssen JM, de Korte CL. BiPlane Cardiac Strain Imaging: A Study on Valvular Aortic Stenosis. IEEE International Ultrasonics Symposium, Beijing, China, Nov. 2008; Oral presentation.
- **Lopata RGP**, Nillesen MM, Hansen HHG, Gerrits IH, Thijssen JM, de Korte CL. Free-shape 2D kernels for Improved Measurement of Rotations and Strains in Shearing Structures. 7<sup>th</sup> Int. Conf. on the Ultrasonic Measurement and Imaging of Tissue Elasticity, Austin, TX, USA, Oct. 2008; Oral presentation.
- **Lopata RGP**, Nillesen MM, Gerrits IH, Kapusta L, Thijssen JM, de Korte CL. 4D Cardiac Strain Imaging for diagnosis of chronic heart failure. Nieuw Licht NVKF, Kaatsheuvel, Netherlands, Sept. 2008; Poster presentation.
- **Lopata RGP**, Nillesen MM, Gerrits IH, Kapusta L, Thijssen JM, de Korte CL. 4D Cardiac Strain Imaging for diagnosis of chronic heart failure. Euroson, Timisoara, Rumania, Jun. 2008; Oral presentation.
- **Lopata RGP**, Nillesen MM, Gerrits IH, Thijssen JM, Kapusta L, de Korte CL. 4D Cardiac Strain Imaging in the Human Heart: Initial in vivo Results. 6<sup>th</sup> Int. Conf. on the Ultrasonic Measurement and Imaging of Tissue Elasticity, Santa Fé, NM, USA, 2007; Oral presentation
- **Lopata RGP**, Nillesen MM, Gerrits IH, Thijssen JM, Kapusta L, de Korte CL. 4D Cardiac Strain Imaging: Methods and Initial Results. IEEE Int. Ultrasonics Symposium, New York, NJ, USA, Oct. 2007; Oral presentation.
- **Lopata RGP**, Nillesen MM, Gerrits, Gerrits IH, Kapusta L, Thijssen JM, de Korte CL. In Vivo 3D Cardiac Elastography in an Animal Model of the Human Heart. 1<sup>st</sup> Dutch Conf. on Biomedical Engineering, Egmond aan Zee, NL, Jan. 2007. Oral presentation
- **Lopata RGP**, Nillesen MM, Gerrits IH, Thijssen JM, Kapusta L, de Korte CL. In Vivo 3D Cardiac Elastography in an Animal Model and Human Heart. EuroEcho 2006, Prague, Czech Republic, Dec. 2006. Invited oral presentation.

- **Lopata RGP**, Nillesen MM, van Dijk JP, Gerrits IH, Thijssen JM, de Korte CL. In vivo 3D Elastography of Induced Skeletal Muscle Contraction. 5<sup>th</sup> Int. Conf. on the Ultrasonic Measurement and Imaging of Tissue Elasticity, Snowbird, UT, USA, Oct. 2006; Oral presentation.
- **Lopata RGP**, Nillesen MM, van de Vosse FN, Gerrits IH, Thijssen JM, Kapusta L, de Korte CL. In vivo 3D Elastography in an Animal Model and Human Heart. 5<sup>th</sup> Int. Conf. on the Ultrasonic Measurement and Imaging of Tissue Elasticity, Snowbird, UT, USA, Oct. 2006; Oral presentation.
- **Lopata RGP**, Nillesen MM, Gerrits IH, Thijssen JM, Kapusta L, de Korte CL. In Vivo 3D Cardiac and Skeletal Muscle Strain Estimation. IEEE Int. Ultrasonics Symposium Vancouver, Canada, Oct. 2006; Poster & Oral presentation.
- **Lopata RGP**, Nillesen MM, Gerrits IH, Kapusta L, Livia, Thijssen JM, de Korte CL. Comparison of Three Different Non-Axial Strain Estimation Techniques for 3D Strain Estimation in Elastic Materials and Tissues. 4<sup>th</sup> Int. Conf. on the Ultrasonic Measurement and Imaging of Tissue Elasticity, Austin, TX, USA; Oct. 2005; Oral presentation.
- **Lopata RGP**, Nillesen MM, Gerrits IH, Kapusta L, Thijssen JM, de Korte CL. 3D Strain Estimation for Isotropic and Anisotropic Materials. IEEE Int. Ultrasonics Symposium, Rotterdam, NL, Sept. 2005; Oral presentation.

---

I – I love the colorful clothes she wears.  
And she's already workin' on my brain.  
I – I only looked in her eyes,  
but I picked up something I just can't explain.

I'm pickin' up good vibrations  
she's giving me excitations.  
Good, good, good – good vibrations.

...

...

.

(- *Good Vibrations* by Brian Wilson, Michael Love & Tony Asher)

---



---

My soul is painted like the wings of butterflies  
Fairy tales of yesterday will grow but never die  
I can fly, my friends

The show must go on  
The show must go on  
I'll face it with a grin, I'm never giving in, on with the show

(- *The Show Must Go On* by Queen)

---

---

# CURRICULUM VITAE

---



## ABOUT THE AUTHOR ...

Richard Godfried Paulus Lopata was born in Oosterhout, the Netherlands (27-02-1980) as an only child of Fred Lopata and Diny Lopata - van de Reijen. He received his Atheneum diploma (cum laude) at the Monsieur Frencken College, Oosterhout, The Netherlands, in 1998. He chose to study BioMedical Engineering at the Eindhoven University of Technology, Eindhoven, The Netherlands. He received his M.Sc. degree in BioMedical Engineering in 2004 with the judicium 'With Great Appreciation' after defending his Master thesis on Dynamic Contrast-Enhanced MR Imaging and Pharmacokinetic Modeling of Tumor Perfusion, under supervision of prof. dr. ir. P.P.J. van den Bosch and dr. ir. N.A.W van Riel. Part of this research was performed at the MRI Institute and Wayne State University in Detroit MI, USA, under supervision of prof. E.M. Haacke.

In november 2004, Richard started work on his PhD project, entitled "3D Functional Imaging of the Heart" at the Clinical Physics Laboratory of the Radboud University Nijmegen Medical Centre under the supervision of dr. ir. C.L. de Korte and prof. dr. ir. J.M. Thijssen. The work was, or had to be, finished in november 2009 after five enjoyable and fruitful years. In this period, he has (co-)authored over ten peer-reviewed papers and won several awards at one national and several international conferences.

Richard has returned to 'the old nest' (Dutch proverb) and was appointed in a post-doc project at the Department of BioMedical Engineering, now residing at both the Eindhoven University of Technology and Maastricht University. The main focus of this project will be the measurement of the mechanical properties of Abdominal Aortic Aneurysms (AAA, or 'Triple A') by means of multi-modality imaging and medical image analysis.

Richard's research interests include strain imaging, elastography, 2D & 3D ultrasound, medical image analysis, muscle dynamics, and cardiovascular disease. Other topics of interest are MRI, signal processing, biological modeling and identifiability analysis. Besides work, most of his time is devoted to his family life, music and playing the drums.

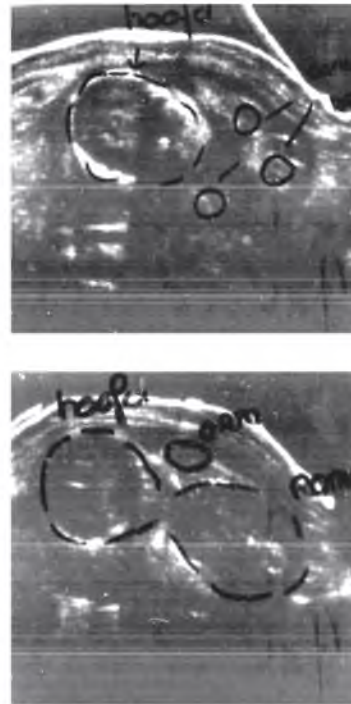


Figure: Sonogram of the author at the age of minus three months (upper) and minus two months (lower). It is clear from these images and the figures presented in the thesis that there is a high correlation between the development of the author and ultrasound equipment.



